Modelling and evaluation of carbon based foam thermoacoustic effect for effective sound generation in fluids

Pierre, Henri Guiraud

Numéro d'ordre : 403

Centrale Lille

Thèse

pour obtenir le grade de :

Docteur

dans la spécialité

« Micro et nano technologies, acoustique et télécommunications »

par

Pierre Guiraud

Doctorat délivré par Centrale Lille

Analyse Théorique et Expérimentale de l'Efficacité de Mousse de Carbone pour Génération Acoustique dans des Milieux Visqueux

---

Modelling and Evaluation of Carbon Based Foam Thermoacoustic Effect for Effective Sound Generation in Fluids

Soutenance le 20 novembre 2020 devant le jury composé de :

M. Franck Levassort	Professeur à l'Université de Tours, GREMAN	(Examinateur, Président)
Mme. Diana Baltean	Maitre de Conférence Univ. Pierre et Marie Curie, LIMSI	(Rapporteure)
M. Pierrick Lotton	Directeur de recherche CNRS, LAUM	(Rapporteur)
Mme. Juliette Pierre	Chargée de recherche CNRS, MPIA	(Examinatrice)
M. Stefano Giordano	Chargé de recherche CNRS, IEMN	(Co-directeur de thèse)
M. Olivier Bou-Matar	Professeur à Centrale Lille, IEMN	(Co-directeur de thèse)
M. Philippe Pernod	Professeur à Centrale Lille, IEMN	(Co-encadrant)
M. Raphael Lardat	Expert Acoustique à Thales Underwater System	(Co-encadrant)
M. Philippe Coquet	Maître de conférence à l'Université de Lille	(Invité, co-encadrant)
M. Philippe Pouliguen	Responsable Acoustique, Ondes Radio-Electrique, DGA	(Invité)

Thèse préparée au Laboratoire International Associé (LIA) LEMAC/LICS
IEMN - Cité Scientifique - Avenue Henri Poincaré
CS 60069 - 59 652 Villeneuve d'Ascq Cedex
Ecole Doctorale SPI 072

“The most exciting phrase to hear in science,
the one that heralds the most discoveries,
is not "Eureka!" (I found it!) but ’That’s funny...”
— Isaac Asimov

“Highly organized research is guaranteed to produce nothing new.”
— Frank Herbert

RÉSUMÉ FRANÇAIS

La reproduction du son est devenue si courante, si connue et si bon marché qu'un livre et quelques connaissances en électronique permettent à n'importe qui de construire un haut-parleur. Le principe de fonctionnement d'un transducteur électroacoustique commun repose sur une bobine et un aimant qui induisent la vibration d'une membrane générant des ondes sonores. Ces systèmes mécaniques ont été étudiés depuis plus de cent ans, sont bien compris et sont utilisés dans de nombreux domaines différents. Les défis actuels en matière de reproduction audio pour les fabricants de hifi sont principalement liés à la compréhension d'un comportement non linéaire spécifique ou à la création de nouvelles formes, de nouvelles géométries pour les haut-parleurs tout en conservant une très haute fidélité de reproduction.

Néanmoins, ces transducteurs électroacoustiques présentent toujours des problèmes inhérents, spécifiques à la manière dont le son est produit. La génération mécanique, par exemple, est un mécanisme résonant (les haut-parleurs ont besoin d'un grand baffle pour les basses fréquences et d'un petit baffle pour les hautes fréquences). L'utilisation de plusieurs haut-parleurs et filtres électroniques est nécessaire pour obtenir une génération sur une large bande de fréquence. En outre, au-dessus des fréquences audibles, les transducteurs électroacoustiques ont des difficultés à fonctionner et sont généralement remplacés par un autre moyen mécanique de produire le son : les dispositifs piézoélectriques. Les sources piézoélectriques sont généralement utilisés pour des applications spécifiques (génération acoustique sous l'eau pour les sonars, génération d'ultrasons... etc) mais restent cependant lourds et, étant également basés sur un principe mécanique, sont donc résonants. À l'heure actuelle, aucun générateur acoustique léger et non résonant n'est disponible.

La génération du son par phénomène thermoacoustique consiste à utiliser un matériau à faible capacité thermique et à haute conductivité thermique pour engendrer une onde sonore. Chaque fois qu'une énergie alternative est fournie au matériau, le profil de température de l'échantillon suit la variation de l'énergie. Cette variation rapide de la température excitera l'air à proximité de l'échantillon, créant ainsi un état alternatif de compression et d'expansion du milieu dans lequel se trouve le matériau (gaz ou liquide). Dans l'air par exemple, cela créera une onde de pression et donc un son. Un matériau approprié pour créer ce phénomène thermoacoustique est appelé un thermophone.

La facilité d'accès croissante à des machines à forte valeur technologiques pour la fabrication de matériaux nanostructurés a en grande partie contribué à raviver l'intérêt pour les thermophones au XXIème siècle. Divers thermophones ont été étudiés et des modèles théoriques ont été développés en parallèle de ces expériences. Contrairement à leurs homologues mécaniques, les thermophones génèrent un son à large bande jusqu'au MHz. De plus, le processus de génération acoustique est indépendant de leur forme et leur procédé de fabrication les rend légers avec une géométrie très flexible. Les thermophones ont cependant montré une très faible efficacité par rapport aux haut-parleurs traditionnels. Ils sont également très fragiles et restent un sujet de recherche très spécialisé qui empêche des améliorations rapides et généralisées. Malgré cela, les thermophones constituent une alternative prometteuse pour la génération acoustique des années à venir.

Parmi les thermophones les plus récemment testés il y a les mousses thermoacoustiques à base de carbone. Leur géométrie unique permet d'augmenter la surface de contact avec l'air nécessaire pour que le processus thermoacoustique se produise efficacement. Dans ce manuscrit de thèse, l'accent sera mis sur la compréhension du processus thermoacoustique et plus spécifiquement sur la génération de matériaux en forme de mousse. Ainsi, les thermophones peuvent-ils remplacer les haut-parleurs traditionnels ? Auront-ils une place dans les dispositifs sonores des prochaines années ? et enfin est ce que les structures en mousse représentent la forme la plus adaptée à la génération thermoacoustique ?

Cette thèse CIFRE-Défense a été réalisée dans le cadre d'un projet de collaboration entre l'Institut d'Electronique, de Microélectronique et de Nanotechnologie (IEMN), Thales TUS et l'UMI CINTRA de Singapour (CNRS, Thales, Nanyang Technological University).

Le premier chapitre de cette thèse présente une analyse approfondie de l'état de l'art de l'histoire de la thermoacoustique et plus particulièrement du thermophone au cours des 200 dernières années. Le contexte et le but de ce travail y sont détaillés en se basant sur la littérature existante présentée. Le deuxième chapitre fournit les détails mathématiques sur la construction des modèles théoriques. Des modèles multicouches en milieux continus appelés une température (1T) sont créés sur la base d'hypothèses de propagation d'ondes planes, d'ondes cylindriques et d'ondes sphériques. Un nouveau modèle basé sur une hypothèse dite de deux températures (2T) est également créé pour les ondes planes afin de représenter plus précisément la génération thermoacoustique dans les thermophones en forme de mousse. Ces modèles sont comparés

aux modèles et expériences de la littérature dans le troisième chapitre. Ils sont analysés et une compréhension approfondie des capacités des thermophones est fournie. Enfin, le quatrième chapitre présente des expériences réalisées en partenariat avec CINTRA Singapour et plus particulièrement avec la doctorante Ngoh Zhi-Lin. Des mousses 3D à base de carbone (3D-C) créées à CINTRA sont utilisées et leurs performances confrontées à nos modèles théoriques. De plus, d'autres expériences acoustiques mais aussi de caractérisations réalisées à l'IEMN sont décrites et analysées. Le rayonnement acoustique est ainsi expliqué et des conseils de manipulation sont fournis. Les pistes expérimentales et les applications possibles sont enfin discutées pour des travaux futurs.

En ce qui concerne les modèles théoriques, le modèle multicouche 1T pour ondes planes permet d'avoir une réelle flexibilité dans la conception des thermophones, jamais atteinte auparavant dans la littérature. Ce faisant, il permet d'améliorer la compréhension des thermophones et la façon de les améliorer. Les modèles multicouches cylindriques et sphériques équivalents offrent un avantage similaire mais d'un intérêt moindre. Il est constaté que ces géométries se retrouvent surtout à l'échelle micro et que le besoin d'un modèle multicouche complexe n'est pas aussi établi que pour des ondes planes. Néanmoins, ces modèles sont les premiers à prendre en compte la propagation d'ondes dans le solide et à considérer la viscosité des milieux de propagations. Quant au modèle 2T, il est prouvé qu'il permet une meilleure représentation du rayonnement thermoacoustique des matériaux épais de type mousse. Cette idée de l'existence simultanée d'un solide et d'un fluide n'avait jamais été appliquée auparavant à la génération thermoacoustique.

L'étude qui en résulte concorde avec diverses analyses théoriques et expérimentales tirées de la littérature où les thermophones sont utilisés dans un certain nombre de configurations différentes. De plus, de nouvelles situations sont étudiées en utilisant la flexibilité de nos modèles. L'influence de l'épaisseur de la couche hydrophobe sur un échantillon immergé dans de l'eau est par exemple étudiée et pourrait par la suite être confrontée à des mesures réelles.

En utilisant diverses configurations expérimentales, des mesures prouvent l'efficacité de la génération acoustique des mousses de carbone dans l'air jusqu'à 1MHz. Cependant des difficultés liées à la manipulation de ces échantillons sont soulevées et peuvent servir de guide pour les futurs utilisateurs expérimentaux. Tout bien considéré, la géométrie de la mousse présente la propriété très intéressante d'avoir une surface spécifique élevée permettant une grande surface de contact pour éviter la surchauffe et pour permettre la génération de l'effet thermoacoustique à grande échelle. Malgré cela, à ce jour ses performances n'atteignent pas l'efficacité maximale théorique atteinte uniquement par

les forêts de nanotubes de carbone (CNT). L'amélioration apportée à la structure ne compense pas la faible efficacité de l'échantillon. Il est néanmoins espéré que cette thèse sensibilisera quand à l'intérêt de créer de nouvelles structures dans un but thermoacoustique, dans l'espoir d'améliorer la génération du son à partir des thermophones.

Dans l'ensemble, les thermophones sont une alternative prometteuse pour la production de sons. Bien que leur faible efficacité actuelle les empêche de remplacer les haut-parleurs commerciaux, leur mécanisme de génération sonore non mécanique induit une large bande de fréquences de fonctionnement. En outre, leur légèreté, leur géométrie flexible, leur petite taille et leur faible coût de production en font une nouvelle alternative potentielle pour des applications de sonar ou de transducteurs ultrasoniques. Le 3D-C présente notamment un avantage par rapport aux CNT pour la fabrication à grande échelle, car les CNT nécessitent un processus fastidieux consistant à utiliser un nanomanipulateur pour acquérir leurs brins à partir de forêts de CNT. La capacité du 3D-C et des thermophones en général à émettre un son de manière thermoacoustique mérite donc d'être étudiée en profondeur.

"It is sometimes an appropriate response to reality to go insane."

— Philip K. Dick

ACKNOWLEDGEMENTS

I would like first to thank Philippe Coquet (CNRS, UMI CINTRA) and Philippe Pernod (Centrale Lille, IEMN), who have settled a general framework of collaboration between the international laboratory UMI CINTRA and the AIMAN-FILMS Group of IEMN. I also would like to thank them, together with Olivier Bou Matar (Centrale Lille, IEMN), Stefano Giordano (CNRS, IEMN), Martine Doisy (Thales TUS), Raphael Lardat (Thales TUS), and Edwin Theo (NTU), for establishing this thesis CIFRE-Defense project within the latter framework. Many thanks to Thales TUS, ANRT (Association Nationale pour la Recherche et la Technologie), and DGA (Direction Générale de l'Armement) for their financial support of the thesis, and to Philippe Pouliguen who followed regularly the work for DGA.

This thesis is the conclusion of 3 years of work in the amazing AIMAN FILM group. The kindness and dedication that those people display everyday not only in research but also to teach, despite the ever challenging higher education environment is truly inspiring. Namely, I would like to thank Philippe Pernod who may was hard to reach but always took extra time when he could to temper my feelings and to provide me with insightful stories. Many thanks as well to Raphael Lardat who was also very positive about the work and myself even during indecisive time. Thank you to Philippe Coquet, Dunlin Tan, Ngoh Zhi Lin and the whole CINTRA laboratory for their warm welcome during my stay in Singapore and for the long distance work. This was a very rewarding experience and I will forever be grateful to have worked with you. Thank you to Olivier Bou-Matar for all the help, discussions and for being one of the most well-adjusted person I know. Always doing extra for everyone around him, personally and professionally. Last but not least, I can not emphasize enough how thankful I am to Stefano Giordano. In the most obvious way, thank you for being there all along the thesis, for the discussions and for bearing me and my need to talk out loud my inner thoughts. Thanks to you this thesis started with strong foundations and it would not have been the same without you. Thank you also personally for being such a kind and humble person, always being positive and cheering me and the other PhD students up.

Aside from the professional help, it is also necessary to acknowledge all the moral support I received from this team. In that regard, I first need to thank Manon for being my PhD sister. You were always here when I needed to vent or just have a break so thank you, those 3 years would have been very sad without you. Many thanks as well to Nicolas, Yannick, Munique, Karim, Aurelien, Mathias and Djamila for everything, and good luck to the new PhD generation Thomas and Romain. Don't worry it is over sooner than you think, just try to enjoy the ride. Thanks to those I am forgetting and lastly, I will probably not be the only one to thank the Foosball table which was maybe, just maybe, a reason for the drop in PhD productivity at some point.

Even though I am trying to not make this section as big as the manuscript, it would be unfair to not mention all the people outside of work that also were a part of those 3 years. To the other PhD students or just friends from different groups sharing a similar weight, Vincent, Dimitri, Davide, Saliha... thank you for the blind tests, the beers, the rock climbing and the rest. Similar thanks to Tom and Caro for the board games and to Lucie and Victor for all of the above. Thank you to my roommates Adrien, Laura, Clement and François which were a bigger part of it than they might know. Many thanks as well to Leonard and Thibault who were my senior PhD roommates by adoption. You were there at a point when I was not sure where I was, and even if you left early as you were supposed to, your music stayed with me until the end (boom lay...). 3 years seems short but all those people appeared and disappeared when they had to and for that I am thankful.

Finally, I should not forget that I was not alone either before those 3 years. As it will take forever to mention everyone, very shortly thank you to my friends from Montpellier, from Centrale and from DTU to have been there all those week-ends and to still be here when need be, even though life makes it more rare and more precious. Thank you to my parents to have always allowed me to do what I deemed to be right and for helping me become what I am today. I will always be grateful, I love you. At long last, I would like to express my loving gratitude to Florence. Those 3 years have not been easy on us but today more than ever we are ready to do whatever it takes to be together. I am eager to finish this part of my life and to start a new one with you.

And thank you for reading this Manuscript, sorry it is a bit long but at least it is thorough. Good luck.

PUBLICATIONS

Some ideas and figures have appeared previously in the following publications:

1. P. Guiraud, S. Giordano, O. Bou-Matar, P. Pernod and R. Lardat, J. Sound Vibr. **455**, 275 (2019), DOI: 10.1016/j.jsv.2019.05.001 [1]
2. P. Guiraud, S. Giordano, O. Bou-Matar, P. Pernod and R. Lardat, J. Appl. Phys. **126**, 165111 (2019), DOI: 10.1063/1.5121395 [2]
3. Z.L. Ngoh, P. Guiraud, D. Tan, S. Giordano, O. Bou-Matar, E. Teo, P. Pernod, P. Coquet, R. Lardat, Carbon **169**, 382-394 (2020), DOI: 10.1016/j.carbon.2020.06.045 [3]

INTRODUCTION

Sound reproduction has become so common so well known and so cheap that anyone with a book and some electronic knowledge could build a loudspeaker. The basic working principle of a common electroacoustic transducer consist of a coil/magnet core which induces vibration of a membrane system eventually generating sound waves. Those mechanical system have been studied for more than a hundred years, are well understood and are used in many different areas. Today's challenges regarding audio reproduction for hifi manufacturer are mostly about understanding peculiar non linear behavior or about trying to create new shapes, new geometries for loudspeakers while keeping a very high reproduction fidelity.

Nonetheless those electroacoustic transducers still have some inherent issues specific to the way the sound is produced. The mechanical generation for instance is a resonant mechanism (loudspeakers need a large baffle for low frequencies and a small one for high frequencies) and the use of multiple drivers and filters are needed to achieve an almost wideband generation. Furthermore, above the hearing range electroacoustic transducer have difficulties to perform and are usually replaced with another mechanical way to produce sound: piezoelectric devices. Piezoelectric devices are usually used for specific applications (underwater for sonar application, ultrasound generation... etc) but are heavy and are also mechanically based and thus resonant. As of today, no lightweight and non-resonant alternative are currently available.

Sound generation using thermoacoustics consists of using a material with a low thermal capacity and a high thermal conductivity to generate sound. Whenever an alternative power is supplied to the material, the temperature's profile of the sample will follow the power's variation. This rapidly changing temperature will excite the air in the vicinity of the sample hence creating an alternative state of compression and expansion of the medium in which the material is (gas or liquid). In air for instance, this will create a pressure wave and thus sound. A suitable material to create this thermoacoustic phenomenon is called a thermophone.

Due in part to the growing ease of access of technological machinery for the fabrication of nano-structured materials, an interest toward thermophones has been rekindle in the XXI_{th} century. Various thermophones have been studied and theoretical models have developed alongside those experiments. Unlike their mechanical counterpart, ther-

mophones display more wideband sound generation (up to the MHz), are lightweight and do not use any rare earth material. Additionally, the thermoacoustic generation process being independent of the shape of the sample allows them to have a very flexible geometry. Thermophones however have shown a very low efficiency compared to traditional speakers. They are also very fragile and are still a very niche research subject, preventing fast and widespread improvements. In spite of that, thermophones are a promising alternative for acoustic generation in the following years.

One of the most recently tested thermophones are carbon based thermoacoustic foams. Their unique geometry allows for an increased contact surface with the air necessary for the thermoacoustic process to occur efficiently. In this work the focus will revolve around the understanding of the thermoacoustic process and more specifically applied to the generation of foam like materials. Several questions are now raised like: can thermophone replace traditional loudspeaker? Will they have a place in the sound generation devices in the following years? and are foam like structures the most adapted shape?

The first chapter of this thesis presents an extensive state of the art literature review of the history of thermoacoustics and more specifically thermophone in the past 200 years. The context and motivation of this work is presented based on the existing literature. The second chapter provides the mathematical details of the theoretical models created. Continuous multilayer models are created assuming plane waves, cylindrical waves and spherical waves propagation. A novel model based on a two temperatures assumption is also created for plane waves in order to represent more accurately the thermoacoustic generation of foam like thermophones. Those models are compared to models and experiments from the literature and the analysis is presented in the third chapter, providing a deep understanding of thermophone capabilities. Lastly, chapter four presents experiments realised at and in partnership with CINTRA Singapore and the PhD student Ngoh Zhi-Lin. 3D carbon based foam created in CINTRA were used and confronted to our theoretical models. Additional measurements performed at the IEMN are also presented and insights regarding the acoustic radiation as well as manipulation advice are given. Experimental leads and possible applications are finally discussed for future work.

CONTENTS

ITO Indium Tin Oxyde

PET Polyethylene Terephthalate

SPL Sound Pressure Level

PDMS Polydimethylsiloxane

CNT Carbon Nanotube

PAN Poly Acrylonitril Nanofibers

MWNT Multiwalled Carbon Nanotube

SWCNT Single Walled Carbon Nanotubes

GF Graphene Foam

CVD Chemical Vapor Deposition

Ni Nickel

GS Graphene Sponge

rGO Reduced Graphene Oxide

HCPUA Heat Capacity per Unit Area

AC Alternative Current

DC Direct Current

AMAC Amplitude Modulation Alternative Current

PAM Pulse Amplitude Modulation

PWM Pulse Width Modulation

PDM Pulse Density Modulation

FCAC Spectral Envelope Decimation of AC

TCAC Dynamic Linear Compression of AC

THD Total Harmonic Distortion

2T Two Temperature

3D-C Three Dimensional Graphene Foam

PBI Polybenzimidazole

NF Near Field

FF Far Field

FDGF Freeze Dried Graphene Foam

SFM Spectral Flatness Measure

THD Total Harmonic Distortion

SC Spectral Centroid

SS Spectral Spread

DSC Differential Scanning Calorimetry

AFM Atomic Force Microscopy

∇	gradient
$\dot{x}$	Lagrangian, material derivative
$\frac{\partial}{\partial x}$	Eulerian derivative
η_{ijk}	Levi-Civita symbol
δ_{ij}	Kronecker symbol

Ω	Spatial domain in $\mathbb{R}^3$	
t	time	$[s]$
$\vec{x}$	Eulerian coordinate vector	$[m]$
$\vec{X}$	Lagrangian coordinate vector	$[m]$
$\vec{v}$	Particle velocity vector	$[m.s^{-1}]$
$\vec{a}$	Acceleration vector	$[m.s^{-2}]$
$\hat{T}$	Cauchy stress tensor	$[N.m^{-2}]$
$\hat{L} = \frac{\partial \vec{v}}{\partial \vec{x}}$	Velocity gradient	$[s^{-1}]$
$\hat{D} = \frac{1}{2}(\hat{L} + \hat{L}^T)$	Symmetric part of $\hat{L}$	
ρ	Density	$[kg.m^{-3}]$
$\vec{b}$	Body force density	$[N.m^{-3}]$
q	Heat flow	$[W.m^{-2}]$
Q_0	Heat density supplied	$[W.m^{-3}]$
e	Specific internal energy	$[J.kg^{-1}]$
T	Temperature	$[K]$
S	Entropy	$[J.K^{-1}]$
σ_s	Entropy production density	$[J.K^{-1}.m^{-3}.s^{-1}]$
s	Entropy density for unit of mass	$[J.K^{-1}.kg^{-1}]$
p	Pressure	$[Pa]$
$\tilde{p}$	Normal Stress Tensor	$[Pa]$
V	Volume	$[m^3]$
M	Mass	$[kg]$
λ	1^{st} viscosity coefficient	$[Pa.s]$
μ	2^{nd} viscosity coefficient (dynamic, shear viscosity)	$[Pa.s]$
f_h	Helmholtz free energy density	$[J.kg^{-1}]$
κ	Thermal conductivity	$[W.K^{-1}.m^{-1}]$
α_T	Coefficient of volumetric expansion	$[K^{-1}]$
κ_T	Coefficient of isothermal compressibility	$[Pa^{-1}]$
B	bulk modulus	$[Pa]$
C_p	Specific heat at constant pressure	$[J.kg^{-1}.K^{-1}]$

C_V	Specific heat at constant volume	$[J.kg^{-1}.K^{-1}]$
f	Frequency	$[Hz]$
ω	Radial frequency	$[rad.s^{-1}]$
k	Wavenumber	$[rad.m^{-1}]$
λ_f	Wavelength	$[m]$
C_0	Wave velocity	$[m.s^{-1}]$
$\hat{\eta}$	Green Lagrange Tensor	
$\hat{\epsilon}$	Almansi Euler tensor	
$\hat{T}_e$	Elastic stress tensor	
$\hat{T}_V$	Viscous stress tensor	
$\hat{\hat{V}}$	Viscous Tensor	
$\hat{K}$	Thermal Conductivity tensor	
$\vec{u}$	Displacement vector	$[m]$
λ_0	1^{st} Lamé elastic coefficient	$[Pa]$
μ_0	2^{nd} Lamé elastic coefficient	$[Pa]$
v_L	Longitudinal wave velocity	$[m.s^{-1}]$
v_T	Transverse wave velocity	$[m.s^{-1}]$
ν	Poisson ratio	
$H_i^{(1,2)}$	Cylindrical Hankel Function of first or second kind and of order i	
β_s	Heat loss coefficient in solids	$[W.K^{-1}m^{-2}]$

Part I

STATE OF THE ART AND MOTIVATION

1 UNDERSTANDING A THERMOPHONE

Today, sound reproduction has become a part of everyday life. Whether it is for musical purposes or speech reproductions, loudspeakers are used everywhere for professional and personal use. They are made of a coil/magnet core that induce vibration of a membrane system, eventually generating sound waves. For very specific needs (buzzer device, underwater application...), piezoelectric devices can also be used, but they remain a minority compared to loudspeakers. The efficiency of those devices has largely been proven but despite huge technological improvement of those technologies over the past century, some limitations remain. Indeed, those mechanical systems are inherently resonant and only the use of multiple drivers and filters allows to achieve an almost wideband generation across the hearing range (20-20kHz). Furthermore the use of magnet and rare earth materials make loudspeakers and piezoelectric speakers overall heavy and expensive. As of today no widely used alternative is currently available for cheap, lightweight and wideband sound generation.

In this Chapter it will be shown that Thermophones are promising candidates for sound generators displaying such properties. Those devices are using a thermoacoustic effect to generate sound, meaning that it is not mechanically based and so does not create any resonances. To put it in a nutshell, due to the high thermal conductivity and low thermal capacity of the material used, whenever a varying energy is supplied to the device, its temperature profile will follow the energy variation even at high frequencies. The air in the vicinity of the sample will compress and dilate as a result of the varying temperature, thus generating sound as described in Fig.1.

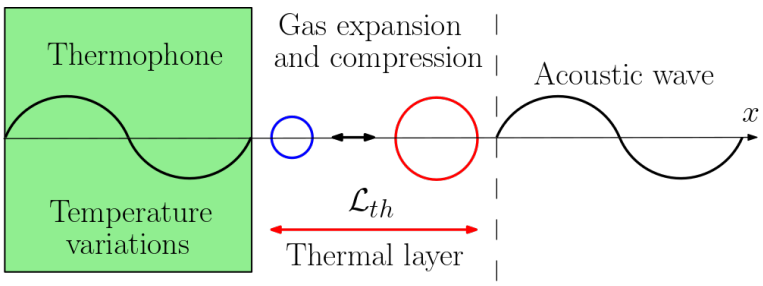

Figure 1: Schematic of thermoacoustic sound generation

In order to figure out how and when this physical properties was discovered, an historical review will first be presented. It will help understanding why thermophones where not as investigated as mechanical loudspeakers and why thermophones were not of prime interest for a long time. A state of the art of the current theoretical models used in the literature is then laid out which will help in the understanding of the main advantages of thermoacoustic generation. The necessary properties to make an efficient thermophone are also explained. Those information are necessary to understand fully the next section displaying all the different working thermophones used in the literature. Different types of materials and geometries are reported as working thermophones but not all display similar efficiency. Different techniques to try and improve thermophones' efficiency in the literature are then described. Those idea all have a specific commercial application in mind for thermophones proving the interest in this kind of technology. Finally, now aware of thermoacoustics' history as well as of its technological state, this first Chapter will end by highlighting the weak points of the literature and point out the objectives of this Thesis work.

1.1 THERMOPHONE'S HISTORY

In this section a chronological historic of thermophones is laid down. It will be shown that thermophones as an alternative to mechanical speakers have been known for about as long as traditional speakers, and that even though they were neglected for a long while, they recently gained a lot of interest.

1.1.1 *Before 1920: Early Observations and Experiments*

Back in the XVIth Century, a Buddhist monk reports in his diary the use of a Kibitsunokama in historical Japanese Shrine Ritual. As seen in Fig.2, it consists of an barrel mounted on an iron bowl. A mesh grid inside the barrel is covered with rice grains and liquid water is heated inside the bowl. This would produce a sound used for fortune telling in former Japan [4].

This phenomenon of sound produced with heat using a tube was later reproduced in 1777 by Dr.Higgins students [5]. Those "singing flames" experiments were formalised in two different forms by Sondhauss and Rijke in 1850 and 1859 respectively [6, 7]. The experimental setups now bearing their names can be seen in Fig.3 as used by Herschel in 1874.

The Rijke tube is a simple vertical cylinder open on both ends with a heat source (wire mesh or gause) inserted in one half of the tube. A

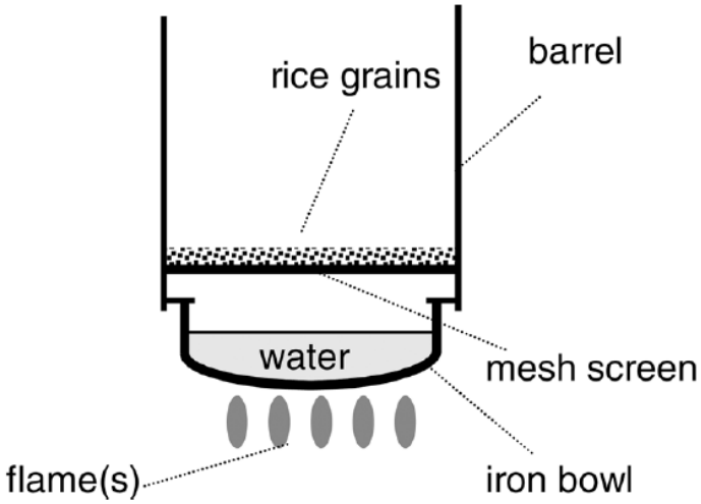

Figure 2: Schematic of a Kibitsunomaka [4]

convective gas flow coming through the tube is heated by the mesh and the expansion, compression of the gas as it interacts with the walls of the tube creates a standing wave. Sound is then heard proportionally to the length of the tube. It is understood that the Kibitsunokama was just an early form of a Rijke tube.

The Sondhauss tube is an open/close tube with a bulbous structure at the close end. When the closed end is heated, sound is produced from the compression/expansion of the air as it flows gradually from the cool region in neck to the hotter part in the bulb. The emitted frequency is dependent on the structure of the bulb and the length of the neck. This experiment is also informally known by glass blowers who have been hearing sound when blown glass bulbs began to cool down. Those experiments are the early stages of what will be called thermoacoustic engines and refrigerators, where the relationship between an acoustical standing wave and a heated stack inside a tube is exploited one way or another. Sound can be created by differences in heat and, conversely, sound can be used to create hot and cold temperatures. The theoretical framework of thermoacoustic generators can be found in the equation of Swift (1988) [8] but will no longer be discussed in this thesis as this is not its subject.

It is interesting to realise that Sondhauss tube looks similar to well known Helmholtz resonator. As a matter of fact, Helmholtz published his book *Sensation of Tone* in the same period, precisely in 1863 [11]. In this book, Helmholtz worked on the production of vowel sound, a topic which Alexandre Graham Bell was also working on. However, due to the fact that A.G. Bell did not speak German, a mistranslation of Helmholtz's book lead Bell to think that the "tuning fork contraption"

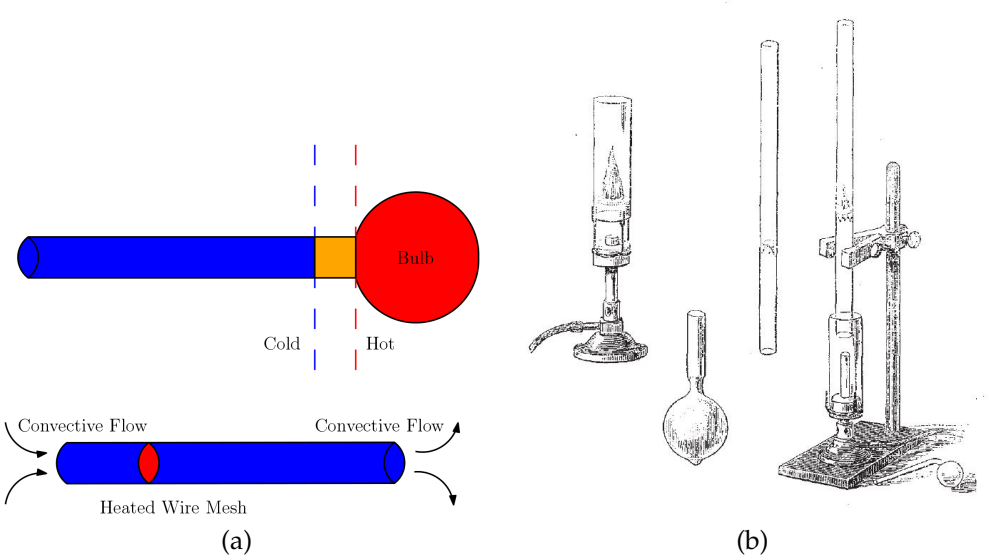

Figure 3: Schematics (a) and drawings (b) of the Sondhauss and Rijke Tubes experiments used by Herschel in 1874 [9, 10]

that Helmholtz was using were electrically driven [12]. This misunderstanding lead Bell to work on the production of sound using electricity and eventually invented the telephone in 1876.

The invention of the telephone increased the interest of sound production by all means. In 1878 Rayleigh laid down the theory of the Sondhauss and Rijke tubes [13] and the same year the term "thermophone" was first coined by Weisendanger [14]. In this letter Weisendanger provides an alternative to Bell's telephone which, he described, "*will soon pass over the to the long list of scientific toys*". Thin insulated wires produced sound through the passage of current which was then amplified with a resonator. If Weisendanger failed to engage much more research on thermophones, some very ground breaking ideas can be found. For instance he pointed out the advantage of not needing a magnet or membrane, and he foresaw the difficulty to find material that would be able to follow the "*successions of changes in temperature so infinitely rapid*". Actually, he even already recommended the use of carbon as potentialy efficient thermophones. At this point however, the sound generation was explained by the thermal expansion of the wire due to the fluctuating heat. Those comments and assumptions will be confirmed or disproved in the next section.

The idea that straight metal pieces could produce sound if driven by a battery was also reported by Preece in 1880 [15] but this momentum of research on thermophones was shifted by the publication of Bell & Tainter in 1880 about a photophone (Fig.4) [16]. This lead to the invention of

yet another side branch of thermoacoustic called photothermoacoustic, where instead of generating the thermoacoustic process using electricity, it is created using light. Some interesting early work triggered by Bell & Tainter was done in 1881 by Preece [17] and Mercadier [18–20]. If the focus of this thesis is on thermophone, its history is closely related to photothermoacoustic and will be mentioned again throughout this thesis. For the interested reader, a more thorough historical review of photoacoustics in general and its more recent applications can be found in Manohar & Razansky (2016) [21].

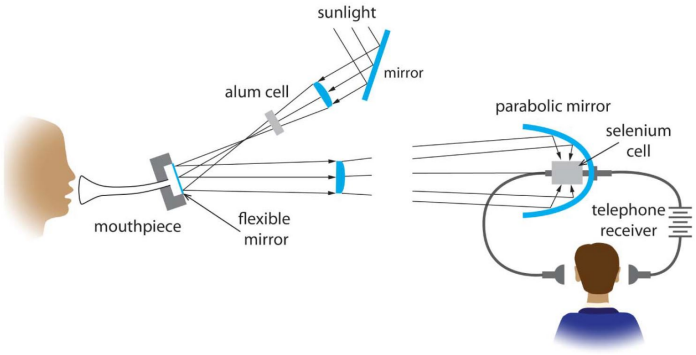

Figure 4: Schematic of a working Photophone as described in 1880 [16, 21]

In 1898 Braun also investigated thermophones[9] and, as Weisendanger a few years priors, attributed the sound generation to the thermal expansion of the sample. In 1915 De Lange rekindled an interest in thermophones [22] that lead to the publication of what is considered the first main paper about thermoacoustic theory by Arnold & Crandall in 1917 [23]. This theoretical model was improved by Wente the same year [24].

In the XIXth century, acoustics was of primary interest and the major fields of thermoacoustics were developed during that time. Early experiments highlighted the relationship between sound and heat in a tube with a stack that will later lead to thermoacoustic engines and refrigerators. The invention of the telephone was of prime importance at that time, and while trying to improve it, thermophones were created. Photothermoacoustics was then discovered while trying to communicate using light, opening a new scientific field of research. The improvement of the telephone and of loudspeakers reduced the interest on thermophones and we had to wait for the early XXth century for the thermoacoustic phenomena to be understood and put into equations, paving the way for understanding and improvements of thermophones.

1.1.2 *1920 to 2000: Forgotten and Disinterested*

One would think that with Arnorld & Crandall's theory on thermophone, an interest would surge about this field of research. On the contrary though, thermophone have then been left aside for a long time. In the first half of the XXth century, thermophones were relegated as potential calibration device for microphones. The idea was first investigated by Wente in 1921 [25] and was latter developed by Sivian and Ballantine in the 1930's [26, 27]. At this point the thermophone is admittedly the equivalent of a pistonphone and no other use is seriously considered.

In 1947 Fairbank investigates the thermophone as a source of sound in liquids. This novel idea faced similar limitations as fifty years prior being mainly "*the heater element [which] should be as thin as possible with a low heat capacity and high thermal conductivity*" [28]. Furthermore, the experiment was conducted in liquid helium and liquid hydrogen to have more convenient diffusivity and thermal expansion than in water. This left room for improvement to use thermophones as compact precision sound sources for underwater purposes.

In 1955 thermally induced sound fields are again investigated using conservation equations [29] and detailed theory on the gold sheet thermophone used by Balantine in 1932 seen in Fig.5, is laid down by Trilling [29]. Once again however, this article in French failed to rekindled an interest for the thermophone and mainly the photoacoustic remained of interest at that time [21]. A Generalised theory of the photoacoustic effect based on the conservation equation is written in 1978 by McDonald [30] and is worth mentioning here since, for simplicity, the article assumes that all absorbed light is converted to thermal energy and that the light is sinusoidally chopped. In other words, this photoacoustic theory is also valid for regular thermophones where the thermal energy is provided by an electrical current instead of light.

Thermophones had to wait for the end of the XXth century before technological improvement allowed the fabrication of efficient thermophones. In 1999 Shinoda *et al.* tested a thin aluminium film on porous silicon and was able to measure 74dB at 3.5cm distance with a power consumption of $1W.cm^{-2}$. This thermophone also displayed a flat frequency response up to 100kHz [32]. This article won back scientific interest toward thermophones and proved that the main obstacle of thermoacoustics was the fabrication of suitable devices, as foreseen by Weisendanger one hundred years too early [14].

In the XXth century, despite an early theoretical development of thermoacoustic theory, thermophones' efficiency were still far from competing with traditional loudspeaker. Some tried to use them for micro-

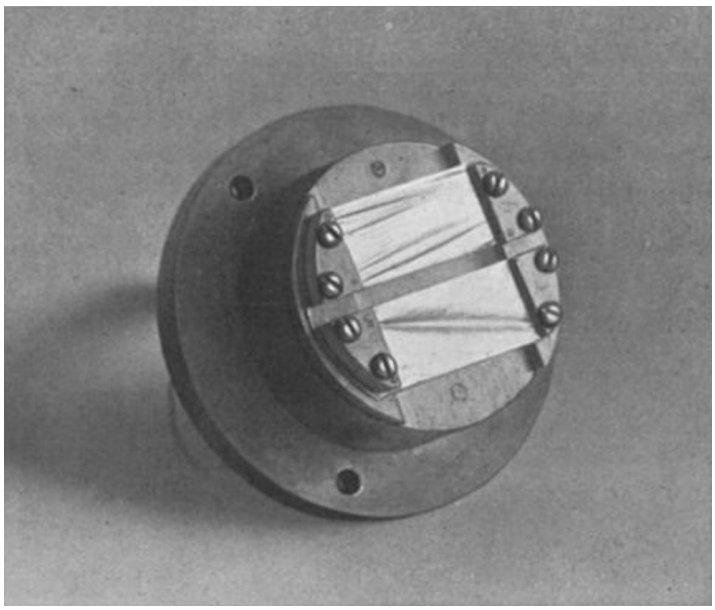

Figure 5: Gold sheet thermophone of Ballantine 1932 [27, 31]

phone calibration but all in all the lack of adapted material prevented any major improvement in this field. Only in 1999 new results with thin aluminium film on porous silicon initiated a wake up call that technological processes were mature enough for the fabrication of new relevant thermophones.

1.1.3 *2000 Onward: Regained Interest and Proliferation of Materials*

Most thermophones can be regrouped by geometry. Weisendanger in 1878 used wires [14] but were then quickly replaced by thin metal strips by Arnold & Crandall in 1917 [23]. Similarly, gold sheets were used by Balantine in 1932 [27] as seen in Fig.5 and such metal sheets continue to be tested as thermophones today[32]. This section aims to be as exhaustive as possible and to present all working thermophones used in the literature for the past 20 years. In order to highlight their main similarity, they are regrouped by geometry.

1.1.3.1 *Sheets and Papers*

One could argue that, in 1999, if Shinoda defended that thermoacoustics was generated from a porous silicon sample, it was actually the thin aluminum sheet that acted as a thermophone and the porous silicon was only an adequate substrate. This new thermophone allowed Kihara *et*

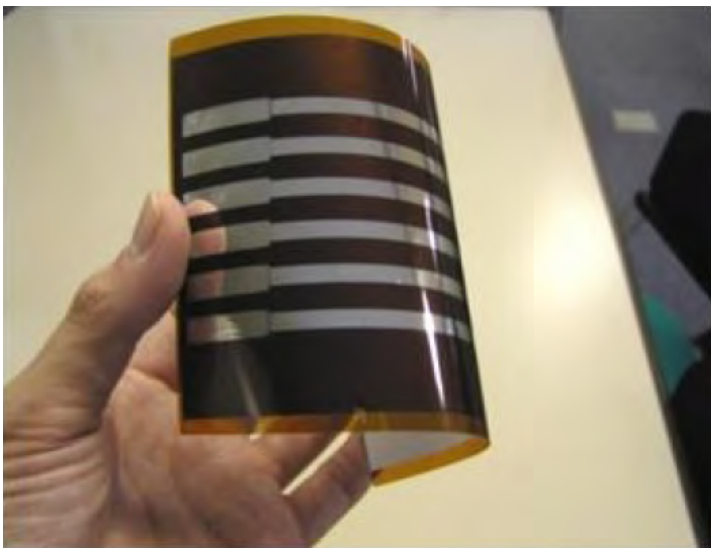

Figure 6: Flexible aluminium electrode Thermophone [37]

al. in 2006 to take advantage of the ultrasonic sound generation to reproduce mouse pups vocalizations [33]. In 2011, Tian *et al.* published multiple papers about thermophones. Making use of the high electrical conductivity, the flexibility and of the transparency of Indium Tin Oxide (ITO), films of ITO on glass and polyethylene terephthalate (PET) were reported as working thermophone [34]. The interest of having transparent and flexible sheets of thermophones was hindered by the low Sound Pressure Level (SPL) reported compared to previous thermophones. Another one of Tian *et al.* article was better received as it displayed a SPL about as high as the best thermophone at the time. This thermophone was made of Graphene film on a paper substrate [35].

Those new sheet thermophone with improved performance started a trend of papers that tried many kind of metal films on many different substrate while never quite reaching the efficiency of Tian *et al.* Graphene on paper. In 2012 Suk *et al.* used a monolayer graphene film on a glass, PET and polydiméthylsiloxane (PDMS) substrate and investigated the influence of the curvature of the sample on its acoustic radiation [36]. In fact, if some of the presented thermophones are considered flexible, due to their fragile state a substrate is required to avoid breaking them. Hence most metal films are only as flexible as their substrate. For instance, the thermophone of aluminium electrodes on polyimide made by Nakajima and Sugimoto in 2012 can be bent at will as seen in Fig.6 [37].

The same year Chitnis *et al.* tested gold sheet on dried porous silicon [38]. The next year Koshida *et al.* tested once again Aluminum sheets on porous silicon [39] and Daschewski *et al.* displayed recorded SPL in the MHz range of Titane and ITO film on quartz glass and polycar-

bonate [40]. In 2016, Tsai *et al.* used ITO film on ITO glass [41] and in 2017 Zhang *et al.* changed the geometry of graphene and used woven graphene on PET and on porous copper mesh substrate [42].

Some of those thermophones performed better than others but none had a high enough SPL to match the most efficient ones. Those being, as of now, the graphene film thermophones. It will however be seen that most of those low SPL can be, in part, attributed to the systematic use of a substrate in direct contact with the thermophone. Metal films and sheets on substrate were so proven to be capable of being used as thermophone. Nonetheless, the wire thermophone used by Weisendanger can not be considered comparable to the presented thermophones in this section and different geometries can still be thought off when talking about thermophones.

1.1.3.2 *Suspended Wires*

One of today most used way to create thermophones is by using wires like Weisendanger in 1878 [14]. However, when we are here talking about wires, we are actually mostly talking of random or highly aligned sheets made of nanowires. If Weisendanger did use a coil of wire at the time, the limited acoustical level heard was directly related to the thickness of the wires. As it will be proven later in this thesis, their thickness raised their thermal capacity preventing good thermoacoustic radiation. Modern thermophones are then made of nanowires in order to reduce the losses due to stored heat.

The most investigated of the recent Thermophones are the ones made out of free standing Carbon NanoTubes (CNT) seen in Fig.7. The interest in CNT arose in 2008 when Xiao *et al.* [43] published an article reporting their various advantages as thermophones and their potential applications. It includes experimental measurements displaying SPL of up to 100dB at 30kHz at a recording distance of 5cm, as well as an improved theoretical model based on Arnold & Crandall theory. This model takes into account the heat stored by the thermophone which was neglected in 1917's model. The very good agreement between theory and experiment as well as the compelling high SPL made CNT thermophone of prime interest. It can be noted that this interest was slightly biased by the non normalised SPL displayed (input power of 3*W*). As a comparison, Shinoda's experiments recorded a maximum of 70dB at 30kHz but the recording was done at 3.5cm and used normalised power. This corresponds to SPL of about 40dB and 65dB once normalised with distance and power, for Shinoda and Xiao respectively. Beside its high

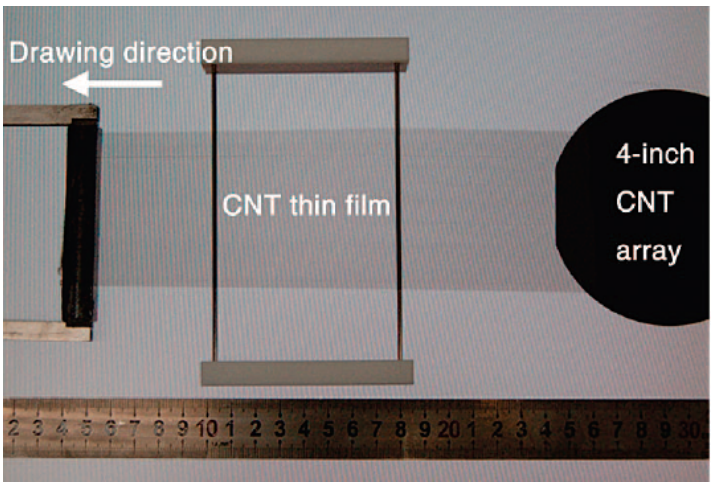

Figure 7: CNT Thermophone fabrication [43]

SPL, the rising interest in CNT can also be attributed to the cheap cost of fabrication and the ease of access of this material.

Other metal nanowires were tested following CNT. Most of them were freestanding but some were also tested on substrate. In 2009 free standing aluminum wires displayed thermoacoustic capabilities [44]. In 2011 silver wires were tested on PET, glass [45] and later on Kapton, and were compared to gold sheet on glass and Kapton as well [46]. Additionally, gold nanowires on glass were tested in 2014 [47]. In like manners and in order to exploit the advantages of nanowire geometry, free standing PolyAcrylonitril Nanofibers (PAN) were also employed. Gold, ITO or simply carbon were electrospun to PAN sheets and thermoacousticaly tested [48, 49].

The experimental results of all those samples were, more often than not, conclusively compared to theoretical models, but did not managed to reach CNT's efficiency. The lead focus regarding nanowire thermophones remained on CNT and MultiWalled Carbon NanoTube (MWNT) forest, sheet or web [48, 50–54]. In 2015 Mason *et al.* managed to test a single suspended carbon nanotube [55]. This 2µm long tube is, within the author's knowledge, the smallest acoustic system to date.

It was seen that wires, and more specifically nanowires sheets, are very promising thermophone candidates. CNT based sheets display the highest sound pressure level in the literature and many different materials have been tested. As of the writing of this PhD manuscrit, the most efficient thermophone in air has been recorded by Romanov *et al.* in 2019 [56]. It is made of free standing Single Walled Carbon Nanotubes (SWCNT) and reaches 95% of the theoretical maximum efficiency reachable by thermophones [57]. For the sake of comparison, it can be noted

that Xiao's CNT reached 80% of this maximal theoretical efficiency ten years prior.

1.1.3.3 *3D Structures*

Even though fabrication methods have improved and materials used are becoming more and more efficient since the discovery of thermoacoustics, no major novel geometry of thermophone has been talked about yet. So far, presented thermophones, whether they are made of a bulk film or a sheet of nanowires, are displayed in thin two dimensional geometries with or without substrates. It was seen that such shapes are just improved ones from those used now more than 100 years ago. Recently, 3D geometrical structures made of carbon are becoming more widely available and display promising results as potential thermophones.

In 2012 Pettes *et al.* investigated the electrical and thermal properties of graphene based foam (GF) fabricated using Chemical Vapor Deposition (CVD) [58]. This method uses a nickel (Ni) foam structure on which a few layer of graphene and ultrathin graphite are grown before removal of the Ni structure using a chemical etchant, leaving the freestanding GF see in Fig.8b. This method was perfected in this paper and GF displayed promising electrical and thermal properties for thermacoustic applications. CVD based samples kept being used in the following years but not as thermophone yet. Variation on the grown material and so on the properties of the foam and its potential application were made, Boron-Nitrite Carbon foam were created for instance as seen in Fig.8a [59, 60].

At the same time, graphene sponge (GS) seen in Fig.9 fabricated by solvothermal reaction in alcohol also displayed a high surface area and a high electrical conductivity [61], thus also making it a potential thermophone. Furthermore, its high mechanical stability [62] would be of interest compared to the presented current thermophone that are very fragile. The use of a substrate is the most common solution to help facilitate the handling of the thermophone without breaking it but it comes with thermal performances drawbacks as previously observed.

Both of those samples were tested in 2015 and displayed thermoacoustics capabilities [48, 63]. However this kind of thermophones were not tested extensively as compared to nanowire or metal sheets. This can be attributed to, both, the even more recent creation of those samples and the fact that they do not exceed the SPL reached by CNT or graphene sheets. CVD based samples are nonetheless still investigated with different structures as it is seen in Tu *et al.* in 2019 where vertical graphene films are made using microwave plasma CVD [64].

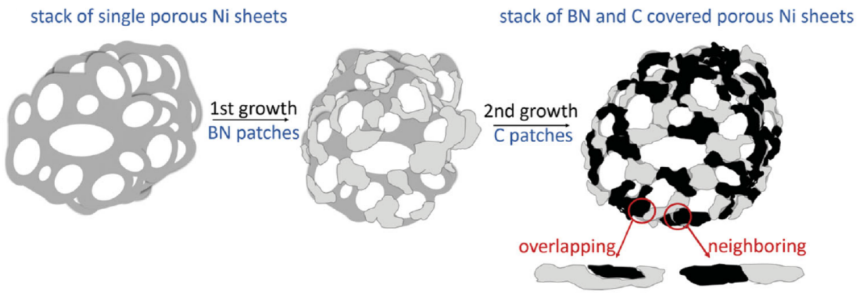

(a)

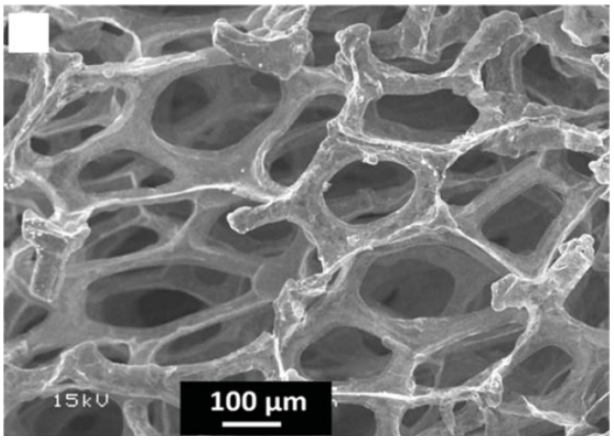

(b)

Figure 8: CVD growth schematic (a) and SEM picture of a graphene foam (b) [59]

Lastly, the last kind of thermophones that was recently developed are laser scribed graphene. Tao *et al.* in 2016 and 2017 scribed porous graphene on polyimide as well as reduced graphene oxide (rGO) deposited on a PET substrate as seen in Fig.10 [65, 66]. They both displayed decent thermoacoustic properties while not quite reaching CNT efficiency. Yeklangi *et al.* in 2018 build up and improved those laser scribed graphene by adding a CNT layer on top of rGO [67]. It increased significantly the SPL radiation while still remaining below the most efficient thermophones.

Beside the traditional metal and nanowire sheets, thermophones in porous or spongious forms have also been tested. Laser scribed graphene was also tested even more recently for its thermoacoustic properties but none of them displayed comparable results as the traditional geometries. Those investigations still deserve interest as they are a minority in the field of thermoacoustics and very few papers actually venture in trying new shapes for thermophones.

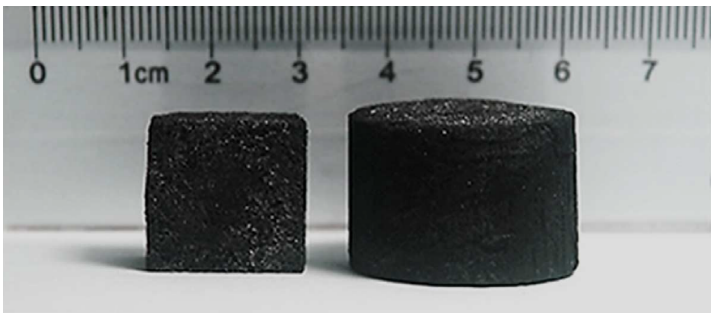

Figure 9: Graphene sponge [62]

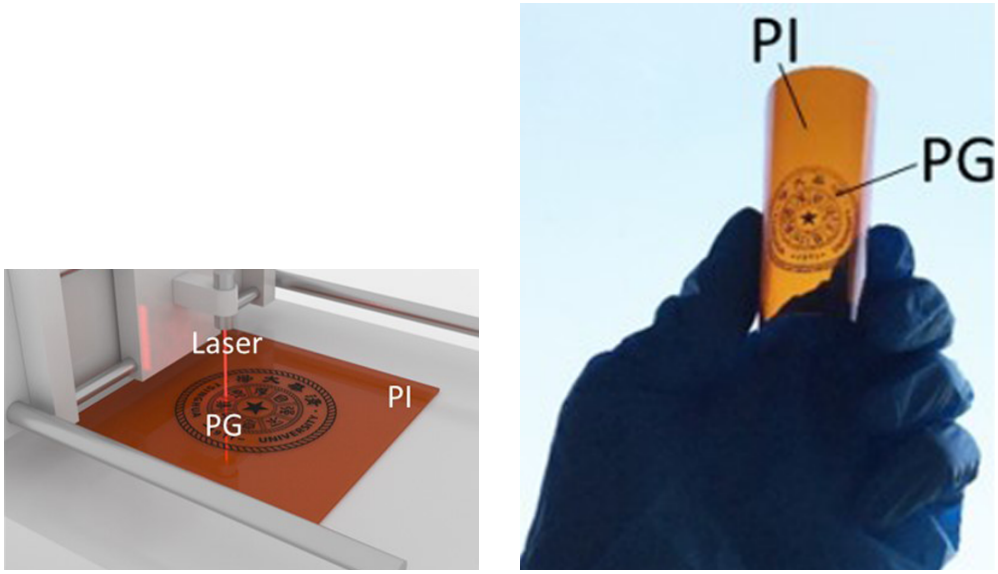

(a) (b)

Figure 10: Schematic of the laser scribing process of Porous Graphene (PG) on polyimide (PI) (a) and the associated picture of the resulting film (b) [65]

Metamaterials can be defined as materials that exhibit properties that are not found in a natural state. Based on this definition every thermophones is a metamaterial as it was seen that even though sound is generated by heat is some cases, those are all byproducts of human interactions (religious rituals, glass making... etc). The XIXth century has seen the discovery of thermoacoustics and thermophones. A first theoretical model was formalised in the early XXth century but was no longer investigated due to the lack of suitable, cheap and efficient devices. Technological improvement in the fabrication of nanostructured devices in the early XXIst century allowed Shinoda *et al.* to exhibit a working thermophone in 1999. This article started a surge of experiments of various structured devices, made of many different materials, as potential thermophones. It was seen that metal films and nanowire

sheets remain the most investigated kind of geometry and that carbon based thermophones display the highest efficiency for all geometries.

However, if the first historical theoretical model was mentioned, no recent theories on thermoacoustic sound generation have been presented yet. We will now investigate the theoretical models that have been developed alongside the discoveries of the various presented thermophones. The main parameters to create working thermophones will be highlighted as well as their main acoustical characteristics.

For the sake of simplicity of comparison, Table 2 regroups all the previously cited experiments and compares the measured SPL at $1m$, for $1kHz$ and with $1W$ of input power. It has to be noted that when reported measurements do not display SPL at $1kHz$, an estimated decrease of $20dB/dec$ has been used to estimate the SPL at such frequency [40, 68].

Table 2: Comparison of SPL from thermophones tested in the literature normalised at 1kHz, 1m and 1W

Ref.	Thermophone	Substrate	Recording Frequency (kHz)	Recording Distance (mm)	Input Power (W)	SPL (dB) Normalised
[57]	**Theoretical Maximum**		**3**	**70**	**1**	**43.36**
[69]	CNT film	Free standing	1	150	4.5	**38.46**
[38]	Gold	Dried porous hydrogel	2	30	0.51	**37.35**
[56]	SWCNT	Free standing	1	30	1	**36.54**
[43]	CNT film	Free standing	1	50	4.5	**35.92**
[70]	CNT film	Free standing	1	115	0.85	**35.63**
[48]	CNT sheet	Free standing	1	30	1	**35.54**
[35]	Graphene	Paper	3	50	1	**32.44**
[48]	Gold PAN sheet	Free standing	1	100	1	**32**
[51]	MWNT Web	Free standing	1	500	5.26	**29.55**
[49]	aerogel sheet PBI	Free standing	1	30	1	**29.54**
[48]	Graphene sponge	Free standing	1	30	1	**29.54**
[48]	ITO PAN sheet half coated	Free standing	1	30	1	**29.54**
[43]	CNT film	Glass	1	50	4.5	**28.92**
[71]	Graphene	On polymer mesh	1	50	1	**27.98**
[57]	Aluminum wires	Silicon (5µm air gap)	3	70	1.2	**25.78**
[67]	CNT/LSG	PET	1	30	0.6	**24.98**
[63]	Freeze dried GF	Glass	2	30	1	**24.52**
[44]	Aluminum wires	Free standing	1	80	1.9	**22.49**
[42]	Woven Graphene	Porous copper mesh	10	10	1	**22**
[72]	Aluminum wires	Si	1	70	1.9	**21.33**
[45]	Silver Nanowire Film	PET	1	50	1	**20.98**
[48]	ITO PAN sheet full coated	Free standing	1	30	1	**20.54**
[73]	Gold film	Silica aerogel	1	1000	1	**20**
[51]	MWNT Film	Free standing	1	500	5.26	**19.55**
[74]	Tungsten	Free standing	1	10	9.5	**19.45**
[65]	Porous graphene	Polyimide	1	15	1	**18.52**
[66]	Reduced Graphene Oxide	PET	1	15	1	**18.52**
[32]	Aluminum	Porous Silicon	1	35	1	**15.88**
[39]	Aluminum	Porous Silicon	1	10	1	**15**
[49]	C-PAN	Free standing	1	30	1	**14.54**
[67]	Laser scribed Graphene	PET	1	30	2.2	**13.69**
[34]	ITO	Glass	1	50	0.2	**12.96**
[34]	ITO	PET	1	50	0.2	**12.96**
[48]	MWNT sponge	Free standing	1	30	1	**12.54**

[48]	MWNT Forest	Free standing	1	30	1	**11.54**
[63]	Natural drying GF	Glass	2	30	1	**11.52**
[55]	CNT single wire	Suspended	16	10	0	**9.9**
[46]	gold film/silver wires	Kapton	1	1000	1	**6**
[36]	Graphene	PDMS	1	30	0.25	**5.58**
[40]	ITO film	Polycarbonate	10	60	1	**4.56**
[73]	Gold film	Kapton	1	1000	1	**4**
[75]	Multilayer graphene film	PDMS	1	10	0.6	**2.44**
[41]	ITO film	ITO glass	3	50	1	**2.44**
[46]	gold film/silver wires	Glass	1	1000	1	**1**
[36]	Graphene	PET	1	30	0.25	**0.58**
[42]	Woven Graphene	PET	10	10	1	**0**
[42]	Single Layer Graphene	PET	10	10	1	**0**
[75]	Multilayer graphene film	PET	1	10	0.6	**-0.56**
[76]	Silver Nanowire Film	Kapton	1	500	35.36	**-0.99**
[47]	Gold wires	Glass	5	30	0.6	**-4**
[45]	Silver Nanowire Film	Glass	1	50	1	**-4.02**
[40]	ITO film	Quartz glass	10	60	1.04	**-5.78**
[73]	Gold film	Glass	1	1000	1	**-8**
[33]	Aluminum	Porous Silicon	20	50	2.3	**-8.28**
[36]	Graphene	Glass	1	30	0.25	**-8.42**
[40]	Titane film	Quartz glass	10	60	4.5	**-8.5**
[75]	Multilayer graphene film	Glass	1	10	0.6	**-9.56**
[40]	Titane film	Quartz glass	10	20	2.32	**-11.29**

1.2 EXISTING THEORETICAL MODELS OF THERMOACOUSTICS

In order to study thermoacoustic generation, many theoretical models have been developed and improved over the years. Knowing the most common thermophone geometries, we will now investigate the main models that have been created to understand the advantages and disadvantages of thermophones.

1.2.1 *Thermal Balance Models*

From a theoretical point of view, most analyses of the thermophone principle used the so-called *piston based model*. These approaches are based on a heat flow balance equation taking into account the convection, the conduction, the radiation losses and the heat stored in the material. The first attempt to use this method to model a thermophone in free field was done by Arnold and Crandall in their pioneering investigation where, however, they neglected the heat stored within the thermophone [23]. Boullosa *et al.* created their own version of the *piston model* in 2006 for planar and cylindrical thermophone but failed to communicate the phenomena in a convincing way [77]. The heat capacity term forgotten by Arnold & Crandall was then added in the investigation performed by Xiao *et al.* in 2008 [43]. Hence, unlike Boulossa *et al.*, the high SPL displayed by the experiment (previously mentioned), plus the ready to use pressure estimation equation for thermophone, made Xiao *et al.* article one of the most cited in this field of research.

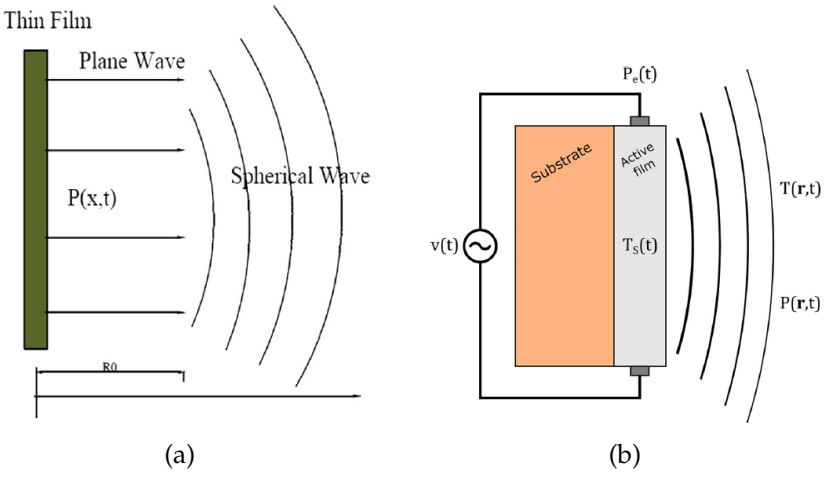

Figure 11: Structure of thermophones: (a) free standing [78] and (b) on substrate [76]

In 2013, Daschewski *et al.* used the heat flow balance equation and added the influence of a substrate (or backing) on free standing thermophone response (Fig.11), and the effect of the viscous dissipation in the propagation medium [40, 79]. Based on this equation, influence of heat flux, heat capacity and heat convection was statistically analysed in 2015 by Bin *et al.* [80]. It demonstrated that heat convection is negligible in ambient air condition. Dacheswski *et al.* approach was later successfully used by Kim *et al.* to describe the behavior of a graphene thermophone deposited on a polymer-mesh substrate in 2016 [71]. Successively in 2017, La Torraca *et al.* added conduction and convection contributions to the model and also took the thickness of the substrate into account [76]. They proved once again that using thick substrate in direct contact with the thermophone will result in thermal losses in the substrate thus reducing the thermoacoustic sound generation. This explains why free standing thermophone presented in Section 1.1.3 performed on average better than those on substrate.

Substrate Influence

1.2.2 *Conservation Equations Models*

Another approach used for modeling thermoacoustic effect is based on the classical conservation laws of continuum mechanics applied in a propagation medium, typically without viscosity. These equations were elaborated by MacDonald *et al.* for studying the photoacoustic effect in 1978 as mentioned in Section 1.1.2 [30]. More recently, the same set of equations has been adopted also for thermoacoustics analysis. This coupled set of equations was firstly solved in 2010 by Hu *et al.* for a thermophone placed on a substrate, generating sound in a perfect gas [81]. This model was validated against Shinoda's experimental data [32], and was later adapted to evaluate the far field pressure and to consider the influence of the so-called Heat Capacity per Unit Area (HCPUA) [82]. HCPUA was proven to be necessary low for efficient thermoacoustic radiation and is defined as the product of the thermophone's thickness, its density, and its heat capacity. A refined analysis of Hu *et al.* methodology has been performed in 2012 to study the influence of the main thermophone parameters on its wideband frequency response [68]. This formalised that, in the far field, thermophones radiate sound in a linearly proportional fashion with increasing frequency before reaching a plateau and decreasing at very high frequency, usually in the MHz range.

Heat Capacity Per Unit Area Influence

Thermophone Frequency Response

The following years, Hu *et al.* modified this approach to investigate a spherical geometry of thermophone (acoustic monopole), generalized it to arbitrary sources, before considering a cylindrical geometry (Fig.12),

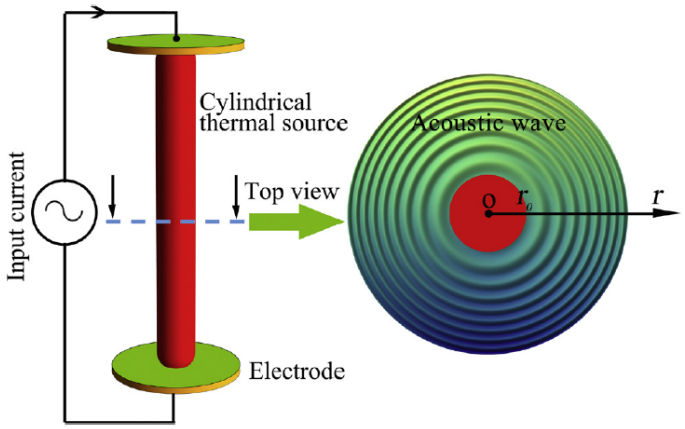

Figure 12: Cylindrical thermophone and its acoustic wave propagation [87]

in 2012 [83], 2014 [84] and 2017 respectively [85]. Based on Hu *et al.* model, in 2017 Xing *et al.* have done a sensitivity analysis on some influential factors for thermoacoustics efficiency [75]. Lastly in 2019, Mao *et al.* added the influence of viscosity to Hu *et al.* equations [86].

Investigation by Lim *et al.* in 2013 proposed to merge the equations of the continuum mechanics with the thermal balance of the *piston based model* [78]. They properly defined the sound generation electrically driven by Joule effect and related it to the thermal balance of the *piston model* to have a more accurate description of input power supplied to the thermophone. They applied it to a free field configuration, eventually leading to a good agreement with experimental results (obtained from Ref. [43]). It is important to understand that since the sound generation is based on a Joule effect, the output power is a squared function of the input one. Meaning that if a pure sinusoidal alternative current drives the samples, the heard acoustical frequency will be of twice the input one. This will be more thoroughly explained in the later part of this thesis.

Joule Driven Sound Generation

Based on this work, in 2015 Tong *et al.* added the influence of an air gap between the thermophone and a substrate as described in Fig.13, which represents a promising technique to improve the thermophone efficiency [72]. A generalized theory was then developed by Liu *et al.* in 2018 to describe point source, line source and line array thin film thermophones in free field and in half space with an air gap over the substrate [88]. It can be noted that, similarly, Asadzadeh *et al.* in 2015 modeled thermacoustics projectors' sound generation using those two alternative forms of energy conducted to the fluid, here described as *piston* and conservation equation model [89]. The lack of novel analysis however hindered on the visibility of the paper compared to Lim and Tong team's papers or Hu *et al.* previous articles.

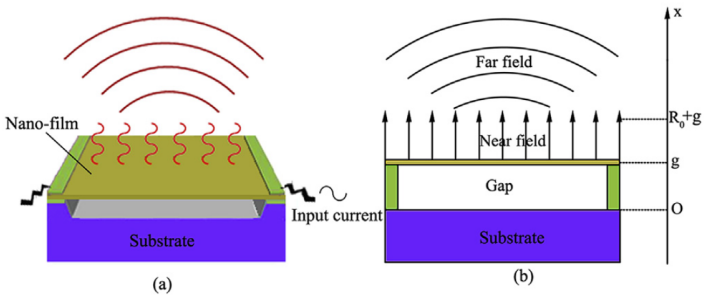

Figure 13: Thermophone over a substrate [72]

Maximum Theroretical Limit

Notably, the properties of nanoscale thermophones have been studied by Vesterinen *et al.* in 2010, eventually obtaining generic ultimate limits for the thermophone efficiency [57] as mentioned in Section 1.1.3.2 and used in Table 2. This maximum limit for thermophone has since been widely used in later papers as it explicitly shows the linear relationship between thermoacoustic efficiency and input power. The theory was confirmed against experiments and finite difference method simulations. This model was later improved by Brown *et al.* [74] by considering line thermophones of finite length.

Many variations of the same set of equations have then been used to describe thermoacoustic sound generation. The main results from those theoretical analysis can be summed up as follows:

- The thermophone material should have a low HCPUA [43, 89].
- The substrate should have a low thermal effusivity, meaning that it should not be able to exchange thermal heat easily with its surroundings [75, 76].
- If the material is efficient enough (low HCPUA mainly), at a fixed input power in the far field, the frequency spectra will display a linear increase in SPL with frequency before reaching a plateau going to ultrasonic range [40, 68].
- The acoustic generation is power driven and the efficiency is linearly increasing with input power [57, 74].
- Since the sound generation is created by Joule effect, an Alternative Current (AC) will generate a sound wave at twice the electrical driving frequency [23, 78].

1.3 UNDERSTANDING, APPLICATION AND IMPROVEMENTS

Thanks to Section 1.2, we are now aware of the main thermoacoustic properties of thermophones as well as some limits. It is then of primary importance to understand what those thermophones can be used for before trying to improve them. This section aims to put into light the interest of thermophones and the research that has been made to use them in a commercial or industrial fashion.

1.3.1 *Potential Uses and Applications*

First and foremost, it is important to realise that we will mention in this section only applications directly related to thermophones and not thermoacoustics as a whole. Engine and refrigerator which are promising thermoacoustic application are not of interest here [8, 90–92] as explained before. Similarly, photothermoacoustic or thermoacoustic's tomography for health care applications are not of interest here [93–95]. Lastly, if thermophones's samples can also be used for thermal management in electronics [60, 96–98], their thermoacoustic properties are not used in this case and so will not be discussed. Lastly, some peculiar experimental use of thermophones like using a cooling fan on the thermophone [99], or mounting it a single plate cantilever device for butterfly acoustic flame extinction [100] are not investigated.

The most self evident use for thermophone is as an alternative to traditional loudspeakers [96, 101–104]. It was one of the first presented use by Xiao *et al.* in 2008 when they put CNT on a school flag allowing it to do school announcements [43]. Furthermore, it is easily noticeable that this is of prime interest as the frequency range investigated in the literature is, more often than not, the hearing range. Overall, enclosed thermoacoustic loudspeakers did not display outstanding results due to the weak radiated SPL of thermophones [105]. However, taking advantage of the seemingly size independent radiation of thermophones, thermoacoustic earphones were investigated (see Fig.14). They are made of laser scribed thermophones [106, 107], CNT arrays [108] or even novel MXene based thermophone [109] and display encouraging results as compared to commercial earphones. Applications in mobile phone or military purposes can also be considered when very small acoustical transducers are needed [55].

It was understood from Section 1.2 that thermophones actually perform better in a high frequency range. Knowing this, thermophones can be designed for ultrasonic applications [110, 111] and can be patented as such [112]. For instance, they were used also as ultrasonic earphones

Figure 14: Earphone made of CNT array [108]

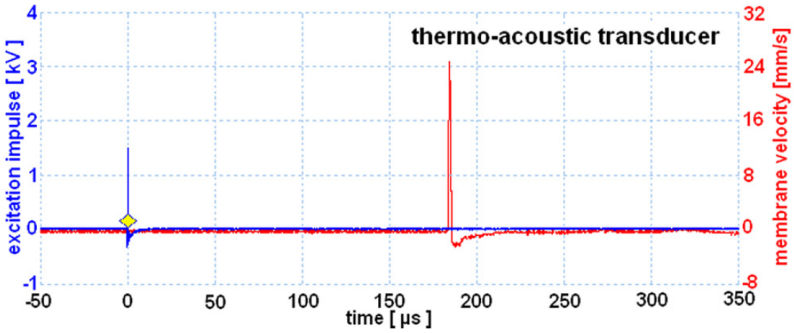

Figure 15: Measured membrane velocity after excitation with a thermo-acoustic airborne ultrasound transducers placed $60 \pm 3\text{mm}$ from the membrane. Transducers were excited with 1.5kV 500ns impulses. The mass of polymer membrane was $12.641\ \text{g/m}^2$ [40]

for dogs by Tian *et al.* in 2014 [113] but the most compelling case for ultrasonic application was done by Daschewski *et al.* in their 2013 work [40, 114]. Making use of the flat frequency response of thermophones, they were used as ultrasound transducers and displayed a very sharp impulse response as seen in Fig.15.

So far, the presented uses for thermophones rely mainly on their acoustic capability and their peculiar acoustic spectrum. Nonetheless, the flexibility of their design, not being bound to any shape or forms but only to the fabrication process, allows for other applications. They can be used for environmental acoustic purposes and more specifically active noise control. Their design allows them to be shaped in any form

so if placed on a noise generator and the right signal processing is applied, noise level can be actively significantly reduced [115–117]

Another current use of the flexible design of thermophones is to make skin wearable devices and more specifically artificial throats as seen in Fig.16. Laser scribed thermophones [118, 119] or hybrid nanomembrane made of transparent silver nanowires [120] coupled to piezoresistive materials or nanomembranes microphone (using a triboelectric voltage) are used to detect vibrations of vocal cords and to reproduce them. This technology could be used as health care sensors, voice based security systems or help persons in situations of handicap [121].

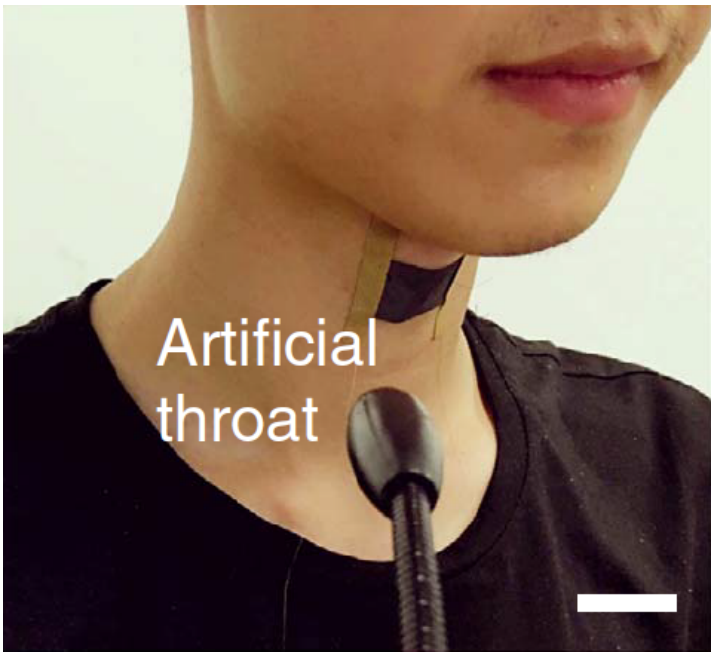

Figure 16: Skin wearable artificial throat [118]

Finally, it is interesting to realise that in the literature, a great deal of articles mention the use of thermophone as potential underwater sound generator for sonar application [40, 48, 68, 122, 123] but very few actually investigate it. As a matter of fact, the light weight of thermophones compared to piezoelectric transducers or regular loudspeakers make thermophones of prime interest to reduce the overall weight of sonars. Furthermore, having no moving part makes it easier to suppress back radiation from a thermophone than from a piezoelectric transducer which will always emit in both direction and in anti phase. This helps to perform noiseless and more directive sonar detections. Aliev *et al.* are the ones being the most advanced on this matter [124] and unmanned undersea vehicles are already starting to use this technology [125, 126].

Thermophones should not be simplified as less efficient loudspeakers. If it was seen that work is being done to use them as replacement for loudspeakers, and more specifically small size transducers, their inherently unique frequency spectrum make them better candidates for ultrasonic transducers. Their flexible geometry also allows for active noise cancellation or skin wearable acoustical devices. Lastly their light weight make them very attractive for underwater sound generator. However some obstacle still remain. For instance thermophones acoustical radiation is not very efficient yet. Furthermore, despite the large amount of different potential material, most efficient thermophones are still very fragile. Lastly, due to their non linear sound generation process, they are not adapted to work with common regular AC amplifiers. Research trying to dismiss those concerns will now be investigated.

1.3.2 *Optimising Material and Geometry*

It was seen that it is of prime interest to optimise thermophone's radiation for loudspeaker applications. One direction this optimisation can take is by using today's flexibility of fabrication process to design an optimal shape for thermoacoutic generation. For instance, even with the interest for theoretical model of thermophone in cylindrical shape [77, 85, 87], few thermophones differ from the traditional metal films or sheets of nanotubes, despite the claimed flexibility of said thermophones.

Stacked Thermophones

One possible solution to improve SPL delivered by thermophone is to stack multiple layers of thermophone's sheet as seen in Fig.17. The idea behind it being that by adding multiple layers, the radiated sound will then be improved as those layers will act as coherent sound sources. It was first tested by Aliev *et al.* in 2014 [52] in an attempt to improve thermal management of thermophones. No theoretical model was associated to it and five years had past before Zhou *et al.* created a theoretical model for such stacked thermophones [127].

Another property of thermophones which could improve acoustical radiation is the influence of thermophones' size, and more specifically their radiating area. It was seen that small thermophones can be of interest commercially (earphones, smartphones...) but being able to fabricate large size thermophone could help in creating thermoacoustic loudspeakers. Due to fabrication limitation of the nanomaterials used, thermophone are usually of a relatively small size. Hence only CNT have been used so far as large thermophone. For instance by Barnard *et al.* in 2014 [128], and Wang *et al.* in 2018 [69]. The influence of increasing the size of thermophone was proved to be negligible on its frequency

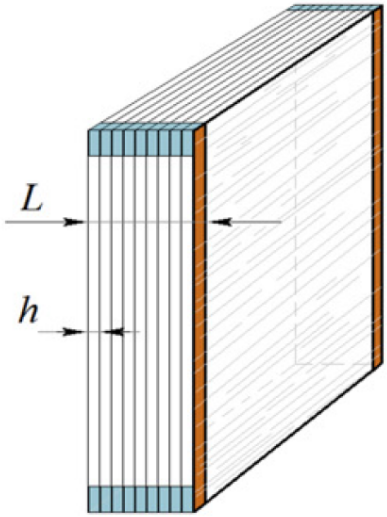

Figure 17: Stacked CNT layers [52]

spectra as the decreasing power density induced by the larger area is compensated by the increased coherent radiation of the greater surface. This will be discussed later in this thesis as well as resulting acoustic radiations.

Despite those scarce tentative for more ambitious thermophones, it was seen in Section 1.1.3.3 that new thermophones' geometry are being discovered and tested every year. A promising lead could be the use of 3D thermophones like GF and GS [48, 63, 129]. Sbrockey *et al.* even tried in 2018 to propose a way to improve electrical contact by protecting metal pads from the template used for CVD grown samples [130]. However, very few experiments have been performed with those kind of samples and since they did not display high enough SPL, they were discarded as scientific curiosity. Focus remains since then on Graphene film and CNT. Nonetheless, just like GF was not right away tested for its thermoacoustics properties [58], it is highly likely that new carbon based geometry are currently discovered due to the improvement of technologies but are not considered as potential thermophones yet. For instance, 3D printed GF by Sha *et al.* in 2017 seen in Fig.18 could be potential thermophones but are not yet tested [131].

Today, new thermophones are mainly discovered out of scientific curiosity. The thermoacoustic capabilities of a tested device are still relegated as a side effect and are not the main objective of the creation of those sample. This method was valid when thermoacoustics was not well understood but with the current state of knowledge regarding thermophones, new structures should be designed whose primary goal is to improve thermoacoustic radiation for loudspeaker or medical

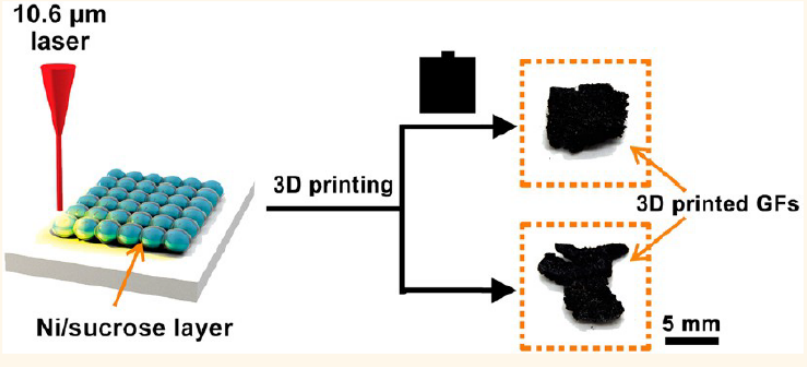

Figure 18: 3D laser printed GF [131]

applications. Despite the many theoretical models, within the authors' knowledge, no sample has been created for the sole purpose of thermoacoustic application. Some solutions for improved thermoacoustic radiation have been presented in this section but there is still room for improvement.

1.3.3 *Gases and Encapsulation for a Resonant Device*

Instead of changing thermophones to improve airborne sound generation, some have been trying to use them in different working conditions to try and find an optimal use for those devices. More specifically, as early as 1947, Fairbank *et al.* tested thermophone in liquid Helium and liquid Hydrogen as compact precision sound source [28]. Underwater work was mentioned but not tested due to thermophone's limitation at the time and the more suitable thermal expansion coefficient and compressibility of liquid Helium and Hydrogen compared to water for those experiments. Thermophone waited up until 2010 before being tested underwater again when Aliev *et al.* investigated the response of a carbon nanotube projector placed in water [122]. They provided evidence that the hydrophobicity of the nanotubes in water generates an air layer around the nanotubes that increases the pressure generation efficiency of the thermophone. This work aimed at creating lightweight underwater sound source as, currently, heavy piezoelectric devices are the main way of underwater sound generation (mainly used in sonar devices). However, during immersion into water the MWNT was collapsing even with a protective sheet attached to it.

In order to solve this problem, research has been focused on studying encapsulated thermophone systems, developed in order to obtain a protection from the liquid medium. Fig.19 encapsulation example comes from Tong *et al.* in 2013, when they laid down a theoretical model for

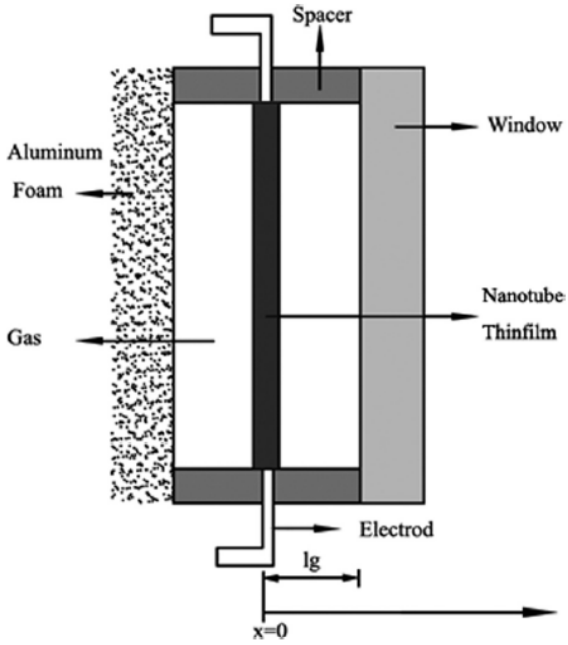

Figure 19: Example of thermophone encapsulation [132]

encapsulated CNT and observed a resonance in the frequency spectrum directly proportional to the size of the encapsulation [132]. Furthermore, Tong *et al.*, Barnard *et al.* as well as Aliev *et al.*, the same year took advantage of the encapsulation of thermophone to test its acoustic radiation in different gases and liquids (air, Argon, Helium, Azote, Freon, Xenon, Sulfur hexafluoride, water, Methanol) [132–134]. Similar gaseous influence investigations were reported in 2011 by Xiao *et al.* without encapsulation [70], as well as with Tong *et al.* in 2016 with a cylindrical model without encapsulation in air and Nitrogen [87]. In 2017 Dzikowicz investigated enclosed cylindrical fiber array thermophone for underwater application, and positively confronted his theoretical model with experiments in Helium and Argon gases [135]. Lastly in 2018 Shin *et al.* made use of resonant encapsulated CNT for practical audio purposes [136].

In order to improve the handling of thermophones and prevent mechanical damages due to their fragile state, thermophones have been encapsulated. This allowed for better handling and prevented direct damage to samples when immersed in various liquids and gases. This solution was aimed at using thermophones as underwater sound sources but by doing so, resonances appeared due to the solid encapsulation. The specific flat frequency spectrum of thermophones is then no longer of use. Nonetheless, the light weight and the lack of moving parts of thermophones remains of prime interest for underwater transducer applications.

1.3.4 *Input Signal and Pre-Processing*

One of the most undeniable issue about thermoacoustic sound generation is the fact that the output acoustic frequency will follow the temperature variation of the sample (Joule effect). Hence, for an AC signal of frequency f driving a thermophone, the acoustical signal heard will be at $2f$ as the temperature of the sample will follow the absolute variation of current and can not take negative values, as explained in Fig.20. Electrically speaking, thermophone are power driven as opposed to loudspeaker or piezoelectric devices that are driven by electrical potential.

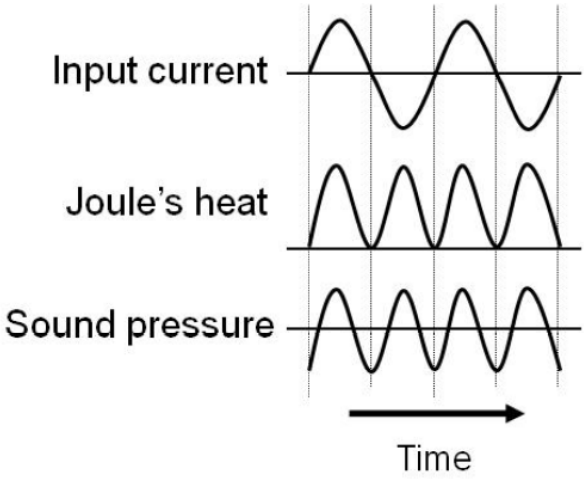

Figure 20: Thermoacoustic sound generated by Joule heating [37]

Once this principle known, one can either just use AC and expect an output signal of twice the input frequency, or add a Direct Current signal (DC) to the AC one so that the temperature variation of the sample stay in a positive range. As a result the acoustical frequency heard will be the same as the input one. Both methods are the ones mostly used in the literature and a qualitative quantification comparison of those input signals can be found quite recently in Bouman *et al.* or Heath *et al.* in 2016 and 2017 respectively [137, 138].

Amplitude Modulation

Nonetheless, other input signal were tested like the Amplitude Modulation of Alternative Current (AMAC) in 2006 by Boullosa *et al.* [139]. AMAC uses the idea that thermophone are more efficient at very high frequency. Hence if a high carrier frequency (above hearing range of 20kHz) has its amplitude modulated by a frequency in the hearing range, the modulating frequency should be the only one heard. The results were promising but due to the non linearity of thermophone (power driven), harmonics appeared making it not adapted for complex signals (conversation, music...). Another usage of the high frequency efficiency of thermophone consists of using short pulse modulation trains:

pulse of amplitude, width or density modulation (respectively PAM, PWN and PDM). PDM was used by Koshida *et al.* in 2013 as seen in Fig.21 [39] and Tong *et al.* in 2017 [123] before PAM, PWM and PDM were compared by Aliev *et al.* in 2018 for his enclosed CNT [140]. Less intuitive input signal borrowed from the hearing aid industry were also tested like spectral envelope decimation of AC signal (FCAC) and dynamic linear compression of AC signal (TCAC) by Bouman *et al.* in a following work in 2017 [141]. Heterodyning possibilities as well as modulated DC with fixed AC for a flatter hearing range frequency response was also tried by Heath *et al.* in 2017 [138]. Nonetheless, none of the above mentioned methods displayed impressive enough results to replace easy AC testing.

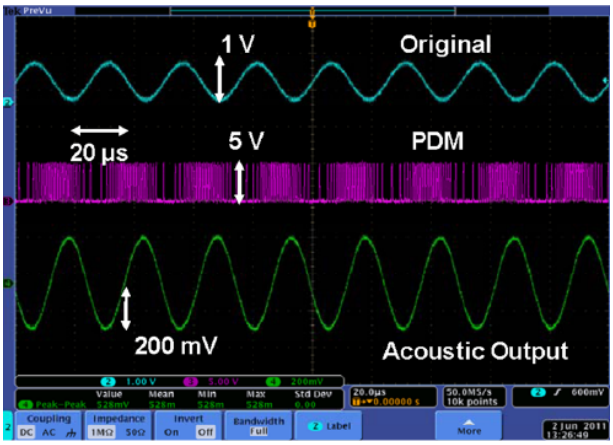

Figure 21: PDM signal supplied to a thermophone [39]

The interest of investigating modified electrical signal used to drive a thermophone comes from a desire to use them as commercial loudspeaker. Henceforth, the possibility to use currently available amplifier to drive thermophones with complex musical signals is of prime interest. This is proven by the fact that most of the above cited literature are comparing subjectively the sound quality of recorded signal and evaluate their total harmonic distortion (THD) [39, 128, 137, 141]. THD is a parameter that allows an objective evaluation of the quality of the signal by studying the ratio between the fundamental and its harmonics. Nonetheless, if the presented techniques are working with pure tone reproduction, due to the non linearity of the thermoacoustic process, harmonics occur in all cases and hinders understandable reproduction of complex signals. As a consequence, none of the above mentioned method are commercially viable yet.

Total Harmonic Distortion

One last technique that can be considered to allow the reproduction of complex signals is to apply a square root function to the input signal. This would avoid the non linearity of the output signal on which

a square function is applied (as explained in Section 1.2.2). Sugimoto *et al.* designed an electronic black box to do that electrically in 2016 but the circuits' plan are not communicated and so the results are not reproducible [142]. Tong *et al.* did a similar experiment with simple signals in 2017 [123] but a real easy pre processing implementation to apply a square root function to the input signal was only presented in 2019 by LaTorraca [143]. This method allows to use any commercial AC amplifier to play any kind of complex signal with low distortion provided that the adequate pre processing has been applied before hand to the signal. This adaptive pre distortion method will be detailed later on in this thesis as well as some observed downsides.

In order to facilitate the use of thermophone as a regular loudspeaker in the market, it has to be compatible with current commercially available AC amplifier. The non linear sound generation of thermophones prevent simple reproduction of complex signals with only those amplifiers. Some solutions from the literature were provided in this section. Complex electrical signal making sometime use of the ultrasonic efficiency of thermophones have been presented (ACDC, AMAC, PWM...) as well as electronic or signal processing solutions. Promising results were observed but no easy universal solution has yet been found. As of now, the desired solution has to be chosen according to the aim goal of the thermophone (music reproduction, single frequency generation...).

1.4 CURRENT LITERATURE'S LIMITATIONS

In Section 1.1 a detailed historic of thermoacoustics related to thermophones has been given. It was shown that, even though thermophones have been discovered in the XIXth century and that an incomplete but promising model has been laid out in the early XXth century, only the start of the XXIst century has permitted the surge of thermophones' interest. Many different thermophones have been tested in the past two decades. The most efficient thermophones known to date are similar as the ones 150 years ago, meaning that they are made of sheets of wires (currently nanowires) and metal films. For both geometries the material that display the highest SPL is carbon (CNT and graphene respectively). Only very recently, new thermophone geometries have been tested, constituted by 3D graphene foam, sponge or laser scribed structures.

Nonetheless, even though it is always of common interest to study and try different combinations of materials and substrates in an emerging field, most of those papers were written by researchers mainly working in material science and not really active in applied acoustics. This re-

sulted in many papers which observed and presented some basic acoustic results with thermophones as novel (diffraction and interference for instance). If a presented thermophone was indeed novel, the associated analysis of the acoustic radiation was mainly a verification of known results. It is then very important to distinguish the thermoacoustic effect from the acoustic propagation, as standard acoustic results can be used in the later case.

Furthermore, one of the most enduring blunder in the literature is that, despite a clear interest in acoustic radiation in the hearing range, most frequency spectrum presented are using a linear scale instead of a logarithmic one. This is once again an oversight coming from the fact that the sheer evidence of thermoacoustic capability demonstrated by the presented sample seems to outweighs any kind of acoustical analysis. Thermoacoustics might not be a worldwide hot topic but it is not a new field by any length. Hence, the acoustic analysis of thermophones should not be dissociated from its thermal capacities. Being able to produce a working thermophone should not be a self sufficient result, not unless the current theoretical limits are not reached or pushed.

In Section 1.2, the main theoretical models have been presented. An historical review on how and why those models where created or improved was explained. However, each of the summarized models have been developed to describe the behavior of a specific thermophone configuration with well defined identifying characteristics. Moreover, in each model some physical features have been neglected to simplify the analysis, and to obtain explicit results. For instance, the viscosity of the propagation medium is not considered in most models.

In addition, these models do not consider the acoustic wave propagation within the active solid layers. Therefore, the influence of potential resonances within the solid layers is not investigated in the literature. If sometimes mentioned [74], resonances are assumed to be in a frequency range higher than the one of interest. Also, even though those models have proved to accurately reproduce experimental results, a more unifying thermoacoustic model that could be used in many different cases and which would allow for easy comparison between geometries, is still missing.

Furthermore, none of the current models tackle the problem of complex geometries like graphene sponge or graphene foam. As most thermophones can be simplified to a cylinder or a film with a thickness, no theoretical is adapted to those 3D geometries. As a consequence it is not possible to conceive an optimal 3D geometry for thermoacoustic sound generation solely based on an existing theoretical model. Those models

are only used for comparison and for understanding, not as a tool of improvement of thermophones.

Lastly in Section 1.3, the many advantages of thermophones were shown to be of interest in various domains of applications. The most obvious application as audible sound generator, whether it is as loudspeakers, earphones or small size transducers, still faces many challenges preventing thermophones from going on the market. The main issue being their low efficiency. Using them as ultrasonic transducer, ANC transducers or skin wearable health devices makes use of other advantages of thermophones, but the lack of interest prevents the growth and the commercialisation of such devices.

It was seen that despite having reached high technological maturation, very few novel geometries have been tested so far as thermophones. Most of current thermophones are still based on nanowires or metal sheets as 150 years ago. 3D graphene or laser scribed materials displayed interesting properties but are not investigated in depth as their complex geometry make them more difficult to produce and their thermoacoustics capabilities did not exceed the most efficient ones. Thermophones are still tested for their applications instead of being designed for them.

Thermophones were then used in different medium (gaseous and liquid) to improve their sound radiation and investigate potential sonar applications. By testing them underwater, researchers highlighted their fragile condition and, in order to avoid damages, they were encapsulated. This encapsulation however created a resonant device and the unique frequency spectrum of thermophones is then no longer valid. The main advantages of thermophones being, namely, their flexibility, their light weight, their cheapness (they do not use any rare material), the fact that no moving part is involved and their peculiar flat frequency response up to MHz regions, encapsulating them prohibit the use of this last advantage. Despite that, the need for alternative to piezoelectric underwater transducers is great and light weight underwater transducers without moving parts are still of prime interest.

Ultimately, the type of input electrical signal provided to thermophone was investigated. The non linear thermoacoustic sound generation by Joule effect make it challenging for thermophone to play complex input signals. If it is possible to exploit the higher efficiency of thermophone at high frequency to create pure tone in the hearing range, its non linear behavior creates undesired harmonics. Hence only a very recent adaptive pre distortion method seems currently available for thermophone to play music using only an AC signal, deliverable by any commercial amplifier [143]. This highlighted again the interest that

thermophones hold toward commercial loudspeaker use. Nonetheless, many progress still have to be made as the THD and the efficiency of thermophones are still not comparable to traditional loudspeaker levels.

1.5 MOTIVATIONS AND EXPECTATIONS OF THE THESIS

Up to now, an extensive historical review of thermoacoustic sound generation, and more specifically, of thermophone for the last two centuries has been given. The last two decades of discovery and tests regarding thermoacoustic capacities of new materials has been presented alongside the theoretical formulation of the thermoacoustic sound generation in different cases. Based on the advantages of thermophones, the more promising applications have been presented. Followed by idea for improvement whether it is in regards of geometry, design, or signal processing for thermophones. Lastly the main issues and limitations that can be commonly found in the literature have been emphasized.

Based on the statement made by 1.4, a more unifying theoretical model has yet to be implemented. This thesis will first provide a theoretical model that can be applied for the vast majority of current thermophone configurations for both, plane, cylindrical and spherical wave generation. The conservation equations will be solved with the least among of assumptions and the models will be validated by comparing simulations with models and experiments from the literature.

Employing this theoretical model, thermoacoustic radiation will be studied and explained in many different cases. The theoretical model will be used as a tool of understanding most of the results in the literature without having to create a large amount of different working samples.

A second theoretical model will also be created which aims is to explain thermoacoustic sound generation in a foam like geometry using a so called *two temperatures* (2T) model. Its purpose is to fill a gap that has been shown currently in the literature regarding 3D thermophones.

In order to validate this 2T model, experiments will be conducted with three dimensional Graphene foam (3D-C). Different theoretical concerns will be proven again, and results will be confronted to other kind of thermophones. Those experiments aim at improving the understanding of thermophones and the way they should handled. Thermal and acoustical concerns will be studied hand in hand and insights about the optimal use of thermophones will be provided.

Many literature experiments will be reproduced. The capabilities of sound reproduction will be tested as well as tryouts of encapsulation for underwater applications.

This thesis goal is to provide a deep understanding of thermophones' thermoacoustic sound generation. By reading this thesis, you should gain insights on how thermophones should be used and for what purposes based on their inherent properties and not only on the specific performances of a single sample. The reader should be able to answer the question, are thermophones groundbreaking metamaterials for sound generation or just another toys for scientific curiosity?

Part II

THERMOACOUSTIC MODELLING

2

THEORETICAL MULTILAYERS MODELS

This Chapter provides the mathematical and theoretical background necessary for the analytical understanding of the thermoacoustic generation process. It also deals in the creation of several theoretical models for thermoacoustic sound generation.

At first the conservation equations upon which the models will be constructed are derived from the constitutive equation in both, fluid and solid phases, with arbitrary thermal and viscous properties. For the interested reader, Appendix A.1 constructs the constitutive equations starting from Lagrangian and Eulerian formalisms.

The conservation equations are then used to describe thermoacoustic plane wave generation from a thermophone and its near field propagation in both fluid and solid medium. An ideal planar thermophone is then formalised for simulation purposes and extended to a multilayer model to be implemented later in Matlab.

The exact same thought process is then applied for near field thermoacoustic generation of cylindrical and spherical waves. Ideal cylindrical and spherical thermophones are then investigated and their models are extended to multilayered ones as well.

Lastly what is called a two temperatures (2T) model is formulated for foamlike geometry thermophone. The model is adapted and solved for plane wave generation in near field similarly as the previous models.

The first time reader is invited to skip Sections 2.3 and 2.4 and to refer to the summary written before Section 2.5.

2.1 FORMALISM FOR FLUID AND SOLID PHASES

This section aims at writing the basic equations for fluid and solid phases with arbitrary thermal and viscous properties. Using the general balance equations being the conservation of mass, linear momentum, angular momentum, energy as well as the local form of the balance of entropy, the equations for the model are established.

2.1.1 *Summary on the Balance Equation*

The balance equations set up in Appendix A.1.4 in Eqs.(474), (481), (490), (499) and (504) are written respectively as

- **Conservation of mass**

$$\dot{\rho} + \rho\vec{\nabla}\cdot\vec{v} = 0, \tag{1}$$

- **Conservation on linear momentum**

$$\rho\dot{\vec{v}} = \vec{\nabla}\cdot\hat{T} + \vec{b}, \tag{2}$$

- **Conservation on angular momentum**

$$\hat{T} = \hat{T}^{T}, \tag{3}$$

- **Conservation of energy**

$$\rho\dot{e} = \hat{T} : \hat{D} - \vec{\nabla}\cdot\vec{q} + Q_0, \tag{4}$$

- **Local form of the balance of entropy**

$$\rho\dot{s} = -\vec{\nabla}\cdot(\frac{\vec{q}}{T}) + \frac{Q_0}{T} + \sigma_s, \quad \sigma_s \geqslant 0, \tag{5}$$

with ρ density [$kg.m^{-3}$], $\dot{\rho}$ its Lagrangian/material derivative, $\vec{v}$ particle velocity vector [$m.s^{-1}$], $\hat{T}$ Cauchy stress tensor [$N.m^{-2}$], $\vec{b}$ body force density [$N.m^{-3}$] , e specific internal energy [$J.kg^{-1}$], $\hat{L} = \frac{\partial\vec{v}}{\partial\vec{x}}$ velocity gradient [s^{-1}], $\hat{D} = \frac{1}{2}(\hat{L} + \hat{L}^{\dagger})$ symmetric part of $\hat{L}$, q heat flow [$W.m^{-2}$], Q_0 heat density supplied [$W.m^{-3}$] , s entropy density per unit of mass [$J.K^{-1}.kg^{-1}$], T temperature [K] and σ_s entropy production density [$J.K^{-1}.m^{-3}.s^{-1}$].

To obtain the final Eulerian form we have to consider the relation $\dot{x} = \frac{\partial x}{\partial t} + \vec{\nabla}x\cdot\vec{v}$ which is discussed in Appendix A.1. While Eqs.(1), (2) and (4) are useful to define the motion of the continuum medium, Eqs.(3) and (5) are crucial to define the constitutive equations of the material. Indeed the balance equations are not sufficient to solve a given problem and they must be completed with a set of equations describing the behavior of the material under motion or deformation. The entropy balance is very important to give the most general form of the constitutive equations. We will describe this procedure for fluids and solids and we will show the linearised form of the final equations.

2.1.2 *Fluids with Arbitrary Thermal and Viscous Properties*

The previously introduced scheme is now developed in a fluid medium. It gives very important results under the so-called hypothesis of local equilibrium. It means that we consider a thermodynamic equilibrium at any point of the system. In other words, the continuum medium is decomposed in a number of elemental cells where the thermodynamic equilibrium is attained with good approximation, but the overall system is out-of-equilibrium. This assumption leads to a closed form expression for the entropy production, useful to define the transport processes. For fluids, local equilibrium can be described by the following law, which is true at any point of the system (Lagrangian vision)

$$\frac{de}{dt} = T\frac{ds}{dt} - p\frac{d}{dt}\left(\frac{1}{\rho}\right). \tag{6}$$

This equation has been written in terms of quantity for unit of mass, so the classical term pdV is substituted by $p\frac{dV}{M} = pd(\frac{1}{M/V}) = pd(\frac{1}{\rho})$ with V the volume in $[m^3]$, M the mass in $[kg]$ and p the pressure in $[Pa]$.

The local equilibrium is imposed without considering the possible gradients within the system. These gradients are responsible for the overall non reversibility of the process and of the out-of-equilibrium state of the system. The fact that we impose a local equilibrium and that we have a global out-of-equilibrium state is not a paradox but it is rather an approximation that must be verified by comparing the theoretical results with experimental ones.

We study the effects of Eq.(6) on the entropy balance. Using the conservation of mass (Eq.(1)) we have

$$\begin{aligned}\frac{de}{dt} &= T\frac{ds}{dt} - p(-\frac{1}{\rho^2})\frac{d\rho}{dt},\\ &= T\frac{ds}{dt} + \frac{p}{\rho^2}(-\rho\vec{\nabla}\cdot\vec{v}),\\ &= T\frac{ds}{dt} - \frac{p}{\rho}\,\vec{\nabla}\cdot\vec{v}.\end{aligned} \tag{7}$$

The energy variation is given by the heat exchanged and by the hydrostatic work (fluids). The idea is to inject Eq.(7) into Eq.(4) (balance of energy) and to compare with Eq.(5) (balance of entropy). Eq.(4) becomes

$$\rho T\dot{s} - p\vec{\nabla}\cdot\vec{v} = \hat{T} : \hat{D} - \vec{\nabla}\cdot\vec{q} + Q_0, \tag{8}$$

or

$$\rho\dot{s} = \frac{p}{T}\vec{\nabla}\cdot\vec{v} + \frac{1}{T}\hat{T} : \hat{D} - \frac{1}{T}\vec{\nabla}\cdot\vec{q} + \frac{Q_0}{T}. \tag{9}$$

Eq.(9) can be elaborated as

$$\rho\dot{s} = \frac{p}{T}\vec{\nabla}\cdot\vec{v} + \frac{1}{T}\hat{T} : \hat{D} - \vec{\nabla}\cdot(\frac{\vec{q}}{T}) - \frac{1}{T^2}\vec{q}\cdot\vec{\nabla}T + \frac{Q_0}{T}. \tag{10}$$

The comparison between Eq.(5) and (10) provides the entropy production

$$\sigma_s = \frac{p}{T}\vec{\nabla}\cdot\vec{v} + \frac{1}{T}\hat{T} : \hat{D} - \frac{1}{T^2}\vec{q}\cdot\vec{\nabla}T \geqslant 0. \tag{11}$$

Now for viscous fluid we have to admit a stress tensor $\hat{T}$ composed of an hydrostatic term $-p\hat{I}$ and an arbitrary viscous term $\hat{g}(\hat{D})$ which depends only on the symmetric part of the velocity gradient since the viscous effects are absent for rigid motions. $\hat{T}$ is written as

$$\hat{T} = -p\hat{I} + \hat{g}(\hat{D}). \tag{12}$$

Moreover, $\vec{q}$ describe the heat transfer within the material and, therefore, depends on the temperature gradient

$$\vec{q} = \vec{f}(\vec{\nabla}T). \tag{13}$$

Eq.(11) now gives

$$\sigma_s = \frac{p}{T}\vec{\nabla}\cdot\vec{v} + \frac{1}{T}(-p)\hat{I} : \hat{D} + \frac{1}{T}\hat{g}(\hat{D}) : \hat{D} - \frac{1}{T^2}\vec{f}(\vec{\nabla}T)\cdot\vec{\nabla}T \ \geqslant 0. \tag{14}$$

Entropy Production

This leads to $\hat{I} : \hat{D} = \mathrm{tr}(\hat{D}) = \mathrm{tr}\left(\frac{\partial\vec{v}}{\partial\vec{x}}\right) = \vec{\nabla}\cdot\vec{v}$, and finally

$$\sigma_s = \frac{1}{T}\hat{g}(\hat{D}) : \hat{D} - \frac{1}{T^2}\vec{f}(\vec{\nabla}T)\cdot\vec{\nabla}T \ \geqslant 0. \tag{15}$$

The entropy production of an irreversible process always admits a bilinear structure. We observe that $\sigma_s > 0$ (irreversible process) only if the gradients $\hat{D}$ and $\vec{\nabla}T$ are present in the system. Additionally, it is noticed that $\hat{D}$ generates $\hat{T}$ and $\vec{\nabla}T$ generates $\vec{q}$. For an isotropic fluid the two effects are independent (see the Curie law in Appendix A.2) and the functions $\hat{g}$ and $\vec{f}$ can be linearised separately as

Phenomenological Relations

$$\begin{cases} \hat{g} = 2\mu\hat{D} + \lambda\,\mathrm{tr}(\hat{D})\hat{I} = \hat{\hat{V}}\hat{D}, \\ \vec{f} = -\kappa\vec{\nabla}T, \end{cases} \tag{16}$$

where $\hat{\hat{V}}$ and κ must be positive to fulfill Eq.(15). λ and μ are the viscosity coefficients in [Pa.s] and represents the isotropic form of $\hat{\hat{V}}$. κ is the so-called thermal conductivity $[W.K^{-1}.m^{-1}]$. Eq.(16) represents the

phenomenological relations and the linear coefficients are the so-called phenomenological coefficients.

The equations governing the dynamics of a viscous fluid with thermal conduction are finally the following

$$\begin{cases} \dot{\rho} + \rho\vec{\nabla}\cdot\vec{v} = 0, & \text{balance of mass} \\ \rho\dot{\vec{v}} = \vec{\nabla}\cdot\hat{T} + \vec{b}, & \text{balance of linear momentum} \\ \hat{T} = -p\hat{I} + 2\mu\hat{D} + \lambda\,\mathrm{tr}(\hat{D})\hat{I}, & \text{stress tensor} \\ \rho\dot{e} = \hat{T} : \hat{D} - \vec{\nabla}\cdot\vec{q} + Q_0, & \text{balance of energy} \\ \vec{q} = -\kappa\vec{\nabla}T, & \text{heat transfer} \\ p = p(\rho, T), & \\ e = e(\rho, T). & \end{cases} \tag{17}$$

Eqs.(17f,g) represent the equilibrium behavior of the material which is accepted locally. From the point of view of the thermodynamics, they can be obtained through the introduction of Helmholtz free energy density $f_h = e - Ts$ in $[J.kg-1]$, yielding $f_h = f_h(\rho, T)$ and

$$\begin{cases} p = -\frac{\partial f_h}{\partial(\frac{1}{\rho})}, \\ s = -\frac{\partial f_h}{\partial T}. \end{cases} \tag{18}$$

In classical thermodynamics Eq.(18a) is typically found in the form $P = -\frac{\partial F_h}{\partial V}$ which corresponds to $p = -\frac{\partial(F_h/M)}{\partial(V/M)} = -\frac{\partial f_h}{\partial(\frac{1}{\rho})}$ as reported.

Einstein Notation

We now aim to simplify Eqs.(17). From now on we will use for simplicity the Einstein notation that implies the summation over a set of indexed terms. Using this notation, here with the sum over i, j and k, Eq.(17c) becomes

$$T_{ij} = -p\delta_{ij} + \mu\left(\frac{\partial v_i}{\partial x_j} + \frac{\partial v_j}{\partial x_i}\right) + \lambda\frac{\partial v_k}{\partial x_k}\delta_{ij}, \tag{19}$$

with δ the Kronecker symbol. We then get

$$\frac{\partial T_{ij}}{\partial x_j} = -\frac{\partial p}{\partial x_j}\delta_{ij} + \mu\left(\frac{\partial^2 v_i}{\partial x_j^2} + \frac{\partial^2 v_j}{\partial x_i \partial x_j}\right) + \lambda\frac{\partial^2 v_k}{\partial x_k \partial x_j}\delta_{ij}, \tag{20}$$

or equivalently

$$\vec{\nabla}\cdot\hat{T} = -\vec{\nabla}p + \mu\nabla^2\vec{v} + (\lambda+\mu)\vec{\nabla}(\vec{\nabla}\cdot\vec{v}), \tag{21}$$

which can be used to simplify the linear moment balance of Eq.(17b). Similarly $\hat{T} : \hat{D}$ can be explicitly written as

$$\begin{aligned}
\hat{T} : \hat{D} &= T_{ij} D_{ij}, \\
&= \left[-p\delta_{ij} + \mu \left(\frac{\partial v_i}{\partial x_j} + \frac{\partial v_j}{\partial x_i} \right) + \lambda \frac{\partial v_k}{\partial x_k} \delta_{ij} \right] \frac{1}{2} \left(\frac{\partial v_i}{\partial x_j} + \frac{\partial v_j}{\partial x_i} \right), \\
&= -\frac{p}{2} \left(\frac{\partial v_i}{\partial x_i} + \frac{\partial v_i}{\partial x_i} \right) + \frac{\mu}{2} \left(\frac{\partial v_i}{\partial x_j} + \frac{\partial v_j}{\partial x_i} \right)^2 + \frac{\lambda}{2} \frac{\partial v_k}{\partial x_k} \left(\frac{\partial v_i}{\partial x_i} + \frac{\partial v_i}{\partial x_i} \right), \\
&= -p\vec{\nabla} \cdot \vec{v} + \frac{\mu}{2} \left(\frac{\partial v_i}{\partial x_j} \frac{\partial v_i}{\partial x_j} + 2 \frac{\partial v_i}{\partial x_j} \frac{\partial v_j}{\partial x_i} + \frac{\partial v_j}{\partial x_i} \frac{\partial v_j}{\partial x_i} \right) + \lambda (\frac{\partial v_k}{\partial x_k})^2, \\
&= -p\vec{\nabla} \cdot \vec{v} + \mu \left(\frac{\partial v_i}{\partial x_j} \frac{\partial v_i}{\partial x_j} + \frac{\partial v_i}{\partial x_j} \frac{\partial v_j}{\partial x_i} \right) + \lambda (\vec{\nabla} \cdot \vec{v})^2. \qquad (22)
\end{aligned}$$

Eulerian Continuity, Navier-Stokes and Heat Equations in a Fluid

As a result we have in Eulerian form, the continuity, the Navier-Stokes and the heat equations in a fluid written respectively as

$$\begin{cases}
\frac{\partial \rho}{\partial t} + \vec{\nabla} \cdot (\rho \vec{v}) = 0, \\
\rho \left[\frac{\partial \vec{v}}{\partial t} + (\vec{v} \cdot \vec{\nabla}) \vec{v} \right] = -\vec{\nabla} p + \mu \nabla^2 v + (\lambda + \mu) \vec{\nabla} (\vec{\nabla} \cdot \vec{v}) + \vec{b}, \\
\rho \left[\frac{\partial e}{\partial t} + (\vec{v} \cdot \vec{\nabla}) e \right] = -p\vec{\nabla} \cdot \vec{v} + \mu \left(\frac{\partial v_i}{\partial x_j} \frac{\partial v_i}{\partial x_j} + \frac{\partial v_i}{\partial x_j} \frac{\partial v_j}{\partial x_i} \right) + \lambda (\vec{\nabla} \cdot \vec{v})^2 + \kappa \nabla^2 T + Q_0,
\end{cases} \qquad (23)$$

where, with f_h the Helmholtz free energy density,

$$\begin{cases}
e = f_h + Ts, \\
p = -\frac{\partial f_h}{\partial (1/\rho)}, \\
s = -\frac{\partial f_h}{\partial T}.
\end{cases} \qquad (24)$$

Eqs.(23) and (24) represent the complete system of equation for a viscous fluid with thermal transfer.

The function $f_h(\rho, t)$ comes from the statistical mechanics and takes into consideration the real interactions among atoms or molecules of the fluid. It can be directly correlated to the partition function of the system. The final system of equation has the unknowns $(\rho, \vec{v}, p, T, s, e)$ and, coherently, is composed of 8 equations. The problem is that this system is strongly non linear and it can be only approached numerically for problems involving small deviations around a given equilibrium state, the system can be linearised by generating a simpler mathematical problem. To do this, we suppose that the 8 quantities defined above can be substituted as

$$\phi \to \phi_0 + \varepsilon \phi, \qquad (25)$$

where ϕ_0 is the equilibrium value, ϕ is the perturbation and ε is a small parameter. In Eq.(25) ϕ stands for one of the 8 variables $(\rho, \vec{v}, p, T, s, e)$. It is then understood that from now on, the use of those 8 variables without the subscript $_0$ actually describe their variations around a given equilibrium state. We suppose that $\vec{v}_0 = 0$ since the fluid is considered at rest at equilibrium. On the other hand, ρ_0, p_0, T_0, s_0 and e_0 assume arbitrary values. The continuity equation Eq.(23a) is rewritten as

$$\frac{\partial}{\partial t}(\rho_0 + \varepsilon\rho) = -\vec{\nabla} \cdot [(\rho_0 + \varepsilon\rho)(\vec{v}_0 + \varepsilon\vec{v})]\,. \tag{26}$$

The identity of the terms proportional to ε^0 is

$$\frac{\partial \rho_0}{\partial t} = -\vec{\nabla} \cdot (\rho_0 \vec{v}_0), \tag{27}$$

which is satisfied since ρ_0 is constant and $\vec{v}_0 = 0$. The identity of the terms proportional to ε^1 is

$$\frac{\partial \rho}{\partial t} = -\vec{\nabla} \cdot (\rho_0 \vec{v} + \rho \vec{v}_0). \tag{28}$$

Since $\vec{v}_0 = 0$ the first order equation for ρ is

$$\frac{\partial \rho}{\partial t} + \rho_0 \vec{\nabla} \cdot \vec{v} = 0. \tag{29}$$

The same procedure can be applied to the Navier-Stokes equation Eq.(23b)

$$(\rho_0 + \varepsilon\rho)\left[\frac{\partial \varepsilon \vec{v}}{\partial t} + \varepsilon^2(\vec{v} \cdot \vec{\nabla})\vec{v}\right] = -\vec{\nabla}(p_0 + \varepsilon p) + \mu\varepsilon\nabla^2 v + (\lambda + \mu)\varepsilon\vec{\nabla}(\vec{\nabla} \cdot \vec{v}) + \vec{b}. \tag{30}$$

The terms of order zero give

$$\vec{\nabla} p_0 = \vec{b}, \tag{31}$$

which is the static equilibrium. The terms of order one give

$$\rho_0 \frac{\partial \vec{v}}{\partial t} = -\vec{\nabla} p + \mu\nabla^2 v + (\lambda + \mu)\vec{\nabla}(\vec{\nabla} \cdot \vec{v}), \tag{32}$$

which is the linearised Navier-Stokes equation. Finally, the same thought process is applied to the energy balance. Eq.(23c) delivers

$$\begin{aligned}
&(\rho_0 + \varepsilon\rho)\left[\frac{\partial(e_0 + \varepsilon e)}{\partial t} + (\vec{v} \cdot \vec{\nabla})\varepsilon(e_0 + \varepsilon e)\right] = \\
&-(p_0 + \varepsilon p)\vec{\nabla} \cdot (\varepsilon\vec{v}) + \mu\varepsilon^2\left(\frac{\partial v_i}{\partial x_j}\frac{\partial v_i}{\partial x_j} + \frac{\partial v_i}{\partial x_j}\frac{\partial v_j}{\partial x_i}\right) + \\
&+ \lambda\varepsilon^2(\vec{\nabla} \cdot \vec{v})^2 + \kappa\nabla^2(T_0 + \varepsilon T) + Q_0.
\end{aligned} \tag{33}$$

The identity generated by the zero order terms is

$$\rho_0 \frac{\partial e_0}{\partial t} = \kappa \nabla^2 T_0 + Q_0, \tag{34}$$

which is the stationary thermal conduction. The first order identity is

$$\rho_0 \frac{\partial e}{\partial t} + \rho \frac{\partial e_0}{\partial t} + \rho_0 (\vec{v} \cdot \vec{\nabla}) e_0 = -p_0 \vec{\nabla} \cdot \vec{v} + \kappa \nabla^2 T. \tag{35}$$

We suppose $Q_0 = 0$ (no energy supplied to the system) and e_0 and T_0 constant. Hence, we have that Eq.(34) is always satisfied and Eq.(35) simplifies to

$$\rho_0 \frac{\partial e}{\partial t} = -p_0 \vec{\nabla} \cdot \vec{v} + \kappa \nabla^2 T. \tag{36}$$

This equation can be written in terms of entropy through the first principle $de = Tds - pd(\frac{1}{\rho})$. If we introduce here the perturbations we get

$$d(e_0 + \varepsilon e) = (T_0 + \varepsilon T) d(s_0 + \varepsilon s) - (p_0 + \varepsilon p) d(\frac{1}{\rho_0 + \varepsilon \rho}), \tag{37}$$

where

$$\frac{1}{\rho_0 + \varepsilon \rho} = \frac{1}{\rho_0} \left(\frac{1}{1 + \varepsilon \frac{\rho}{\rho_0}} \right) \approx \frac{1}{\rho_0} (1 - \varepsilon \frac{\rho}{\rho_0}). \tag{38}$$

Hence

$$d(e_0 + \varepsilon e) = (T_0 + \varepsilon T) d(s_0 + \varepsilon s) - (p_0 + \varepsilon p) \frac{1}{\rho_0} d(1 - \varepsilon \frac{\rho}{\rho_0}), \tag{39}$$

where ρ_0 is supposed constant. If also s_0 is considered constant, the first order terms in Eq.(39) yield

$$de = T_0 ds + p_0 \frac{d\rho}{\rho_0^2}, \tag{40}$$

or equivalently

$$\rho_0 \frac{de}{dt} = \rho_0 T_0 \frac{ds}{dt} - p_0 \left(-\frac{1}{\rho_0} \frac{d\rho}{dt} \right). \tag{41}$$

At first order $\frac{d\rho}{dt} \approx \frac{\partial \rho}{\partial t}$ and $-\frac{1}{\rho_0} \frac{\partial \rho}{\partial t} = \vec{\nabla} \cdot \vec{v}$ (see Eq.(29)) and thus

$$\rho_0 \frac{de}{dt} = \rho_0 T_0 \frac{ds}{dt} - p_0 \vec{\nabla} \cdot \vec{v}. \tag{42}$$

Comparing with Eq.(36) we get

$$p_0 T_0 \frac{\partial s}{\partial t} = \kappa \nabla^2 T. \tag{43}$$

Eq.(43) means that the linearised process is isoentropic or adiabatic (locally) if we can neglect the thermal conduction.

Linearised Eulerian Constitutive Equations in a Fluid

The linearised system in a fluid made of the continuity, Navier-Stokes and heat equations is

$$\begin{cases} \frac{\partial \rho}{\partial t} + \rho_0 \vec{\nabla} \cdot \vec{v} = 0, \\ \rho_0 \frac{\partial \vec{v}}{\partial t} = -\vec{\nabla} p + \mu \nabla^2 \vec{v} + (\lambda + \mu) \vec{\nabla} (\vec{\nabla} \cdot \vec{v}), \\ \rho_0 T_0 \frac{\partial s}{\partial t} = \kappa \nabla^2 T. \end{cases} \tag{44}$$

We will now combine Eqs.(44) with $p = p(\rho, T)$ and $s = s(\rho, T)$ to have the system in terms of quantifiable medium constants. For the entropy we have

$$\frac{\partial s}{\partial t} = \left.\frac{\partial s}{\partial T}\right|_{p_0} \frac{\partial T}{\partial t} + \left.\frac{\partial s}{\partial p}\right|_{T_0} \frac{\partial p}{\partial t}, \tag{45}$$

by using the variables T and p instead of ρ and T (note that each couple of independent variables can be used to linearise). Before elaborating Eq.(45) we observe that if we consider two variables x' and y' perturbed with the substitutions $x' = x_0 + \varepsilon x$ and $y' = y_0 + \varepsilon y$, we have

$$\frac{\partial y'}{\partial x'} = \frac{\partial (y_0 + \varepsilon y)}{\partial x'} = \varepsilon \frac{\partial y}{\partial x'} = \varepsilon \frac{\partial y}{\partial x} \frac{1}{\frac{\partial x'}{\partial x}} = \varepsilon \frac{\partial y}{\partial x} \frac{1}{\varepsilon} = \frac{\partial y}{\partial x}. \tag{46}$$

The identity $\frac{\partial y'}{\partial x'} = \frac{\partial y}{\partial x}$ means that the partial derivative between two variables can be calculated either on the original variables or on their perturbations without modifying the result. This leads to

$$C_p = \left.\frac{dq}{dT}\right|_p = T \left.\frac{\partial s}{\partial T}\right|_p, \tag{47}$$

which represent the specific heat at constant pressure in $[J.kg^{-1}.K^{-1}]$. Therefore $\left.\frac{\partial s}{\partial T}\right|_{p_0} = \frac{C_p}{T_0}$ can be used in the first term of Eq.(45). The second

one can be elaborated using the Maxwell equation $\left.\frac{\partial S}{\partial p}\right|_{p_0} = -\left.\frac{\partial V}{\partial T}\right|_{p_0}$, and so

$$\begin{aligned}\left.\frac{\partial s}{\partial p}\right|_{T_0} &= -\left.\frac{\partial (V/M)}{\partial T}\right|_{p_0}, \\ &= -\left.\frac{1}{M}\frac{\partial V}{\partial T}\right|_{p_0}, \\ &= -\frac{V}{M}\left[\frac{1}{V}\left.\frac{\partial V}{\partial T}\right|_{p_0}\right], \\ &= -\frac{1}{\rho_0}\alpha_T, \end{aligned} \tag{48}$$

where

$$\alpha_T = \frac{1}{V}\left.\frac{\partial V}{\partial T}\right|_{p_0}, \tag{49}$$

is the coefficient of volumetric thermal expansion in $[K^{-1}]$. Finally Eq.(45) leads to

Coefficient of Volumetric Expansion

$$\frac{\partial s}{\partial t} = \frac{C_p}{T_0}\frac{\partial T}{\partial t} - \frac{\alpha_T}{\rho_0}\frac{\partial p}{\partial t}. \tag{50}$$

Instead of considering $p = p(\rho, T)$ we can also use $\rho = \rho(p, T)$ as

$$\begin{aligned}\rho_0 + \varepsilon\rho &= \rho(p_0 + \varepsilon p, T_0 + \varepsilon T), \\ &= \rho(p_0, T_0) + \varepsilon \left.\frac{\partial \rho}{\partial p}\right|_{T_0} p + \varepsilon \left.\frac{\partial p}{\partial T}\right|_{p_0} T, \end{aligned} \tag{51}$$

then

$$\rho = \left.\frac{\partial \rho}{\partial p}\right|_{T_0} p + \left.\frac{\partial \rho}{\partial T}\right|_{p_0} T,$$

where

$$\begin{aligned}\left.\frac{\partial \rho}{\partial p}\right|_{T_0} &= M\left.\frac{\partial (\frac{1}{V})}{\partial p}\right|_{T_0}, \\ &= -\left.\frac{M}{V^2}\frac{\partial V}{\partial p}\right|_{T_0}, \\ &= -\frac{M}{V}\left[\frac{1}{V}\left.\frac{\partial V}{\partial p}\right|_{T_0}\right]. \end{aligned} \tag{52}$$

Here $\kappa_T = -\frac{1}{V}\left.\frac{\partial V}{\partial p}\right|_{T_0}$ is the coefficient of isothermal compressibility. In elasticity terms $\frac{1}{\kappa_T}$ is named bulk modulus B. So we have

Bulk Modulus

$$\left.\frac{\partial \rho}{\partial p}\right|_{T_0} = \rho_0 \kappa_T = \frac{\rho_0}{B}. \tag{53}$$

The second derivative follows

$$\left.\frac{\partial \rho}{\partial T}\right|_{p_0} = M \left.\frac{\partial(\frac{1}{V})}{\partial T}\right|_{p_0} = -\frac{M}{V^2}\left.\frac{\partial V}{\partial T}\right|_{p_0} = -\rho_0 \alpha_T. \tag{54}$$

Summing up

Linearised Density Variations

$$\rho = \frac{\rho_0}{B} p - \rho_0 \alpha_T T, \tag{55}$$

which is the linearised form of the $\rho = \rho(p, T)$. Eqs.(44), (50) and (55) describe the linearised model for a thermo-viscous fluid.

In this section, from the balance equations of Section 2.1.1, the Eulerian form of the continuity, Navier-Stokes and heat equations have been formulated. Eqs.(23) represents the complete system of equation for a viscous fluid with thermal transfer. Assuming small deviations around a given equilibrium state for the unknowns $(\rho, \vec{v}, p, T, s, e)$, the system was linearised to Eqs.(44). It was then simplified to have the linearised system for any thermo-viscous fluid only depending only on the variables $(p, \vec{v}, T)$. Hence, substituting Eqs.(50) and (55) in Eq.(44) we have a simplified system [144]

Linearised Conservation Equations in any Thermo-Viscous Fluid

$$\begin{cases} \frac{\rho_0}{B}\frac{\partial p}{\partial t} - \rho_0 \alpha_T \frac{\partial T}{\partial t} + \rho_0 \vec{\nabla}\cdot\vec{v} = 0, \\ \rho_0 \frac{\partial \vec{v}}{\partial t} = -\vec{\nabla} p + \mu \nabla^2 \vec{v} + (\lambda + \mu)\vec{\nabla}(\vec{\nabla}\cdot\vec{v}), \\ \rho_0 C_p \frac{\partial T}{\partial t} - \alpha_T T_0 \frac{\partial p}{\partial t} = \kappa \nabla^2 T. \end{cases} \tag{56}$$

Eq.(56) are respectively the conservation of mass (continuity), of momentum (Navier-Stokes) and of energy (heat). The abusive notations p, T to represent the pressure and temperature variations around a constant state symbolised by the subscript $_0$ will be used throughout this thesis in fluid.

2.1.3 *Solids with Arbitrary Thermal and Viscous Properties*

Similarly as Section 2.1.2, we now aim at writing linearised conservation equations for any thermo-visco elastic anisotropic solid. We consider

a solid elastic material that may undergo arbitrary deformations. As discussed in Section 2.1.1, the balance equations can be written as

$$\dot{\rho} + \rho\vec{\nabla}\cdot\vec{v} = 0, \tag{1}$$
$$\rho\dot{\vec{v}} = \vec{\nabla}\cdot\hat{T} + \vec{b}, \tag{2}$$
$$\hat{T} = \hat{T}^T, \tag{3}$$
$$\rho\dot{e} = \hat{T} : \hat{D} - \vec{\nabla}\cdot\vec{q} + Q_0, \tag{4}$$
$$\rho\dot{s} = -\vec{\nabla}\cdot(\frac{\vec{q}}{T}) + \frac{Q_0}{T} + \sigma_s. \quad \sigma_s \geqslant 0 \tag{5}$$

In order to define the constitutive behavior of a solid it is better to consider the Helmholtz free energy density f_h as function of T and $\hat{F}$ (state of deformation). So we have $f_h = f_h(T, \hat{F})$ and we can use the relation $e = f_h + Ts$ to compare Eq.(4) and (5). To do this we calculate

$$\begin{aligned}\dot{e} &= \dot{f_h} + \dot{T}s + T\dot{s},\\ &= \dot{f_h} - \frac{\partial f_h}{\partial T}\dot{T} + T\dot{s},\end{aligned}$$

where we used the relation $s = -\frac{\partial f_h}{\partial T}$. So we have from Eq.(4)

$$\rho\dot{f_h} - \rho\frac{\partial f_h}{\partial T}\dot{T} + \rho T\dot{s} = \hat{T} : \hat{D} - \vec{\nabla}\cdot\vec{q} + Q_0, \tag{57}$$

which, once divided by T is

$$\begin{aligned}\frac{\rho}{T}\dot{f_h} - \rho\frac{\partial f_h}{\partial T}\frac{\dot{T}}{T} + \rho\dot{s} &= \frac{1}{T}\hat{T} : \hat{D} - \frac{1}{T}\vec{\nabla}\cdot\vec{q} + \frac{Q_0}{T},\\ &= \frac{1}{T}\hat{T} : \hat{D} - \vec{\nabla}\cdot(\frac{\vec{q}}{T}) - \frac{1}{T^2}\vec{q}\cdot\vec{\nabla}T + \frac{Q_0}{T}.\end{aligned} \tag{58}$$

Hence

$$\rho\dot{s} = \rho\frac{\partial f_h}{\partial T}\frac{\dot{T}}{T} - \frac{\rho}{T}\dot{f_h} + \frac{1}{T}\hat{T} : \hat{D} - \vec{\nabla}\cdot(\frac{\vec{q}}{T}) - \frac{1}{T^2}\vec{q}\cdot\vec{\nabla}T + \frac{Q_0}{T}. \tag{59}$$

Principle of Frame Indifference

The relation stating that $f_h = f_h(T, \hat{F})$ can be simplified by means of the principle of material objectivity (or material frame indifference) which says that the energy (and the stress) in the body should be the same regardless of the reference from which it is measure. If we consider an arbitrary motion $\vec{x} = F_t(\vec{X})$, we can obtain the corresponding deformation gradient $\hat{F} = \frac{\partial\vec{x}}{\partial\vec{X}}$. On the other hand, if we consider a roto-translated motion $\vec{x} = \hat{Q}(t)F_t(\vec{X}) + \vec{c}(t)$ (where $\hat{Q}(t)$ is an orthogonal matrix and $\vec{c}(t)$ is an arbitrary vector), then the deformation gradient is $\hat{Q}\hat{F}$. In both cases we must have the same free energy and therefore

$$f_h(T, \hat{F}) = f_h(T, \hat{Q}\hat{F}), \tag{60}$$

for all arbitrary orthogonal operator $\hat{Q}$, meaning they verify $\hat{Q}\hat{Q}^T = \hat{I}$. This principle allows the simplification of the theory. Indeed any non singular tensor can be decomposed in two different ways

Polar Decomposition Theorem

$$\hat{F} = \hat{R}\hat{U} = \hat{V}\hat{R}, \tag{61}$$

where $\hat{R}$ is orthogonal and $\hat{U}$ and $\hat{V}$ are symmetric and positive definite tensors. This is the Cauchy polar decomposition theorem whose proof of existence and uniqueness can be found in Appendix A.4. Hence, using Cauchy decomposition $\hat{F} = \hat{R}\hat{U}$ in Eq.(60)

$$f_h(T, \hat{F}) = f_h(T, \hat{Q}\hat{R}\hat{U}), \quad \forall \hat{Q}. \tag{62}$$

By imposing $\hat{Q} = \hat{R}^T$ we have

$$f_h(T, \hat{F}) = f_h(T, \hat{U}). \tag{63}$$

Changing the variable from $\hat{U}$ to $\hat{U}^2$ we obtain

$$f_h(T, \hat{F}) = g_h(T, \hat{U}^2) = g_h(T, \hat{C}), \tag{64}$$

where $\hat{C} = \hat{U}^2$ is the right Cauchy tensor and g_h is a modified function still representing Helmholtz free energy density after the change of variable. The material frame indifference allows us to use $\hat{C}$ instead of $\hat{F}$. The choice of $\hat{C}$ is convenient since $\hat{C} = \hat{F}^T\hat{F}$ is a rational function of $\hat{F}$. An alternative formulation is based on the second polar decomposition $\hat{F} = \hat{V}\hat{R}$ leads to $f_h(T, \hat{F}) = f_h(T, \hat{V})$ or, with $\hat{V}^2 = \hat{B}$, to $f_h(T, \hat{F}) = g_h(T, \hat{B})$. In order to facilitate reading, the notation f_h will be kept in the following section but is now function of $\hat{C}$. We now continue with the first formulation by calculating $\dot{f_h}$ in Eq.(59)

$$\dot{f_h} = \frac{\partial f_h}{\partial T}\dot{T} + \frac{\partial f_h}{\partial \hat{C}}\dot{\hat{C}}, \tag{65}$$

where

$$\dot{\hat{C}} = \frac{d}{dt}(\hat{F}^T\hat{F}) = \dot{\hat{F}}^T\hat{F} + \hat{F}^T\dot{\hat{F}}. \tag{66}$$

Eq.(59) becomes

$$\begin{aligned}\rho\dot{s} = \rho\frac{\partial f_h}{\partial T}\frac{\dot{T}}{T} - \rho\frac{\partial f_h}{\partial T}\frac{\dot{T}}{T} - \frac{\rho}{T}\frac{\partial f_h}{\partial \hat{C}}(\dot{\hat{F}}^T\hat{F} + \hat{F}^T\dot{\hat{F}}) + \frac{1}{T}\hat{T} : \hat{D} + \\ - \vec{\nabla}\cdot(\frac{\vec{q}}{T}) + \frac{Q_0}{T} - \frac{1}{T^2}\vec{q}\cdot\vec{\nabla}T.\end{aligned} \tag{67}$$

We decompose the stress $\hat{T}$ as the sum of the elastic stress $\hat{T}_e$ and the viscous stress $\hat{T}_V$ where $\hat{T} = \hat{T}_e + \hat{T}_V$. We get

$$\rho\dot{s} = \frac{1}{T}\left[\hat{T}_e : \hat{D} - \rho\frac{\partial f_h}{\partial \hat{C}}(\dot{\hat{F}}^T\hat{F} + \hat{F}^T\dot{\hat{F}})\right] + \frac{1}{T}\hat{T}_V : \hat{D} - \frac{1}{T^2}\vec{q}\cdot\vec{\nabla}T - \vec{\nabla}\cdot(\frac{\vec{q}}{T}) + \frac{Q_0}{T}.$$

(68)

The entropy production given by Eq.(5) is now written as

$$\sigma_s = \frac{1}{T}\left[\hat{T}_e : \hat{D} - \rho\frac{\partial f_h}{\partial \hat{C}}(\dot{\hat{F}}^T\hat{F} + \hat{F}^T\dot{\hat{F}})\right] + \frac{1}{T}\hat{T}_V : \hat{D} - \frac{1}{T^2}\vec{q}\cdot\vec{\nabla}T, \tag{69}$$

whose first term can be elaborated as

$$\begin{aligned}
\hat{T}_e : \hat{D} - \rho\frac{\partial f_h}{\partial \hat{C}}(\dot{\hat{F}}^T\hat{F} + \hat{F}^T\dot{\hat{F}}) &= \mathrm{tr}\left(\hat{T}_e\hat{D} - \rho\frac{\partial f_h}{\partial \hat{C}}\dot{\hat{F}}^T\hat{F} - \rho\frac{\partial f_h}{\partial \hat{C}}\hat{F}^T\dot{\hat{F}}\right), \\
&= \mathrm{tr}\left(\hat{T}_e\hat{D} - \rho\frac{\partial f_h}{\partial \hat{C}}\hat{F}^T\hat{L}^T\hat{F} - \rho\frac{\partial f_h}{\partial \hat{C}}\hat{F}^T\hat{L}\hat{F}\right), \\
&= \mathrm{tr}\left(\hat{T}_e\hat{D} - \rho\frac{\partial f_h}{\partial \hat{C}}\hat{F}^T(\hat{L} + \hat{L}^T)\hat{F}\right), \\
&= \mathrm{tr}\left(\hat{T}_e\hat{D} - 2\rho\frac{\partial f_h}{\partial \hat{C}}\hat{F}^T\hat{D}\hat{F}\right), \\
&= \mathrm{tr}\left(\hat{T}_e\hat{D} - 2\rho\hat{F}\frac{\partial f_h}{\partial \hat{C}}\hat{F}^T\hat{D}\right), \\
&= \left[\hat{T}_e - 2\rho\hat{F}\frac{\partial f_h}{\partial \hat{C}}\hat{F}^T\right] : \hat{D},
\end{aligned} \tag{70}$$

knowing $\dot{\hat{F}} = \hat{L}\hat{F}$ and $\hat{D} = \frac{1}{2}(\hat{L} + \hat{L}^T)$ and $\mathrm{tr}(\hat{A}\hat{B}) = \mathrm{tr}(\hat{B}\hat{A})$ (cyclic property of the trace). Eq.(69) now assumes the form

$$\sigma_s = \frac{1}{T}\left[\hat{T}_e - 2\rho\hat{F}\frac{\partial f_h}{\partial C}\hat{F}^T\right] : \hat{D} + \frac{1}{T}\hat{T}_V : \hat{D} - \frac{1}{T^2}\vec{q}\cdot\vec{\nabla}T. \tag{71}$$

Elastic Constitutive Equation

The first term is purely elastic and so it does not contribute to the entropy production. Hence we have

$$\hat{T}_e = 2\rho\hat{F}\frac{\partial f_h}{\partial \hat{C}}\hat{F}^T, \tag{72}$$

which is the elastic constitutive equation. Moreover we must have

$$\hat{T}_V : \hat{D} \geqslant 0, \tag{73}$$

and

$$\vec{q}\cdot\vec{\nabla}T \leqslant 0. \tag{74}$$

Piola-Kirchhoff Stress Tensor

We can use the first Piola-Kirchhoff stress tensor $\hat{T}^{1PK} = J\hat{T}\hat{F}^{-T}$, with $J = \det(\hat{F})$ scalar seen in Eq.(455) in Appendix A.1.2. In this case Eq.(72) assumes a simpler form

$$\begin{aligned}
\hat{T}_e^{1PK} &= J\hat{T}_e\hat{F}^{-T}, \\
&= 2J\rho\hat{F}\frac{\partial f_h}{\partial \hat{C}}\hat{F}^T\hat{F}^{-T}, \\
&= 2\rho_0\hat{F}\frac{\partial f_h}{\partial \hat{C}},
\end{aligned} \tag{75}$$

since $\rho J = \rho_0$, or

$$\hat{T}_e^{2PK} = \hat{F}^{-1}\hat{T}_e^{1PK} = 2\rho_0 \frac{\partial f_h}{\partial \hat{C}}. \tag{76}$$

The second Piola Kirchhoff stress tensor $\hat{T}^{2PK} = \hat{F}^{-1}\hat{T}^{1PK}$ could also have been used. Finally the strain is often described by the Green-Lagrange tensor

$$\hat{\eta} = \frac{1}{2}(\hat{C} - \hat{I}), \tag{77}$$

instead of $\hat{C}$, or by the Almansi-Euler tensor

$$\hat{\epsilon} = \frac{1}{2}(\hat{I} - \hat{B}^{-1}), \tag{78}$$

instead of $\hat{B}$. Moreover we also introduce the Lagrangian displacement gradient $\hat{J}_L = \frac{\partial \vec{u}}{\partial \vec{X}}$ and the Eulerian displacement gradient $\hat{J}_E = \frac{\partial \vec{u}}{\partial \vec{x}}$ where $\vec{u}$ is the displacement $\vec{u} = \vec{x} - \vec{X}$. We have $\hat{J}_L = \hat{F} - \hat{I}$ and $\hat{J}_E = \hat{I} - \hat{F}^{-1}$. Therefore

Lagrangian and Eulerian Displacement Gradients

$$\hat{\eta} = \frac{1}{2}\left(\hat{J}_L + \hat{J}_L^T + \hat{J}_L^T\hat{J}_L\right), \tag{79}$$

and

$$\hat{\epsilon} = \frac{1}{2}\left(\hat{J}_E + \hat{J}_E^T - \hat{J}_E^T\hat{J}_E\right). \tag{80}$$

Since $d\hat{C} = 2d\hat{\eta}$ we have $\hat{T}_e = \rho\hat{F}\frac{\partial f_h}{\partial \hat{\eta}}\hat{F}^T$ and $\hat{T}_e^{1PK} = \rho_0\hat{F}\frac{\partial f_h}{\partial \hat{\eta}}$ and $\hat{T}_e^{2PK} = \rho_0\frac{\partial f_h}{\partial \hat{\eta}}$.

The obtained equations consist of a closed system which is strongly non linear. As a matter of fact, it is useful to obtain a linearised version of this system. To do this, the extent of the deformation is assumed small. This hypothesis can be explicitly written as $tr(\hat{J}_L\hat{J}_L^T) << 1$ or $tr(\hat{J}_E\hat{J}_E^T) << 1$. We therefore assume that $\hat{J}_L \approx \hat{J}_E = \hat{J}$ and $\hat{J} = \hat{\varepsilon} + \hat{\Omega}$ with $\hat{\varepsilon}$ symmetric and $\hat{\Omega}$ anti symmetric. So we get $\hat{\eta} = \hat{\epsilon} = \hat{\varepsilon}$ and $\hat{U} = \hat{V} = \hat{I} + \hat{\varepsilon}$ and $\hat{R} = \hat{I} + \hat{\Omega}$. Also $\hat{T}_e \approx \hat{T}_e^{1PK} \approx \hat{T}_e^{2PK} = \rho\frac{\partial f_h}{\partial \hat{\varepsilon}} \approx \rho_0\frac{\partial f_h}{\partial \hat{\varepsilon}}$, where $f_h = f_h(T, \hat{\varepsilon})$ and the solid density is assumed constant. The tensor $\hat{\varepsilon}$ is the so called infinitesimal strain tensor and it is defined as

$$\hat{\varepsilon} = \frac{1}{2}(\vec{\nabla}\vec{u} + \vec{\nabla}\vec{u}^T), \tag{81}$$

where $\vec{u}$ is the displacement vector. The Taylor expansion of f_h to the second order using $\hat{M}$ as a thermal tensor and $\hat{\hat{C}}_e$ as an elastic tensor gives

$$f_h(T, \hat{\varepsilon}) = f_{h,0}(T) + (\hat{M} : \hat{\varepsilon})\,(T - T_0) + \frac{1}{2}\hat{\varepsilon} : \hat{\hat{C}}_e\hat{\varepsilon}, \tag{82}$$

with the subscript $_0$ being the equilibrium state as defined in Eq.(25) in fluid. From Eq.(82) we have the entropy density

$$s = -\frac{\partial f_h}{\partial T} = -f'_{h0}(T) - \hat{M} : \hat{\varepsilon}, \tag{83}$$

and the stress tensor (elastic part)

$$\begin{aligned}\hat{T}_e &= \rho_0 \frac{\partial f_h}{\partial \hat{\varepsilon}},\\ &= \rho_0 \hat{M}(T - T_0) + \rho_0 \hat{\hat{C}}_e \hat{\varepsilon},\\ &= \rho_0 \hat{\hat{C}}_e \left[\hat{\varepsilon} + \hat{\hat{C}}_e^{-1} \hat{M}(T - T_0)\right].\end{aligned} \tag{84}$$

We get $\rho_0 \hat{\hat{C}}_e = \hat{\hat{C}}_0$ the stiffness tensor, and $\hat{\hat{C}}_e^{-1}\hat{M} = -\hat{\alpha_T}$ the thermal expansion tensor. We have now

$$\hat{T}_e = \hat{\hat{C}}_0 \left[\hat{\varepsilon} - \hat{\alpha_T}(T - T_0)\right], \tag{85}$$

or

$$\hat{\varepsilon} = \hat{\hat{C}}_0^{-1} \hat{T}_e + \hat{\alpha_T}(T - T_0), \tag{86}$$

with $\hat{\hat{C}}_0^{-1}$ being the compliance tensor (see Appendix A.3). The energy density is

$$\begin{aligned}e &= f_h + T\, s,\\ &= f_{h0}(T) - (\hat{\hat{C}}_0 \hat{\alpha_T} : \hat{\varepsilon})(T - T_0)\frac{1}{\rho_0} + \frac{1}{2}\frac{1}{\rho_0}(\hat{\varepsilon} : \hat{\hat{C}}_0 \hat{\varepsilon}) - T f'_{h0}(T) + \frac{T}{\rho_0}\hat{\hat{C}}_0 \hat{\alpha_T} : \hat{\varepsilon},\\ &= e_0(T) + \frac{1}{\rho_0}(\hat{\hat{C}}_0 \hat{\alpha_T} : \varepsilon) T_0 + \frac{1}{2}\frac{1}{\rho_0}(\hat{\varepsilon} : \hat{\hat{C}}_0 \hat{\varepsilon}),\end{aligned} \tag{87}$$

where $e_0(T) = f_{h0}(T) - T f'_{h0}(T)$ is the energy without deformations. The time derivative is

$$\dot{e} = \frac{\partial e_0(T)}{\partial T}\frac{\partial T}{\partial t} + \frac{1}{\rho_0}(\hat{\hat{C}}_0 \hat{\alpha_T} : \frac{\partial \hat{\varepsilon}}{\partial t}) T_0 + \frac{1}{\rho_0}(\hat{\hat{C}}_0 \hat{\varepsilon} : \frac{\partial \hat{\varepsilon}}{\partial t}). \tag{88}$$

Here $\frac{\partial e_0(T)}{\partial T} = C_V$ and $\hat{T} : \hat{D}$ in Eq.(4) becomes

$$\hat{T} : \hat{D} = \hat{T} : \frac{1}{2}(\hat{L} + \hat{L}^T) = \hat{T} : \frac{\partial \hat{\varepsilon}}{\partial t}. \tag{89}$$

Eq.(4) now assume the form

$$\rho_0 \left[C_V \frac{\partial T}{\partial t} + \frac{1}{\rho_0}(\hat{\hat{C}}_0 \hat{\alpha_T} : \frac{\partial \hat{\varepsilon}}{\partial t}) T_0 + \frac{1}{\rho_0}(\hat{\hat{C}}_0 \hat{\varepsilon} : \frac{\partial \hat{\varepsilon}}{\partial t})\right] = (\hat{T}_e + \hat{T}_V) : \frac{\partial \hat{\varepsilon}}{\partial t} - \vec{\nabla} \cdot \vec{q} + Q_0, \tag{90}$$

where $\hat{T}_e$ is given in Eq.(85) and $\hat{T}_V$ and $\vec{q}$ must satisfy Eqs.(73) and (74). We assume the linear behavior

$$\hat{T}_V = \hat{\hat{V}}\hat{D} = \hat{\hat{V}}\frac{\partial \hat{\varepsilon}}{\partial t}, \tag{91}$$

$$\vec{q} = -\hat{K}\vec{\nabla}T, \tag{92}$$

with $\hat{\hat{V}}$ being a viscous tensor and $\hat{K}$ being a thermal conductivity tensor since we don't know if the solid has thermal isotropic properties. Eq.(90) delivers

$$\rho_0 C_V \frac{\partial T}{\partial t} + \hat{\hat{C}}_0 \hat{\alpha_T} : \frac{\partial \hat{\varepsilon}}{\partial t} T_0 + \hat{\hat{C}}_0 \hat{\varepsilon} : \frac{\partial \hat{\varepsilon}}{\partial t} =$$
$$\hat{\hat{C}}_0 \left[\hat{\varepsilon} - \hat{\alpha_T}(T - T_0)\right] : \frac{\partial \hat{\varepsilon}}{\partial t} + \hat{\hat{V}}\frac{\partial \hat{\varepsilon}}{\partial t} : \frac{\partial \hat{\varepsilon}}{\partial t} + \vec{\nabla}\cdot(\hat{K}\vec{\nabla}T) + Q_0,$$

or

$$\rho_0 C_V \frac{\partial T}{\partial t} = -\hat{C}_0 \hat{\alpha_T} : \frac{\partial \hat{\varepsilon}}{\partial t} T + \hat{\hat{V}}\frac{\partial \hat{\varepsilon}}{\partial t} : \frac{\partial \hat{\varepsilon}}{\partial t} + \vec{\nabla}\cdot(\hat{K}\vec{\nabla}T) + Q_0. \tag{93}$$

Eq.(2) becomes

$$\rho_0 \ddot{\vec{u}} = \vec{\nabla}\cdot\hat{T} + \vec{b} = \vec{\nabla}\cdot\hat{T}_e + \vec{\nabla}\cdot\hat{T}_V + \vec{b}, \tag{94}$$

with (knowing that $\hat{\hat{C}}_0$ is symmetric)

$$\begin{aligned}\vec{\nabla}\cdot\hat{T}_e &= \vec{\nabla}\cdot\hat{\hat{C}}_0\left[\hat{\varepsilon} - \hat{\alpha_T}(T - T_0)\right], \\ &= \vec{\nabla}\cdot(\hat{\hat{C}}_0\vec{\nabla}\vec{u}) - \hat{\hat{C}}_0\hat{\alpha_T}\vec{\nabla}T, \end{aligned}\tag{95}$$

$$\vec{\nabla}\cdot\hat{T}_V = \vec{\nabla}\cdot(\hat{\hat{V}}\frac{\partial \hat{\varepsilon}}{\partial t}). \tag{96}$$

The final constitutive equations for a solid being the conservation of momentum and energy are

Eulerian Constitutive Equations in a Solid

$$\begin{cases} \rho_0 C_V \frac{\partial T}{\partial t} = -\hat{C}_0 \hat{\alpha_T} : \frac{\partial \hat{\varepsilon}}{\partial t} T + \hat{\hat{V}}\frac{\partial \hat{\varepsilon}}{\partial t} : \frac{\partial \hat{\varepsilon}}{\partial t} + \vec{\nabla}\cdot(\hat{K}\vec{\nabla}T) + Q_0, \\ \rho_0 \ddot{\vec{u}} = \vec{\nabla}\cdot(\hat{\hat{C}}_0\vec{\nabla}\vec{u}) - \hat{\hat{C}}_0\hat{\alpha_T}\vec{\nabla}T + \vec{\nabla}\cdot\hat{\hat{V}}\frac{\partial \hat{\varepsilon}}{\partial t} + \vec{b}. \end{cases} \tag{97}$$

Eqs.(97) completely describe the thermo-visco elasticity of an anisotropic solid. They represent a closed system of equations for the unknowns $T(\vec{x}, t)$ and $\vec{u}(\vec{x}, t)$.

It has to be noted that Eq.(97a), although obtained for small deformations, is non linear for the presence of the quadratic terms $\frac{\partial \hat{\varepsilon}}{\partial t} T$ and $\hat{\hat{V}}\frac{\partial \hat{\varepsilon}}{\partial t} : \frac{\partial \hat{\varepsilon}}{\partial t}$. To completely linearise the system we have to neglect the effect of viscosity on the heat transfer, meaning that $\hat{\hat{V}}\frac{\partial \hat{\varepsilon}}{\partial t} : \frac{\partial \hat{\varepsilon}}{\partial t}$ is no longer considered. T must also be linearised as in Eq.(25) for fluid. On the other

hand Eq.(97b) is already linear and maintains the same form. Finally, using the same abusive notation as in fluid (T for temperature variations), the linearised system is

Linearised Constitutive Equations for Anisotropic Solid

$$\begin{cases} \rho_0 C_V \frac{\partial T}{\partial t} = \vec{\nabla} \cdot (\hat{K} \vec{\nabla} T) - \hat{C}_0 \hat{\alpha_T} : \frac{\partial \hat{\varepsilon}}{\partial t} T_0 + Q_0 \\ \rho_0 \ddot{\vec{u}} = \vec{\nabla} \cdot (\hat{\hat{C}}_0 \vec{\nabla} \vec{u}) + \vec{\nabla} \cdot \left(\hat{\hat{V}} \frac{\partial}{\partial t} \vec{\nabla} \vec{u} \right) - \hat{C}_0 \hat{\alpha_T} \vec{\nabla} T + \vec{b} \end{cases} \tag{98}$$

For further applications it is interesting to write Eqs.(98) for an isotropic solid. In this case $\hat{\alpha_T}$ is proportional to the identity matrix $\hat{I}$

$$\hat{\alpha_T} = \frac{\alpha_T}{3} \hat{I}, \tag{99}$$

where α_T is the volumetric thermal expansion coefficient of the solid. Moreover, the tensor $\hat{\hat{C}}_0$ and $\hat{\hat{V}}$ are described by two parameters as

$$\left(\hat{\hat{C}}_0 \hat{S} \right)_{ij} = C_{0_{ijkh}} S_{kh} = 2\mu_0 S_{ij} + \lambda_0 S_{kk} \delta_{ij}, \tag{100}$$

$$\left(\hat{\hat{V}} \hat{S} \right)_{ij} = V_{ijkh} S_{kh} = 2\mu_s S_{ij} + \lambda_s S_{kk} \delta_{ij}, \tag{101}$$

summed over k, where $\hat{S}$ is an arbitrary symmetric matrix on which the operators $\hat{\hat{C}}_0$ and $\hat{\hat{V}}$ are applied, λ_0 and μ_0 are elasticity coefficient (Lamé's coefficients) and λ_s and μ_s are viscosity coefficients (noted λ and μ in the fluid equations). For more details on the tensor form see Appendix A.3. This is a general form for a fourth order tensor that respect the isotropy. The application of $\hat{\hat{C}}_0$ on $\hat{\alpha_T}$ then gives

$$\left(\hat{\hat{C}}_0 \hat{\alpha_T} \right)_{ij} = 2\mu_0 \frac{\alpha_T}{3} \delta_{ij} + \lambda_0 \alpha_T \delta_{ij} = \alpha_T (\lambda_0 + \frac{2}{3} \mu_0) \delta_{ij}. \tag{102}$$

Moreover

$$\begin{aligned} \hat{\hat{C}}_0 \hat{\alpha_T} : \frac{\partial \hat{\varepsilon}}{\partial t} &= \sum_{ij} \alpha_T (\lambda_0 + \frac{2}{3} \mu_0) \delta_{ij} \frac{\partial \varepsilon_{ij}}{\partial t}, \\ &= \sum_{ij} \alpha_T (\lambda_0 + \frac{2}{3} \mu_0) \frac{\partial \varepsilon_{ii}}{\partial t}, \\ &= \sum_{ij} \alpha_T (\lambda_0 + \frac{2}{3} \mu_0) \frac{\partial}{\partial t} \vec{\nabla} \cdot \vec{u}, \end{aligned} \tag{103}$$

where $\vec{u}$ is the displacement vector. Regarding the thermal conductivity we do consider an isotropic tensor

$$\hat{K} = \kappa \hat{I}. \tag{104}$$

The term $\vec{\nabla}\cdot(\hat{\hat{C}}_0\vec{\nabla}\vec{u})$ becomes

$$\begin{aligned}\left[\vec{\nabla}\cdot(\hat{\hat{C}}_0\vec{\nabla}\vec{u})\right]_{ij} &= \frac{\partial}{\partial x_i}T_{ij},\\ &= \frac{\partial}{\partial x_i}\left[\mu_0(\frac{\partial u_i}{\partial x_j}+\frac{\partial u_j}{\partial x_i})+\lambda_0\frac{\partial u_k}{\partial x_k}\delta_{ij}\right],\\ &= \mu_0\frac{\partial^2 u_j}{\partial x_i^2}+\mu_0\frac{\partial^2 u_i}{\partial x_i\partial x_j}+\lambda_0\frac{\partial^2 u_k}{\partial x_k\partial x_i}\delta_{ij},\\ &= (\lambda_0+\mu_0)\frac{\partial^2 u_i}{\partial x_i\partial x_j}+\mu_0\frac{\partial^2 u_j}{\partial x_i^2},\end{aligned} \tag{105}$$

or equivalently

$$\vec{\nabla}\cdot(\hat{\hat{C}}_0\vec{\nabla}\vec{u}) = (\lambda_0+\mu_0)\vec{\nabla}(\vec{\nabla}\cdot\vec{u})+\mu_0\vec{\nabla}^2\vec{u}. \tag{106}$$

Similarly with the viscosity

$$\vec{\nabla}\cdot(\hat{\hat{V}}\frac{\partial}{\partial t}\vec{\nabla}\vec{u}) = (\lambda_s+\mu_s)\vec{\nabla}(\vec{\nabla}\cdot\vec{v})+\mu_s\vec{\nabla}^2\vec{v}, \tag{107}$$

with $\vec{v}=\frac{d\vec{u}}{dt}$ the velocity. Now Eq.(98), written for an isotropic solid is read

Complete System for Isotropic and Homogeneous Solid

$$\begin{cases}\rho_0 C_V\frac{\partial T}{\partial t} = & \kappa\nabla^2 T-\alpha_T(\lambda_0+\frac{2}{3}\mu_0)\frac{\partial}{\partial t}\vec{\nabla}\cdot\vec{u}\;T_0+Q_0,\\ \rho_0\frac{\partial^2\vec{u}}{\partial t^2} = & (\lambda_0+\mu_0)\vec{\nabla}(\vec{\nabla}\cdot\vec{u})+\mu_0\vec{\nabla}^2\vec{u}+(\mu_s+\lambda_s)\vec{\nabla}(\vec{\nabla}\cdot\vec{v})+\\ & +\mu_s\vec{\nabla}^2\vec{v}-\alpha_T(\lambda_0+\frac{2}{3}\mu_0)\vec{\nabla}T+\vec{b},\end{cases} \tag{108}$$

which represent the system of equations for an isotropic and homogeneous solid with thermal, viscous and elastic properties.

For easier comparison with the fluid equation, the Bulk modulus for the solid has to be constructed. Using Eq.(100), Eq.(85) representing the constitutive equation of the solid assumes the following form of the elastic stress $\hat{T}_e$ for the isotropic case

$$T_{e_{ij}} = 2\mu_0\varepsilon_{ij}+\lambda_0\varepsilon_{kk}\delta_{ij}-\alpha_T(\lambda_0+\frac{2}{3}\mu_0)\delta_{ij}T. \tag{109}$$

This relation allows us to identify two important physical interpretations. Firstly, if $T_{e_{ij}}=0,\ \forall i,j$ the solid is free of stress and we have

$$0 = 2\mu_0\varepsilon_{ij}+\lambda_0\varepsilon_{kk}\delta_{ij}-\alpha_T(\lambda_0+\frac{2}{3}\mu_0)\delta_{ij}T. \tag{110}$$

In this condition the deformation is simply induced by the temperature and it is therefore isotropic meaning $\varepsilon_{ij} = \varepsilon\delta_{ij}$. Hence

$$0 = 2\mu_0\varepsilon\delta_{ij} + \lambda_0 3\varepsilon\delta_{ij} - \alpha_T(\lambda_0 + \frac{2}{3}\mu_0)\delta_{ij}T, \tag{111}$$

and so we get $3\varepsilon = \alpha_T T$ or

$$\alpha_T = \frac{\mathrm{tr}(\hat{\varepsilon})}{T}. \tag{112}$$

Since $\mathrm{tr}(\hat{\varepsilon}) = \frac{dV}{V}$ is the variation of volume per unit of volume we obtained again the definition of volumetric thermal expansion of the solid for α_T. We now consider an hydrostatic load applied to the solid at constant temperature $T = T_0$ ($T = 0$ with the abusive notation). We define temporarily $T_{ij} = \sigma\delta_{ij}$ and we get from Eq.(109)

$$\sigma\delta_{ij} = 2\mu_0\varepsilon_{ij} + \lambda_0\varepsilon_{kk}\delta_{ij}. \tag{113}$$

Then $\hat{\varepsilon}$ is diagonal of the form $\varepsilon\hat{I}$ where

$$\varepsilon = \frac{\sigma}{3(\lambda_0 + \frac{2}{3}\mu_0)}. \tag{114}$$

We define the Bulk modulus

$$B_0 = \lambda_0 + \frac{2}{3}\mu_0, \tag{115}$$

such that

$$\mathrm{tr}(\hat{\varepsilon}) = \frac{\sigma}{B_0}. \tag{116}$$

Or, since $\mathrm{tr}(\hat{\varepsilon}) = \frac{dV}{V}$

$$\frac{1}{B_0} = \frac{dV}{V\sigma} = -\frac{dV}{Vp}. \tag{117}$$

It is then deduced that σ is in fact equal to $-p$, the pressure, as used for Eq.(53) in a fluid. Similarly, the term $\frac{1}{B_0} = \kappa_T$ is called the coefficient of isothermal compressibility as in the fluid case.

In this section, similarly as for a fluid medium, starting from the balance equations of Section 2.1.1, the conservation equations of momentum and of energy are written in a solid case. Considering an anisotropic elastic solid, a non linear system is deduced in Eq.(97). By neglecting the effect of viscosity on the heat transfer and assuming small deformation of temperature the linearised system is found in Eq.(98).

An isotropic solid is then assumed and the conservation equation are rewritten for an isotropic, homogeneous solid with thermal, viscous and elastic properties in Eq.(108). Particular properties of the elastic stress tensor are then investigated in order to define the Bulk modulus in the solid and write the system in a similar fashion as Section 2.1.2. Eq.(108) assumes therefore the final form

Final System for Isotropic Homogeneous Solid

$$\begin{cases} \rho_0 C_V \frac{\partial T}{\partial t} = \kappa \nabla^2 T - \alpha_T B_0 \frac{\partial}{\partial t} \vec{\nabla} \cdot \vec{u}\, T_0 + Q_0, \\ \rho_0 \frac{\partial^2 \vec{u}}{\partial t^2} = (\lambda_0 + \mu_0)\vec{\nabla}(\vec{\nabla} \cdot \vec{u}) + \mu_0 \nabla^2 \vec{u} + (\lambda_s + \mu_s)\vec{\nabla}(\vec{\nabla} \cdot \vec{v}) + \mu_s \nabla^2 \vec{v} - \alpha_T B_0 \vec{\nabla} T + \vec{b}. \end{cases} \tag{118}$$

The abusive notation for T representing temperature variations around a constant state symbolised by the subscript $_0$ will now be used throughout this thesis in solid as well as fluid media.

2.2 ONE TEMPERATURE MULTILAYER MODEL FOR PLANE WAVES

In Section 2.1, the conservation equations were laid down for a fluid medium with thermal and viscous properties as seen in Eqs.(56). likewise, the conservation equations for an isotropic, homogeneous solid with thermal, viscous and elastic properties are found in Eqs.(118).

Both of those systems of equations will now be solved in an uni dimensional case. This means that we assume plane wave radiation from the thermophone, propagating along the x axis of a Cartesian coordinate system. An explicit differential equations for the temperature variation T will be found and solved thus providing explicit analytical solution of pressure p, particle velocity v and heat flux q.

This system of equation for p, v, q, T will then be written in matrix form for both fluid and solid media. This will allow for the construction of an ideal thermophone's model which will then be extended to a multilayer thermophone model containing both fluid and solid layers, for plane wave radiation.

Lastly it has to be noted that, from now on the subscripts $_f$ and $_s$ will be used to refer to some fluid or solid parameters respectively. Those subscripts will be used only for similarly defined parameters in Section 2.1 which could confuse the reader. If no subscript is used, the reader can assume that the parameters is for a fluid medium.

2.2.1 *Plane Waves in a Fluid*

All space variables are assumed to depend only on the x direction of a Cartesian coordinate system using $(\vec{e_x}, \vec{e_y}, \vec{e_z})$ as normalised base. This means that $\vec{v}$ can be decomposed as $(v(x,t), 0, 0)$ and Eqs.(56) become

$$\begin{cases} \frac{\rho_{0,f}}{B}\frac{\partial p}{\partial t} - \rho_{0,f}\alpha_T\frac{\partial T}{\partial t} + \rho_{0,f}\frac{\partial v}{\partial x} = 0, \\ \rho_{0,f}\frac{\partial v}{\partial t} = -\frac{\partial p}{\partial x} + (\lambda + 2\mu)\frac{\partial^2 v}{\partial x^2}, \\ \rho_{0,f}C_p\frac{\partial T}{\partial t} - \alpha_T T_0\frac{\partial p}{\partial t} = \kappa\frac{\partial^2 T}{\partial x^2}. \end{cases} \tag{119}$$

In addition, assuming an harmonic time dependence, we can use the simplification $\partial/\partial t \to i\omega$ leading to

$$\begin{cases} i\omega\frac{\rho_{0,f}}{B}p - i\omega\rho_{0,f}\alpha_T T + \rho_{0,f}\frac{\partial v}{\partial x} = 0, \\ i\omega\rho_{0,f}v = -\frac{\partial p}{\partial x} + (\lambda + 2\mu)\frac{\partial^2 v}{\partial x^2}, \\ i\omega\rho_{0,f}C_p T - i\omega\alpha_T T_0 p = \kappa\frac{\partial^2 T}{\partial x^2}. \end{cases} \tag{120}$$

1D Pressure Equation in Fluid

From the 1D continuity equation Eq.(120a) we get the equation for p

$$p = \alpha_T B T - \frac{B}{i\omega}\frac{\partial v}{\partial x}, \tag{121}$$

which can then be substituted in Eq.(120b,c) as

$$\begin{cases} i\omega\rho_{0,f}v = -\alpha_T B\frac{\partial T}{\partial x} + \frac{B}{i\omega}\frac{\partial^2 v}{\partial x^2} + (\lambda + 2\mu)\frac{\partial^2 v}{\partial x^2}, \\ \rho_{0,f}C_p i\omega T - i\omega\alpha_T T_0(\alpha_T B T - \frac{B}{i\omega}\frac{\partial v}{\partial x}) = \kappa\frac{\partial^2 T}{\partial x^2}. \end{cases} \tag{122}$$

Simplifying

$$\begin{cases} i\omega\rho_{0,f}v = -\alpha_T B\frac{\partial T}{\partial x} + (\lambda + 2\mu + \frac{B}{i\omega})\frac{\partial^2 v}{\partial x^2}, \\ i\omega(\rho_{0,f}C_p - \alpha_T^2 T_0 B)T + \alpha_T B T_0\frac{\partial v}{\partial x} = \kappa\frac{\partial^2 T}{\partial x^2}. \end{cases} \tag{123}$$

Relation Specific Heat

We can use the classical relation between C_p and C_V (specific heat at constant volume)

$$C_p - C_V = T_0\frac{V}{M}\alpha_T^2 B, \tag{124}$$

$$\rho_0(C_p - C_V) = T_0\alpha_T^2 B. \tag{125}$$

Here ρ_0 is used without subscript since Eq.(125) is valid also for solid phase. We then obtain $\rho_0 C_p - \alpha_T^2 T_0 B = \rho_0 C_V$ and Eq.(123b) becomes

$$\frac{\partial v}{\partial x} = \frac{\kappa}{\alpha_T B T_0}\frac{\partial^2 T}{\partial x^2} - \frac{i\omega\rho_{0,f}C_V}{\alpha_T B T_0}T. \tag{126}$$

We substitute Eq.(126) in Eq.(123a) and we get v as a function of T

1D Velocity Equation in Fluid

$$v = -\frac{1}{i\omega\rho_{0,f}}\left[\alpha_T B + \frac{i\omega\rho_{0,f}C_V}{\alpha_T T_0 B}(\lambda+2\mu+\frac{B}{i\omega})\right]\frac{\partial T}{\partial x} + \\ +(\lambda+2\mu+\frac{B}{i\omega})\frac{\kappa}{i\omega\rho_{0,f}\alpha_T T_0 B}\frac{\partial^3 T}{\partial x^3}. \tag{127}$$

To obtain a pure equation for T we combine again Eq.(126) with Eq.(123a) as

$$\begin{cases} \frac{d}{dx}(\text{Eq.(123a)}) \Rightarrow i\omega\rho_{0,f}v' = -\alpha_T B T'' + (\lambda+2\mu+\frac{B}{i\omega})v''', \\ \frac{d^2}{dx^2}(\text{Eq.(126)}) \Rightarrow v''' = \frac{\kappa}{\alpha_T T_0 B}T^{iv} - \frac{i\omega\rho_{0,f}C_V}{\alpha_T T_0 B}T''. \end{cases} \tag{128}$$

So using Eq.(123b) we obtain

$$i\omega\rho_{0,f}\left[\frac{\kappa}{\alpha_T T_0 B}T'' - \frac{i\omega\rho_{0,f}C_V}{\alpha_T T_0 B}T\right] = -\alpha_T B T'' + (\lambda+2\mu+\frac{B}{i\omega})\left[\frac{\kappa}{\alpha_T T_0 B}T^{iv} - \frac{i\omega\rho_{0,f}C_V}{\alpha_T T_0 B}T''\right], \tag{129}$$

or equivalently

1D Temperature Variation Differential Equation in a Fluid

$$0 = (\lambda+2\mu+\frac{B}{i\omega})\kappa T^{iv} + \\ -\left[(\lambda+2\mu+\frac{B}{i\omega})i\omega\rho_{0,f}C_V + (i\omega\rho_{0,f}\kappa + \alpha_T^2 T_0 B^2)\right]T'' + \\ -\omega^2\rho_{0,f}^2 C_V T. \tag{130}$$

This is a fourth-order biquadratic linear differential equation for the temperature variations T. If the solution is searched in the form $T(x) = e^{\theta x}$, we have the equation for θ

$$(\lambda+2\mu+\frac{B}{i\omega})\kappa\theta^4 - \left[(\lambda+2\mu+\frac{B}{i\omega})i\omega\rho_{0,f}C_V + (i\omega\rho_{0,f}\kappa + \alpha_T^2 T_0 B^2)\right]\theta^2 - \omega^2\rho_{0,f}^2 C_V = 0. \tag{131}$$

The first simple case to solve can concerns a fluid without viscosity ($\lambda = \mu = 0$) and without thermal conduction ($\kappa = 0$). In this condition we have

$$-(\rho_{0,f}C_V B + \alpha_T^2 T_0 B^2)\theta^2 - \omega^2\rho_{0,f}^2 C_V = 0, \tag{132}$$

and, using Eq.(125), this leads to

$$\theta^2 = -\frac{\omega^2\rho_{0,f}^2 C_V}{\rho_{0,f}C_V B + \alpha_T^2 T_0 B^2} = -\frac{\omega^2\rho_{0,f}}{B}\frac{C_V}{C_p}. \tag{133}$$

Hence

$$\theta^2 = -\frac{\omega^2}{C_0^2},$$
$$\theta = \pm i\omega\frac{1}{C_0}, \tag{134}$$

with

$$C_0^2 = \frac{B}{\rho_{0,f}}\frac{C_p}{C_V},$$
$$C_0 = \sqrt{\frac{B}{\rho_{0,f}}\frac{C_p}{C_V}} = \sqrt{\frac{B}{\rho_{0,f}}\gamma}, \tag{135}$$

and $\gamma = \frac{C_p}{C_V}$. The complete solution for the temperature T is $T(x,t) = e^{i\omega t}e^{\theta x} = e^{i\omega t}e^{\pm i\omega\frac{x}{C_0}} = e^{i\omega(t-\frac{x}{C_0})} + e^{i\omega(t+\frac{x}{C_0})}$, which represent a progressive $(-)$ or regressive $(+)$ wave along the x-axis with velocity C_0. It is the classical expression of the wave velocity in a fluid for an isentropic process (adiabatic and reversible). It is the solution of the classical Helmholtz equation in a fluid

Helmholtz Equation for Isentropic Process

$$\frac{d^2T}{dx^2} + \frac{\omega^2}{C_0}T = 0, \tag{136}$$

which is just Eq.(131) without viscosity and thermal conduction as shown.

For the general case, we aim to rewrite Eq.(131) in terms of the wave velocity C_0 (in our case, the speed of sound). To this aim we divide Eq.(131) by $\rho_{0,f}C_pB$

$$\left[\frac{\kappa(\lambda+2\mu)}{\rho_{0,f}C_pB} + \frac{\kappa}{i\omega\rho_{0,f}C_p}\right]\theta^4 - \left[\frac{i\omega(\lambda+2\mu)}{B}\frac{C_V}{C_p} + \frac{C_V}{C_p} + i\omega\frac{\kappa}{BC_p} + \frac{\alpha_T^2T_0B}{\rho_{0,f}C_p}\right]\theta^2 - \omega^2\frac{\rho_{0,f}C_V}{BC_p} = 0. \tag{137}$$

Using Eq.(125) $\frac{C_V}{C_p} + \frac{\alpha_T^2T_0B}{\rho_{0,f}C_p} = 1$. Thus

$$\left[\frac{\kappa(\lambda+2\mu)}{\rho_{0,f}C_pB} + \frac{\kappa}{i\omega\rho_{0,f}C_p}\right]\theta^4 - \left[1 + i\omega\left(\frac{\kappa}{BC_p} + \frac{(\lambda+2\mu)}{B}\frac{C_V}{C_p}\right)\right]\theta^2 - \omega^2\frac{\rho_{0,f}C_V}{BC_p} = 0. \tag{138}$$

The coefficients for θ^4 can be elaborated as

$$\frac{\kappa(\lambda+2\mu)}{\rho_{0,f}C_pB} + \frac{\kappa}{i\omega\rho_{0,f}C_p} = \frac{C_0\kappa}{BC_p}\frac{(\lambda+2\mu)}{\rho_{0,f}C_0} + \frac{C_0\kappa}{BC_p}\frac{B}{C_0i\omega\rho_{0,f}},$$
$$= l_\kappa\, l_V + l_\kappa\frac{C_0}{i\omega\gamma},$$

where

$$\begin{aligned}\frac{B}{C_0\omega\rho_{0,f}} &= \frac{1}{\omega}\frac{B}{\sqrt{\frac{B}{\rho_{0,f}}\frac{C_p}{C_V}\rho_{0,f}}},\\ &= \frac{1}{\omega}\sqrt{\frac{B}{\rho_{0,f}}\frac{C_V}{C_p}},\\ &= \frac{1}{\omega}\frac{C_V}{C_p}\sqrt{\frac{B}{\rho_{0,f}}\frac{C_p}{C_V}},\\ &= \frac{C_0}{\omega\gamma},\end{aligned}$$

using still $\gamma = \frac{C_p}{C_V}$. Moreover, the coefficients for θ^2, give

$$\begin{aligned}i\omega\left(\frac{\kappa}{BC_p}+\frac{(\lambda+2\mu)}{B}\frac{C_V}{C_p}\right) &= \frac{i\omega}{C_0}\left(\frac{\kappa C_0}{BC_p}+C_0\frac{(\lambda+2\mu)}{\rho_{0,f}}\frac{1}{C_0^2}\right),\\ &= \frac{i\omega}{C_0}\left(\frac{\kappa C_0}{BC_p}+\frac{(\lambda+2\mu)}{\rho_{0,f}C_0}\right),\\ &= \frac{i\omega}{C_0}(l_\kappa+l_V).\end{aligned}$$

In conclusion Eq.(138) becomes

$$l_\kappa(l_V+\frac{C_0}{i\omega\gamma})\theta^4-[1+\frac{i\omega}{C_0}(l_\kappa+l_V)]\theta^2-\frac{\omega^2}{C_0^2}=0, \tag{139}$$

New Simplification Parameters

using the notations

$$\begin{cases}\gamma = \frac{C_p}{C_V},\\ C_0 = \sqrt{\frac{B}{\rho_{0,f}}\gamma}, & [m/s]\\ l_\kappa = \frac{C_0\kappa}{BC_p}, & [m]\\ l_V = \frac{\lambda+2\mu}{\rho_{0,f}C_0}, & [m]\end{cases} \tag{140}$$

where l_κ and l_V are characteristic lengths representing the conduction and the viscous processes, respectively. It is interesting to note that $l_\kappa = (\alpha\gamma)/C_0$ with $\alpha = \kappa/(\rho C_p)$ the so-called thermal diffusivity of the medium.

We will now try to obtain explicit solutions of Eq.(139) to the first order in l_κ and l_V (weak conduction and viscosity). To do this we find the asymptotic solutions of $ax^4+bx^2+c=0$ for small values of a. If $a=0$, the first couple of solution is given by $x^2=-\frac{c}{b}$, which means

$x = \pm\sqrt{-\frac{c}{b}}$. So we search ε such that $x = \pm\sqrt{-\frac{c}{b}} + \varepsilon a$ in order to obtain the solutions to the first order in the parameter a. This case is called regular perturbations. The second couple of solutions called singular perturbations diverges to infinity when $a \to 0$. So we define $y = \sqrt{a}x$ and $ax^4 + bx^2 + c = 0$ is transformed to $y^4 + by^2 + ac = 0$. If $a = 0$ we get $y = \pm\sqrt{-b}$ and the perturbed solution are $y = \pm\sqrt{-b} + \varepsilon a$. We analyze the two cases:

Regular Perturbation

- Case 1

We substitute $x_1 = \pm\sqrt{-\frac{c}{b}} + \varepsilon a$ into $ax_1^4 + bx_1^2 + c = 0$. We have

$$x_1^2 \approx -\frac{c}{b} \pm 2\sqrt{-\frac{c}{b}}\,\varepsilon a,$$
$$x_1^4 \approx (-\frac{c}{b})^2 \pm 4(-\frac{c}{b})\sqrt{-\frac{c}{b}}\,\varepsilon a.$$

Hence

$$a(-\frac{c}{b})^2 \pm 4a(-\frac{c}{b})\sqrt{-\frac{c}{b}}\,\varepsilon a - c \pm 2b\sqrt{-\frac{c}{b}}\,\varepsilon a + c = 0,$$
$$a\frac{c^2}{b^2} \pm 2\varepsilon a\sqrt{-\frac{c}{b}}\,(b - 2\frac{ac}{b}) = 0,$$

and

$$\varepsilon = \pm\frac{1}{2}\sqrt{-\frac{b}{c}}\,\frac{c^2}{b^3(1 - \frac{2ac}{b^2})},$$
$$\approx \pm\frac{1}{2}\sqrt{-\frac{b}{c}}\,\frac{c^2}{b^3}(1 + \frac{2ac}{b^2}).$$

So we approximate

$$\varepsilon = \pm\frac{1}{2}\sqrt{-\frac{b}{c}}\,\frac{c^2}{b^3}, \tag{141}$$

and we get for x_1

$$x_1 = \pm\left[\sqrt{-\frac{c}{b}} - \frac{1}{2}\sqrt{-\frac{b}{c}}\,\frac{c^2}{b^3}a\right]. \tag{142}$$

Singular Perturbation

- Case 2

We substitute $y = \pm\sqrt{-b} + \varepsilon a$ into $y^4 + by^2 + ac = 0$. We have

$$y^2 \approx -b \pm 2\sqrt{-b}\,\varepsilon a,$$
$$y^4 \approx (-b)^2 \pm 4(-b)\sqrt{-b}\,\varepsilon a.$$

Thus

$$(-b)^2 \pm 4(-b)\sqrt{-b}\,\varepsilon a - b^2 \pm 2b\sqrt{-b}\,\varepsilon a + ac = 0,$$
$$ac \pm 2\sqrt{-b}\,\varepsilon a(b - 2b) = 0,$$
$$ac = \pm 2\sqrt{-b}\,\varepsilon ab,$$

and

$$\varepsilon = \pm\frac{c}{2b\sqrt{-b}}.$$

For y we get

$$y = \pm\sqrt{-b} \pm \frac{c}{2b\sqrt{-b}}a, \tag{143}$$

and for $x_2 = \frac{1}{\sqrt{a}}y$ we have

$$x_2 = \pm\left[\sqrt{-\frac{b}{a}} + \frac{1}{2}\frac{c}{b}\sqrt{-\frac{a}{b}}\right]. \tag{144}$$

Finally, using both cases, all solutions of $ax^4 + bx^2 + c = 0$ for small values of a are given by

$$\begin{cases} x_1 = \pm\left[\sqrt{-\frac{c}{b}} - \frac{1}{2}\frac{ac^2}{b^3}\sqrt{-\frac{b}{c}}\right], \\ x_2 = \pm\left[\sqrt{-\frac{b}{a}} + \frac{1}{2}\frac{c}{b}\sqrt{-\frac{a}{b}}\right], \end{cases} \tag{145}$$

which can be simplified as

$$\begin{cases} x_1 = \pm\sqrt{-\frac{c}{b}}\left[1 + \frac{1}{2}\frac{ac}{b^2}\right], \\ x_2 = \pm\sqrt{-\frac{b}{a}}\left[1 - \frac{1}{2}\frac{ac}{b^2}\right]. \end{cases} \tag{146}$$

For our system

$$\begin{cases} a = \frac{C_0}{i\omega\gamma}l_\kappa(1 + \frac{i\omega\gamma}{C_0}l_V), \\ b = -[1 + \frac{i\omega}{C_0}(l_\kappa + l_V)], \\ c = -\frac{\omega^2}{C_0^2}, \end{cases} \tag{147}$$

with $\mathrm{Re}(a) > 0$, $\mathrm{Re}(b) < 0$ and $c < 0$. Application of Eq.(146a) using first order Taylors's series approximation $(1+\varepsilon)^{\alpha} \approx (1+\alpha\varepsilon)$ leads to

$$\begin{aligned}
\theta_1 &\approx \pm\sqrt{-\frac{\omega^2}{C_0^2}\left(1-\frac{i\omega}{C_0}(l_\kappa+l_V)\right)}\left[1+\frac{1}{2}(\frac{C_0}{i\omega\gamma}l_\kappa)(1+\frac{i\omega\gamma}{C_0}l_V)\left(-\frac{\omega^2}{C_0^2}\right)\right.\\
&\quad\left.\left(1-2\frac{i\omega}{C_0}(l_\kappa+l_V)\right)\right],\\
&\approx \pm\left[\frac{i\omega}{C_0}\left(1-\frac{1}{2}\frac{i\omega}{C_0}(l_\kappa+l_V)\right)\left(1-\frac{1}{2}(\frac{C_0}{i\omega\gamma}l_\kappa)\frac{\omega^2}{C_0^2}\right)\right],\\
&= \pm\frac{i\omega}{C_0}\left[1-\frac{1}{2}\frac{i\omega}{C_0}(l_\kappa+l_V)+\frac{1}{2}l_\kappa\frac{i\omega}{C_0\gamma}\right],\\
&= \pm\frac{i\omega}{C_0}\left[1-\frac{1}{2}\frac{i\omega}{C_0}l_V-\frac{1}{2}l_\kappa\frac{i\omega}{C_0}(1-\frac{1}{\gamma})\right].
\end{aligned} \tag{148}$$

The wave solution is of the form $e^{i\omega t}e^{\theta x} = e^{\mathrm{Re}(\theta)x}e^{i(\omega t+\mathrm{Im}(\theta)x)}$. So, for a progressive wave we have

$$\begin{cases} L = -\frac{1}{\mathrm{Re}\theta}, \\ V = -\frac{\omega}{\mathrm{Im}\theta}, \end{cases} \tag{149}$$

in order to get the wave in the classical form $e^{-\frac{x}{L}}e^{i\omega(t-\frac{x}{V})}$ where V represent the phase velocity of the wave and L its attenuation penetration length. The progressive wave corresponds therefore to the sign "-" in Eq.(148) and we have

$$\begin{aligned}
\mathrm{Re}\ \theta_1 &= -\frac{\omega^2}{C_0^2}\frac{1}{2}l_V-\frac{\omega^2}{C_0^2}\frac{1}{2}(1-\frac{1}{\gamma})l_\kappa\\
\mathrm{Im}\ \theta_1 &= -\frac{\omega}{C_0},
\end{aligned}$$

Leading to

$$\begin{cases} L_1 = \frac{2C_0^2}{\omega^2}\frac{1}{l_V+(1-\frac{1}{\gamma})l_\kappa}, \\ V_1 = C_0, \end{cases} \tag{150}$$

where $1-\frac{1}{\gamma} = 1-\frac{C_V}{C_p} = \frac{C_p-C_V}{C_p}$. It is to be noted that $1-\frac{1}{\gamma} > 0$ since $C_p > C_V$.

Using now Eq.(146b)

$$\begin{aligned}
\theta_2 &\approx \pm\sqrt{\frac{1+\frac{i\omega}{C_0}(l_\kappa+l_V)}{\frac{C_0}{i\omega\gamma}l_\kappa(1+\frac{i\omega\gamma}{C_0}l_V)}}\left[1-\frac{1}{2}\frac{C_0}{i\omega\gamma}l_\kappa(1+\frac{i\omega\gamma}{C_0}l_V)(-\frac{\omega^2}{C_0^2})(1-2\frac{i\omega}{C_0}(l_\kappa+l_V))\right],\\
&\approx \pm\sqrt{\frac{i\omega\gamma}{C_0 l_\kappa}}\left(1+\frac{1}{2}\frac{i\omega}{C_0}(l_\kappa+l_V)\right)\left(1-\frac{1}{2}\frac{i\omega\gamma}{C_0}l_V\right)\left[1+\frac{1}{2}\frac{C_0}{i\omega\gamma}l_\kappa\frac{\omega^2}{C_0^2}\right],\\
&= \pm\sqrt{\frac{i\omega\gamma}{C_0 l_\kappa}}\left(1+\frac{1}{2}\frac{i\omega}{C_0}(l_\kappa+l_V)-\frac{1}{2}\frac{i\omega\gamma}{C_0}l_V-\frac{1}{2}\frac{i\omega}{C_0\gamma}l_\kappa\right),\\
&= \pm\sqrt{\frac{i\omega\gamma}{C_0 l_\kappa}}\left[1+\frac{1}{2}\frac{i\omega}{C_0}\left[l_\kappa(1-\frac{1}{\gamma})+l_V(1-\gamma)\right]\right]. \qquad (151)
\end{aligned}$$

For a progressive wave we have

$$\theta_2 = -(\frac{\sqrt{2}}{2}+i\frac{\sqrt{2}}{2})\sqrt{\frac{\omega\gamma}{C_0 l_\kappa}}\left[1+\frac{1}{2}\frac{i\omega}{C_0}\left[l_\kappa(1-\frac{1}{\gamma})+l_V(1-\gamma)\right]\right], \quad (152)$$

since $\sqrt{i} = \pm(\frac{\sqrt{2}}{2}+i\frac{\sqrt{2}}{2})$. Then

$$\begin{aligned}
\theta_2 =& -\frac{\sqrt{2}}{2}\sqrt{\frac{\omega\gamma}{C_0 l_\kappa}}\left[1+\frac{1}{2}\frac{i\omega}{C_0}\left[l_\kappa(1-\frac{1}{\gamma})+l_V(1-\gamma)\right]\right],\\
&-\frac{\sqrt{2}}{2}\sqrt{\frac{\omega\gamma}{C_0 l_\kappa}}\left[i-\frac{1}{2}\frac{\omega}{C_0}\left[l_\kappa(1-\frac{1}{\gamma})+l_V(1-\gamma)\right]\right],\\
\text{Re }\theta_2 =& -\frac{\sqrt{2}}{2}\sqrt{\frac{\omega\gamma}{C_0 l_\kappa}}\left[1-\frac{1}{2}\frac{\omega}{C_0}\left[l_\kappa(1-\frac{1}{\gamma})+l_V(1-\gamma)\right]\right],\\
\text{Im }\theta_2 =& -\frac{\sqrt{2}}{2}\sqrt{\frac{\omega\gamma}{C_0 l_\kappa}}\left[1+\frac{1}{2}\frac{\omega}{C_0}\left[l_\kappa(1-\frac{1}{\gamma})+l_V(1-\gamma)\right]\right],
\end{aligned}$$

and

$$\begin{cases}
L_2 = \frac{2}{\sqrt{2}}\sqrt{\frac{C_0 l_\kappa}{\omega\gamma}}\left[1+\frac{1}{2}\frac{\omega}{C_0}\left[l_\kappa(1-\frac{1}{\gamma})+l_V(1-\gamma)\right]\right],\\
V_2 = \frac{2\omega}{\sqrt{2}}\sqrt{\frac{C_0 l_\kappa}{\omega\gamma}}\left[1-\frac{1}{2}\frac{\omega}{C_0}\left[l_\kappa(1-\frac{1}{\gamma})+l_V(1-\gamma)\right]\right],
\end{cases} \qquad (153)$$

where $1-\frac{1}{\gamma} = 1-\frac{C_V}{C_p} = \frac{C_p-C_V}{C_p}$ and $\gamma-1 = \frac{C_p}{C_V}-1 = \frac{C_p-C_V}{C_V}$.

Acoustic Wavenumber

V is associated with the phase velocity of the wave in the medium and its was proven that $V_1 = C_0$ in Eq.(150b). C_0 being, per definition, the speed of sound in the fluid ($\approx 343 m/s$ in air at 20°C), θ_1 is associated to an acoustical wave generated by thermoacoustic. The associated acoustic wavenumber is then written as $k = i\theta_1$. This interpretation is

corroborated by the definition of L being the penetration length. L_1 becomes infinity for isentropic process ($l_\kappa = l_\nu = 0$) and the wave velocity, independent of dissipative phenomena, assumes the value C_0 in any case. The acoustic wavenumber becomes $k = \omega/C_0$ which is associated to Eq.(136), the isentropic Helmholtz equation.

Thermal Attenuation

Thermal Penetration Length

Regarding θ_2, it was proven that $V_2 = \omega L_2$. The associated wave solution is then written $e^{i\omega t}e^{\pm(1+i)x/L_2}$. This exponentially fast decaying wave is attributed to a thermal wave generated by the thermoacoustic process. The thermal attenuation σ is defined as $-\theta_2$. For weak dissipative process, the thermal penetration length L_{th} is approximated as

$$\begin{aligned} L_{th} =& 2\sqrt{\frac{C_0 l_\kappa}{2\omega\gamma}}, \\ =& \sqrt{\frac{2\alpha}{\omega}}, \end{aligned} \tag{154}$$

with α the thermal diffusivity.

In this section, the conservation equations were solved for an unidimensional case, assuming plane wave radiation and an harmonic time dependence. Equations for the pressure p (Eq.(121)) and the particle velocity v (Eq.(127)) were written depending on the temperature variation T of the fluid. Consequently, a biquadratic fourth order linear differential equation for T was found in Eq.(130). Notably, this equation is equal to Helmholtz equation in the specific case of a reversible adiabatic process. New parameters defined in Eq.(140) were introduced to simplify Eq.(130). This allowed us to determined explicit solutions to the first order of the associated differential equation assuming weak conduction and viscosity. Those solutions are written as

$$\begin{cases} k_f = -i\theta_{ac,f} & = \frac{\omega}{C_0}\left[1 - \frac{1}{2}\frac{i\omega}{C_0}l_V - \frac{1}{2}l_\kappa\frac{i\omega}{C_0}(1-\frac{1}{\gamma})\right], \\ \sigma_f = \theta_{th,f} & = \sqrt{\frac{i\omega\gamma}{C_0 l_\kappa}}\left[1 + \frac{1}{2}\frac{i\omega}{C_0}\left[l_\kappa(1-\frac{1}{\gamma}) + l_V(1-\gamma)\right]\right], \end{cases} \tag{155}$$

with $\theta_{ac,f}$ and $\theta_{th,f}$ the "plus" sign solutions of Eq.(148) and (151), associated to acoustical and thermal waves generated by the thermoacoustic effect. The temperature variation in the fluid is then written as

$$T_f = \left(Ae^{-\theta_{ac,f}x} + Be^{\theta_{ac,f}x} + Ce^{-\theta_{th,f}x} + De^{\theta_{th,f}x}\right)e^{i\omega t}, \tag{156}$$

$$T_f = \left(Ae^{-ik_f x} + Be^{ik_f x} + Ce^{-\sigma_f x} + De^{\sigma_f x}\right)e^{i\omega t}, \tag{157}$$

with ABCD constants. The pressure and the particle velocity can then be deduced using Eq.(121) and Eq.(127).

2.2.2 *Plane Waves in a Solid*

Similarly as in Section 2.2.1, we now investigate the one dimensional case where a longitudinal propagating wave is considered in a solid medium. Therefore in a Cartesian coordinate system $T = T(x,t)$, $\vec{u} = (u(x,t),0,0)$ and $\vec{v} = (v(x,t),0,0)$ where $v = \frac{\partial u}{\partial t}$. Eq.(118) becomes

$$\begin{cases} \rho_{0,s} C_{V,s} \frac{\partial T}{\partial t} = \kappa_s \frac{\partial^2 T}{\partial x^2} - \alpha_{T,s} B_0 T_0 \frac{\partial^2 u}{\partial x \partial t} + Q_0, \\ \rho_{0,s} \frac{\partial v}{\partial t} = (\lambda_0 + 2\mu_0) \frac{\partial^2 u}{\partial x^2} + (\lambda_s + 2\mu_s) \frac{\partial^2 v}{\partial x^2} - \alpha_{T,s} B_0 \frac{\partial T}{\partial x}, \end{cases} \tag{158}$$

where we chose $\vec{b} = 0$.Unlike in a fluid, in a solid Q_0 is kept since energy might be supplied to the system, in our case the thermophone. The aim is to rewrite this system of equation in the same form obtained for the fluid in Eq.(119). To this aim, using Eq.(109), the pressure is defined as

1D Pressure Equation in Solid

$$p = -\left(\hat{T}_e\right)_{11} = -(2\mu_0 + \lambda_0) \frac{\partial u}{\partial x} + \alpha_{T,s} B_0 (T - T_0). \tag{159}$$

It is important to remark that this definition takes into consideration only the thermoelastic part of the total stress. Hence, in order to impose the continuity of the normal stress in a given interface, we have to add the viscous term to Eq.(159). This definition has been introduced only to draw a full comparison with the fluid equations. The system can be rewritten as

$$\begin{cases} \rho_{0,s} C_{V,s} \frac{\partial T}{\partial t} = \kappa_s \frac{\partial^2 T}{\partial x^2} - \alpha_{T,s} B_0 T_0 \frac{\partial v}{\partial x} + Q_0, \\ \rho_{0,s} \frac{\partial v}{\partial t} = -\frac{\partial p}{\partial x} + (\lambda_s + 2\mu_s) \frac{\partial^2 v}{\partial x^2}, \\ \frac{\partial p}{\partial t} = -(2\mu_0 + \lambda_0) \frac{\partial v}{\partial x} + \alpha_{T,s} B_0 \frac{\partial T}{\partial t}, \end{cases} \tag{160}$$

where Eq.(160c) is obtained by differentiating Eq.(159) with respect to time.

Comparing the balance of linear momentum for a solid in Eq.(160b) and for a fluid in Eq.(119b), it is seen that they exhibit similar forms in both cases. Eqs.(160a) and (119c) representing the heat equation, have a different term describing the thermo-mechanical coupling. Lastly Eqs.(160c) and (119a), representing the conservation of mass, have the same structure but different coefficients. This situation must be clarified by obtaining the same form for all three equations and by explaining the differences among the involved parameters. In order to get the same structure for the heat equation, we calculate $\frac{\partial v}{\partial x}$ from Eq.(160c)

$$\frac{\partial v}{\partial x} = \frac{1}{2\mu_0 + \lambda_0} (\alpha_{T,s} B_0 \frac{\partial T}{\partial t} - \frac{\partial p}{\partial t}). \tag{161}$$

Longitudinal and Transverse Wave Velocity

For an isotropic solid we can expect two type of wave: longitudinal and transverse waves. It is well known that they are characterised by the velocities [144]

$$\begin{cases} v_L = \sqrt{\frac{\lambda_0+2\mu_0}{\rho_{0,s}}}, \\ v_T = \sqrt{\frac{\mu_0}{\rho_{0,s}}}, \end{cases} \tag{162}$$

Eq.(161) can be rewritten

$$\frac{\partial v}{\partial x} = \frac{1}{v_L^2 \rho_{0,s}}(\alpha_{T,s} B_0 \frac{\partial T}{\partial t} - \frac{\partial p}{\partial t}). \tag{163}$$

Eq.(160a) now becomes

$$\begin{aligned} \rho_{0,s} C_{V,s} \frac{\partial T}{\partial t} &= \kappa_s \frac{\partial^2 T}{\partial x^2} - \alpha_{T,s} B_0 T_0 \frac{1}{v_L^2 \rho_{0,s}}(\alpha_{T,s} B_0 \frac{\partial T}{\partial t} - \frac{\partial p}{\partial t}) + Q_0, \\ \rho_{0,s} C_{V,s} \frac{\partial T}{\partial t} &= \kappa_s \frac{\partial T^2}{\partial x^2} - \frac{\alpha_{T,s}^2 B_0^2 T_0}{v_L^2 \rho_{0,s}} \frac{\partial T}{\partial t} + \frac{\alpha_{T,s} B_0 T_0}{v_L^2 \rho_{0,s}} \frac{\partial p}{\partial t} + Q_0, \\ (\rho_{0,s} C_{V,s} + \frac{\alpha_{T,s}^2 B_0^2 T_0}{v_L^2 \rho_{0,s}}) \frac{\partial T}{\partial t} &= \kappa_s \frac{\partial T^2}{\partial x^2} + \frac{\alpha_{T,s} B_0 T_0}{v_L^2 \rho_{0,s}} \frac{\partial p}{\partial t} + Q_0. \end{aligned} \tag{164}$$

The first coefficient can be elaborated using the relation between the specific heats defined in Eq.(125), which holds true for solids as well. Therefore

$$\begin{aligned} \rho_{0,s} C_{V,s} + \frac{\alpha_{T,s}^2 B_0^2 T_0}{v_L^2 \rho_{0,s}} &= \rho_{0,s} C_{p,s} - \alpha_{T,s}^2 T_0 B_0 + \alpha_{T,s}^2 T_0 B_0 \frac{B_0}{v_L^2 \rho_{0,s}}, \\ &= \rho_{0,s} C_{p,s} + \rho_{0,s}(C_{p,s} - C_{V,s})(\frac{B_0}{v_L^2 \rho_{0,s}} - 1), \end{aligned} \tag{165}$$

where

$$\frac{B_0}{v_L^2 \rho_{0,s}} = \frac{2\mu_0 + 3\lambda_0}{6\mu_0 + 3\lambda_0} = 1 - \frac{4\mu_0}{3(2\mu_0 + \lambda_0)} = 1 - \frac{4}{3}\frac{v_T^2}{v_L^2}, \tag{166}$$

hence

$$\begin{aligned} \rho_{0,s} C_{V,s} + \frac{\alpha_{T,s}^2 B_0^2 T_0}{v_L^2 \rho_{0,s}} &= \rho_{0,s} C_{p,s} + \rho_{0,s}(C_{p,s} - C_{V,s})(-\frac{4}{3}\frac{v_T^2}{v_L^2}), \\ &= \rho_{0,s} C_{p,s} \left[1 - \frac{C_{p,s} - C_{V,s}}{C_{p,s}} \frac{4}{3}\frac{v_T^2}{v_L^2}\right]. \end{aligned} \tag{167}$$

The heat equation Eq.(160a) becomes

$$\rho_{0,s} C_{p,s} \left[1 - \frac{C_{p,s} - C_{V,s}}{C_{p,s}} \frac{4}{3}\frac{v_T^2}{v_L^2}\right] \frac{\partial T}{\partial t} = \kappa_s \frac{\partial^2 T}{\partial x^2} + 2\alpha_{T,s} T_0 (1 - \frac{4}{3}\frac{v_T^2}{v_L^2}) \frac{\partial p}{\partial t} + Q_0.$$

(168)

Eq.(160c) can also be rewritten

$$\frac{1}{B_0}\frac{\partial p}{\partial t}+\frac{2\mu_0+\lambda_0}{B_0}\frac{\partial v}{\partial x}-\alpha_{T,s}\frac{\partial T}{\partial t}=0, \tag{169}$$

however $\frac{B_0}{2\mu_0+\lambda_0}=\frac{B_0}{v_L^2\rho_{0,s}}=1-\frac{4}{3}\frac{v_T^2}{v_L^2}$ and we get

$$\frac{1}{B_0}\frac{\partial p}{\partial t}+\left(1-\frac{4}{3}\frac{v_T^2}{v_L^2}\right)^{-1}\frac{\partial v}{\partial x}-\alpha_{T,s}\frac{\partial T}{\partial t}=0. \tag{170}$$

1D Equation System in Solid using Transverse and Longitudinal Waves Speed

The final, complete system for the solid is now

$$\begin{cases}\frac{1-\frac{4}{3}\frac{v_T^2}{v_L^2}}{B_0}\frac{\partial p}{\partial t}-\alpha_{T,s}(1-\frac{4}{3}\frac{v_T^2}{v_L^2})\frac{\partial T}{\partial t}+\frac{\partial v}{\partial x}=0,\\ \rho_{0,s}\frac{\partial v}{\partial t}=-\frac{\partial p}{\partial x}+(\lambda_s+2\mu_s)\frac{\partial^2 v}{\partial x^2},\\ \rho_{0,s}C_{p,s}\left[1-\frac{C_{p,s}-C_{V,s}}{C_{p,s}}\frac{4}{3}\frac{v_T^2}{v_L^2}\right]\frac{\partial T}{\partial t}-\alpha_{T,s}T_0(1-\frac{4}{3}\frac{v_T^2}{v_L^2})\frac{\partial p}{\partial t}=\kappa_s\frac{\partial^2 T}{\partial x^2}+Q_0.\end{cases} \tag{171}$$

Comparing with the same system for the fluid in Eq.(119) being

$$\begin{cases}\frac{1}{B}\frac{\partial p}{\partial t}-\alpha_T\frac{\partial T}{\partial t}+\frac{\partial v}{\partial x}=0,\\ \rho_{0,f}\frac{\partial v}{\partial t}=-\frac{\partial p}{\partial x}+(\lambda+2\mu)\frac{\partial^2 v}{\partial x^2},\\ \rho_{0,f}C_{p,f}\frac{\partial T}{\partial t}-\alpha_T T_0\frac{\partial p}{\partial t}=\kappa\frac{\partial^2 T}{\partial x^2},\end{cases}$$

we have obtained the same system of equation providing the change in parameters between fluid and solid as

$$\begin{cases}B=\frac{B_0}{1-\frac{4}{3}\frac{v_T^2}{v_L^2}},\\ \alpha_T=\alpha_{T,s}(1-\frac{4}{3}\frac{v_T^2}{v_L^2}),\\ C_{p,f}=C_{p,s}(1-\frac{C_{p,s}-C_{V,s}}{C_{p,s}},\frac{4}{3}\frac{v_T^2}{v_L^2}),\end{cases} \tag{172}$$

and $C_{V,f}=C_{V,s}$, $\lambda=\lambda_s$, $\mu=\mu_s$, $\kappa=\kappa_s$. It is interesting to observe that all the parameters are unchanged if $v_T=0$, a property effectively characterising a fluid where only longitudinal waves can propagate and no transverse waves. It can also be noted that the ratio $\frac{v_L}{v_T}$ can be written in terms of the Poisson ratio ν as

$$\frac{v_L}{v_T}=\sqrt{2}\sqrt{\frac{1-\nu}{1-2\nu}}, \tag{173}$$

with $-1 < \nu < \frac{1}{2}$. Another interesting property can be observed if we define $Z = 1 - \frac{4}{3}\frac{\nu_T^2}{\nu_L^2}$. The parameters changes in Eq.(172) become

$$\begin{cases} B = \frac{B_0}{Z}, \\ \alpha_T = Z\alpha_{T,s}, \\ C_{p,f} = C_{p,s}(Z + \frac{C_{V,s}}{C_{p,s}}(1-Z)). \end{cases} \tag{174}$$

Using this notation it can be easily proven that the thermodynamic relation between C_p and C_V of Eq.(125) is conserved in both solid and fluid phases, meaning that if $\rho_{0,f}(C_{p,f} - C_{V,f}) = \alpha_T^2 B T_0$ then $\rho_{0,s}(C_{p,s} - C_{V,s}) = \alpha_{T,s}^2 B_0 T_0$ and reciprocally.

Regarding the heat density supplied Q_0 supposed uniform, an approximation can be found if it is assumed that the solid can not be deformed. This leads to $C_{p,s} = C_{V,s}$, $\frac{\partial p}{\partial t} = 0$ and $\frac{\partial^2 T}{\partial x^2} = 0$. Eq.(171c) now becomes

$$\rho_{0,s} C_{p,s} \frac{\partial T}{\partial t} = Q_0,$$

Particular Solution of Temperature Variations

and so

$$T = \frac{Q_0}{\rho_{0,s} C_{p,s} i\omega}. \tag{175}$$

Eq.(175) represent the particular solution of the associated differential equation of the temperature variations in the solid.

In this section, we first defined the pressure as well as the longitudinal and transverse wave speed in the solid in Eq.(159) and Eqs.(162) respectively. This allowed us to write the system of equation composed of the conservation of mass, linear momentum and energy, with the newly defined parameters in Eq.(171). This system was compared to the one found for fluid medium in Eq.(119) and it was seen that, provided a specific change in parameters in Eq.(172) which adds the influence of transverse waves (not present in a fluid), both systems were identical with the added heat density supplied in the solid. This means that all the thought process used in Section 2.2.1 is also valid for a solid. The temperature variation in the solid can then be written

$$T_s = \left(A e^{-\theta_{ac,s} x} + B e^{\theta_{ac,s} x} + C e^{-\theta_{th,s} x} + D e^{\theta_{th} x} \right) e^{i\omega t} + T_{Q_0}\,, \tag{176}$$

$$T_s = \left(A e^{-ik_s x} + B e^{ik_s x} + C e^{-\sigma_s x} + D e^{\sigma_s x} \right) e^{i\omega t} + T_{Q_0}\,, \tag{177}$$

with $ABCD$ constants,

$$T_{Q_0} = \frac{Q_0}{\rho_{0,s} C_{p,s} i\omega} \tag{178}$$

a constant term to take into account the supplied energy as seen in Eq.(175), and

$$\begin{cases} k_s = -i\theta_{ac,s} & = \frac{\omega}{C_{0,s}}\left[1 - \frac{1}{2}\frac{i\omega}{C_{0,s}} l_{V,s} - \frac{1}{2} l_{\kappa,s}\frac{i\omega}{C_{0,s}}(1 - \frac{1}{\gamma_s})\right], \\ \sigma_s = \theta_{th,s} & = \sqrt{\frac{i\omega\gamma_s}{C_{0,s} l_{\kappa,s}}}\left[1 + \frac{1}{2}\frac{i\omega}{C_{0,s}}\left[l_{\kappa,s}(1 - \frac{1}{\gamma_s}) + l_{V,s}(1 - \gamma_s)\right]\right], \end{cases} \tag{179}$$

the associated acoustical and thermal wavenumbers generated by the thermoacoustic effect in the solid. The pressure and the particle velocity can be deduced using Eq.(159) and Eq.(127) respectively (provided adequate parameters change).

2.2.3 *Ideal Plane Thermophone*

We will here investigate what we define as an ideal thermophone. In this specific case, the solid part of the thermophone is not considered and is represented as an ideal boundary condition creating a temperature gradient with the propagating medium. By solving this case, it will provide knowledge on how a thermophone sound radiation spectrum should ideally be. This easily implementable model will also be used as a stepping stone before creating our multilayer model.

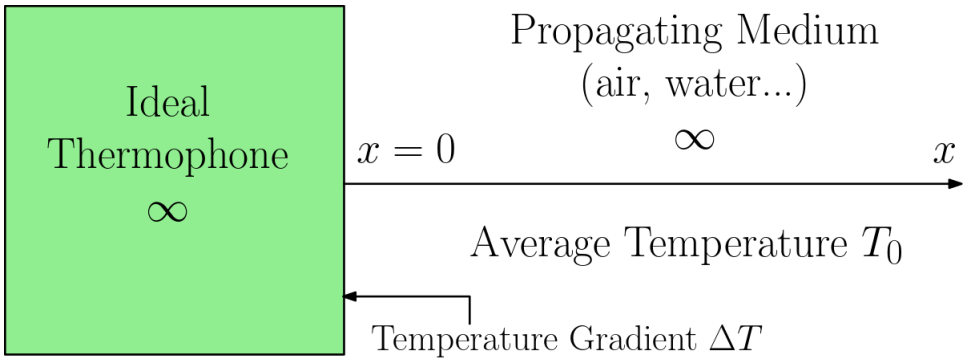

Figure 22: Schematic of the perfect thermophone model 1D

In a simple one dimensional model as seen on Fig.22, considering only progressive waves in the x direction and using Eq.(155) the temperature variation T in the medium can be written in the form

$$T(x) = \left(Ae^{-\theta_{ac}x} + Be^{-\theta_{th}x}\right) e^{i\omega t}, \tag{180}$$

with A and B constants. No subscripts are used here since, even though the propagating medium is most likely a fluid (air for instance), those

equations are still valid for solid propagation. The first order approximation solutions for θ_{ac} and θ_{th} were calculated in Eqs.(155). Using Eq.(180), the particle velocity and the pressure can then be inferred with Eqs.(127) and (121) respectively. Assuming that the gradient of temperature between the medium and the thermophone is ΔT and that the thermophone is rigid we have the two boundary conditions

$$\begin{cases} T(x=0) = \Delta T, \\ v(x=0) = 0, \end{cases} \tag{181}$$

at $x = 0$ being the limit between the thermophone and the propagating medium. Using those boundary conditions and Eq.(127) with Eq.(180) we found that

$$\begin{cases} A = \frac{-\theta_{th}\Delta T(L_1+L_2\theta_{th}^2)}{L_1(\theta_{ac}-\theta_{th})+L_2(\theta_{ac}^3-\theta_{th}^3)}, \\ B = \Delta T - A, \end{cases} \tag{182}$$

with L_1 and L_2 being the coefficients of Eq.(127)

$$L_1 = -\frac{1}{i\omega\rho}\left[\alpha_T B + \frac{i\omega\rho C_V}{\alpha_T T_0 B}(\lambda + 2\mu + \frac{B}{i\omega})\right], \tag{183}$$

$$L_2 = (\lambda + 2\mu + \frac{B}{i\omega})\frac{\kappa}{i\omega\rho\alpha_T T_0 B}, \tag{184}$$

so that $v = L_1\frac{\partial T}{\partial x} + L_2\frac{\partial^3 T}{\partial x^3}$.

The constants A and B being determined, the pressure, particle velocity and temperature variations can be estimated for any position x and at any frequency f. The results of this model and of the following one will be analysed in Section 3.

2.2.4 *Transfer Matrix with N Layers*

In Section 1.5, the need for a flexible theoretical model which should be able to simulate a number of different geometries was highlighted. The evaluated parameters in Sections 2.2.1 and 2.2.2 are here rewritten in a matrix form in order to create a uni dimensional multilayer model whose variable geometry is shown in Fig.23. The number N of layers can be changed and each layer can be made of a different material, either solid or liquid (air, water, silicon, carbon...) with an volumetric input energy coefficient. The size $l_j - l_{j-1}$ ($\forall j \in [2, N-1]$) of the layers can also be changed except for the first and the last ones which are supposed to

be semi-infinite and without any input volumetric source. This scheme will be adopted to describe the behavior of different configurations of thermophone devices in the following sections.

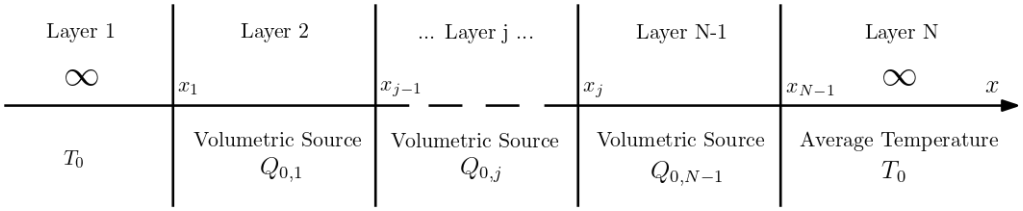

Figure 23: Schematic of a generalized version of the thermophone model with N layers in 1D

3 Layers Model

To facilitate the understanding of the model's construction, a 3 layers model will first be investigated before being extended to N number of layers. It is composed of a thermophone of thickness l_s on a semi infinite substrate and radiating in a semi infinite propagating medium as seen in Fig.24. They will be referred to by the subscripts $_s$, $_b$ and $_g$ respectively in this section. The substrate and the thermophone are solid layers and the propagating medium is a fluid layer. As such, they will be described by the equations in Section 2.2.2 and 2.2.1 respectively.

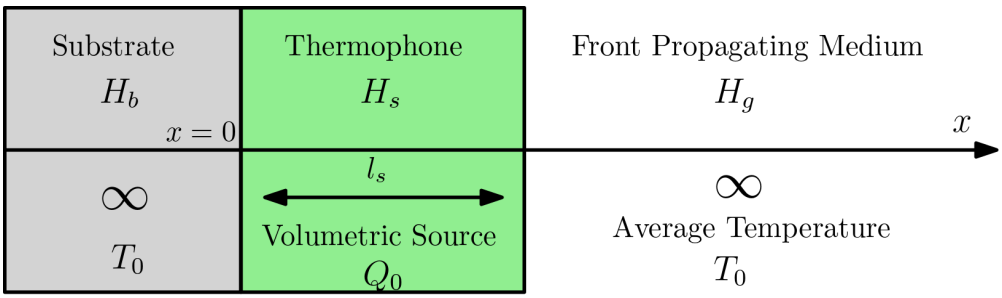

Figure 24: Schematic of the thermophone model with common 3 layers being the substrate b the thermophone s and the propagating fluid g

It has to be noted that it was proven that by using the parameters change of Eq.(172), the variable T, ν, p have similar defining equations in both fluid and solid. Hence, if the following results are here based on Section 2.2.1 for fluids, they are also valid for solids. We here use the notation k and σ to relate more closely to the standard definition of the acoustic wavenumber but for easy comparison with the following models it is important to remember that $k = -i\theta_{ac}$ and $\sigma = \theta_{th}$ as defined in Eq.(155).

Based on Eq.(157) the temperature variations T can be expressed as

$$T(x) = Ae^{-ikx} + Be^{ikx} + Ce^{-\sigma x} + De^{\sigma x} + T_{Q_0}, \tag{185}$$

with T_{Q_0} being as defined in Eq.(178) if energy is supplied to the medium, or equal to 0 if not. Using Eq.(127), the particle velocity v can be rewritten as a function of A, B, C, D, k and σ as

$$\begin{aligned} v =& A(L_1(-ik) + L_2(-ik)^3)e^{-ikx} + B(L_1(ik) + L_2(ik)^3)e^{ikx} + \\ & C(L_1(-\sigma) + L_2(-\sigma)^3)e^{-\sigma x} + D(L_1(\sigma) + L_2(\sigma)^3)e^{\sigma x}, \end{aligned} \tag{186}$$

with L_1, L_2 as Eqs.(183) and (184). The same can be done with p using Eq.(121)

$$\begin{aligned} p =& A(\alpha_T B - \frac{B}{i\omega}(L_1(-ik)^2 + L_2(-ik)^4))e^{-ikx} + \\ & B(\alpha_T B - \frac{B}{i\omega}(L_1(ik)^2 + L_2(ik)^4))e^{ikx} + \\ & C(\alpha_T B - \frac{B}{i\omega}(L_1(-\sigma)^2 + L_2(-\sigma)^4))e^{-\sigma x} + \\ & D(\alpha_T B - \frac{B}{i\omega}(L_1(\sigma)^2 + L_2(\sigma)^4))e^{\sigma x}. \end{aligned} \tag{187}$$

Normal Stress Tensor

It is to be noted however that the continuity of pressure between two media is true only without any viscosity (only the elastic stress tensor is taken into account). The normal stress tensor $\tilde{p} = -\hat{T}_{11}$ is then defined. It holds the stress continuity between layers as the first component of the stress tensor matrix (as seen for a solid in Eq.(159)) for all cases. It is explicitly written as

$$\tilde{p} = -(\hat{T}_e)_{11} - (\hat{T}_V)_{11} = p - (\lambda + 2\mu)\frac{\partial v}{\partial x}, \tag{188}$$

leading to

$$\begin{aligned} \tilde{p} =& A(\alpha_T B - (\frac{B}{i\omega} + \lambda + 2\mu)(L_1(-ik)^2 + L_2(-ik)^4))e^{-ikx} + \\ & B(\alpha_T B - (\frac{B}{i\omega} + \lambda + 2\mu)(L_1(ik)^2 + L_2(ik)^4))e^{ikx} + \\ & C(\alpha_T B - (\frac{B}{i\omega} + \lambda + 2\mu)(L_1(-\sigma)^2 + L_2(-\sigma)^4))e^{-\sigma x} + \\ & D(\alpha_T B - (\frac{B}{i\omega} + \lambda + 2\mu)(L_1(\sigma)^2 + L_2(\sigma)^4))e^{\sigma x}. \end{aligned} \tag{189}$$

Finally the general equation for the heat flux q in a medium can be written as

$$q = -\kappa\frac{\partial T}{\partial x}, \tag{190}$$

which give the equation for q in one dimension as

$$q = A\kappa ikxe^{-ikx} - B\kappa ike^{ikx} + C\kappa\sigma e^{-\sigma x} - D\kappa\sigma e^{\sigma x}. \tag{191}$$

Eqs.(185), (186), (187) and (191) can be rewritten in Matrix form as

$$\begin{bmatrix} \tilde{p} \\ v \\ q \\ T \end{bmatrix} = H(x) \begin{bmatrix} A \\ B \\ C \\ D \end{bmatrix} \tag{192}$$

where $H(x)$ being a 4×4 matrix. Alternatively we can decompose H as $H(x) = H^{(a)}H^{(b)}(x)$ with

$$H^{(a)} = \begin{bmatrix} \mathcal{F}(-ik) & \mathcal{F}(ik) & \mathcal{F}(-\sigma) & \mathcal{F}(\sigma) \\ -ik\mathcal{G}(-ik) & ik\mathcal{G}(ik) & -\sigma\mathcal{G}(-\sigma) & \sigma\mathcal{G}(\sigma) \\ \kappa ik & -\kappa ik & \kappa\sigma & -\kappa\sigma \\ 1 & 1 & 1 & 1 \end{bmatrix}, \tag{193}$$

and

$$H^{(b)}(x) = \begin{bmatrix} e^{-ikx} & 0 & 0 & 0 \\ 0 & e^{ikx} & 0 & 0 \\ 0 & 0 & e^{-\sigma x} & 0 \\ 0 & 0 & 0 & e^{\sigma x} \end{bmatrix}. \tag{194}$$

The functions $\mathcal{F}$ and $\mathcal{G}$ being pair functions defined as

$$\mathcal{F}(\eta) = \alpha_T B - \left(\frac{B}{i\omega} + \lambda + 2\mu\right)(L_1\eta^2 + L_2\eta^4), \tag{195}$$

$$\mathcal{G}(\eta) = L_1 + L_2\eta^2. \tag{196}$$

Eqs.(189) and (192) are also valid in a solid, provided that the changes of Eq.(172) are respected. For instance, the normal stress tensor is written

$$\begin{aligned} \tilde{p} =& A(\alpha_{T,s}B_0 - (\frac{B_0}{i\omega}\frac{1}{1-\frac{4}{3}\frac{v_T^2}{v_L^2}} + \lambda_s + 2\mu_s)(L_{1,s}(-ik_s)^2 + L_{2,s}(-ik_s)^4))e^{-ik_s x} + \\ & B(\alpha_{T,s}B_0 - (\frac{B_0}{i\omega}\frac{1}{1-\frac{4}{3}\frac{v_T^2}{v_L^2}} + \lambda_s + 2\mu_s)(L_{1,s}(ik_s)^2 + L_{2,s}(ik_s)^4))e^{ik_s x} + \\ & C(\alpha_{T,s}B_0 - (\frac{B_0}{i\omega}\frac{1}{1-\frac{4}{3}\frac{v_T^2}{v_L^2}} + \lambda_s + 2\mu_s)(L_{1,s}(-\sigma_s)^2 + L_{2,s}(-\sigma_s)^4))e^{-\sigma_s x} + \\ & D(\alpha_{T,s}B_0 - (\frac{B_0}{i\omega}\frac{1}{1-\frac{4}{3}\frac{v_T^2}{v_L^2}} + \lambda_s + 2\mu_s)(L_{1,s}(\sigma_s)^2 + L_{2,s}(\sigma_s)^4))e^{\sigma_s x}, \end{aligned} \tag{197}$$

with

$$L_{1,s} = -\frac{1}{i\omega\rho_s}\left[\alpha_{T,s}B_0 + \frac{i\omega\rho_s C_{V,s}}{\alpha_{T,s}T_0 B_0}(\lambda_s + 2\mu_s + \frac{B_0}{i\omega}\frac{1}{1-\frac{4}{3}\frac{v_T^2}{v_L^2}})\right], \quad (198)$$

$$L_{2,s} = (\lambda_s + 2\mu_s + \frac{B_0}{i\omega}\frac{1}{1-\frac{4}{3}\frac{v_T^2}{v_L^2}})\frac{\kappa_s}{i\omega\rho_s\alpha_{T,s}T_0 B_0}, \quad (199)$$

Hence, from now on, for any layer j the constants of the medium will have the subscript j and the matrices will be as $H_j^{(a)} = H_j^{(a)}(f, \rho_j, \alpha_{Tj}, B_j, C_{Vj}, C_{pj}, T_0, \lambda_j, \mu_j, \kappa_j, \lambda_{0j}, \mu_{0j})$ and $H_j^{(b)} = H_j^{(b)}(k_j, \sigma_j, x)$. In the case of interest shown in Fig.24, there are three layers: the substrate b, the thermophone s, and the propagating medium g. The equations can be written as

$$\begin{bmatrix} \tilde{p} \\ v \\ q \\ T \end{bmatrix}_b = H_b \begin{bmatrix} A_b \\ B_b \\ C_b \\ D_b \end{bmatrix}, \quad (200)$$

$$\begin{bmatrix} \tilde{p} \\ v \\ q \\ T \end{bmatrix}_s = H_s \begin{bmatrix} A_s \\ B_s \\ C_s \\ D_s \end{bmatrix} + \begin{bmatrix} \alpha_{T,s}B_s T_{Q_0,s} \\ 0 \\ 0 \\ T_{Q_0,s} \end{bmatrix}, \quad (201)$$

$$\begin{bmatrix} \tilde{p} \\ v \\ q \\ T \end{bmatrix}_g = H_g \begin{bmatrix} A_g \\ B_g \\ C_g \\ D_g \end{bmatrix}, \quad (202)$$

(203)

with $Q_{0,s}$ being the volumetric source of the thermophone in $[W/m^3]$ and $T_{Q_0,s}$ as in Eq.(178). In order to fully determine the system the coefficients A_j, B_j, C_j, D_j have to be found. The only assumption made is that the substrate and the medium are semi infinite. This means that there are no waves propagating in the direction $+x$ in the substrate and $-x$ in the medium. This boundary conditions can be written as $A_b = C_b = 0$ and $B_g = D_g = 0$. Another boundary condition is the

continuity of $\tilde{p}$, v, q and T at the boundaries of the layers. This leads at $x = 0$

$$H_b(x=0)\begin{bmatrix}0\\B_b\\0\\D_b\end{bmatrix} = H_s(x=0)\begin{bmatrix}A_s\\B_s\\C_s\\D_s\end{bmatrix} + \begin{bmatrix}\alpha_{T,s}B_s T_{Q_0,s}\\0\\0\\T_{Q_0,s}\end{bmatrix}, \quad (204)$$

with $H_b^{(b)}(x=0) = H_s^{(b)}(x=0) = I$ the identity matrix. At $x = l_s$

$$H_s(x=l_s)\begin{bmatrix}A_s\\B_s\\C_s\\D_s\end{bmatrix} + \begin{bmatrix}\alpha_{T,s}B_s T_{Q_0,s}\\0\\0\\T_{Q_0,s}\end{bmatrix} = H_g(x=l_s)\begin{bmatrix}A_g\\0\\C_g\\0\end{bmatrix}. \quad (205)$$

Eq.(204) and (205) leads to

$$\begin{bmatrix}0\\B_b\\0\\D_b\end{bmatrix} = H_b^{-1}(0)\, H_s(0)\, H_s(l_s)^{-1}\, H_g(l_s)\begin{bmatrix}A_g\\0\\C_g\\0\end{bmatrix} + H_b^{-1}(0)(1 - H_s(0)\, H_s(l_s)^{-1})\begin{bmatrix}\alpha_{T,s}B_s T_{Q_0,s}\\0\\0\\T_{Q_0,s}\end{bmatrix}, \quad (206)$$

simplified as

$$\begin{bmatrix}0\\B_b\\0\\D_b\end{bmatrix} = \overline{M}\begin{bmatrix}A_g\\0\\C_g\\0\end{bmatrix} + \hat{M}\begin{bmatrix}\alpha_{T,s}B_s T_{Q_0,s}\\0\\0\\T_{Q_0,s}\end{bmatrix}. \quad (207)$$

A_g, C_g, B_b and D_b can then be found using both

$$0 = \begin{bmatrix}\overline{M}_{11} & \overline{M}_{13}\\ \overline{M}_{31} & \overline{M}_{33}\end{bmatrix}\begin{bmatrix}A_g\\C_g\end{bmatrix} + \begin{bmatrix}\hat{M}_{11} & \hat{M}_{14}\\ \hat{M}_{31} & \hat{M}_{34}\end{bmatrix}\begin{bmatrix}\alpha_{T,s}B_s T_{Q_0,s}\\T_{Q_0,s}\end{bmatrix}, \quad (208)$$

$$\begin{bmatrix}B_b\\D_b\end{bmatrix} = \begin{bmatrix}\overline{M}_{21} & \overline{M}_{23}\\ \overline{M}_{41} & \overline{M}_{43}\end{bmatrix}\begin{bmatrix}A_g\\C_g\end{bmatrix} + \begin{bmatrix}\hat{M}_{21} & \hat{M}_{24}\\ \hat{M}_{41} & \hat{M}_{44}\end{bmatrix}\begin{bmatrix}\alpha_{T,s}B_s T_{Q_0,s}\\T_{Q_0,s}\end{bmatrix}. \quad (209)$$

Eq.(204) or Eq.(205) can then be used to found A_s, B_s, C_s and D_s. Finally $\tilde{p}$, v, q and T can be evaluated at any x using Eqs.(200), (201) and (202).

Global N layers model

In order to have a more flexible one dimensional model that is able to study multiple thermophone layers, the transfer matrix method is used on a N layers model as shown in Fig.23. The assumptions used for this model are: the layers at the extremities (1 and N) are semi infinite, each layer is potentially a source (has a volumetric source coefficient $Q_{0,j}$) except at the extremities ($Q_{0,1} = Q_{0,N} = 0$), and the length of each layer j is $l_j - l_{j-1}$. The type of material of each layer (fluid or solid) is not specified since the material differences are taken into account in their transfer matrices H_j. Eqs.(200), (201) and (202) can be written in the general form for a layer j

$$\begin{bmatrix} \tilde{p} \\ v \\ q \\ T \end{bmatrix}_j = H_j \begin{bmatrix} A_j \\ B_j \\ C_j \\ D_j \end{bmatrix} + \begin{bmatrix} \alpha_{T,j} B_j T_{Q_0,j} \\ 0 \\ 0 \\ T_{Q_0,j} \end{bmatrix}, \tag{210}$$

with $T_{Q_0,j} = \frac{Q_{0,j}}{i\omega\rho_j C_{Vj}}$ as in Eq.(178). The continuity at l_j, $\forall j \in [1, N-1]$ now becomes

$$H_j(l_j) \begin{bmatrix} A_j \\ B_j \\ C_j \\ D_j \end{bmatrix} + \begin{bmatrix} \alpha_{T,j} B_j T_{Q_0,j} \\ 0 \\ 0 \\ T_{Q_0,j} \end{bmatrix} = H_{j+1}(l_j) \begin{bmatrix} A_{j+1} \\ B_{j+1} \\ C_{j+1} \\ D_{j+1} \end{bmatrix} + \begin{bmatrix} \alpha_{T,j+1} B_{j+1} T_{Q_0,j+1} \\ 0 \\ 0 \\ T_{Q_0,j+1} \end{bmatrix}. \tag{211}$$

Knowing that $A_1 = C_1 = 0$ and $B_N = D_N = 0$ due to the semi infinite size of the layers at the edge, and following the same thought process as with three layers we obtain

$$\begin{bmatrix} 0 \\ B_1 \\ 0 \\ D_1 \end{bmatrix} = M_0 \begin{bmatrix} A_N \\ 0 \\ C_N \\ 0 \end{bmatrix} + \sum_{n \in [2,N-1]} M_{Q_{0,n}} \begin{bmatrix} \alpha_{T,n} B_n T_{Q_0,n} \\ 0 \\ 0 \\ T_{Q_0,n} \end{bmatrix}, \tag{212}$$

with n being the layers with a volumetric source and

$$M_0 = H_1^{-1}(l_1) \left[\prod_{j=2}^{N-1} H_j(l_{j-1})\, H_j^{-1}(l_j) \right] H_N(l_{N-1}), \tag{213}$$

$$M_{Q_{0,n}} = H_1^{-1}(l_1) \left[\prod_{j=2}^{n-1} H_j(l_{j-1})\, H_j^{-1}(l_j) \right] \left[1 - H_n(l_{n-1})\, H_n^{-1}(l_n) \right]. \tag{214}$$

Eq.(212) gives A_N, C_N, B_1, and D_1. This allows the calculation of any coefficient $ABCD_j$ using either equations

$$\begin{bmatrix} A_j \\ B_j \\ C_j \\ D_j \end{bmatrix} = H_j^{-1}(l_j) \left[H_{j+1}(l_j) \begin{bmatrix} A_{j+1} \\ B_{j+1} \\ C_{j+1} \\ D_{j+1} \end{bmatrix} + \begin{bmatrix} \alpha_{T,j+1} B_{j+1} T_{Q_0,j+1} \\ 0 \\ 0 \\ T_{Q_0,j+1} \end{bmatrix} - \begin{bmatrix} \alpha_{T,j} B_j T_{Q_0,j} \\ 0 \\ 0 \\ T_{Q_0,j} \end{bmatrix} \right], \tag{215}$$

$$\begin{bmatrix} A_j \\ B_j \\ C_j \\ D_j \end{bmatrix} = H_j^{-1}(l_{j-1}) \left[H_{j-1}(l_{j-1}) \begin{bmatrix} A_{j-1} \\ B_{j-1} \\ C_{j-1} \\ D_{j-1} \end{bmatrix} + \begin{bmatrix} \alpha_{T,j-1} B_{j-1} T_{Q_0,j-1} \\ 0 \\ 0 \\ T_{Q_0,j-1} \end{bmatrix} - \begin{bmatrix} \alpha_{T,j} B_j T_{Q_0,j} \\ 0 \\ 0 \\ T_{Q_0,j} \end{bmatrix} \right], \tag{216}$$

$\forall j \in [1, N-1]$ and $\forall j \in [2, N]$ for Eqs.(215) and (216) respectively. Finally $\tilde{p}$, v, q, T can be found for any x with Eq.(210).

In this section we introduced the normal stress tensor and the heat flux in Eqs.(189) and (190) respectively. This allowed to write the system of equations in a matrix form as seen in Eq.(192) with the variables $\tilde{p}, v, q, T$. As an introduction, a 3 layers model was solved allowing the determination of all the variable at any position in space and time, and at any frequency. This method was then extended to a more general N layers model. Its only assumptions are semi infinite layers at both ends as well as continuity for the variables $\tilde{p}, v, q, T$ at the boundary of each layers. Unknown constants $ABCD_j$ in each layers are found and the main fields $\tilde{p}, v, q, T$ are estimated for any position within each layer and for any frequency through Eq.(192). This is what we call the 1T, 1D multilayer model.

2.3 ONE TEMPERATURE MULTILAYER MODEL FOR CYLINDRICAL WAVES

Section 2.2 solved the conservation equation of Section 2.1 for a uni dimensional model assuming plane wave generation. In a similar fashion, starting back to the conservation equations for a fluid with thermal and viscous properties in Eqs.(56), as well as for an isotropic homogeneous solid with thermal, viscous and elastic properties in Eqs.(118), we will now solve those equations assuming a cylindrical geometry.

Using a cylindrical coordinate system, the aim is similar to the one in Section 2.2. Explicit analytical solutions of the parameters T, p, v and q are investigated before being rewritten in a matrix form for both fluid and solid media. An ideal cylindrical thermophone will then be investigated before extending the model to a multilayer one, as previously explained.

The cylinder shaped thermophone is for now supposed to be infinitely thin in the r direction, infinitely long in the z direction and all physical properties are independent of the angle θ. This leads to parameters being solely dependent on the distance with the cylinder r.

2.3.1 *Cylindrical Waves in a Fluid*

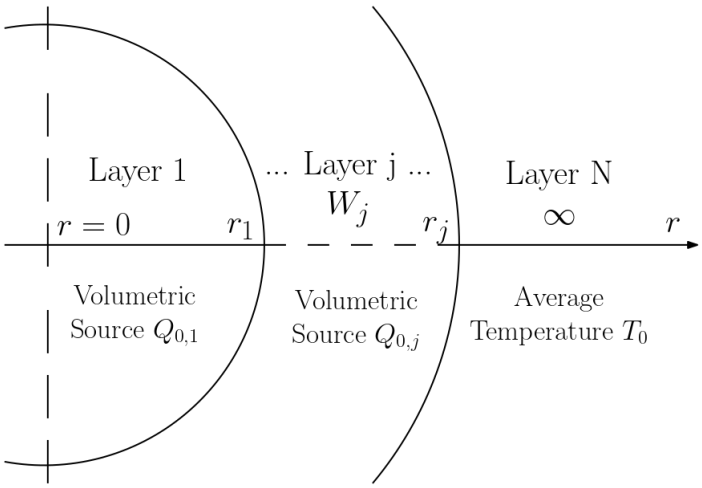

Figure 25: Schematic of the thermophone model in 2D, here with N layers

Using the general equations in a fluid in Eq.(56), a cylindrical geometry is now investigated as seen in Fig.25. The pressure, particle velocity and temperature variation can be written as

$$\begin{cases} p = p(r), \\ T = T(r), \\ \vec{v} = \frac{\vec{r}}{r} v(r), \end{cases} \tag{217}$$

with $\vec{r} = x\vec{e_x} + y\vec{e_y}$ and $\|\vec{r}\| = r = \sqrt{x^2 + y^2}$. In order to write Eqs.(56) in cylindrical coordinates, each component of those equations has to be

rewritten using the parameters of Eq.(217). This leads to (details can be found in Appendix A.5)

$$\begin{cases} \vec{\nabla} p = \frac{\vec{r}}{r}\frac{\partial p}{\partial r}, \\ \vec{\nabla}.\vec{v} = \frac{1}{r}v + \frac{\partial v}{\partial r}, \\ \vec{\nabla}(\vec{\nabla}.\vec{v}) = \frac{\vec{r}}{r}\left(-\frac{1}{r^2}v + \frac{1}{r}\frac{\partial v}{\partial r} + \frac{\partial^2 v}{\partial r^2}\right), \\ \nabla^2\vec{v} = \frac{\vec{r}}{r}\left(-\frac{1}{r^2}v + \frac{1}{r}\frac{\partial v}{\partial r} + \frac{\partial^2 v}{\partial r^2}\right), \\ \nabla^2 T = \frac{1}{r}\frac{\partial T}{\partial r} + \frac{\partial^2 T}{\partial r^2}. \end{cases} \tag{218}$$

Using Eqs.(218), Eqs.(56) now become

$$\begin{cases} i\omega\frac{1}{B}p - i\omega\alpha_T T + \frac{1}{r}\frac{\partial}{\partial r}(rv) = 0, \\ i\omega\rho_{0,f}v = -\frac{\partial p}{\partial r} + (\lambda + 2\mu)(-\frac{1}{r^2}v + \frac{1}{r}\frac{\partial v}{\partial r} + \frac{\partial^2 v}{\partial r^2}), \\ i\omega\rho_{0,f}C_p T - i\omega\alpha_T T_0 p = \kappa(\frac{1}{r}\frac{\partial T}{\partial r} + \frac{\partial^2 T}{\partial r^2}), \end{cases} \tag{219}$$

with $\frac{1}{r}\frac{\partial}{\partial r}(rv) = \frac{1}{r}(v + r\frac{\partial v}{\partial r})$. The aim is to write the pressure p and the particle velocity v as a function of the temperature T and find the differential equation that T solves similarly as in Section 2.2. To this aim Eq.(219a) can be rewritten in the same form as Eq.(121)

2D Pressure Equation in Fluid

$$p = \alpha_T B T - \frac{B}{i\omega}(\frac{1}{r}v + \frac{\partial v}{\partial r}). \tag{220}$$

Here the pressure p does not take the viscosity into account and so in order to have a continuity between different media (solid, fluid) we need to define $\tilde{p}$ the normal stress tensor in cylindrical coordinates. Using Eqs.(91) and (101) we have

2D Normal Stress Tensor in Fluid

$$\begin{aligned} \tilde{p} &= -\hat{T}_{11}, \\ &= -(\hat{T}_e)_{11} - (\hat{T}_V)_{11}, \\ &= p - 2\mu\frac{\partial v}{\partial r} - \lambda\frac{1}{r}\frac{\partial}{\partial r}(rv), \\ &= \alpha_T B T - \left(\frac{B}{i\omega} + \lambda\right)\frac{1}{r}\frac{\partial}{\partial r}(rv) - 2\mu\frac{\partial v}{\partial r}. \end{aligned} \tag{221}$$

By deriving Eq.(220)

$$\begin{aligned} \frac{\partial p}{\partial r} &= \alpha_T B\frac{\partial T}{\partial r} - \frac{B}{i\omega}\frac{\partial}{\partial r}(\frac{1}{r}v + \frac{\partial v}{\partial r}), \\ &= \alpha_T B\frac{\partial T}{\partial r} - \frac{B}{i\omega}(-\frac{1}{r^2}v + \frac{1}{r}\frac{\partial v}{\partial r} + \frac{\partial^2 v}{\partial r^2}), \end{aligned} \tag{222}$$

and injecting it in Eq.(219b) we now have

$$i\omega\rho_{0,f}v = -\alpha_T B\frac{\partial T}{\partial r} + (\lambda + 2\mu + \frac{B}{i\omega})\frac{\partial}{\partial r}(\frac{1}{r}\frac{\partial}{\partial r}(rv)). \tag{223}$$

The same way by injecting Eq.(220) in Eq.(219c) and using Eq.(125) we have

$$\begin{aligned}
&i\omega\rho_{0,f}C_p T - i\omega\alpha_T T_0(\alpha_T B T - \frac{B}{i\omega}(\frac{1}{r}v + \frac{\partial v}{\partial r})) = \kappa(\frac{1}{r}\frac{\partial T}{\partial r} + \frac{\partial^2 T}{\partial r^2}),\\
&i\omega(\rho_{0,f}C_p - \alpha_T^2 T_0 B)T + \alpha_T T_0 B(\frac{1}{r}v + \frac{\partial v}{\partial r}) = \kappa(\frac{1}{r}\frac{\partial T}{\partial r} + \frac{\partial^2 T}{\partial r^2}),\\
&\frac{1}{r}\frac{\partial}{\partial r}(rv) = \frac{\kappa}{\alpha_T T_0 B}(\frac{1}{r}\frac{\partial T}{\partial r} + \frac{\partial^2 T}{\partial r^2}) - \frac{i\omega\rho_{0,f}C_V}{\alpha_T B T_0}T.
\end{aligned} \tag{224}$$

2D Particle Velocity Equation in Fluid

By injecting Eq.(224) into Eq.(223) it allows us to write v as a function of T only

$$\begin{aligned}
i\omega\rho_{0,f}v =& -\alpha_T B\frac{\partial T}{\partial r} + (\lambda + 2\mu + \frac{B}{i\omega})\frac{\partial}{\partial r}\left[\frac{\kappa}{\alpha_T T_0 B}(\frac{1}{r}\frac{\partial T}{\partial r} + \frac{\partial^2 T}{\partial r^2}) - \frac{i\omega\rho_{0,f}C_V}{\alpha_T B T_0}T\right],\\
v =& -\frac{1}{i\omega\rho_{0,f}}\left[\alpha_T B + (\lambda + 2\mu + \frac{B}{i\omega})\frac{i\omega\rho_{0,f}C_V}{\alpha_T B T_0}\right]\frac{\partial T}{\partial r} +\\
&+ (\lambda + 2\mu + \frac{B}{i\omega})\frac{\kappa}{i\omega\rho_{0,f}\alpha_T T_0 B}\frac{\partial}{\partial r}(\frac{1}{r}\frac{\partial T}{\partial r} + \frac{\partial^2 T}{\partial r^2}).
\end{aligned} \tag{225}$$

To obtain a pure equation for T we apply $\frac{1}{r}\frac{\partial}{\partial r}(r*)$ to Eq.(223)

$$\begin{aligned}
&i\omega\rho_{0,f}\frac{1}{r}\frac{\partial}{\partial r}(rv) = -\alpha_T B\frac{1}{r}\frac{\partial}{\partial r}(r\frac{\partial T}{\partial r}) + (\lambda + 2\mu + \frac{B}{i\omega})\frac{1}{r}\frac{\partial}{\partial r}\left[r\frac{\partial}{\partial r}[\frac{1}{r}\frac{\partial}{\partial r}(rv)]\right],\\
&i\omega\rho_{0,f}\left[\frac{\kappa}{\alpha_T T_0 B}\frac{1}{r}\frac{\partial}{\partial r}(r\frac{\partial T}{\partial r}) - \frac{i\omega\rho_{0,f}C_V}{\alpha_T B T_0}T\right] = -\alpha_T B\frac{1}{r}\frac{\partial}{\partial r}(r\frac{\partial T}{\partial r}) +\\
&\quad + (\lambda + 2\mu + \frac{B}{i\omega})\frac{1}{r}\frac{\partial}{\partial r}\left[r\frac{\partial}{\partial r}\left[\frac{\kappa}{\alpha_T T_0 B}\frac{1}{r}\frac{\partial}{\partial r}(r\frac{\partial T}{\partial r}) - \frac{i\omega\rho_{0,f}C_V}{\alpha_T B T_0}T\right]\right],
\end{aligned}$$

using Eq.(224) and knowing that $\frac{1}{r}\frac{\partial}{\partial r}(r\frac{\partial T}{\partial r}) = \frac{1}{r}\frac{\partial T}{\partial r} + \frac{\partial^2 T}{\partial r^2}$. Using the notations

$$\begin{cases}
T^{ii} & = DT = \frac{1}{r}\frac{\partial}{\partial r}(r\frac{\partial T}{\partial r}),\\
T^{iv} = (T^{ii})^{ii} & = DDT = \frac{1}{r}\frac{\partial}{\partial r}\left[r\frac{\partial}{\partial r}[\frac{1}{r}\frac{\partial}{\partial r}(r\frac{\partial T}{\partial r})]\right],
\end{cases} \tag{226}$$

the fourth order differential equation of T can be written

$$(\lambda + 2\mu + \frac{B}{i\omega})\kappa T^{iv} - \left[(\lambda + 2\mu + \frac{B}{i\omega})i\omega\rho_{0,f}C_V + \alpha_T^2 B^2 T_0 + i\omega\rho\kappa\right]T^{ii} - \omega^2\rho^2 C_V T = 0, \tag{227}$$

which is similar to Eq.(130) with a different derivatives for T. Following the same though process and notations as for plane waves defined in Eq.(140), Eq.(227) can be written as

2D Temperature Variation Differential Equation in a Fluid

$$l_\kappa(l_V - i\frac{C_0}{\omega\gamma})T^{iv} - [1 + \frac{i\omega}{C_0}(l_\kappa + l_V)]T^{ii} - \frac{\omega^2}{C_0^2}T = 0. \tag{228}$$

The four solutions of the associated equation of Eq.(228) $a\theta^4 - b\theta^2 - c = 0$ are written of the form $\pm\theta_1$ and $\pm\theta_2$. The fourth order differential equation of Eq.(228) can so be written as

$$a(D + (i\theta_1)^2)(D + (i\theta_2)^2)T = 0, \tag{229}$$

with D defined as in Eq.(226), $b = a(\theta_1^2 + \theta_2^2)$ and $c = -a\theta_1^2\theta_2^2$. We define Ψ as

$$\Psi = [D + (i\theta_2)^2]T. \tag{230}$$

Leaving aside the factor a for readability, Eq.(229) becomes

$$\begin{aligned} [D + (i\theta_1)^2]\Psi &= 0, \\ \frac{1}{r}\frac{\partial\Psi}{\partial r} + \frac{\partial^2\Psi}{\partial r^2} + (i\theta_1)^2\Psi &= 0, \end{aligned} \tag{231}$$

whose solution is

$$\Psi = AH_0^{(1)}(i\theta_1 r) + BH_0^{(2)}(i\theta_1 r), \tag{232}$$

with A, B constants and $H_i^{(1/2)}$ being the cylindrical Hankel function of order i and first or second kind. The equation for T becomes

$$\begin{aligned} [D + (i\theta_2)^2]T &= AH_0^{(1)}(i\theta_1 r) + BH_0^{(2)}(i\theta_1 r), \\ \frac{1}{r}\frac{\partial}{\partial r}(r\frac{\partial T}{\partial r}) + (i\theta_2)^2 T &= AH_0^{(1)}(i\theta_1 r) + BH_0^{(2)}(i\theta_1 r). \end{aligned} \tag{233}$$

This non homogeneous differential equation gives the general solution of the temperature variation as

$$T(r) = CH_0^{(1)}(i\theta_2 r) + DH_0^{(2)}(i\theta_2 r) + ps, \tag{234}$$

with *ps* being a particular solution of Eq.(233) and C, D constants. In order to find the final solution of T, the particular solution of Eq.(233) is gonna be determined by finding separate solution for $AH_0^{(1)}(i\theta_1 r)$ and $BH_0^{(2)}(i\theta_1 r)$ which then are going to be added to form the final particular solution.

- Case 1: $\frac{1}{r}\frac{\partial}{\partial r}(r\frac{\partial T_1}{\partial r}) + (i\theta_2)^2 T_1 = AH_0^{(1)}(i\theta_1 r)$.

We are looking for a particular solution of the form

$$T_1(r) = a(r)H_0^{(1)}(i\theta_2 r) + b(r)H_0^{(2)}(i\theta_2 r). \tag{235}$$

The system of equation for a second order inhomogeneous equation of this kind leads to a system of equation of the form (see Appendix A.6 for more details)

$$\begin{cases} \frac{da}{dr}H_0^{(1)}(i\theta_2 r) + \frac{db}{dr}H_0^{(2)}(i\theta_2 r) = 0, \\ \frac{da}{dr}\frac{d}{dr}H_0^{(1)}(i\theta_2 r) + \frac{db}{dr}\frac{d}{dr}H_0^{(2)}(i\theta_2 r) = AH_0^{(1)}(i\theta_1 r). \end{cases} \tag{236}$$

Based on equation 10.6.3 of NIST Handbook of Mathematical Functions [145]

$$\frac{d}{dr}H_0^{(1,2)}(i\theta_2 r) = -i\theta_2 H_1^{(1,2)}(i\theta_2 r). \tag{237}$$

Eq.(236) can be rewritten in matrix form as

$$\begin{bmatrix} H_0^{(1)}(i\theta_2 r) & H_0^{(2)}(i\theta_2 r) \\ H_1^{(1)}(i\theta_2 r) & H_1^{(2)}(i\theta_2 r) \end{bmatrix} \begin{bmatrix} \frac{da}{dr} \\ \frac{db}{dr} \end{bmatrix} = \begin{bmatrix} 0 \\ -\frac{A}{i\theta_2}H_0^{(1)}(i\theta_1 r) \end{bmatrix}. \tag{238}$$

Knowing that the inverse of a Matrix can be written as $A^{-1} = \frac{com(A)^\dagger}{det(A)}$ and using the recurrence relation 10.5.5 in NIST [145]

$$H_{\nu+1}^{(1)}(z)H_\nu^{(2)}(z) - H_\nu^{(1)}(z)H_{\nu+1}^{(2)}(z) = -\frac{4i}{\pi z}, \tag{239}$$

we found the solution

$$\begin{bmatrix} \frac{da}{dr} \\ \frac{db}{dr} \end{bmatrix} = -\frac{\pi r}{4i} \begin{bmatrix} H_1^{(2)}(i\theta_2 r) & -H_0^{(2)}(i\theta_2 r) \\ -H_1^{(1)}(i\theta_2 r) & H_0^{(1)}(i\theta_2 r) \end{bmatrix} \begin{bmatrix} 0 \\ -\frac{A}{i\theta_2}H_0^{(1)}(i\theta_1 r) \end{bmatrix}. \tag{240}$$

Lastly equation 10.22.4 in NIST [145] states that

$$\int C_\nu(gz)D_\nu(hz)dz = \frac{z[gC_{\nu+1}(gz)D_\nu(hz) - hC_\nu(gz)D_{\nu+1}(hz)]}{g^2 - h^2}, \tag{241}$$

with C_ν and D_ν being any cylinder function of order ν not necessarily distinct, and g, h being constants. This leads to

$$\begin{cases} a = \frac{A\pi}{4i}\frac{r}{(i\theta_1)^2-(i\theta_2)^2}\left[i\theta_1 H_1^{(1)}(i\theta_1 r)H_0^{(2)}(i\theta_2 r) - i\theta_2 H_0^{(1)}(i\theta_1 r)H_1^{(2)}(i\theta_2 r)\right], \\ b = \frac{A\pi}{4i}\frac{r}{(i\theta_1)^2-(i\theta_2)^2}\left[i\theta_2 H_1^{(1)}(i\theta_2 r)H_0^{(1)}(i\theta_1 r) - i\theta_1 H_0^{(1)}(i\theta_2 r)H_1^{(1)}(i\theta_1 r)\right]. \end{cases} \tag{242}$$

Using Eq.(235) and the Wronskian relation of Eq.(239) we have the first particular solution T_1

$$T_1 = \frac{A}{\theta_1^2 - \theta_2^2} H_0^{(1)}(i\theta_1 r) = \tilde{A} H_0^{(1)}(i\theta_1 r). \tag{243}$$

We now investigate the second part of the particular solution.

- Case 2: $\frac{1}{r}\frac{\partial}{\partial r}(r\frac{\partial T_2}{\partial r}) + (i\theta_2)^2 T_2 = B H_0^{(2)}(i\theta_1 r)$.

We are looking for a particular solution of the form

$$T_2(r) = a(r) H_0^{(1)}(i\theta_2 r) + b(r) H_0^{(2)}(i\theta_2 r). \tag{244}$$

Beside the change of the constant A to B and the fact that we are now looking for a second kind Hankel function, since the integration of Eq.(241) works for any cylindrical function, the same though process as above can be use. We then have

$$T_2 = \frac{B}{\theta_1^2 - \theta_2^2} H_0^{(2)}(i\theta_1 r) = \tilde{B} H_0^{(2)}(i\theta_1 r). \tag{245}$$

In this section the system of conservation equation was rewritten in cylindrical coordinates in Eqs.(219). The pressure and the normal stress tensor were written in Eqs.(220) and (221) respectively. The particle velocity equation was deduced in Eq.(225) and the 4_{th} order differential equation for T was written in Eqs.(227) and (228) using the notation of Eq.(140). The associated solutions of the differential equation are the same as in Section 2.2.1 Eq.(155). A final solution of Eq.(227) for T are eventually found as

2D Temperature Variation

$$T(r) = \tilde{A} H_0^{(1)}(i\theta_{ac,f} r) + \tilde{B} H_0^{(2)}(i\theta_{ac,f} r) + C H_0^{(1)}(i\theta_{th,f} r) + D H_0^{(2)}(i\theta_{th,f} r), \tag{246}$$

with

$$\tilde{A} = \frac{A}{\theta_{ac,f}^2 - \theta_{th,f}^2}, \tag{247}$$

$$\tilde{B} = \frac{B}{\theta_{ac,f}^2 - \theta_{th,f}^2}. \tag{248}$$

2.3.2 *Cylindrical Waves in a Solid*

The cylindrical geometry will now be investigated for a solid medium. Based on Eqs.118 and using Appendix A.5, the constitutive equations in a solid become

$$\begin{cases} \rho_{0,s} C_{V,s} i\omega T = \kappa_s \frac{1}{r}\frac{\partial}{\partial r}(r\frac{\partial T}{\partial r}) - \alpha_{T,s} B_0 T_0 \frac{1}{r}\frac{\partial}{\partial r}(rv) + Q_0, \\ \rho_{0,s} i\omega v = \left(\frac{\lambda_0+2\mu_0}{i\omega} + \lambda_s + 2\mu_s\right)\frac{\partial}{\partial r}\left(\frac{1}{r}\frac{\partial}{\partial r}(rv)\right) - \alpha_{T,s} B_0 \frac{\partial T}{\partial r}, \end{cases} \tag{249}$$

with $\frac{\partial}{\partial t} = i\omega$, Q_0 (the heat density energy supplied) uniform, $\vec{b} = 0$ and knowing that $\frac{\partial u}{\partial t} = v$. When injecting $\frac{1}{r}\frac{\partial}{\partial r}(rv)$ of Eq.(249a) into Eq.(249b), v can be written as a function of T alone as

2D Particle Velocity Equation in Solid

$$\begin{aligned} v = \frac{1}{i\omega\rho_{0,s}}\Bigg[\frac{1}{\alpha_{T,s}B_0T_0}\left(\frac{\lambda_0+2\mu_0}{i\omega}+\lambda_s+2\mu_s\right)\Bigg(-\rho_{0,s}C_{V,s}i\omega\frac{\partial T}{\partial r}+ \\ + \kappa_s\frac{\partial}{\partial r}\left(\frac{1}{r}\frac{\partial}{\partial r}\left(r\frac{\partial T}{\partial r}\right)\right)\Bigg) - \alpha_{T,s}B_0\frac{\partial T}{\partial r}\Bigg], \end{aligned} \tag{250}$$

$$\begin{aligned} = \frac{-1}{i\omega\rho_{0,s}}\left[\frac{C_{V,s}i\omega\rho_{0,s}}{\alpha_{T,s}B_0T_0}\left(\frac{\lambda_0+2\mu_0}{i\omega}+\lambda_s+2\mu_s\right)+\alpha_{T,s}B_0\right]\frac{\partial T}{\partial r}+ \\ + \frac{\kappa_s}{i\omega\rho_{0,s}\alpha_{T,s}B_0T_0}\left(\frac{\lambda_0+2\mu_0}{i\omega}+\lambda_s+2\mu_s\right)\frac{\partial}{\partial r}\left(\frac{1}{r}\frac{\partial}{\partial r}\left(r\frac{\partial T}{\partial r}\right)\right). \end{aligned} \tag{251}$$

By multiplying Eq.(251) by $\frac{1}{r}\frac{\partial}{\partial r}(r*)$ and using again Eq.(249a)

$$\begin{aligned} \rho_{0,s}i\omega\frac{1}{r}\frac{\partial}{\partial r}(rv) = \Bigg[\frac{1}{\alpha_{T,s}B_0T_0}\left(\frac{\lambda_0+2\mu_0}{i\omega}+\lambda_s+2\mu_s\right) \\ \left(-\rho C_{V,s}i\omega\frac{1}{r}\frac{\partial}{\partial r}\left(r\frac{\partial T}{\partial r}\right)+\kappa_s\frac{1}{r}\frac{\partial}{\partial r}\left(r\frac{\partial}{\partial r}\left(\frac{1}{r}\frac{\partial}{\partial r}\left(r\frac{\partial T}{\partial r}\right)\right)\right)\right)\Bigg] \\ - \alpha_{T,s}B_0\frac{1}{r}\frac{\partial}{\partial r}\left(r\frac{\partial T}{\partial r}\right), \end{aligned} \tag{252}$$

$$= \frac{\rho_{0,s}i\omega}{\alpha_{T,s}B_0T_0}\left[-\rho_{0,s}C_{V,s}i\omega T + \kappa_s\frac{1}{r}\frac{\partial}{\partial r}\left(r\frac{\partial T}{\partial r}\right)+Q_0\right], \tag{253}$$

2D Temperature Variation Differential Equation in a Solid

a differential equation for T is found

$$\begin{aligned} &(\lambda_s+2\mu_s+\frac{\lambda_0+2\mu_0}{i\omega})\kappa_s T^{iv}+ \\ &-\left[(\lambda_s+2\mu_s+\frac{\lambda_0+2\mu_0}{i\omega})i\omega\rho_{0,s}C_{V,s}+\alpha_{T,s}^2B_0^2T_0+i\omega\rho_{0,s}\kappa_s\right]T^{ii}+ \\ &-\omega^2\rho_{0,s}^2C_{V,s}T = \rho_{0,s}i\omega Q_0, \end{aligned} \tag{254}$$

using the notation introduced in Eq.(226). Beside the supplied input power Q_0, Eq.(254) is similar to Eq.(227) for fluid with only B changed

to $\lambda_0 + 2\mu_0$ for the solid. Henceforth, even if the solutions θ of the associated differential equation will be different between fluid and solid, all the thought process associated to finding T in Eq.(246) is still valid for a solid. Finally, in order to add the supplied energy to the final equation of T, using the hypothesis that the solid can not be deformed and Eq.(178), T is written

2D Temperature Variations

$$T(r) = \tilde{A}H_0^{(1)}(i\theta_{ac,s}r) + \tilde{B}H_0^{(2)}(i\theta_{ac,s}r) + CH_0^{(1)}(i\theta_{th,s}r) + DH_0^{(2)}(i\theta_{th,s}r) + T_{Q_0}. \tag{255}$$

We are now investigating the pressure in the solid case. By definition a force $d\vec{f}$ applied on a surface dS, the pressure can be written using the stress tensor $\hat{T}$ as $d\vec{f} = \hat{T}\vec{n}dS$. By definition, the pressure p is $dF = -pdS$. This leads to

$$p = -\hat{T}_e\vec{n}.\vec{n} = -T_{e_{ij}}\frac{X_iX_j}{r^2}, \tag{256}$$

with $\vec{n} = \frac{\vec{X}}{r}$ and X_i the coordinates of $\vec{r}$ in cartesian coordinates. It is important to note that a plane strain hypothesis has been used in Eq.(256). This means that the stress is acting perpendicularly to the length of the cylinder leading to $X_3 = 0$ and $\frac{\partial}{\partial X_3} = 0$. Using Eq.(109), $\hat{\epsilon}$ the infinitesimal stress tensor as defined in Eq.(81) and, as defined for $\vec{v}$ in Eq.(217), $\vec{u} = \frac{\vec{r}}{r}u(r)$, the elastic tensor can be written

$$\hat{T}_e = \begin{bmatrix} 2\mu_0\frac{\partial u_1}{\partial X_1} + \lambda_0\epsilon_{kk} - \alpha_{T,s}B_0T & \mu_0\left(\frac{\partial u_1}{\partial X_2} + \frac{\partial u_2}{\partial X_1}\right) & 0 \\ \mu_0\left(\frac{\partial u_1}{\partial X_2} + \frac{\partial u_2}{\partial X_1}\right) & 2\mu_0\frac{\partial u_2}{\partial X_2} + \lambda_0\epsilon_{kk} - \alpha_{T,s}B_0T & 0 \\ 0 & 0 & -\alpha_{T,s}B_0T \end{bmatrix}. \tag{257}$$

The partial derivative of u are

$$\frac{\partial u_i}{\partial X_j} = \frac{X_iX_j}{r^2}\frac{\partial u}{\partial r} + \frac{r^2\delta_{ij} - X_iX_j}{r^3}u, \tag{258}$$

and so

$$\begin{aligned}\hat{T}_{eij}\frac{X_iX_j}{r^2} =& \frac{2\mu_0}{r^2}\left(\frac{(X_iX_j)^2}{r^2}\frac{\partial u}{\partial r} - \frac{(r^2\delta_{ij} - X_iX_j)X_iX_j}{r^3}u\right) + \\ &+ (\lambda_0\epsilon_{kk} - \alpha_{T,s}B_0T)\frac{X_iX_j\delta_{ij}}{r^2},\end{aligned} \tag{259}$$

with $\epsilon_{kk} = tr(\hat{\epsilon}) = \frac{1}{r}u + \frac{\partial u}{\partial r}$. This leads to

2D Pressure Equation in Solid

$$p = \alpha_{T,s}B_0T - \frac{2\mu_0}{i\omega}\frac{\partial v}{\partial r} - \frac{\lambda_0}{i\omega}\frac{1}{r}\frac{\partial}{\partial r}(rv). \tag{260}$$

2D Normal Stress Tensor Equation in Solid

Here the pressure p is only defined with the elastic stress tensor and so in order to have a stress continuity between different media (solid, fluid) we need to define $\tilde{p}$ as (using Eqs.(91) and (101))

$$\begin{aligned}\tilde{p} &= -\hat{T}\vec{n}.\vec{n},\\ &= -(\hat{T}_e)\vec{n}.\vec{n} - (\hat{T}_V)\vec{n}.\vec{n},\\ &= p - 2\mu_s\frac{\partial v}{\partial r} - \lambda_s\frac{1}{r}\frac{\partial}{\partial r}(rv),\\ &= \alpha_{T,s}B_0T - \left[2(\frac{\mu_0}{i\omega}+\mu_s)\frac{\partial v}{\partial r} + (\frac{\lambda_0}{i\omega}+\lambda_s)\frac{1}{r}\frac{\partial}{\partial r}(rv)\right].\end{aligned} \tag{261}$$

In order to explicit the differences in wavenumbers between solid and liquid media, a first order approximation solution of Eq.(254) will be determined for the associated homogeneous fourth order differential equation of T. This was not done in Section 2.2.2 since it was decided to rewrite the system in term of transverse and longitudinal wave speed in order to draw an easier comparison. Eq.(254) becomes

$$\begin{aligned}0 =&(\lambda_s + 2\mu_s + \frac{\lambda_0+2\mu_0}{i\omega})\kappa_s\theta^4 +\\ &-\left[(\lambda_s+2\mu_s+\frac{\lambda_0+2\mu_0}{i\omega})i\omega\rho_{0,s}C_{V,s} + \alpha_{T,s}^2B_0^2T_0 + i\omega\rho_{0,s}\kappa_s\right]\theta^2 +\\ &-\omega^2\rho_{0,s}^2C_{V,s}.\end{aligned} \tag{262}$$

It will be seen that this equation is also the one associated to spherical wave radiation following Eq.(314) in the following Section 2.4.2. Using similar notations as in Eq.(140) we define

$$\begin{cases}\gamma_s = \frac{C_{p,s}}{C_{V,s}},\\ C_{0,s} = \sqrt{\frac{B_0}{\rho_{0,s}}\gamma_s}, & [m/s]\\ C_L = \frac{\lambda_0+2\mu_0}{\rho_{0,s}C_{0,s}}, & [m/s]\\ l_{\kappa,s} = \frac{C_{0,s}\kappa}{B_0C_{p,s}}, & [m]\\ l_{V,s} = \frac{\lambda_s+2\mu_s}{\rho C_{0,s}}, & [m].\end{cases} \tag{263}$$

Following the same thought process as for Eq.(139), Eq.(262) can be written

$$\left(l_{\kappa,s}l_{V,s} + l_{\kappa,s}\frac{C_L}{i\omega}\right)\theta^4 - \left[\frac{i\omega}{C_{0,s}}(l_{V,s}+l_{\kappa,s}+\frac{C_L}{i\omega}) + 1 - \frac{1}{\gamma_s}\right]\theta^2 - \frac{\omega^2}{C_{0,s}^2} = 0. \tag{264}$$

The general form of the asymptotic solutions for the equations of the form $a\theta^4 + b\theta^2 + c = 0$ has been proven to be

$$\begin{cases} \theta_{ac,s} = \pm\sqrt{-\frac{c}{b}}\left(1 + \frac{1}{2}\frac{ac}{b^2}\right), \\ \theta_{th,s} = \pm\sqrt{-\frac{b}{a}}\left(1 - \frac{1}{2}\frac{ac}{b^2}\right), \end{cases} \tag{265}$$

as in Eq.(146) with now

$$\begin{cases} a = l_{\kappa,s}\frac{C_L}{i\omega}(1 + l_{V,s}\frac{i\omega}{C_L}), \\ b = -(1 - \frac{1}{\gamma_s} + \frac{C_L}{C_{0,s}})\left(1 + \frac{i\omega}{C_{0,s}}(l_{\kappa,s} + l_{V,s})(1 - \frac{1}{\gamma_s} + \frac{C_L}{C_{0,s}})^{-1}\right), \\ c = -\frac{\omega^2}{C_{0,s}^2}. \end{cases} \tag{266}$$

Using Eq.(266), Eq.(265), the first order Taylor's series approximation and a first order approximation on $l_{\kappa,s}$ and $l_{V,s}$ (weak conduction and weak viscosity)

$$\begin{cases} 1 \pm \frac{ac}{b^2} = & 1 \pm \frac{1}{2}l_{\kappa,s}\frac{C_L}{i\omega}\frac{-\omega^2}{C_{0,s}^2}(1 - \frac{1}{\gamma_s} + \frac{C_L}{C_{0,s}})^{-2}, \\ \sqrt{\frac{-c}{b}} = & \frac{i\omega}{C_{0,s}}(1 - \frac{1}{\gamma_s} + \frac{C_L}{C_{0,s}})^{-1/2}\left(1 + \frac{i\omega}{C_{0,s}}(l_{\kappa,s} + l_{V,s})(1 - \frac{1}{\gamma_s} + \frac{C_L}{C_{0,s}})^{-1/2}\right), \\ \sqrt{\frac{-b}{a}} = & (\frac{i\omega}{l_{\kappa,s}C_L})^{1/2}(1 - \frac{1}{2}\frac{i\omega}{C_L}l_{V,s}) \\ & (1 - \frac{1}{\gamma_s} + \frac{C_L}{C_{0,s}})^{1/2}(1 + \frac{1}{2}\frac{i\omega}{C_{0,s}}(l_{\kappa,s} + l_{V,s})(1 - \frac{1}{\gamma_s} + \frac{C_L}{C_{0,s}})^{-1}). \end{cases} \tag{267}$$

This leads to

$$\begin{cases} \theta_{ac,s} = & \frac{i\omega}{C_{0,s}}(1 - \frac{1}{\gamma_s} + \frac{C_L}{C_{0,s}})^{-1/2}\left[1 - l_{V,s}\frac{i\omega}{2C_{0,s}}(1 - \frac{1}{\gamma_s} + \frac{C_L}{C_{0,s}})^{-1} + \right. \\ & \left. - l_{\kappa,s}\frac{i\omega}{2C_{0,s}}\left((1 - \frac{1}{\gamma_s} + \frac{C_L}{C_{0,s}})^{-1} - \frac{C_L}{C_{0,s}}(1 - \frac{1}{\gamma_s} + \frac{C_L}{C_{0,s}})^{-2}\right)\right], \\ \theta_{th,s} = & (\frac{i\omega}{l_{\kappa,s}C_L})^{1/2}(1 - \frac{1}{\gamma_s} + \frac{C_L}{C_{0,s}})^{1/2}\left[1 + \frac{i\omega}{2C_{0,s}}\left[l_{\kappa,s}\left[(1 - \frac{1}{\gamma_s} + \frac{C_L}{C_{0,s}})^{-1} + \right.\right.\right. \\ & \left.\left.\left. - (1 - \frac{1}{\gamma_s} + \frac{C_L}{C_{0,s}})^{-2}\frac{C_L}{C_{0,s}}\right] + l_{V,s}\left[(1 - \frac{1}{\gamma_s} + \frac{C_L}{C_{0,s}})^{-1} - \frac{C_{0,s}}{C_L}\right]\right]\right]. \end{cases} \tag{268}$$

Eqs.(268) are consistent with Eq.(148) and Eq.(151) if C_L is replaced by $\frac{C_{0,s}}{\gamma_s}$. This similitude is coming from the calculation of the coefficient of θ^2 in both cases. Furthermore, since the associated homogeneous fourth order differential equation for T is the same in a fluid (Eq.(227)) and a solid (Eq.(254), by changing B to $\lambda_0 + 2\mu_0$, Eqs.(268) are also valid in a fluid with the appropriate parameters changes.

In this section, the system of equations of Eq.(249) for a solid in a cylindrical coordinate system is solved. The velocity equation is found

in Eq.(251) and the differential equation associated to T is found in Eq.(254). The pressure and the normal stress tensor are then defined in Eqs.(260) and (261) respectively.

Due to the similarity of the differential equation for T in a fluid and in a solid, the temperature variation is written similarly as in the fluid in Eq.(255). The differences are found in the wavenumbers θ_{ac} and θ_{th} in the two kind of media. Using the parameters defined in Eq.(263), a first order approximation for weak thermal conduction and weak viscosity in a solid is found in Eqs.(268). From this form, by changing $\lambda_0 + 2\mu_0$ to the Bulk modulus in a fluid, Eqs.(155) for plane wave in a fluid are found again which gives coherence between the models having similar associated differential equations.

2.3.3 *Ideal Cylindrical Thermophone*

Having solved the equations for cylindrical radiations in both fluid and solid we will now try to investigate what we call an ideal cylindrical thermophone. In this case the solid part of the thermophone is not considered yet and is represented as an ideal boundary with the propagating medium at which there is a gradient of temperature. This easily implementable model will used as a reference and first step for the understanding of the multilayer model.

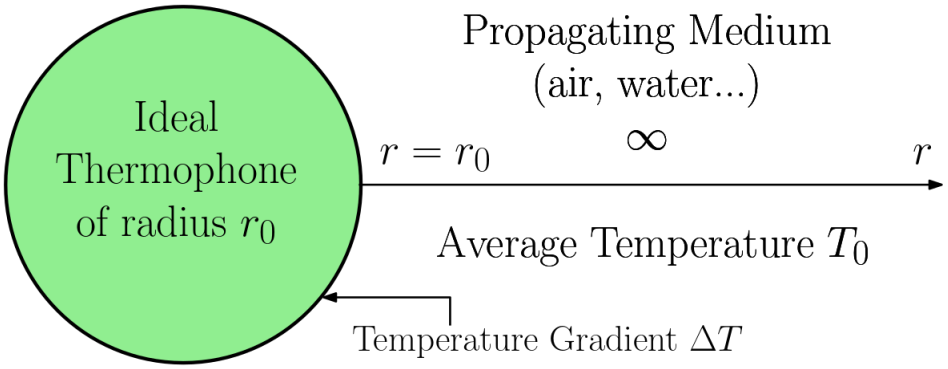

Figure 26: Schematic of the perfect thermophone model 2D

A simple cylindrical model is seen in Fig.26. Only progressive waves in the r direction of the xy plane is considered. Using Eq.(246), the temperature variation T in the medium can be written in the form

$$T(r) = AH_0^{(2)}(i\theta_{ac}r) + BH_0^{(2)}(i\theta_{th}r), \tag{269}$$

with A and B constants. No subscripts are used here since, even though the propagating medium is most likely a fluid (air for instance), those

equations are still valid for solid propagation. The first order approximation solutions for θ_{ac} and θ_{th} were calculated in Eqs.(268) in a solid and in were proven to be the same as Eqs.(155) in a fluid. From the temperature variations, the particle velocity and the pressure can be inferred using Eqs.(225) and (220) respectively. We write L_1 and L_2 the coefficients of Eq.(225) so that $v = L_1\frac{\partial T}{\partial r} + L_2\frac{\partial}{\partial r}(\frac{1}{r}\frac{\partial T}{\partial r} + \frac{\partial^2 T}{\partial r^2})$ (like in Eqs.(183) and (184)). In order to rewrite v and p as function of Hankel function we use equations 10.6.2 and 10.6.1 of NIST [145] being respectively

$$C'_\nu(z) = z'(-C_{\nu+1}(z) + \frac{\nu}{z}C_\nu(z)), \tag{270}$$

$$C'_\nu(z) = z'(C_{\nu-1}(z) - \frac{\nu}{z}C_\nu(z)), \tag{271}$$

$$C_{\nu-1}(z) + C_{\nu+1}(z) = \frac{2\nu}{z}C_\nu(z), \tag{272}$$

with C_ν any cylindrical function of order ν. This leads to

$$T' = -iA\theta_{ac}H_1^{(2)}(i\theta_{ac}r) - iB\theta_{th}H_1^{(2)}(i\theta_{th}r), \tag{273}$$

$$\begin{aligned} T'' = &-A\theta_{ac}^2H_2^{(2)}(i\theta_{ac}r) - B\theta_{th}^2H_2^{(2)}(i\theta_{th}r) + \\ &- iA\theta_{ac}\frac{1}{r}H_1^{(2)}(i\theta_{ac}r) - iB\theta_{th}\frac{1}{r}H_1^{(2)}(i\theta_{th}r). \end{aligned} \tag{274}$$

Using Eqs.(273) and (274) along with Eq.(272) we found that

$$\frac{1}{r}T' + T'' = A\theta_{ac}^2H_0^{(2)}(i\theta_{ac}r) + B\theta_{th}^2H_0^{(2)}(i\theta_{th}r), \tag{275}$$

and so with Eq.(270)

$$\frac{\partial}{\partial r}(\frac{1}{r}T' + T'') = -Ai\theta_{ac}^3H_1^{(2)}(i\theta_{ac}r) - Bi\theta_{th}^3H_1^{(2)}(i\theta_{th}r). \tag{276}$$

We now inject Eq.(276) in Eq.(225) to have the final system

Analytical Cylindrical Equation for T and v

$$T(r) = AH_0^{(2)}(i\theta_{ac}r) + BH_0^{(2)}(i\theta_{th}r), \tag{277}$$

$$v(r) = -iA\theta_{ac}\left[L_1 + L_2\theta_{ac}^2\right]H_1^{(2)}(i\theta_{ac}r) - iB\theta_{th}\left[L_1 + L_2\theta_{th}^2\right]H_1^{(2)}(i\theta_{th}r). \tag{278}$$

Assuming that the gradient of temperature between the medium and the thermophone is ΔT and that the thermophone is rigid we have two boundary conditions

$$\begin{cases} T(r = r_0) = \Delta T, \\ v(r = r_0) = 0, \end{cases} \tag{279}$$

with $r = r_0$ being the radius of the cylindrical thermophone (the limit with the propagating medium). Using the boundary conditions along with the system of Eq.(277) and (278) we found the constants

$$\begin{cases} A = -\Delta T \left[\frac{\theta_{th}(L_1+L_2\theta_{th}^2)H_1^{(2)}(i\theta_{th}r_0)}{\theta_{ac}(L_1+L_2\theta_{ac}^2)H_1^{(2)}(i\theta_{ac}r_0)H_0^{(2)}(i\theta_{th}r_0)-\theta_{th}(L_1+L_2\theta_{th}^2)H_1^{(2)}(i\theta_{th}r_0)H_0^{(2)}(i\theta_{ac}r_0)} \right], \\ B = \Delta T \left[\frac{\theta_{ac}(L_1+L_2\theta_{ac}^2)H_1^{(2)}(i\theta_{ac}r_0)}{\theta_{ac}(L_1+L_2\theta_{ac}^2)H_1^{(2)}(i\theta_{ac}r_0)H_0^{(2)}(i\theta_{th}r_0)-\theta_{th}(L_1+L_2\theta_{th}^2)H_1^{(2)}(i\theta_{th}r_0)H_0^{(2)}(i\theta_{ac}r_0)} \right]. \end{cases} \tag{280}$$

Following Eq.(220), the pressure p is the last parameter to be determined explicitly in this ideal case. First v needs to be derived using Eq.(278) and Eq.(271)

$$\begin{aligned} v' = &- iA\theta_{ac}(L_1 + L_2\theta_{ac}^2)\left[i\theta_{ac}H_0^{(2)}(i\theta_{ac}r) - \frac{i\theta_{ac}}{i\theta_{ac}r}H_1^{(2)}(i\theta_{ac}r) \right] + \\ &- iB\theta_{th}(L_1 + L_2\theta_{th}^2)\left[i\theta_{th}H_0^{(2)}(i\theta_{th}r) - \frac{i\theta_{th}}{i\theta_{th}r}H_1^{(2)}(i\theta_{th}r) \right], \end{aligned} \tag{281}$$

leading to

$$\frac{1}{r}v + v' = A\theta_{ac}^2(L_1 + L_2\theta_{ac}^2)H_0^{(2)}(i\theta_{ac}r) + B\theta_{th}^2(L_1 + L_2\theta_{th}^2)H_0^{(2)}(i\theta_{th}r). \tag{282}$$

Analytical Cylindrical Equation for p and $\tilde{p}$

Finally going back to Eq.(220), the final explicit form of p in this ideal cylindrical case is

$$\begin{aligned} p = \; & A\left[\alpha_T B - \theta_{ac}^2\frac{B}{i\omega}(L_1 + L_2\theta_{ac}^2) \right] H_0^{(2)}(i\theta_{ac}r) + \\ & + B\left[\alpha_T B - \theta_{th}^2\frac{B}{i\omega}(L_1 + L_2\theta_{th}^2) \right] H_0^{(2)}(i\theta_{th}r). \end{aligned} \tag{283}$$

If $\tilde{p}$, the normal stress tensor, is investigated, following Eq.(221) it can be written

$$\begin{aligned} \tilde{p} = \; & A\left[\left[\alpha_T B - \theta_{ac}^2\left(\frac{B}{i\omega} + \lambda + 2\mu\right)(L_1 + L_2\theta_{ac}^2) \right] H_0^{(2)}(i\theta_{ac}r) + \right. \\ & \left. -2\mu\frac{i\theta_{ac}}{r}(L_1 + L_2\theta_{ac}^2)H_1^{(2)}(i\theta_{ac}r) \right] + \\ & + B\left[\left[\alpha_T B - \theta_{th}^2\left(\frac{B}{i\omega} + \lambda + 2\mu\right)(L_1 + L_2\theta_{th}^2) \right] H_0^{(2)}(i\theta_{th}r) + \right. \\ & \left. -2\mu\frac{i\theta_{th}}{r}(L_1 + L_2\theta_{th}^2)H_1^{(2)}(i\theta_{th}r) \right]. \end{aligned} \tag{284}$$

We have here investigated the radiation of an ideal cylindrical thermophone. We first derived Eq.(246) in order to find explicit analytical equations for the particle velocity (Eq.(278)) and eventually the pressure (Eq.(283)) and the normal stress tensor as well (Eq.(284)). Assuming that that the propagating medium is semi infinite, only progressive waves are considered. Using the boundary conditions in Eq.(279), the two constant parameters associated to the progressive waves are determined in Eqs.(280). Variables T, v, p and $\tilde{p}$ are then fully determined.

2.3.4 *Transfer Matrix with N Layers*

The thought process associated to the explicit resolution of a perfect cylindrical thermophone with a single propagating layer is now extended to a multilayer model for cylindrical thermophones. As seen in Fig.27, N layers of concentric cylinders are investigated. The layer at the extremity (layer N) is supposed to be semi infinite, and each layer $j \in [1, N-1]$ potentially has a volumetric input source $Q_{0,j}$ ($Q_{0,N} = 0$). The thickness of each "tube" layer j is $r_j - r_{j-1}$ with r_j the external radius of the j_{th} concentric layer. The type of material of each layer (fluid or solid) is not specified since the material differences are taken into account in the inherent parameters of their defining matrix.

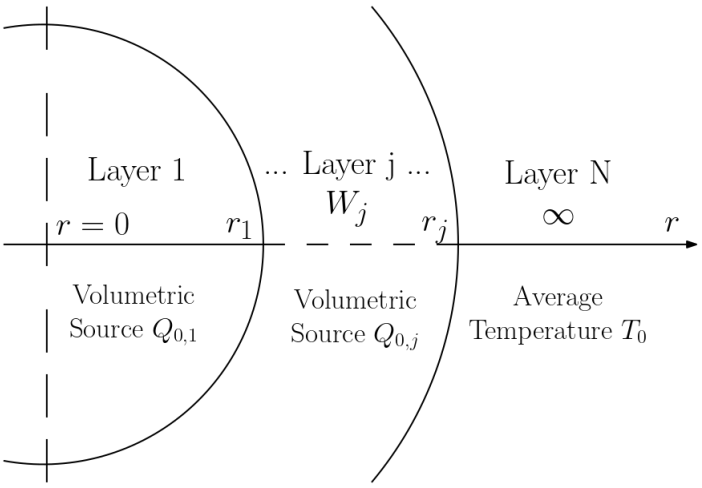

Figure 27: Schematic of a generalized version of the thermophone model with N layers in 2D

Similarly as in Section 2.2.4, first we define heat flux as

$$\vec{q} = -\kappa\vec{\nabla}T = -\kappa\frac{\vec{r}}{r}\frac{\partial T}{\partial r}. \tag{285}$$

We also define T_{Q_0} as Eq.(178) and $\mathcal{F}$ and $\mathcal{G}$ pair as

$$\mathcal{F}(\eta) = \alpha_T B - \left(\frac{B}{i\omega} + \lambda + 2\mu\right)(L_1\eta^2 + L_2\eta^4), \tag{195}$$

$$\mathcal{G}(\eta) = L_1 + L_2\eta^2. \tag{196}$$

Considering that all derivative and recurrence properties used in Section 2.3.3 are valid for all cylindrical Bessel and Hankel functions, the general form of the parameters $\tilde{p}, \nu, q, T$ in a fluid can be found to be

$$\begin{cases} \tilde{p}(r) = & A\left[\mathcal{F}(\theta_{ac})H_0^{(1)}(i\theta_{ac}r) - 2\mu i\frac{\theta_{ac}}{r}\mathcal{G}(\theta_{ac})H_1^{(1)}(i\theta_{ac}r)\right] + \\ & B\left[\mathcal{F}(\theta_{ac})H_0^{(2)}(i\theta_{ac}r) - 2\mu i\frac{\theta_{ac}}{r}\mathcal{G}(\theta_{ac})H_1^{(2)}(i\theta_{ac}r)\right] + \\ & C\left[\mathcal{F}(\theta_{th})H_0^{(1)}(i\theta_{th}r) - 2\mu i\frac{\theta_{th}}{r}\mathcal{G}(\theta_{th})H_1^{(1)}(i\theta_{th}r)\right] + \\ & D\left[\mathcal{F}(\theta_{th})H_0^{(2)}(i\theta_{th}r) - 2\mu i\frac{\theta_{th}}{r}\mathcal{G}(\theta_{th})H_1^{(2)}(i\theta_{th}r)\right] + \alpha_T B T_{Q_0}, \\ \nu(r) = & -Ai\theta_{ac}\mathcal{G}(\theta_{ac})H_1^{(1)}(i\theta_{ac}r) - Bi\theta_{ac}\mathcal{G}(\theta_{ac})H_1^{(2)}(i\theta_{ac}r) + \\ & -Ci\theta_{th}\mathcal{G}(\theta_{th})H_1^{(1)}(i\theta_{th}r) - Di\theta_{th}\mathcal{G}(\theta_{th})H_1^{(2)}(i\theta_{th,f}r), \\ q(r) = & Ai\theta_{ac}\kappa H_1^{(1)}(i\theta_{ac}r) + Bi\theta_{ac}\kappa H_1^{(2)}(i\theta_{ac}r) + \\ & Ci\theta_{th}\kappa H_1^{(1)}(i\theta_{th}r) + Di\theta_{th}\kappa H_1^{(2)}(i\theta_{th}r), \\ T(r) = & AH_0^{(1)}(i\theta_{ac}r) + BH_0^{(2)}(i\theta_{ac}r) + \\ & CH_0^{(1)}(i\theta_{th}r) + DH_0^{(2)}(i\theta_{th}r) + T_{Q_0}. \end{cases} \tag{286}$$

Those equations also apply for a solid with Eqs.(261), (251) and (255) respectively for $\tilde{p}$, ν and T provided the appropriate change in parameters. Equations' outline do not change beside replacing $\frac{B}{i\omega}$ by $\frac{\lambda_0+2\mu_0}{i\omega}$ in $\mathcal{F}$ and $\mathcal{G}$, as seen when comparing Eqs.(225) with (251), and $\tilde{p}$ being written as

$$\tilde{p}(r) = A\left[\mathcal{F}(\theta_{ac})H_0^{(1)}(i\theta_{ac}r) - 2(\mu + \frac{\mu_0}{i\omega})i\frac{\theta_{ac}}{r}\mathcal{G}(\theta_{ac})H_1^{(1)}(i\theta_{ac}r)\right] + \ldots \text{ etc} \tag{287}$$

We are able to rewrite Eqs.(286) as function of matrices in a layer j as

$$\begin{bmatrix} \tilde{p} \\ \nu \\ q \\ T \end{bmatrix}_j = W_j \begin{bmatrix} A_j \\ B_j \\ C_j \\ D_j \end{bmatrix} + \begin{bmatrix} \alpha_{T,j}B_j T_{Q_0,j} \\ 0 \\ 0 \\ T_{Q_0,j} \end{bmatrix}, \tag{288}$$

with W being similar to matrice H in Section 2.2.4 and $T_{Q_0,s} = \frac{Q_{0,j}}{\rho_{0,j} C_{V,j} i\omega}$. W is then written as

$$W = \begin{bmatrix} \mathcal{F}(\theta_{ac})H_0^{(1)}(i\theta_{ac}r)+ & \mathcal{F}(\theta_{ac})H_0^{(2)}(i\theta_{ac}r)+ & \\ -2i\mu\frac{\theta_{ac}}{r}\mathcal{G}(\theta_{ac})H_1^{(1)}(i\theta_{ac}r) & -2i\mu\frac{\theta_{ac}}{r}\mathcal{G}(\theta_{ac})H_1^{(2)}(i\theta_{ac}r) & \\ -i\theta_{ac}\mathcal{G}(\theta_{ac})H_1^{(1)}(i\theta_{ac}r) & -i\theta_{ac}\mathcal{G}(\theta_{ac})H_1^{(2)}(i\theta_{ac}r) & \dots \\ i\theta_{ac}\kappa H_1^{(1)}(i\theta_{ac}r) & i\theta_{ac}\kappa H_1^{(2)}(i\theta_{ac}r) & \\ H_0^{(1)}(i\theta_{ac}r) & H_0^{(2)}(i\theta_{ac}r) & \end{bmatrix}$$
$$\begin{bmatrix} \mathcal{F}(\theta_{th})H_0^{(1)}(i\theta_{th}r)+ & \mathcal{F}(\theta_{th})H_0^{(2)}(i\theta_{th}r)+ \\ -2i\mu\frac{\theta_{th}}{r}\mathcal{G}(\theta_{th})H_1^{(1)}(i\theta_{th}r) & -2i\mu\frac{\theta_{th}}{r}\mathcal{G}(\theta_{th})H_1^{(2)}(i\theta_{th}r) \\ -i\theta_{th}\mathcal{G}(\theta_{th})H_1^{(1)}(i\theta_{th}r) & -i\theta_{th}\mathcal{G}(\theta_{th})H_1^{(2)}(i\theta_{th}r) \\ i\theta_{th}\kappa H_1^{(1)}(i\theta_{th}r) & i\theta_{th}\kappa H_1^{(2)}(i\theta_{th}r) \\ H_0^{(1)}(i\theta_{th}r) & H_0^{(2)}(i\theta_{th}r) \end{bmatrix}. \quad (289)$$

As of now and as described in Fig.27, $r = 0$ is the center of the cylinder and due to the angular symmetry only $r > 0$ is considered. In order to avoid any discontinuity at $r = 0$ we define in the first layer that $A_1 = B_1$ and $C_1 = D_1$ knowing that $H_1^{(1)}(z) \sim -H_1^{(2)}(z)$ when $z \to 0$ (Eq.(10.7.7) in NIST [145]). The last layer N is consider to be semi infinite so only propagating waves are assumed and $A_N = C_N = 0$. In addition to those boundary conditions, the continuity of the parameters $\tilde{p}$, v, q and T is assumed between two layers. Following the same thought process as in Section 2.2.4 and using the continuity of the parameters between layers we found

$$\begin{bmatrix} A_1 \\ A_1 \\ C_1 \\ C_1 \end{bmatrix} = M_0 \begin{bmatrix} 0 \\ B_N \\ 0 \\ D_N \end{bmatrix} + \sum_{n\in[1,N-1]} M_{Q_{0,n}} \begin{bmatrix} \alpha_{T,n} B_n T_{Q_0,n} \\ 0 \\ 0 \\ T_{Q_0,n} \end{bmatrix}, \quad (290)$$

with n being the layers with a volumetric source and

$$M_0 = W_1^{-1}(r_1) \left[\prod_{j=2}^{N-1} W_j(r_{j-1})\, W_j^{-1}(r_j)\right] W_N(r_{N-1}), \quad (291)$$

with

$$\begin{cases} M_{Q_{0,1}} = & -W_1^{-1}(r_1), \\ M_{Q_{0,n}} = & W_1^{-1}(r_1)\ \left[\prod_{j=2}^{n-1} W_j(r_{j-1})\ W_j^{-1}(r_j)\right]\ \left[1 - W_n(r_{n-1})\ W_n^{-1}(r_n)\right], \\ & \forall n \in [2, N-1], \\ M_{Q_{0,N}} = & W_1^{-1}(r_1)\ \left[\prod_{j=2}^{N-1} W_j(r_{j-1})\ W_j^{-1}(r_j)\right]. \end{cases} \tag{292}$$

Eq.(290) can be re written as

$$\begin{bmatrix} 1 & 0 & -M_0(1,2) & -M_0(1,4) \\ 1 & 0 & -M_0(2,2) & -M_0(2,4) \\ 0 & 1 & -M_0(3,2) & -M_0(3,4) \\ 0 & 1 & -M_0(4,2) & -M_0(4,4) \end{bmatrix} \begin{bmatrix} A_1 \\ C_1 \\ B_N \\ D_N \end{bmatrix} = \begin{bmatrix} \sum_n M_{Q_{0,n}}(1,1)\alpha_{T,n}B_n T_{Q_0,n} + \\ \sum_n M_{Q_{0,n}}(1,4)T_{Q_0,n} \\ \sum_n M_{Q_{0,n}}(2,1)\alpha_{T,n}B_n T_{Q_0,n} + \\ \sum_n M_{Q_{0,n}}(2,4)T_{Q_0,n} \\ \sum_n M_{Q_{0,n}}(3,1)\alpha_{T,n}B_n T_{Q_0,n} + \\ \sum_n M_{Q_{0,n}}(3,4)T_{Q_0,n} \\ \sum_n M_{Q_{0,n}}(4,1)\alpha_{T,n}B_n T_{Q_0,n} + \\ \sum_n M_{Q_{0,n}}(4,4)T_{Q_0,n} \end{bmatrix}. \tag{293}$$

Eq.(290) or Eq.(293) gives A_1, C_1, B_N, and D_N. This allows the calculation of any coefficient $ABCD_j$ using either

$$\begin{bmatrix} A_j \\ B_j \\ C_j \\ D_j \end{bmatrix} = W_j^{-1}(r_j) \left[W_{j+1}(r_j) \begin{bmatrix} A_{j+1} \\ B_{j+1} \\ C_{j+1} \\ D_{j+1} \end{bmatrix} + \begin{bmatrix} \alpha_{T,j+1}B_{j+1}T_{Q_0,j+1} \\ 0 \\ 0 \\ T_{Q_0,j+1} \end{bmatrix} - \begin{bmatrix} \alpha_{T,j}B_j T_{Q_0,j} \\ 0 \\ 0 \\ T_{Q_0,j} \end{bmatrix} \right], \tag{294}$$

$$\begin{bmatrix} A_j \\ B_j \\ C_j \\ D_j \end{bmatrix} = W_j^{-1}(r_{j-1}) \left[W_{j-1}(r_{j-1}) \begin{bmatrix} A_{j-1} \\ B_{j-1} \\ C_{j-1} \\ D_{j-1} \end{bmatrix} + \begin{bmatrix} \alpha_{T,j-1} B_{j-1} T_{Q_0,j-1} \\ 0 \\ 0 \\ T_{Q_0,j-1} \end{bmatrix} - \begin{bmatrix} \alpha_{T,j} B_j T_{Q_0,j} \\ 0 \\ 0 \\ T_{Q_0,j} \end{bmatrix} \right], \tag{295}$$

$\forall j \in [1, N-1]$ and $\forall j \in [2, N]$ respectively. Finally $\tilde{p}$, v, q, T can be found for any r with Eq.(288).

In this section, a model for a cylindrical thermophones made of N concentric layers was solved. First the normal stress tensor, particle velocity, heat flux and temperature variation in a medium were written in a matrix form in Eq.(288) for both fluid and solid medium (provided that the specified parameter changes are made). The continuity of $\tilde{p}$, v, q, T between layers added to the hypotheses of non discontinuity at the center of the cylinder as well as a semi infinite layer N allowed for the system of equation to be explicitly solved for all parameters, at any position r in any layers and for any frequency f.

2.4 ONE TEMPERATURE MULTILAYER MODEL FOR SPHERICAL WAVES

Through Section 2.2 and 2.3 the conservation equations of Section 2.1.1 were solved for plane wave and cylindrical wave radiations respectively. Using the same though process and conservation equations, the system will be solved one last time for spherical wave radiations.

The system of equations will be solved first in a fluid and then a solid medium using a spherical coordinate system. Using the explicit analytical solutions of the parameters T, p, v and q, the system will be written in a matrix form. It will allows to solve the system in a much easier fashion. First it will be done in the case of an ideal spherical thermophone before being extended to a multilayer model.

The radiating sphere has a radius r and the spherical symmetry makes all physical properties independent of azimuth and elevation angle. This leads to the parameters being solely dependent on the distance with the center of the sphere r.

2.4.1 *Spherical Waves in a Fluid*

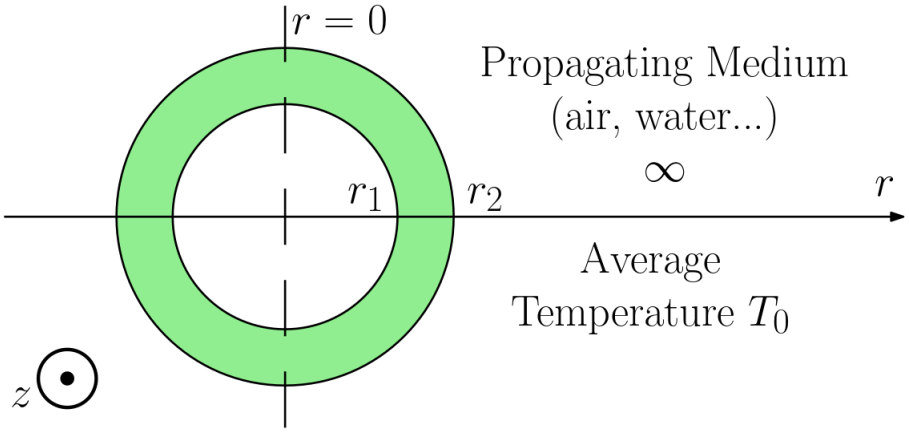

Figure 28: Schematic of the thermophone model in 3D with 3 layers

Using the general equations in a fluid of Eqs.(56), spherical wave radiation is now investigated as seen in Fig.28. They now can be written

$$\begin{cases} p = p(r), \\ T = T(r), \\ \vec{v} = \frac{\vec{r}}{r} v(r), \end{cases} \tag{296}$$

with $\vec{r} = x\vec{e_x} + y\vec{e_y} + z\vec{e_z}$, $\|\vec{r}\| = r = \sqrt{x^2+y^2+z^2}$ and x, y, z the cartesian coordinates. In order to write Eqs.(56) in spherical coordinate each component of those equations has to be rewritten using the parameters of Eq.(296). This leads to (details can be found in Appendix A.5.2)

$$\begin{cases} \vec{\nabla} p = \frac{\vec{r}}{r} \frac{\partial p}{\partial r}, \\ \vec{\nabla}.\vec{v} = \frac{1}{r^2} \frac{\partial}{\partial r}(r^2 v), \\ \vec{\nabla}(\vec{\nabla}.\vec{v}) = \frac{\vec{r}}{r} \left(\frac{\partial}{\partial r} \left(\frac{1}{r^2} \frac{\partial}{\partial r}(r^2 v) \right) \right), \\ \nabla^2 \vec{v} = \frac{\vec{r}}{r} \left(\frac{\partial}{\partial r} \left(\frac{1}{r^2} \frac{\partial}{\partial r}(r^2 v) \right) \right), \\ \nabla^2 T = \frac{1}{r^2} \frac{\partial}{\partial r}(r^2 \frac{\partial T}{\partial r}). \end{cases} \tag{297}$$

Conservation Equations in Fluid with Spherical coordinates

Using Eqs.(297), Eqs.(56) now becomes

$$\begin{cases} i\omega \frac{1}{B} p - i\omega \alpha_T T + \frac{1}{r} \frac{\partial}{\partial r}(rv) = 0, \\ i\omega \rho v = -\frac{\partial p}{\partial r} + (\lambda + 2\mu) \frac{\partial}{\partial r} \left(\frac{1}{r^2} \frac{\partial}{\partial r}(r^2 v) \right), \\ i\omega \rho C_p T - i\omega \alpha_T T_0 p = \kappa \frac{1}{r^2} \frac{\partial}{\partial r}(r^2 \frac{\partial T}{\partial r}), \end{cases} \tag{298}$$

with $\frac{1}{r^2}\frac{\partial}{\partial r}(r^2 v) = \frac{2}{r}v + \frac{\partial v}{\partial r}$. The aim is to write the pressure p and the particle velocity v as a function of the temperature variation T and find the differential equation that T solves similarly as before. To this aim Eq.(298a) can be rewritten in the same form as Eq.(121)

3D Pressure Equation in Fluid

$$p = \alpha_T B T - \frac{B}{i\omega}\frac{1}{r^2}\frac{\partial}{\partial r}(r^2 v). \tag{299}$$

Here the pressure p does not take the viscosity into account and so in order to have a continuity between different media (solid, fluid) we need to define the normal stress tensor $\tilde{p}$ in spherical coordinates. Using the stress tensor just as in Eq.(256), $\tilde{p}$ is defined as

3D Normal Stress Tensor in Fluid

$$\begin{aligned}
\tilde{p} &= -\hat{T}\vec{n}.\vec{n}, \\
&= -(\hat{T}_e)\vec{n}.\vec{n} - (\hat{T}_V)\vec{n}.\vec{n}, \\
&= p - 2\mu\frac{\partial v}{\partial r} - \lambda\frac{1}{r^2}\frac{\partial}{\partial r}(r^2 v), \\
&= \alpha_T B T - \left(\frac{B}{i\omega} + \lambda\right)\frac{1}{r^2}\frac{\partial}{\partial r}(r^2 v) - 2\mu\frac{\partial v}{\partial r}.
\end{aligned} \tag{300}$$

By deriving Eq.(299)

$$\begin{aligned}
\frac{\partial p}{\partial r} &= \alpha_T B\frac{\partial T}{\partial r} - \frac{B}{i\omega}\frac{\partial}{\partial r}\left(\frac{1}{r^2}\frac{\partial}{\partial r}(r^2 v)\right), \\
&= \alpha_T B\frac{\partial T}{\partial r} - \frac{B}{i\omega}(-\frac{2}{r^2}v + \frac{2}{r}\frac{\partial v}{\partial r} + \frac{\partial^2 v}{\partial r^2}),
\end{aligned} \tag{301}$$

and injecting it in Eq.(298b) we now have

$$i\omega\rho v = -\alpha_T B\frac{\partial T}{\partial r} + (\lambda + 2\mu + \frac{B}{i\omega})\frac{\partial}{\partial r}\left(\frac{1}{r^2}\frac{\partial}{\partial r}(r^2 v)\right). \tag{302}$$

The same way by injecting Eq.(299) in Eq.(298c) we have

$$\begin{aligned}
i\omega\rho C_p T - i\omega\alpha_T T_0(\alpha_T B T - \frac{B}{i\omega}\frac{1}{r^2}\frac{\partial}{\partial r}(r^2 v)) &= \kappa\frac{1}{r^2}\frac{\partial}{\partial r}(r^2\frac{\partial T}{\partial r}), \\
i\omega(\rho C_p - \alpha_T^2 T_0 B)T + \alpha_T T_0 B\frac{1}{r^2}\frac{\partial}{\partial r}(r^2 v) &= \kappa\frac{1}{r^2}\frac{\partial}{\partial r}(r^2\frac{\partial T}{\partial r}), \\
\frac{1}{r}\frac{\partial}{\partial r}(rv) = \frac{\kappa}{\alpha_T T_0 B}\frac{1}{r^2}\frac{\partial}{\partial r}(r^2\frac{\partial T}{\partial r}) - \frac{i\omega\rho C_V}{\alpha_T B T_0}T,
\end{aligned} \tag{303}$$

knowing the specific heat relation of Eq.(125). By injecting Eq.(303) into Eq.(302) it allows us to write v as a function of T only

3D Particle Velocity Equation in Fluid

$$\begin{aligned}
i\omega\rho v = &-\alpha_T B\frac{\partial T}{\partial r} + (\lambda + 2\mu + \frac{B}{i\omega})\frac{\partial}{\partial r}\left[\frac{\kappa}{\alpha_T T_0 B}\frac{1}{r^2}\frac{\partial}{\partial r}(r^2\frac{\partial T}{\partial r}) - \frac{i\omega\rho C_V}{\alpha_T B T_0}T\right], \\
v = &-\frac{1}{i\omega\rho}\left[\alpha_T B + (\lambda + 2\mu + \frac{B}{i\omega})\frac{i\omega\rho C_V}{\alpha_T B T_0}\right]\frac{\partial T}{\partial r} + \\
&+ (\lambda + 2\mu + \frac{B}{i\omega})\frac{\kappa}{i\omega\rho\alpha_T T_0 B}\frac{\partial}{\partial r}\left(\frac{1}{r^2}\frac{\partial}{\partial r}(r^2\frac{\partial T}{\partial r})\right).
\end{aligned} \tag{304}$$

To obtain a pure equation for T we apply $\frac{1}{r^2}\frac{\partial}{\partial r}(r^2*)$ to Eq.(302)

$$
\begin{aligned}
&i\omega\rho\frac{1}{r^2}\frac{\partial}{\partial r}(r^2 v) = -\alpha_T B\frac{1}{r^2}\frac{\partial}{\partial r}(r^2\frac{\partial T}{\partial r}) + (\lambda+2\mu+\frac{B}{i\omega})\frac{1}{r^2}\frac{\partial}{\partial r}\left[r^2\frac{\partial}{\partial r}[\frac{1}{r^2}\frac{\partial}{\partial r}(r^2 v)]\right],\\
&i\omega\rho\left[\frac{\kappa}{\alpha_T T_0 B}\frac{1}{r^2}\frac{\partial}{\partial r}(r^2\frac{\partial T}{\partial r}) - \frac{i\omega\rho C_V}{\alpha_T B T_0}T\right] = -\alpha_T B\frac{1}{r^2}\frac{\partial}{\partial r}(r^2\frac{\partial T}{\partial r}) +\\
&\quad + (\lambda+2\mu+\frac{B}{i\omega})\frac{1}{r^2}\frac{\partial}{\partial r}\left[r^2\frac{\partial}{\partial r}\left[\frac{\kappa}{\alpha_T T_0 B}\frac{1}{r^2}\frac{\partial}{\partial r}(r^2\frac{\partial T}{\partial r}) - \frac{i\omega\rho C_V}{\alpha_T B T_0}T\right]\right],
\end{aligned}
$$

using Eq.(303) and knowing that $\frac{1}{r^2}\frac{\partial}{\partial r}(r^2\frac{\partial T}{\partial r}) = \frac{2}{r}\frac{\partial T}{\partial r} + \frac{\partial^2 T}{\partial r^2}$. Re defining the notations

$$
\begin{cases}
T^{ii} = DT = \frac{1}{r^2}\frac{\partial}{\partial r}(r^2\frac{\partial T}{\partial r}),\\
T^{iv} = (T^{ii})^{ii} = DDT = \frac{1}{r^2}\frac{\partial}{\partial r}\left[r^2\frac{\partial}{\partial r}[\frac{1}{r^2}\frac{\partial}{\partial r}(r^2\frac{\partial T}{\partial r})]\right],
\end{cases}
\tag{305}
$$

3D Temperature Variation Differential Equation in a Fluid

the fourth order differential equation of T can be written

$$
\begin{aligned}
0 =&(\lambda+2\mu+\frac{B}{i\omega})\kappa T^{iv} +\\
&-\left[(\lambda+2\mu+\frac{B}{i\omega})i\omega\rho C_V + \alpha_T^2 B^2 T_0 + i\omega\rho\kappa\right]T^{ii} +\\
&-\omega^2\rho^2 C_V T,
\end{aligned}
\tag{306}
$$

which is similar to Eq.(227) with a different definition of D. Following the same though process and notation as for cartesian coordinates, Eq.(306) can be written as

$$
l_\kappa(l_V + \frac{C_0}{i\omega\gamma})T^{iv} - [1 + \frac{i\omega}{C_0}(l_\kappa + l_V)]T^{ii} - \frac{\omega^2}{C_0^2}T = 0,
\tag{307}
$$

with the parameters defined in Eqs.(140). The four solutions of the associated differential equation $a\theta^4 - b\theta^2 - c = 0$ are written of the form $\pm\theta_1$ and $\pm\theta_2$. Eq.(307) assumes a similar form as Eq.(139) in Section 2.2.1. θ_i are then defined as in Eq.(155).

It can be shown that if T is written of the form $T(r) = \frac{e^{\pm\theta_i r}}{r}$ then

$$
\begin{cases}
DT = \theta_i^2 T,\\
DDT = \theta_i^4 T.
\end{cases}
\tag{308}
$$

θ_i being a solution to the associated fourth order differential equation, then $T(r) = \frac{e^{\pm\theta_i r}}{r}$ is the form of the solution for Eq.(307).

In this section, the conservation equations were written in spherical coordinates in Eqs.(298). The pressure, normal surface tension and particle velocity were then written as functions of the temperature variation

in Eqs.(299), (300) and (304) respectively. The differential equation for T was found in Eq.(306) and rewritten in Eq.(307) with the parameters defined in Eqs.(140). The associated homogeneous 4_{th} order differential equation being the same in fluid regardless of the coordinate system (Cartesian, cylindrical or spherical), the associated wavenumber solutions are found in Eq.(155). The final solution of Eq.(306) is then

3D Temperature Variation

$$T(r) = A\frac{-e^{\theta_{ac}r}}{r} + B\frac{e^{\theta_{ac}r}}{r} + C\frac{-e^{\theta_{th}r}}{r} + D\frac{e^{\theta_{th}r}}{r}, \tag{309}$$

with ABCD constants.

2.4.2 *Spherical Waves in a Solid*

The spherical geometry will now be investigated in a solid. Based on Eqs.(118) and using Appendix A.5.2 the constitutive equations in a solid becomes

$$\begin{cases} \rho_{0,s} C_{V,s} i\omega T = \kappa_s \frac{1}{r^2}\frac{\partial}{\partial r}(r^2 \frac{\partial T}{\partial r}) - \alpha_{T,s} B_0 T_0 \frac{1}{r^2}\frac{\partial}{\partial r}(r^2 v) + Q_0, \\ \rho_{0,s} i\omega v = \left(\frac{\lambda_0 + 2\mu_0}{i\omega} + \lambda_s + 2\mu_s\right)\frac{\partial}{\partial r}\left(\frac{1}{r^2}\frac{\partial}{\partial r}(r^2 v)\right) - \alpha_{T,s} B_0 \frac{\partial T}{\partial r}, \end{cases} \tag{310}$$

with $\frac{\partial}{\partial t} = i\omega$, Q_0 (the heat density energy supplied) uniform, $\vec{b} = 0$ and knowing that $\frac{\partial u}{\partial t} = v$. When injecting $\frac{1}{r^2}\frac{\partial}{\partial r}(r^2 v)$ of Eq.(310a) into Eq.(310b), v can be written as a function of T alone as

3D Particle Velocity Equation in Solid

$$\begin{aligned} v = \frac{1}{i\omega\rho_{0,s}}\Bigg[&\frac{1}{\alpha_{T,s}B_0T_0}\left(\frac{\lambda_0+2\mu_0}{i\omega}+\lambda_s+2\mu_s\right)\left(-\rho_{0,s}C_{V,s}i\omega\frac{\partial T}{\partial r}+\right. \\ &\left.+\kappa_s\frac{\partial}{\partial r}\left(\frac{1}{r^2}\frac{\partial}{\partial r}\left(r^2\frac{\partial T}{\partial r}\right)\right)\right)-\alpha_{T,s}B_0\frac{\partial T}{\partial r}\Bigg], \end{aligned} \tag{311}$$

$$\begin{aligned} = \frac{-1}{i\omega\rho_{0,s}}\Bigg[&\frac{C_{V,s}i\omega\rho_{0,s}}{\alpha_{T,s}B_0T_0}\left(\frac{\lambda_0+2\mu_0}{i\omega}+\lambda_s+2\mu_s\right)+\alpha_{T,s}B_0\Bigg]\frac{\partial T}{\partial r}+ \\ &+\frac{\kappa_s}{i\omega\rho_{0,s}\alpha_{T,s}B_0T_0}\left(\frac{\lambda_0+2\mu_0}{i\omega}+\lambda_s+2\mu_s\right)\frac{\partial}{\partial r}\left(\frac{1}{r^2}\frac{\partial}{\partial r}\left(r^2\frac{\partial T}{\partial r}\right)\right). \end{aligned} \tag{312}$$

By multiplying Eq.(312) by $\frac{1}{r^2}\frac{\partial}{\partial r}(r^2 *)$ and using Eq.(310a)

$$\begin{aligned} \rho_{0,s}i\omega\frac{1}{r^2}\frac{\partial}{\partial r}(r^2 v) &= \left[\frac{1}{\alpha_{T,s}B_0T_0}\left(\frac{\lambda_0+2\mu_0}{i\omega}+\lambda_s+2\mu_s\right)\right. \\ &\quad \left.\left(-\rho_{0,s}C_{V,s}i\omega\frac{1}{r^2}\frac{\partial}{\partial r}\left(r^2\frac{\partial T}{\partial r}\right)+\kappa_s\frac{1}{r^2}\frac{\partial}{\partial r}\left(r^2\frac{\partial}{\partial r}\left(\frac{1}{r^2}\frac{\partial}{\partial r}\left(r^2\frac{\partial T}{\partial r}\right)\right)\right)\right)\right]+ \\ &\quad -\alpha_{T,s}B_0\frac{1}{r^2}\frac{\partial}{\partial r}\left(r^2\frac{\partial T}{\partial r}\right), \\ &= \frac{\rho_{0,s}i\omega}{\alpha_{T,s}B_0T_0}\left[-\rho_{0,s}C_{V,s}i\omega T+\kappa_s\frac{1}{r^2}\frac{\partial}{\partial r}\left(r^2\frac{\partial T}{\partial r}\right)+Q_0\right]. \end{aligned} \tag{313}$$

3D Temperature variation Differential Equation in a Solid

Using the notation introduced in Eq.(305), a differential equation for T is found

$$\begin{aligned}&(\lambda_s+2\mu_s+\frac{\lambda_0+2\mu_0}{i\omega})\kappa_s T^{iv}+\\&-\left[(\lambda_s+2\mu_s+\frac{\lambda_0+2\mu_0}{i\omega})i\omega\rho_{0,s}C_{V,s}+\alpha_{T,s}^2B_0^2T_0+i\omega\rho_{0,s}\kappa_s\right]T^{ii}+\\&-\omega^2\rho_{0,s}^2C_{V,s}T=\rho_{0,s}i\omega Q_0.\end{aligned}\tag{314}$$

Beside the supplied input power Q_0, Eq.(314) is similar to Eq.(306) for fluid with only B changed to $\lambda_0+2\mu_0$ for the solid. Henceforth, the solutions $\theta_{1,2}$ of the associated differential equation will are found in Eq.(268) this time. All the thought process associated to finding T as in Eq.(309) is still valid for a solid though. Finally, in order to add the supplied energy to the final equation of T, using the hypothesis that the solid can not be deformed T is written and using Eq.(178)

3D Temperature Variations

$$T(r)=A\frac{e^{-\theta_{ac,s}r}}{r}+B\frac{e^{\theta_{ac,s}r}}{r}+C\frac{e^{-\theta_{th,s}r}}{r}+D\frac{e^{\theta_{th,s}r}}{r}+T_{Q_0},\tag{315}$$

with ABCD constants.

We are now investigating the pressure in the solid case. By definition a force $d\vec{f}$ applied on a surface dS can be written using the stress tensor $\hat{T}$ as $d\vec{f}=\hat{T}\vec{n}dS$. By definition, the pressure p is $dF=-pdS$. This leads to

$$p=-\hat{T}_e\vec{n}.\vec{n}=-T_{e_{ij}}\frac{X_iX_j}{r^2},\tag{316}$$

with $\vec{n}=\frac{\vec{X}}{r}$ and X_i the coordinates of $\vec{r}$ in cartesian coordinates. Using Eq.(109), $\hat{\epsilon}$ the infinitesimal stress tensor as defined in Eq.(81) and, as defined for $\vec{v}$ in Eq.(296), $\vec{u}=\frac{\vec{r}}{r}u(r)$, the elastic tensor can be written

$$\hat{T}_e=\begin{bmatrix}2\mu_0\frac{\partial u_1}{\partial X_1}+\lambda_0\epsilon_{kk}-\alpha_{T,s}B_0T & \mu_0\left(\frac{\partial u_1}{\partial X_2}+\frac{\partial u_2}{\partial X_1}\right) & \mu_0\left(\frac{\partial u_1}{\partial X_3}+\frac{\partial u_3}{\partial X_1}\right)\\ \mu_0\left(\frac{\partial u_1}{\partial X_2}+\frac{\partial u_2}{\partial X_1}\right) & 2\mu_0\frac{\partial u_2}{\partial X_2}+\lambda_0\epsilon_{kk}-\alpha_{T,s}B_0T & \mu_0\left(\frac{\partial u_2}{\partial X_3}+\frac{\partial u_3}{\partial X_2}\right)\\ \mu_0\left(\frac{\partial u_1}{\partial X_3}+\frac{\partial u_3}{\partial X_1}\right) & \mu_0\left(\frac{\partial u_2}{\partial X_3}+\frac{\partial u_3}{\partial X_2}\right) & 2\mu_0\frac{\partial u_3}{\partial X_3}+\lambda_0\epsilon_{kk}-\alpha_{T,s}BT\end{bmatrix}.\tag{317}$$

The partial derivative of u are

$$\frac{\partial u_i}{\partial X_j}=\frac{X_iX_j}{r^2}\frac{\partial u}{\partial r}+\frac{r^2\delta_{ij}-X_iX_j}{r^3}u,\tag{318}$$

and so

$$\hat{T}_{eij}\frac{X_iX_j}{r^2} = \frac{2\mu_0}{r^2}\left(\frac{(X_iX_j)^2}{r^2}\frac{\partial u}{\partial r} - \frac{(r^2\delta_{ij} - X_iX_j)X_iX_j}{r^3}u\right) + (\lambda_0\epsilon_{kk} - \alpha_{T,s}B_0T)\frac{X_iX_j\delta_{ij}}{r2}, \tag{319}$$

with $\epsilon_{kk} = tr(\hat{\epsilon}) = \frac{2}{r}u + \frac{\partial u}{\partial r}$. This leads to

3D Pressure Equation in Solid

$$p = \alpha_{T,s}B_0T - \frac{2\mu_0}{i\omega}\frac{\partial v}{\partial r} - \frac{\lambda_0}{i\omega}\frac{1}{r^2}\frac{\partial}{\partial r}(r^2v). \tag{320}$$

Here the pressure p is only defined with the elastic stress tensor and so in order to have a stress continuity between different media (solid, fluid) we need to define $\tilde{p}$ with the viscous stress tensor as (using Eq.(91) and (101))

3D Normal Stress Tensor in Solid

$$\begin{aligned}\tilde{p} &= -\hat{T}\vec{n}.\vec{n},\\ &= -(\hat{T}_e)\vec{n}.\vec{n} - (\hat{T}_V)\vec{n}.\vec{n},\\ &= p - 2\mu_s\frac{\partial v}{\partial r} - \lambda_s\frac{1}{r^2}\frac{\partial}{\partial r}(r^2v),\\ &= \alpha_{T,s}B_0T - \left[2(\frac{\mu_0}{i\omega} + \mu_s)\frac{\partial v}{\partial r} + (\frac{\lambda_0}{i\omega} + \lambda_s)\frac{1}{r^2}\frac{\partial}{\partial r}(r^2v)\right].\end{aligned} \tag{321}$$

In this Section, the system of equations Eqs.(310) in a solid, was used to find the particle velocity as function of the temperature variation in Eq.(312). The 4_{th} order differential equation of T was found in Eq.(314). Its similar form as in cylindrical coordinates allowed to define the associated solutions as in Eq.(268), leading to the explicit form of T in Eq.(315). Lastly, by definition of the elastic stress tensor the pressure was written in a solid in Eq.(320). The viscous stress tensor was then added to define the normal stress tensor in Eq.(321) for continuity purposes.

2.4.3 *Ideal Spherical Thermophone*

The conservation equations have been solved in a spherical geometry for both fluid and solid media. We shall now investigate the thermoacoustic generation of an ideal spherical thermophone. In this case the solid part is of the thermophone is not considered and is represented as an ideal rigid boundary in which there is an ideal temperature gradient boundary condition. This easily implementable model will used as a reference and a first step for the understanding of the multilayer model.

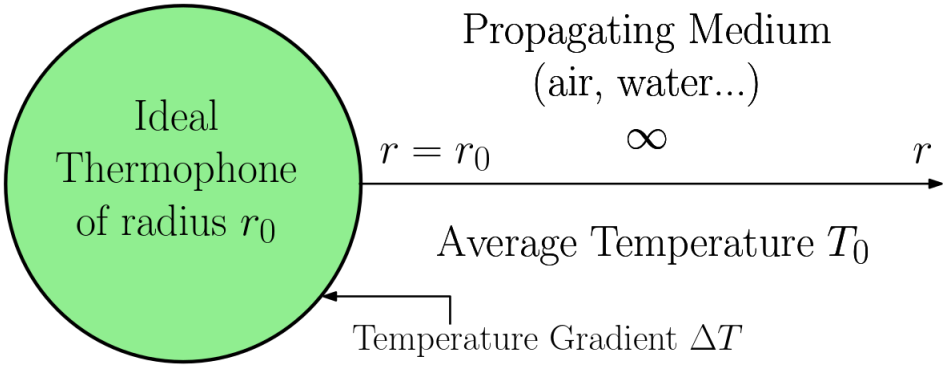

Figure 29: Schematic of the perfect thermophone model 3D

Assuming azimuth and elevation angle symmetry a simple uni dimensional model considering only progressive waves in the r direction can be used, as seen in Fig.29. The medium is semi infinite so only propagating waves are considered. No subscripts are used here since, even though the propagating medium is most likely a fluid (air for instance), the presented equations are still valid for solid propagation with the appropriate changes in parameters. With Eq.(309), the temperature variation T in the propagating medium can be written in the form

$$T(r) = A\frac{e^{-\theta_{ac} r}}{r} + B\frac{e^{-\theta_{th} r}}{r}, \tag{322}$$

with A and B constants and the first order approximation solutions for θ_{ac} and θ_{th} calculated in for cylindrical waves in Eq.(268) for solid and Eq.(155) for fluid. From the temperature, the particle velocity and the pressure can be inferred using Eqs.(304) and (299) respectively. We write L_1 and L_2 the coefficients of Eq.(304) so that $v = L_1\frac{\partial T}{\partial r} + L_2\frac{\partial}{\partial r}(\frac{2}{r}\frac{\partial T}{\partial r} + \frac{\partial^2 T}{\partial r^2})$ (Eqs.(183) and (184)). This leads to

$$T' = -A\left(\theta_{ac} + \frac{1}{r}\right)\frac{e^{-\theta_{ac} r}}{r} - B\left(\theta_{th} + \frac{1}{r}\right)\frac{e^{-\theta_{th} r}}{r}, \tag{323}$$

$$T'' = A\left(\theta_{ac}^2 + \frac{2\theta_{ac}}{r} + \frac{2}{r^2}\right)\frac{e^{-\theta_{ac} r}}{r} + B\left(\theta_{th}^2 + \frac{2\theta_{th}}{r} + \frac{2}{r^2}\right)\frac{e^{-\theta_{th} r}}{r}, \tag{324}$$

$$T''' = -A\left(\theta_{ac}^3 + \frac{3\theta_{ac}^2}{r} + \frac{6\theta_{ac}}{r^2} + \frac{6}{r^3}\right)\frac{e^{-\theta_{ac} r}}{r} + \\ - B\left(\theta_{th}^3 + \frac{3\theta_{th}^2}{r} + \frac{6\theta_{th}}{r^2} + \frac{6}{r^3}\right)\frac{e^{-\theta_{th} r}}{r}. \tag{325}$$

Analytical Spherical Equations for T and v

Using Eq.(323) and (324) we have the system

$$T(r) = A\frac{e^{-\theta_{ac}r}}{r} + B\frac{e^{-\theta_{th}r}}{r}, \tag{326}$$

$$v(r) = -A(\theta_{ac} + \frac{1}{r})(L_1 + L_2\theta_{ac}^2)\frac{e^{-\theta_{ac}r}}{r} - B(\theta_{th} + \frac{1}{r})(L_1 + L_2\theta_{th}^2)\frac{e^{-\theta_{th}r}}{r}. \tag{327}$$

Assuming that the gradient of temperature between the medium and the thermophone is ΔT and that the thermophone is rigid we have the two boundary conditions

$$\begin{cases} T(r = r_0) = \Delta T, \\ v(r = r_0) = 0, \end{cases} \tag{328}$$

with $r = r_0$ being the radius of the spherical thermophone (the limit with the propagating medium). Using Eqs.(328) boundary conditions along with the system of Eq.(326) and (327) we found the constants

$$\begin{cases} A = \Delta T r_0 e^{\theta_{ac} r_0} \left[\frac{-(\theta_{th} + \frac{1}{r})(L_1 + L_2\theta_{th}^2)}{L_1(\theta_{ac} - \theta_{th}) + L_2(\frac{\theta_{ac}^2 - \theta_{th}^2}{r} + \theta_{ac}^3 - \theta_{th}^3)} \right], \\ B = \Delta T r_0 e^{\theta_{th} r_0} \left[\frac{-(\theta_{ac} + \frac{1}{r})(L_1 + L_2\theta_{ac}^2)}{L_1(\theta_{th} - \theta_{ac}) + L_2(\frac{\theta_{th}^2 - \theta_{ac}^2}{r} + \theta_{th}^3 - \theta_{ac}^3)} \right]. \end{cases} \tag{329}$$

We now aim to write p explicitly following Eq.(299). First v of Eq.(327) needs to be derived as

$$\begin{aligned} v' =& A(\theta_{ac}^2 + \frac{2\theta_{ac}}{r} + \frac{2}{r^2})(L_1 + L_2\theta_{ac}^2)\frac{e^{-\theta_{ac}r}}{r} + \\ & B(\theta_{th}^2 + \frac{2\theta_{th}}{r} + \frac{2}{r^2})(L_1 + L_2\theta_{th}^2)\frac{e^{-\theta_{th}r}}{r}, \end{aligned} \tag{330}$$

leading to

$$\frac{2}{r}v + v' = A\theta_{ac}^2(L_1 + L_2\theta_{ac}^2)\frac{e^{-\theta_{ac}r}}{r} + B\theta_{th}^2(L_1 + L_2\theta_{th}^2)\frac{e^{-\theta_{th}r}}{r}. \tag{331}$$

Finally coming back to Eq.(299), the final explicit form of p in this ideal spherical case is

Analytical Spherical Equations for p and $\tilde{p}$

$$\begin{aligned} p = & \quad A\left[\alpha_T B - \frac{B}{i\omega}\theta_{ac}^2(L_1 + L_2\theta_{ac}^2)\right]\frac{e^{-\theta_{ac}r}}{r} + \\ & + B\left[\alpha_T B - \frac{B}{i\omega}\theta_{th}^2(L_1 + L_2\theta_{th}^2)\right]\frac{e^{-\theta_{th}r}}{r}. \end{aligned} \tag{332}$$

If $\tilde{p}$ is investigated, following Eq.(300) it can be written

$$\begin{aligned} \tilde{p} = & \quad A\left[\alpha_T B - (\tfrac{B}{i\omega} + \lambda + 2\mu)\theta_{ac}^2(L_1 + L_2\theta_{ac}^2) - 2\mu(\tfrac{2\theta_{ac}}{r} + \tfrac{2}{r^2})(L_1 + L_2\theta_{ac}^2)\right]\tfrac{e^{-\theta_{ac}r}}{r} \\ + & \quad B\left[\alpha_T B - (\tfrac{B}{i\omega} + \lambda + 2\mu)\theta_{th}^2(L_1 + L_2\theta_{th}^2) - 2\mu(\tfrac{2\theta_{th}}{r} + \tfrac{2}{r^2})(L_1 + L_2\theta_{th}^2)\right]\tfrac{e^{-\theta_{th}r}}{r}. \end{aligned} \tag{333}$$

Considering an ideal spherical thermophone radiating in free field, the analytical explicit equations for the temperature variations and the particle velocity are deduced in Eqs.(326) and (327). The constant factors associated to the two propagating waves are found in Eq.(329) using the boundary conditions of Eq.(328). The pressure and normal stress tensor are then also explicitely written in Eq.(332) and (333) respectvely. All variable p, $\tilde{p}$, v and T are then explicitly determined for all position r and for any frequency f.

2.4.4 *Transfer Matrix with N Layers*

The thought process associated to the resolution of an ideal spherical thermophone will now be used to create a more flexible model with multiple concentric spherical layers as seen in Fig.30. N concentric layers are assumed and the extreme layer (N_{th} one) is supposed to be semi infinite and each layer $j \in [1, N-1]$ potentially has a volumetric source $Q_{0,j}$ ($Q_{0,N} = 0$). The thickness of each "shell" layer j is $r_j - r_{j-1}$ with r_j the external radius of the j_{th} concentric layer. The type of material of each layer (fluid or solid) is not specified since medium differences are taken into account in the inherent parameters of their defining matrix.

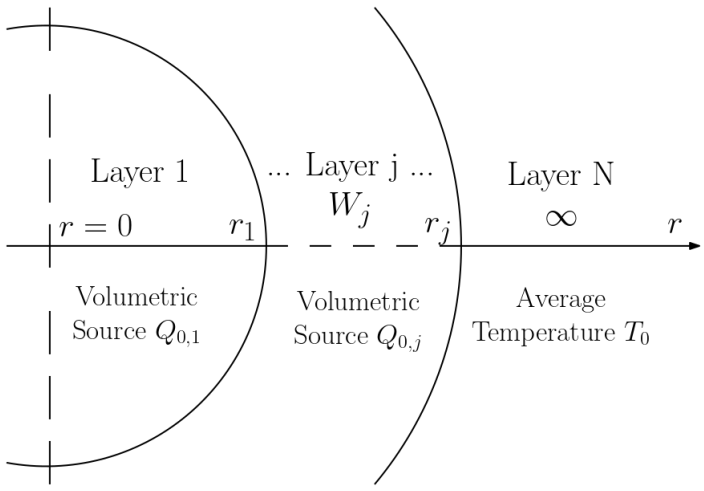

Figure 30: Schematic of a generalized version of the thermophone model with N layers in 3D

Equations found in 2.4.3 are extended with regressive waves. Thermal flux $\vec{q}$ is defined as

$$\vec{q} = -\kappa \vec{\nabla} T = -\kappa \frac{\vec{r}}{r} \frac{\partial T}{\partial r}, \tag{334}$$

T_{Q_0} as in Eq.(178) and $\mathcal{F}$ and $\mathcal{G}$ again as

$$\mathcal{F}(\eta) = \alpha_T B - \left(\frac{B}{i\omega} + \lambda + 2\mu\right)(L_1\eta^2 + L_2\eta^4), \tag{195}$$

$$\mathcal{G}(\eta) = L_1 + L_2\eta^2. \tag{196}$$

the general form of the parameters $\tilde{p}, \nu, q, T$ in a fluid in 3D can be found to be

$$\begin{cases} \tilde{p}(r) = & A\left[\mathcal{F}(\theta_{ac}) - 2\mu\frac{2}{r}(\frac{1}{r} + \theta_{ac})\mathcal{G}(\theta_{ac})\right]\frac{e^{-\theta_{ac}r}}{r} + \\ & B\left[\mathcal{F}(\theta_{ac}) - 2\mu\frac{2}{r}(\frac{1}{r} - \theta_{ac})\mathcal{G}(\theta_{ac})\right]\frac{e^{\theta_{ac}r}}{r} + \\ & C\left[\mathcal{F}(\theta_{th}) - 2\mu\frac{2}{r}(\frac{1}{r} + \theta_{th})\mathcal{G}(\theta_{th})\right]\frac{e^{-\theta_{th}r}}{r} + \\ & D\left[\mathcal{F}(\theta_{th}) - 2\mu\frac{2}{r}(\frac{1}{r} - \theta_{th})\mathcal{G}(\theta_{th})\right]\frac{e^{\theta_{th}r}}{r}, \\ \nu(r) = & -A(\frac{1}{r} + \theta_{ac})\mathcal{G}(\theta_{ac})\frac{e^{-\theta_{ac}r}}{r} - B(\frac{1}{r} - \theta_{ac})\mathcal{G}(\theta_{ac})\frac{e^{\theta_{ac}r}}{r} + \\ & -C(\frac{1}{r} + \theta_{th})\mathcal{G}(\theta_{ac})\frac{e^{-\theta_{th}r}}{r} - D(\frac{1}{r} - \theta_{th})\mathcal{G}(\theta_{th})\frac{e^{\theta_{th}r}}{r}, \\ q(r) = & A(\frac{1}{r} + \theta_{ac})\kappa\frac{e^{-\theta_{ac}r}}{r} + B(\frac{1}{r} - \theta_{ac})\kappa\frac{e^{\theta_{ac}r}}{r} + \\ & C(\frac{1}{r} + \theta_{th})\kappa\frac{e^{-\theta_{th}r}}{r} + D(\frac{1}{r} - \theta_{th})\kappa\frac{e^{\theta_{th}r}}{r}, \\ T(r) = & A\frac{e^{-\theta_{ac}r}}{r} + B\frac{e^{\theta_{ac}r}}{r} + C\frac{e^{-\theta_{th}r}}{r} + D\frac{e^{\theta_{th}r}}{r}. \end{cases} \tag{335}$$

Those equations also apply for a solid with Eqs.(261), (251) and (255) respectively for $\tilde{p}$, ν and T provided the appropriate change in parameters. Equations' outline do not change beside replacing $\frac{B}{i\omega}$ by $\frac{\lambda_0+2\mu_0}{i\omega}$ in $\mathcal{F}$ and $\mathcal{G}$, as seen when comparing Eqs.(304) with (312), and $\tilde{p}$ being written as

$$\tilde{p}(r) = A\left[\mathcal{F}(\theta_{ac}) - 2(\mu + \frac{\mu_0}{i\omega})\frac{2}{r}(\frac{1}{r} + \theta_{ac})\mathcal{G}(\theta_{ac})\right]\frac{e^{-\theta_{ac}r}}{r} + \ldots \text{ etc} \tag{336}$$

We are able to rewrite Eqs.(335) as a function of matrices in a layer j as

$$\begin{bmatrix} \tilde{p} \\ \nu \\ q \\ T \end{bmatrix}_j = W_j \begin{bmatrix} A_j \\ B_j \\ C_j \\ D_j \end{bmatrix} + \begin{bmatrix} \alpha_{T,j} B_j T_{Q_0,j} \\ 0 \\ 0 \\ T_{Q_0,j} \end{bmatrix}, \tag{337}$$

with $T_{Q_0,j} = \frac{Q_{0,j}}{\rho_{0,j} C_{V,j} i\omega}$, and $W(r) = W^{(a)}(r)W^{(b)}(r)$ as in Section 2.2.4. $W^{(a)}$ and $W^{(b)}$ can be written as

$$W^{(a)} = \begin{bmatrix} \mathcal{F}(\theta_{ac})+ & \mathcal{F}(\theta_{ac})+ & \\ -2\mu\frac{2}{r}(\frac{1}{r}+\theta_{ac})\mathcal{G}(\theta_{ac}) & -2\mu\frac{2}{r}(\frac{1}{r}-\theta_{ac})\mathcal{G}(\theta_{ac}) & \\ -(\frac{1}{r}+\theta_{ac})\mathcal{G}(\theta_{ac}) & -(\frac{1}{r}-\theta_{ac})\mathcal{G}(\theta_{ac}) & \dots \\ (\frac{1}{r}+\theta_{ac})\kappa & (\frac{1}{r}-\theta_{ac})\kappa & \\ 1 & 1 & \end{bmatrix}$$

$$\begin{bmatrix} \mathcal{F}(\theta_{th})+ & \mathcal{F}(\theta_{th})+ & \\ -2\mu\frac{2}{r}(\frac{1}{r}+\theta_{th})\mathcal{G}(\theta_{th}) & -2\mu\frac{2}{r}(\frac{1}{r}-\theta_{th})\mathcal{G}(\theta_{th}) & \\ -(\frac{1}{r}+\theta_{th})\mathcal{G}(\theta_{th}) & -(\frac{1}{r}-\theta_{th})\mathcal{G}(\theta_{th}) & \\ (\frac{1}{r}+\theta_{th})\kappa & (\frac{1}{r}-\theta_{th})\kappa & \\ 1 & 1 & \end{bmatrix},$$

and

$$W^{(b)} = \begin{bmatrix} \frac{e^{-\theta_{ac} r}}{r} & 0 & 0 & 0 \\ 0 & \frac{e^{\theta_{ac} r}}{r} & 0 & 0 \\ 0 & 0 & \frac{e^{-\theta_{th} r}}{r} & 0 \\ 0 & 0 & 0 & \frac{e^{\theta_{th} r}}{r} \end{bmatrix}. \tag{338}$$

Here $W^{(a)}$ is written with the equations in a fluid but with the appropriate changes the equivalent matrix for a solid can be found. $W^{(b)}$ is written in its global form and the differences between solid and fluid lie in the values of θ_{ac} and θ_{th}.

We consider $r = 0$ at the center of the sphere and due to the angular symmetry only $r > 0$ is considered. In order to avoid any discontinuity at $r = 0$ we define in the first layer that $A_1 = -B_1$ and $C_1 = -D_1$ knowing that $e^z \sim 1 + z$ when $z \to 0$. The last layer N is consider to be semi infinite so only propagating waves are assumed and $B_N = D_N = 0$. Following the same thought process as in 2.2.4 and using the continuity of the parameters between layers we found

$$\begin{bmatrix} A_1 \\ -A_1 \\ C_1 \\ -C_1 \end{bmatrix} = M_0 \begin{bmatrix} A_N \\ 0 \\ C_N \\ 0 \end{bmatrix} + \sum_{n\in[1,N-1]} M_{Q_{0,n}} \begin{bmatrix} \alpha_{T,n} B_n T_{Q_0,n} \\ 0 \\ 0 \\ T_{Q_0,n} \end{bmatrix}, \tag{339}$$

with n being the layers with a volumetric source and

$$M_0 = W_1^{-1}(r_1) \left[\prod_{j=2}^{N-1} W_j(r_{j-1})\, W_j^{-1}(r_j)\right] W_N(r_{N-1}), \tag{340}$$

$$\begin{cases} M_{Q_{0,1}} = & -W_1^{-1}(r_1), \\ M_{Q_{0,n}} = & W_1^{-1}(r_1) \left[\prod_{j=2}^{n-1} W_j(r_{j-1})\, W_j^{-1}(r_j)\right] \left[1 - W_n(r_{n-1})\, W_n^{-1}(r_n)\right], \\ & \forall n \in [2, N-1], \\ M_{Q_{0,N}} = & W_1^{-1}(r_1) \left[\prod_{j=2}^{N-1} W_j(r_{j-1})\, W_j^{-1}(r_j)\right]. \end{cases} \tag{341}$$

Eq.(339) can be re written as

$$\begin{bmatrix} 1 & 0 & -M_0(1,1) & -M_0(1,3) \\ -1 & 0 & -M_0(2,1) & -M_0(2,3) \\ 0 & 1 & -M_0(3,1) & -M_0(3,3) \\ 0 & -1 & -M_0(4,1) & -M_0(4,3) \end{bmatrix} \begin{bmatrix} A_1 \\ C_1 \\ A_N \\ C_N \end{bmatrix} = \begin{bmatrix} \sum_n M_{Q_{0,n}}(1,1)\alpha_{T,n}B_n T_{Q_0,n} + \\ \quad \sum_n M_{Q_{0,n}}(1,4) T_{Q_0,n} \\ \sum_n M_{Q_{0,n}}(2,1)\alpha_{T,n}B_n T_{Q_0,n} + \\ \quad \sum_n M_{Q_{0,n}}(2,4) T_{Q_0,n} \\ \sum_n M_{Q_{0,n}}(3,1)\alpha_{T,n}B_n T_{Q_0,n} + \\ \quad \sum_n M_{Q_{0,n}}(3,4) T_{Q_0,n} \\ \sum_n M_{Q_{0,n}}(4,1)\alpha_{T,n}B_n T_{Q_0,n} + \\ \quad \sum_n M_{Q_{0,n}}(4,4) T_{Q_0,n} \end{bmatrix}. \tag{342}$$

Eq.(339) or Eq.(342) gives A_1, C_1, A_N, and C_N. This allows the calculation of any coefficient $ABCD_j$ using either

$$\begin{bmatrix} A_j \\ B_j \\ C_j \\ D_j \end{bmatrix} = W_j^{-1}(r_j) \left[W_{j+1}(r_j) \begin{bmatrix} A_{j+1} \\ B_{j+1} \\ C_{j+1} \\ D_{j+1} \end{bmatrix} + \begin{bmatrix} \alpha_{T,j+1} B_{j+1} T_{Q_0,j+1} \\ 0 \\ 0 \\ T_{Q_0,j+1} \end{bmatrix} - \begin{bmatrix} \alpha_{T,j} B_j T_{Q_0,j} \\ 0 \\ 0 \\ T_{Q_0,j} \end{bmatrix} \right], \tag{343}$$

$$\begin{bmatrix} A_j \\ B_j \\ C_j \\ D_j \end{bmatrix} = W_j^{-1}(r_{j-1}) \left[W_{j-1}(r_{j-1}) \begin{bmatrix} A_{j-1} \\ B_{j-1} \\ C_{j-1} \\ D_{j-1} \end{bmatrix} + \begin{bmatrix} \alpha_{T,j-1} B_{j-1} T_{Q_0,j-1} \\ 0 \\ 0 \\ T_{Q_0,j-1} \end{bmatrix} - \begin{bmatrix} \alpha_{T,j} B_j T_{Q_0,j} \\ 0 \\ 0 \\ T_{Q_0,j} \end{bmatrix} \right], \tag{344}$$

$\forall j \in [1, N-1]$ and $\forall j \in [2, N]$ respectively. Finally $\tilde{p}$, v, q, T can be found for any r with Eq.(337).

In this section, a model for a spherical thermophones made of N concentric layers was solved. First the normal stress tensor, particle velocity, heat flux and temperature variation in a medium were written in a matrix form in Eq.(335) for both fluid and solid medium (provided that the specified parameter changes are made). The continuity of $\tilde{p}$, v, q, T between layers added to the hypotheses of non discontinuity at the center of the sphere as well as a semi infinite layer N allowed for the system of equation to be explicitly solved for all parameters, at any position r in any layers and for any frequency f.

SUMMING UP PLANE, CYLINDRICAL AND SPHERICAL WAVES MAIN EQUATIONS

To facilitate the understanding of the past sections, the main equations for plane, cylindrical and spherical waves are here rewritten for easy comparison.

In fluid

In fluid, the main differential equation for the temperature is written as

$$\begin{aligned} 0 = &(\lambda + 2\mu + \frac{B}{i\omega})\kappa T^{iv} + \\ &- \left[(\lambda + 2\mu + \frac{B}{i\omega})i\omega\rho_{0,f}C_V + (i\omega\rho_{0,f}\kappa + \alpha_T^2 T_0 B^2)\right] T'' + \\ &- \omega^2\rho_{0,f}^2 C_V T, \end{aligned} \tag{345}$$

and is valid for plane, cylindrical and spherical waves. The difference being in the differentials of T which will induce different solutions based on the coordinate system. The temperature is then written

$$T_f = \left(Ae^{-\theta_{ac}x} + Be^{\theta_{ac}x} + Ce^{-\theta_{th}x} + De^{\theta_{th}x}\right) e^{i\omega t} + T_{Q_0}, \tag{346}$$

$$T(r) = AH_0^{(1)}(i\theta_{ac}r) + BH_0^{(2)}(i\theta_{ac}r) + CH_0^{(1)}(i\theta_{th}r) + DH_0^{(2)}(i\theta_{th}r) + T_{Q_0}, \tag{347}$$

and

$$T(r) = A\frac{e^{-\theta_{ac}r}}{r} + B\frac{e^{\theta_{ac}r}}{r} + C\frac{e^{-\theta_{th}r}}{r} + D\frac{e^{\theta_{th}r}}{r} + T_{Q_0}, \tag{348}$$

for plane, cylindrical and spherical wave respectively. The constant term $T_{Q_0} = 0$ in fluid medium and the wavenumbers are the same in all three cases since they are found from the same differential equation, Eq.(345), as

$$\begin{cases} \theta_{ac,f} &= \frac{i\omega}{C_0}\left[1 - \frac{1}{2}\frac{i\omega}{C_0}l_V - \frac{1}{2}l_\kappa\frac{i\omega}{C_0}(1 - \frac{1}{\gamma})\right], \\ \theta_{th,f} &= \sqrt{\frac{i\omega\gamma}{C_0 l_\kappa}}\left[1 + \frac{1}{2}\frac{i\omega}{C_0}\left[l_\kappa(1 - \frac{1}{\gamma}) + l_V(1 - \gamma)\right]\right]. \end{cases} \tag{349}$$

Pressure and velocity, are then deduced using the conservation equations.

In solid

Plane wave generation in solid medium has been investigated in terms of longitudinal and transversal waves. We were then able to found exactly the same conservation equations in solid as in fluid provided that the following changes are applied

$$\begin{cases} B = \frac{B_0}{1-\frac{4}{3}\frac{v_T^2}{v_L^2}}, \\ \alpha_T = \alpha_{T,s}(1-\frac{4}{3}\frac{v_T^2}{v_L^2}), \\ C_{p,f} = C_{p,s}(1-\frac{C_{p,s}-C_{V,s}}{C_{p,s}},\frac{4}{3}\frac{v_T^2}{v_L^2}). \end{cases} \tag{350}$$

This kind of analogy was not possible for cylindrical and spherical waves but a similar thought process as for plane wave in fluids is applied. As such, a similar differential equation for T is found as

$$\begin{aligned} &(\lambda_s+2\mu_s+\frac{\lambda_0+2\mu_0}{i\omega})\kappa_s T^{iv}+ \\ &-\left[(\lambda_s+2\mu_s+\frac{\lambda_0+2\mu_0}{i\omega})i\omega\rho_{0,s}C_{V,s}+\alpha_{T,s}^2B_0^2T_0+i\omega\rho_{0,s}\kappa_s\right]T^{ii}+ \\ &-\omega^2\rho_{0,s}^2C_{V,s}T=\rho_{0,s}i\omega Q_0. \end{aligned} \tag{351}$$

This equation is similar to Eq.(345) with the added constant term of supplied energy and with the change B to $\lambda_0+2\mu_0$. The derivative of T are similar to the ones in fluid though and so the temperature in solid is written as in Eqs.(347), and (348). However $T_{Q_0}\neq 0$ and the wavenumbers are different and are found as

$$\begin{cases} \theta_{ac,s} = & \frac{i\omega}{C_{0,s}}(1-\frac{1}{\gamma_s}+\frac{C_L}{C_{0,s}})^{-1/2}\left[1-l_{V,s}\frac{i\omega}{2C_{0,s}}(1-\frac{1}{\gamma_s}+\frac{C_L}{C_{0,s}})^{-1}+\right. \\ & \left.-l_{\kappa,s}\frac{i\omega}{2C_{0,s}}\left((1-\frac{1}{\gamma_s}+\frac{C_L}{C_{0,s}})^{-1}-\frac{C_L}{C_{0,s}}(1-\frac{1}{\gamma_s}+\frac{C_L}{C_{0,s}})^{-2}\right)\right], \\ \theta_{th,s} = & (\frac{i\omega}{l_{\kappa,s}C_L})^{1/2}(1-\frac{1}{\gamma_s}+\frac{C_L}{C_{0,s}})^{1/2}\left[1+\frac{i\omega}{2C_{0,s}}\left[l_{\kappa,s}\left[(1-\frac{1}{\gamma_s}+\frac{C_L}{C_{0,s}})^{-1}+\right.\right.\right. \\ & \left.\left.\left.-(1-\frac{1}{\gamma_s}+\frac{C_L}{C_{0,s}})^{-2}\frac{C_L}{C_{0,s}}\right]+l_{V,s}\left[(1-\frac{1}{\gamma_s}+\frac{C_L}{C_{0,s}})^{-1}-\frac{C_{0,s}}{C_L}\right]\right]\right]. \end{cases} \tag{352}$$

Eqs.(352) are consistent with Eqs.(349) if C_L is replaced by $\frac{C_{0,s}}{\gamma_s}$. The other variables, pressure and velocity, are then found using the conservation equations and the subsequent multilayer matricial model is created in a similar fashion in all three cases.

2.5 TWO TEMPERATURES MODEL FOR PLANE WAVES

With Sections 2.2, 2.3 and 2.4, the goal was to use the general constitutive equations defined for fluid and solid media in Section 2.1 to create flexible analytical models in matricial form. However, despite the multiple geometries investigated and the flexibility of each models, none of them are targeted for the thermoacoustic generation of thick foamlike materials. A two-temperature model is presented here in order to gain a deeper insight into the thermoacoustic behavior of thermophones based on highly porous foamlike materials.

This model introduces local non equilibrium between the temperatures of the solid foam and the fluid embedded inside it [146–150]. It means that two different temperatures are considered for each phase of the generating layer. The balance equations for the fluid are coupled with the heat equation for the foam through a set of boundary conditions describing the exchange of energy at each contact surface between fluid and foam. This is the most important difference between this model and previous ones: while in previous models, the heat exchange between generating layer and fluid occurs only at the two external surfaces due to assumption of a bulk continuous solid, in the present case, the actual distribution of fluid within the pores and the heat exchanges at any foam-fluid contact are considered. This process is able to explain the high efficiency observed in real thermophones based on foam or spongelike materials.

Therefore, a model is elaborated to take into account the effect of the fluid (typically air) embedded within the pores of the active solid phase, i.e. the coupling between the fluid and the micro- or nano-structured porous solid in the active region. It is solved for plane wave generation before being written in a matrix form. A multilayer model is then created which allows for an easy design of the multiple foam-fluid contacts in the thermophone. It can be noted that the development of equations in the following section are not as explicitly written as before since the same though process as in Section 2.2.1 is used and similar equations are deduced.

2.5.1 *Simplified Conservation Equation*

A thermophone radiating in free field is considered as shown in Fig.31. The central active layer of the thermophone is assumed to be made of a porous material with a very high porosity (e.g., larger than 90%), with an undeformable solid microstructure. The fluid motion within the pores of the thermophone region can be described by the conserva-

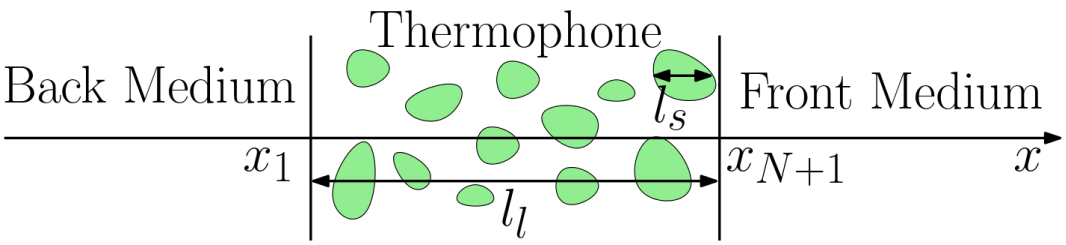

Figure 31: Schematic of a porous thermophone radiating in free field (symmetrically in back and front media). The thermophone layer has a width l_l and foam branches of average diameter l_s. The volumetric source Q_0 is supplied to the foam structure by Joule effect.

tion equations in Eqs.(56). However, due to the possible high frequency of the energy supplied to the thermophone to induce thermoacoustic effect, the local thermal equilibrium is not attained between fluid and solid phases. Therefore, the conservation equations in the fluid can be coupled with the energy conservation for the solid phase, where an input power density Q_0 is introduced (Joule effect), and a temperature $T_s \neq T_f$ is considered. The combination of such equations represents the non thermal equilibrium between fluid and solid. In other terms, since the temperatures of fluid and solid are sensibly different on the two sides of a real contact interface, a phenomenological two-temperature model has to be considered to effectively take account of this non thermal equilibrium. Each layer is therefore described by the following set of equations

2T System of Equations

$$\frac{1}{B}\frac{\partial p}{\partial t} - \alpha_T \frac{\partial T_f}{\partial t} + \vec{\nabla}\cdot\vec{v} = 0, \tag{353}$$

$$\rho_0 \frac{\partial \vec{v}}{\partial t} = -\vec{\nabla} p + \mu\nabla^2\vec{v} + (\lambda+\mu)\vec{\nabla}(\vec{\nabla}\cdot\vec{v}), \tag{354}$$

$$\rho_0 C_p \frac{\partial T_f}{\partial t} - \alpha_T T_0 \frac{\partial p}{\partial t} = \kappa\nabla^2 T_f, \tag{355}$$

$$\rho_{0,s} C_{v,s} \frac{\partial T_s}{\partial t} = \kappa_s \nabla^2 T_s + Q_0, \tag{356}$$

where the last equation represent the added energy conservation in the solid foam instead of using the system described by Eqs.(118). This system is investigated in a one-dimensional case (plane wave propagation along the x axis) with an harmonic time dependence as in Section 2.2. Then, one gets

2T System of Equations for Plane waves

$$\frac{i\omega}{B}p - i\omega\alpha_T T_f + \frac{dv}{dx} = 0, \tag{357}$$

$$i\omega\rho_0 v = -\frac{dp}{dx} + (\lambda + 2\mu)\frac{d^2v}{dx^2}, \tag{358}$$

$$i\omega\rho_0 C_p T_f = \kappa\frac{d^2T_f}{dx^2} + i\omega\alpha_T T_0 p, \tag{359}$$

$$i\omega\rho_{0,s} C_{v,s} T_s = \kappa_s\frac{d^2T_s}{dx^2} + Q_0. \tag{360}$$

Thermophone Homogenized Parameters

Importantly in these equations, the terms $\rho_{0,s}$, $C_{v,s}$ and κ_s must be considered as the homogenized values over the whole volume of the generation layer. Indeed, the two temperature model implicitly considers two effective phases (fluid and foam, in our case), both occupying the whole region of the thermophone layer. Therefore, for each phase the homogenized values for all physical properties have to be considered[146–150]. However, since the materials display a very high porosity, the homogenized parameters are adopted only for the foam phase.

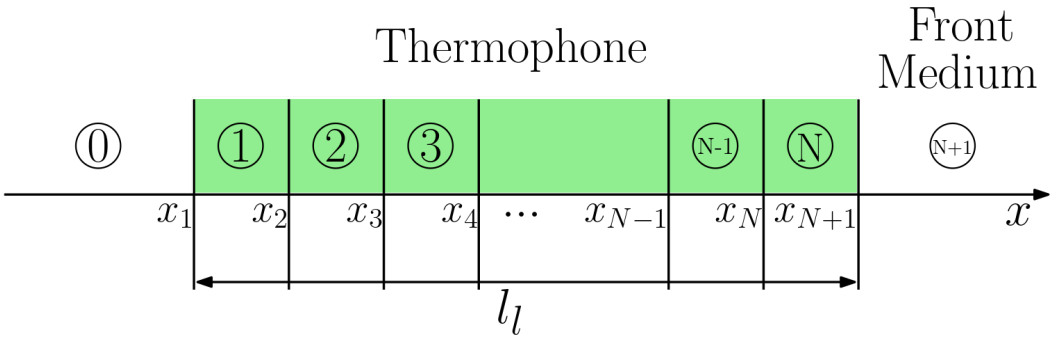

Figure 32: Two-temperature representation of the porous thermophone. In each layer, a temperature T_f is associated to the fluid within the pores, and a temperature $T_s \neq T_f$ is associated to the solid foam branches. The interfaces control the energy exchange between foam and fluid.

To better take into consideration the morphology of the porous structure within the generation layer, an exchange of energy at the contact surfaces between pores and foam branches is introduced. This scheme can be mimicked by a series of interfaces, which are represented in Fig.32 in our uni dimensional case. The energy exchange between fluid in the pores and solid branches is written in the boundary conditions that are summarized below. To write these conditions, the definition of the heat flux is introduced in the fluid phase as $q = -\kappa dT/dx$ and in the solid foam phase as $q_s = -\kappa_s dT_s/dx$ (Eq.(190)). Moreover, instead of considering the pressure p, the normal surface tension $\tilde{p}$ is adopted as $\tilde{p} = p - (\lambda + 2\mu)dv/dx$, which takes into account the viscous stress (Eq.(188)). Now, in each layer of the thermophone (layers from 1 to N,

see Fig.32), there are four variables $\tilde{p}, \nu, T_f$ and q for the fluid and two variables T_s and q_s for the branches. On the other hand, in the back and front media (layers 0 and $N+1$), there are only the variables for the fluid, namely $\tilde{p}, \nu, T$ and q. An index $i \in [0, N+1]$ is associated to these variables to identify the layer where they are defined. For the interfaces within the thermophone (from x_2 to x_N), boundary conditions are found as

2T Boundary Conditions

$$\tilde{p}_{i-1}(x_i) = \tilde{p}_i(x_i), \tag{361}$$
$$\nu_{i-1}(x_i) = \nu_i(x_i), \tag{362}$$
$$T_{f,i-1}(x_i) = T_{f,i}(x_i), \tag{363}$$
$$T_{s,i-1}(x_i) = T_{s,i}(x_i), \tag{364}$$
$$q_i(x_i) = q_{i-1}(x_i) + g(T_{s,i}(x_i) - T_{f,i}(x_i)), \tag{365}$$
$$q_{s,i}(x_i) = q_{s,i-1}(x_i) - g(T_{s,i}(x_i) - T_{f,i}(x_i)), \tag{366}$$

for all $i \in [2, N]$. While the first four relations represent the classical continuity of normal stress, velocity and temperatures, the last two relations represent the energy exchanged between solid branches and fluid. Indeed, if $T_{s,i}(x_i) \geqslant T_{f,i}(x_i)$ a positive quantity of energy leaves the foam and moves to the surrounding fluid. This process is controlled by a new parameter g $[W/(m^2K)]$, describing the fluid/solid coupling at the interfaces. Concerning the first interface at x_1 (back medium/thermophone), the boundary conditions are

$$\tilde{p}_0(x_1) = \tilde{p}_1(x_1), \tag{367}$$
$$\nu_0(x_1) = \nu_1(x_1), \tag{368}$$
$$T_{f,0}(x_1) = T_{f,1}(x_1), \tag{369}$$
$$q_1(x_1) = q_0(x_1) + g(T_{s,1}(x_1) - T_{f,1}(x_1)), \tag{370}$$
$$q_{s,1}(x_1) = -g(T_{s,1}(x_1) - T_{f,1}(x_1)). \tag{371}$$

Finally at the last interface x_{N+1} (thermophone/front medium) boundary conditions are written as

$$\tilde{p}_N(x_{N+1}) = \tilde{p}_{N+1}(x_{N+1}), \tag{372}$$
$$\nu_N(x_{N+1}) = \nu_{N+1}(x_{N+1}), \tag{373}$$
$$T_{f,N}(x_{N+1}) = T_{f,N+1}(x_{N+1}), \tag{374}$$
$$q_{N+1}(x_{N+1}) = q_N(x_{N+1}) + g(T_{s,N}(x_{N+1}) - T_{f,N}(x_{N+1})), \tag{375}$$
$$0 = q_{s,N}(x_{N+1}) - g(T_{s,N}(x_{N+1}) - T_{f,N}(x_{N+1})). \tag{376}$$

It is interesting to observe that this proposed two-temperature model differs form the classical two-temperature model described in the literature [146–150]. Indeed, in our case the exchange of energy is confined at all interfaces representing the contacts between fluid and foam. This

process is not continuous and therefore it is not implemented within the balance equations defined in each layer (see Eqs.(357) to (360)). On the other hand, it is important to also note that in this thermophone model the heating of the fluid is a process distributed (although not continuously) within the whole region of the generation layer (at all the fluid/foam contacts) and not only at the external interfaces (at x_1 and x_{N+1}) as in the classical thermophone models developed in the first part of this Section 2 For this reason, it is better suited to represent the behavior of thick and porous thermophone devices.

Definition of Coupling Coefficient g

A specific discussion concerns the parameter g, which is the only new parameter introduced in this model. The real total contact area between the solid foam and air is given by $a\rho_s V$, where a is the specific area of the foam in $[m^2/kg]$, ρ_s is the foam density $[kg/m^3]$, and V is the total foam volume $[m^3]$, with $a\rho_s$ is the interfacial area per unit volume. On the other hand, the effective contact area introduced in our model is given by NS, where N is the number of layers in Fig.32 and S is their area $[m^2]$. On the basis of these premises, g can be defined as

$$NSg = a\rho_s V h, \tag{377}$$

where h is the real heat film transfer coefficient $[W/(m^2K)]$ (convective and radiative). One simply obtains

$$g = \frac{a\rho_s V h}{NS} = \frac{a\rho_s h l_l}{N}, \tag{378}$$

where $l_l = V/S$. With the reasonable values $a = 1000–2000$ m2/g[151, 152], $h = 200\ W/(m^2K)$[153], $\rho_s = 30\ kg/m^3$, $l_l = 0.1–1$mm, and $N = 10$, one obtains $g \approx 10^5\ W/(m^2K)$, which is used throughout all the thesis.

The solution for the physical variables defined in each layer of the model can be found as follows. From Eq.(357) the pressure can be obtained as

2T Pressure Equation

$$p = \alpha_T B T_f - \frac{B}{i\omega}\frac{dv}{dx}. \tag{379}$$

Then, the normal surface tension $\tilde{p}$ becomes

2T Normal Surface Tension

$$\tilde{p} = \alpha_T B T_f - (\lambda + 2\mu + \frac{B}{i\omega})\frac{dv}{dx}. \tag{380}$$

Using Eq.(380) along with Eqs.(357) to (360), the velocity is eventually found as

2T Particle Velocity Equation

$$v = -\frac{1}{i\omega\rho}\left[\alpha_T B + \frac{i\omega\rho C_v}{\alpha_T T_0 B}(\lambda + 2\mu + \frac{B}{i\omega})\right]\frac{dT_f}{dx} + \\ + (\lambda + 2\mu + \frac{B}{i\omega})\frac{\kappa}{i\omega\rho\alpha_T T_0 B}\frac{d^3T_f}{dx^3}, \tag{381}$$

where the thermodynamic relationship between the specific heats $\rho(C_p - C_v) = T_0\alpha_T^2 B$ of Eq.(125) has been used. The fourth order differential equation for T_f can be then found in the form

2T Differential Equation for T_f

$$\begin{aligned} 0 =& (\lambda + 2\mu + \frac{B}{i\omega})\kappa\frac{d^4T_f}{dx^4} + \\ & - \left[(\lambda + 2\mu + \frac{B}{i\omega})i\omega\rho C_v + (i\omega\rho\kappa + \alpha_T^2 T_0 B^2)\right]\frac{d^2T_f}{dx^2} + \\ & - \omega^2\rho^2 C_v T_f, \end{aligned} \tag{382}$$

coherently with Eq.(130). The solutions of Eq.(382) represent thermal and acoustical modes that will be described by σ_{th} and k_{ac}, respectively. The temperature in the fluid can be therefore written with two progressive and two regressive waves as

2T Temperature in Fluid

$$T_f = Ae^{-ik_{ac}x} + Be^{+ik_{ac}x} + Ce^{-\sigma_{th}x} + De^{+\sigma_{th}x}. \tag{383}$$

On the other hand, from the energy conservation in the solid, Eq.(360), the temperature T_s can be easily written with only thermal waves as

2T Temperature in Solid

$$T_s = Ee^{-\sigma_{solid}x} + Fe^{+\sigma_{solid}x} + T_{s,Q_0}, \tag{384}$$

with T_{s,Q_0} being the particular solution of Eq.(360) given by

$$T_{s,0} = \frac{Q_0}{\rho_{0,s}C_{v,s}i\omega}, \tag{178}$$

and A, B, C, D, E and F are constants to be determined. k_{ac} and σ_{th} are the solutions of the algebraic fourth-order (biquadratic) characteristic equation associated to Eq.(382). Since the exact solutions are rather cumbersome, it is useful to assume a weak thermal conduction and a weak viscosity of the adopted medium. Under these hypotheses and using the notations in Eq.(140), the asymptotic solutions of Eq.(382) can be obtained in the form

$$k_{ac} = \frac{\omega}{C_0}\left[1 - \frac{1}{2}\frac{i\omega}{C_0}l_v - \frac{1}{2}\frac{i\omega}{C_0}l_k(1 - \frac{1}{\gamma})\right], \tag{385}$$

$$\sigma_{th} = \sqrt{\frac{i\omega\gamma}{C_0 l_k}}\left[1 + \frac{1}{2}\frac{i\omega}{C_0}l_k(1 - \frac{1}{\gamma}) + \frac{1}{2}\frac{i\omega}{C_0}l_v(1 - \gamma)\right]. \tag{386}$$

The detailed proof of Eqs.(385) and (386) is given in the Section 2.2.1 to determine Eq.(155). These results represent the first order expansions (with small κ, λ and μ) of the solutions of the algebraic equation associated with Eq.(382). For the fluid this is a good approximation in the frequency range of interest for the thermophone applications. If necessary, the values of σ_{th} and k_{ac} can be obtained numerically, without

any assumption on the material parameters. On the other hand, through Eq.(360), the propagation constant in the solid can also be found as

2T Thermal Mode in Solid

$$\sigma_{solid} = \sqrt{\frac{i\omega\rho_{0,s}C_{v,s}}{\kappa_s}}. \tag{387}$$

The set of solutions in a layer, concerning the fluid variables, is obtained as

$$\begin{aligned}
\tilde{p} &= A\mathcal{F}(ik_{ac})e^{-ik_{ac}x} + B\mathcal{F}(ik_{ac})e^{ik_{ac}x} + \\
&\quad + C\mathcal{F}(\sigma_{th})e^{-\sigma_{th}x} + D\mathcal{F}(\sigma_{th})e^{\sigma_{th}x}, && (388)\\
v &= -Aik_{ac}\mathcal{G}(ik_{ac})e^{-ik_{ac}x} + Bik_{ac}\mathcal{G}(ik_{ac})e^{ik_{ac}x} + \\
&\quad - C\sigma_{th}\mathcal{G}(\sigma_{th})e^{-\sigma_{th}x} + D\sigma_{th}\mathcal{G}(\sigma_{th})e^{\sigma_{th}x}, && (389)\\
q &= A\kappa ik_{ac}e^{-ik_{ac}x} - B\kappa ik_{ac}e^{ik_{ac}x} + \\
&\quad + C\kappa\sigma_{th}e^{-\sigma_{th}x} - D\kappa\sigma_{th}e^{\sigma_{th}x}, && (390)\\
T &= Ae^{-ik_{ac}x} + Be^{ik_{ac}x} + Ce^{-\sigma_{th}x} + De^{\sigma_{th}x}, && (391)
\end{aligned}$$

with the functions

$$\mathcal{F}(\eta) = \alpha_T B - \left(\frac{B}{i\omega} + \lambda + 2\mu\right)(L_1\eta^2 + L_2\eta^4), \tag{195}$$

$$\mathcal{G}(\eta) = L_1 + L_2\eta^2, \tag{196}$$

and L_1 and L_2 being the coefficients (see Eq.(381))

$$L_1 = -\frac{1}{i\omega\rho}\left[\alpha_T B + \frac{i\omega\rho C_v}{\alpha_T T_0 B}(\lambda + 2\mu + \frac{B}{i\omega})\right], \tag{183}$$

$$L_2 = (\lambda + 2\mu + \frac{B}{i\omega})\frac{\kappa}{i\omega\rho\alpha_T T_0 B}. \tag{184}$$

In this section the defining characteristics of the two temperatures model is explained. Due to the thickness and the high porosity of foam-like thermophones (more than 90%), regular continuous thermoacoustic models cannot be used. The 2T model assumes that, for a thermophone radiating in free field, the solid and the fluid coexists in the sample as seen in Fig.31. Due to the high frequency of the energy supplied to the thermophone, the local thermal equilibrium is not attained between the two phases and different temperatures have to be considered for the fluid (T_f) and the solid (T_s).

An uni dimensional model in Cartesian coordinates is considered and conservation equations are written for a fluid in Eq.(357) to (359). A simplified energy conservation equation for the solid's temperature is

written in Eq.(360) to take the simultaneous existence of T_f and T_s into account. It is seen that conservation equations for the fluid are the same as in Section 2.2. Hence, parameters in the fluids are found in Eqs.(388) to (391) similarly as in Section 2.2.1. T_s is solved in Eq.(384) with thermal mode defined in Eq.(387).

Finally, the main novelty of this model lies in the introduction of a coupling coefficient g defined in Eq.(378). Since the energy is supplied to the solid phase, in order for the energy to be provided to the fluid phase, virtual interfaces are defined in places where the fluid and the solid coexists. At those interfaces a flux of energy is provided proportionally to the gradient of temperature $T_s - T_f$, enabling the thermoacoustic generation. All boundary conditions are found in Eqs.(361) to (376). The explicitly defined parameters plus the well constructed boundary conditions will now allow us to write the system in matrix form and solve it for any point in space.

2.5.2 *Transfer Matrix with N Discretised Layers*

Eqs.(388) to (391) can be rewritten in a matrix form as the previous sections. This form will help us to solve the model since a lot of intermediate layers have to be defined in order to take into account the numerous branches inside the foamlike thermophone. Those numerous boundaries make the model difficult to solve without the use of matrices. By defining the matrix

$$H^{(a)} = \begin{bmatrix} \mathcal{F}(ik_{ac}) & \mathcal{F}(ik_{ac}) & \mathcal{F}(\theta_{th}) & \mathcal{F}(\theta_{th}) \\ -ik_{ac}\mathcal{G}(ik_{ac}) & ik_{ac}\mathcal{G}(ik_{ac}) & -\theta_{th}\mathcal{G}(\theta_{th}) & \theta_{th}\mathcal{G}(\theta_{th}) \\ \kappa ik_{ac} & -\kappa ik_{ac} & \kappa\theta_{th} & -\kappa\theta_{th} \\ 1 & 1 & 1 & 1 \end{bmatrix}, \tag{392}$$

and

$$H^{(b)}(x) = \begin{bmatrix} e^{-ik_{ac}x} & 0 & 0 & 0 \\ 0 & e^{ik_{ac}x} & 0 & 0 \\ 0 & 0 & e^{-\theta_{th}x} & 0 \\ 0 & 0 & 0 & e^{\theta_{th}x} \end{bmatrix}, \tag{393}$$

2T Matrix System in Fluid

the general solution in a given fluid layer is given by

$$\begin{bmatrix} \tilde{p}_i(x) \\ v_i(x) \\ q_i(x) \\ T_i(x) \end{bmatrix} = H(x) \begin{bmatrix} A_i \\ B_i \\ C_i \\ D_i \end{bmatrix}, \tag{394}$$

with $H(x) = H^{(a)}H^{(b)}(x)$ for $i \in [0, N+1]$. It is important to observe that the relations $A_0 = C_0 = B_{N+1} = D_{N+1} = 0$ must be imposed since the media at edges are supposed semi infinite (free field radiation). In other words, no progressive wave in the back medium (identified by $i = 0$) and no regressive wave in the front medium (identified by $i = N+1$) are considered. Similarly, the general solution for the solid/foam variables in a given layer is given by

2T Matrix System in Solid

$$\begin{bmatrix} q_{s,i}(x) \\ T_{s,i}(x) \end{bmatrix} = G(x) \begin{bmatrix} E_i \\ F_i \end{bmatrix} + \begin{bmatrix} 0 \\ T_{s,0} \end{bmatrix}, \tag{395}$$

for $i \in [1, N]$. Here, the matrix

$$G(x) = \begin{bmatrix} \kappa_s \sigma_{solid} e^{-\sigma_{solid} x} & -\kappa_s \sigma_{solid} e^{\sigma_{solid} x} \\ e^{-\sigma_{solid} x} & e^{\sigma_{solid} x} \end{bmatrix}, \tag{396}$$

is introduced.

The knowledge of the complete solution of the problem for all the physical variables in all layers (see Eqs.(394) and (395)) allows to implement the boundary conditions given in Eqs.(361) to (376). Indeed, it is not difficult to prove that these conditions are represented by $6N+4$ linear equations, with exactly $6N+4$ unknown coefficients. The system is well posed and can therefore always be solved by standard numerical methods as seen in previous sections. $\tilde{p}$, v, q, T_f, q_s, T_f are then identified for all position x and at all frequency f.

Those boundary conditions are then now explicitly written in matrix form. The continuity of p, v, T in the fluid are written

$$p_i(x_i) = p_{i+1}(x_i) \Leftrightarrow H_{i,x_i}(1,:)\mathtt{ABCD}_i = H_{i+1,x_i}(1,:)\mathtt{ABCD}_{i+1}, \tag{397}$$
$$v_i(x_i) = v_{i+1}(x_i) \Leftrightarrow H_{i,x_i}(2,:)\mathtt{ABCD}_i = H_{i+1,x_i}(2,:)\mathtt{ABCD}_{i+1}, \tag{398}$$
$$T_i(x_i) = T_{i+1}(x_i) \Leftrightarrow H_{i,x_i}(4,:)\mathtt{ABCD}_i = H_{i+1,x_i}(4,:)\mathtt{ABCD}_{i+1}, \tag{399}$$

and knowing that there is no reflections from the boundary layers $A_1 = C_1 = B_N = D_N = 0$. Continuity of T in the solid is written

$$T_{s,j}(x_j) = T_{s,j+1}(x_j) \Leftrightarrow G_{j,x_j}(2,:)\mathtt{EF}_j = G_{j+1,x_j}(1,:)\mathtt{EF}_{j+1}, \tag{400}$$

and since the solid does not exist in the boundary layers we have $E_1 = F_1 = E_N = F_N = 0$. Lastly, heat flux interaction in the fluid and solid medium is

$$\begin{aligned} q_{i+1}(x_i) &= q_i(x_i) + g(T_{s,i}(x_i) - T_i(x_i)) \\ \Leftrightarrow H_{i+1,x_i}(3,:)\mathtt{ABCD}_{i+1} &= H_{i,x_i}(3,:)\mathtt{ABCD}_i \\ &\quad + g(G_{i,x_i}(2,:)\mathtt{EF}_i - H_{i,x_i}(4,:)\mathtt{ABCD}_i) + gT_{s,0}, \end{aligned} \tag{401}$$

$$\begin{aligned} q_{s,j+1}(x_j) =& q_{s,j}(x_j) - g(T_{s,j}(x_j) - T_j(x_j)) \\ \Leftrightarrow G_{j+1,x_j}(1,:)\mathtt{EF}_{j+1} =& G_{j,x_j}(1,:)\mathtt{EF}_j \\ &- g(G_{j,x_j}(2,:)\mathtt{EF}_j - H_{j,x_j}(4,:)\mathtt{ABCD}_j) - gT_{s,0}, \end{aligned} \tag{402}$$

or equivalently, since the temperature are continuous in the solid and the fluids

$$\begin{aligned} q_{i+1}(x_i) =& q_i(x_i) + g(T_{s,i+1}(x_i) - T_{i+1}(x_i)) \\ \Leftrightarrow H_{i+1,x_i}(3,:)\mathtt{ABCD}_{i+1} =& H_{i,x_i}(3,:)\mathtt{ABCD}_i + g(G_{i+1,x_i}(2,:)\mathtt{EF}_{i+1} \\ &- H_{i+1,x_i}(4,:)\mathtt{ABCD}_{i+1}) + gT_{s,0}, \end{aligned} \tag{403}$$

$$\begin{aligned} q_{s,j+1}(x_j) =& q_{s,j}(x_j) - g(T_{s,j+1}(x_j) - T_{j+1}(x_j)) \\ \Leftrightarrow G_{j+1,x_j}(1,:)\mathtt{EF}_{j+1} =& G_{j,x_j}(1,:)\mathtt{EF}_j - g(G_{j+1,x_j}(2,:)\mathtt{EF}_{j+1} \\ &- H_{j+1,x_j}(4,:)\mathtt{ABCD}_{j+1}) - gT_{s,0}. \end{aligned} \tag{404}$$

2.6 ADDED HEAT LOSS AT THE INTERFACES

It is important to notice that the models created in Sections 2.2 through 2.5 do not take into account heat losses at solid interfaces. Hence, in order for heat loss to be implemented rigorously in our models, we need to suitably modify the continuity equation for the heat flux at each interface of the system both for 1T and 2T models. Those modification will here be explicitly written.

2.6.1 *1T models modifications*

We consider for now the continuity of heat flux in any geometry of a 1T model. In particular, considering a layer i, the heat flux balance boundary condition at the interfaces of the system can be written

$$-\vec{\beta}_{s,i}T(l_{i-1}) - \kappa_{i-1}\vec{\nabla}T(l_{i-1}) = -\kappa_i\vec{\nabla}T(l_{i-1}), \tag{405}$$

$$-\kappa_i\vec{\nabla}T(l_i) = -\kappa_{i+1}\vec{\nabla}T(l_i) + \vec{\beta}_{s,i}T(l_i). \tag{406}$$

More specificaly in the case of plane wave radiations it can be written as

$$-\beta_{s,i}T(l_{i-1}) - \kappa_{i-1}\frac{dT}{dx}(l_{i-1}) = -\kappa_i\frac{dT}{dx}(l_{i-1}), \quad (407)$$

$$-\kappa_i\frac{dT}{dx}(l_i) = -\kappa_{i+1}\frac{dT}{dx}(l_i) + \beta_{s,i}T(l_i), \quad (408)$$

where the coefficient $\beta_{s,i}$ is associated to a solid phase and models the influence of heat conduction, convection, and radiation losses. The total loss is considered proportional to the temperature.

2.6.2 *2T model modifications*

To introduce the heat loss effect in the 2T model similarly as for 1T, Eqs.(365),(370) and (375) must be substituted with

$$q_i(x_i) = q_{i-1}(x_i) + g(T_{s,i}(x_i) - T_i(x_i)) - \beta_{s,i}T_i(x_i), \quad (409)$$

$$q_1(x_1) = q_0(x_1) + g(T_{s,1}(x_1) - T_1(x_1)) - \beta_{s,i}T_1(x_1), \quad (410)$$

$$q_{N+1}(x_{N+1}) = q_N(x_{N+1}) + g(T_{s,N}(x_{N+1}) - T_N(x_{N+1})) - \beta_{s,i}T_N(x_{N+1}), \quad (411)$$

where the coefficient $\beta_{s,i}$ is associated to a solid phase and models the influence of heat conduction, convection, and radiation losses. The total loss is considered proportional to the temperature.

In this section a new coefficient β_s is introduced, which quantifies the rate of heat loss per unit area in $[W.K^{-1}.m^{-2}]$ at the interface of solid/fluid media. It is shown that it can be added to the heat flux continuity boundary condition in all 1T and 2T models. It is considered proportional to the temperature and while this is a good approximation for losses due to conduction and convection, it is however a poor representation of the radiated heat which is typically proportional to the fourth power of the temperature. Nevertheless, this approximation is valid since thermal losses by radiation in a thermophone were proven to be negligible in most of cases [55]. Papers which take β_s into account usually determined its value through experimental results [43, 76, 78] and more general approaches for considering imperfect interfaces can be found in the literature [154, 155].

2.7 FAR FIELD RADIATION FROM PLANE SOURCE

The models created in Sections 2.2 and 2.5 assume infinitely large plane surfaces. This allows us to have near field (NF) estimation of the sound

pressure and while this helps for the understanding of thermoacoustic sound generation, it fails to represent real measurement made in the far field (FF) of finite size thermophones. In order to be able to compare those NF estimation with real life measurement, Rayleigh's integral was implement.

For a plane surface of finite size at $z = 0$ vibrating with the velocity v, each point of the plane can be considered as a point source. As such each point will generate sound pressure and the total sound field is found by superposition using Rayleigh's second integral. The sound field for a finite vibrating panel in free field mounted on a infinite rigid baffle is then obtained by integrating over the finite panel as

Rayleigh's Integral

$$p_{FF}(x,y,z) = \frac{i\omega\rho_g}{4\pi}\int\int_{[-L_x,L_x],[-L_y,L_y]} v(x',y')\frac{e^{-ik\sqrt{(x-x')^2+(y-y')^2+z^2}}}{\sqrt{(x-x')^2+(y-y')^2+z^2}}dx'dy'. \tag{412}$$

with x, y, z being the coordinate of the observation point and x', y' those of the generation point. The subscript $_{FF}$ stands for far field. Here we divided by 4π since we considered the point source to radiate in free field and not mounted on a backplate which would double the pressure [156–158]. In order to compare to on axis experimental results we define $x = y = 0$ and z as the distance between the microphone and the thermophone. The thermophone equivalent vibrating surface is assumed to be at the thermal layer length $\mathcal{L}_{th} = \frac{\nu_{th}}{\omega} = 2\sqrt{\frac{C_0 l_k}{2\omega\gamma}} = \sqrt{\frac{2\alpha}{\omega}}$ as defined in Eq.(154).

By estimating the pressure at the thermal layer still in the near field and applying Eq.(412) it is then possible to compare our model to real measurement of plane, finite size thermophones. This was here applied for plane surfaces but the theory is also valid for cylinder or sphere thermophone in the far field. Due to the standard shapes of thermophone, only the plane case is explicitly written.

CONCLUSION

In this Chapter, different theoretical models have been created based on the conservation equations. The goal was to create flexible models which could be adapted to many different geometries and which could replace many various models found in the literature that are not easily comparable. Another model was also constructed whose objective was to simulate thermoacoustic sound generation from thick, foamlike thermophone geometries.

In Section 2.1 the conservation of mass, momentum and energy have been written in linear form assuming small deformations of $(\rho, \vec{v}, p, T, s, e)$. This was first done for a viscous fluid with thermal transfer in Eq.(56) Section 2.1.2 before considering an isotropic, homogeneous solid with thermal, viscous and elastic properties in Eq.(118) Section 2.1.3.

Sections 2.2, 2.3 and 2.4 solved those systems of equations for plane wave, cylindrical wave and spherical wave radiation respectively. Using the conservation equations, pressure p, particle velocity v and heat flux q were written as function of the temperature variations T. Beside having differences in the derivative of the variables due to the differences in the coordinate system used in each case (Cartesian, cylindrical and spherical respectively), the associated 4_{th} order biquadratic linear differential equation associated to the temperature variation are similar in all geometries whether in fluid (Eqs.(130), (227) and (306)) or solid (Eqs.(171), (254) and (314)) media. The modes solutions of the associated differential equation are then similar in all cases. Assuming weak thermal conduction and viscosity, a first order approximations of those modes are found in Eqs.(155) and (268) for fluid and solid respectively. They represent the wavenumbers of two progressives and regressive waves associated to thermal and acoustic waves generated by the thermoacoustic process.

The temperature variations are then written explicitly in each cases. For instance, T in solid is found in Eqs.(176), (255) and (315). p, v and q are then explicitly deduced. At the same time the normal stress tensor $\tilde{p}$ was defined to replace the pressure which is not continuous between media. Those systems of equations were solved in all three geometries in an "ideal thermophone" case in which the thermophone is represented as an ideal gradient of temperature and the wave propagates in a single, semi infinite medium. Building on this ideal case, the equations were then written in a matrix form allowing the extension of the model to a multilayer one in which the layers at the extremities are supposed semi infinite and the continuity of $\tilde{p}$, v, q, T is preserved at each layer interface. 3 flexible models were then created for 3 different types of geometry and for any kind of medium (solid or fluid).

Afterward, a two temperature model for thick foamlike thermophones was created in Section 2.5. Due to the high porosity of those materials and the potentially high input power supplied to the thermophone, non thermal equilibrium is assumed between the two phases. Hence, a model in which the pores of the thermophone (solid) and the fluid inside of it coexist with different temperatures is assumed. This case is analysed for plane wave generation and so most equations are similar as in Section 2.2. The novelty resides in the addition of a coupling coefficient g allowing the transfer of energy at the interface solid/fluid. The model is then written in a matrix form for multilayer resolution. However, unlike the previous models, this multilayer model is only meant for a single thermophone radiating in free field. The layers here representing the branches of the foam, the 2T model is meant to be a better representation of foamlike materials which should not be simulated as continuous medium as in any 1T models. This will be proven in the next chapter.

In Section 2.6 it was shown that both 1T and 2T models lack to take into account the heat losses by conduction, convection and radiation at solid/fluid interfaces. A coefficient β_s proportional to temperature variations was then introduced in the heat flux conservation equation in order to quantify those losses if needed.

Lastly Section 2.7 extended the near field estimation of the pressure from the model to the far field for finite size thermophones. Using Rayleigh's integral, the sound radiation in the far field of a finite size thermophone was deduced from the velocity in the near field calculated by our models.

Models created in this chapter will now be confronted to models from the literature. They will then be used for analysis of the thermoacoustic radiation process and compared to experimental results.

Part III

SIMULATION ANALYSIS

3

MODELS VALIDATION AND ANALYSIS

This chapter aims at providing a thorough understanding of thermophone's radiation in different geometries. The models created in Chapter 2 will be confronted to theoretical models and experiments from the literature in order to validate them.

At first the multilayer model for plane waves will be investigated. Due to the variety of literature model regarding plane wave generation, validating the model also permits a detailed analysis of thermoacoustic sound generation behavior. Various standard thermophone configurations will be investigated before the flexibility of the presented model is used to study novel configurations. This analysis along with the theoretical description of the corresponding model are the contents of the first published article of this PhD [1].

The multilayer model for cylindrical and spherical waves are then considered. Similarly, those models are compared to models from the literature. However, due to the lack of interest in those geometries, fewer comparisons are available. Nonetheless, the interest in those geometries is legitimate as they can describe the thermoacoustic effect of thermophones at a different scale. For instance it can represent the microscopic tubular shape of foams or CNT, whereas they are often approximated as plane surfaces at a macroscopic scale. Specific geometries are explored and this analysis along with the associated theoretical model are in consideration for publication as a fourth paper.

Lastly the novel 2T theoretical model is analysed and compared with the results provided by the literature and the 1T model. The relevance of using a 2T model is explained and an exhaustive comparison between 1T and 2T models is made to understand in which case each model is more appropriate. This analysis along with the associated theoretical model is published in the second article of this work [2].

3.1 PLANE WAVE, ONE TEMPERATURE MODEL

The multilayer model created in Section 2.2 is here compared to models from the literature as well as experiments. Once the model is validated and the thermophone sound generation process understood, novel thermophones configurations are investigated.

3.1.1 *Comparison and Analysis with Literature's models*

In this Section, we take into consideration different configurations of thermophone devices and we analyze their frequency response by means of the previously introduced procedure. In addition, we compare our results with those of several models discussed in recent literature. The values of the physical parameters defining the materials (air, water, thermophone, solid substrate) used in this analysis are listed in Tables 3 and 4. The other parameters depend on the system investigated and can be found in Table 5. The most important quantity considered is the sound pressure level, which is defined by the following expression

Sound Pressure Level

$$\mathrm{SPL} = 20\log_{10}\left(\frac{p_{\mathrm{rms}}}{p_{\mathrm{ref}}}\right), \tag{413}$$

where p_{rms} is the root mean square pressure (i.e. $|p|/\sqrt{2}$, where p is the complex pressure introduced in previous sections) and p_{ref} is the reference sound pressure being, by definition, 20μPa in air and 1μPa in water.

It should also be noted that all plots in this section display sound pressure level in the near field (NF) only. If some models from the literature have their equation in the far field (FF), they can be converted back in near field by using Rayleigh distance

Rayleigh's Distance

$$R_0 = \frac{Af}{C_0}, \tag{414}$$

where A is the thermophone surface, $f = \frac{\omega}{2\pi}$ is the frequency and C_0 the wave velocity. The approximation used is then

$$p_{\mathrm{FF}} = p_{\mathrm{NF}}\frac{R_0}{d}, \tag{415}$$

where d is the distance between the position of observation and the active surface of the thermophone. This simplified version of far field estimation is the one employed in the literature hence why the more precise Rayleigh's integral described in Section 2.7 for far field estimation is not yet used.

	ρ [kg· m^{-3}]	C_p [J·kg^{-1}· K^{-1}]	C_v [J·kg^{-1}· K^{-1}]	B [Pa]	α_T [K^{-1}]
Gas, air (g)	1.20	9.96×10^2	7.17×10^2	1.01×10^5	3.33×10^{-3}
Thermophone (s)	0.03×10^3	2.38×10^2	2.38×10^2	2.78×10^5	0.6×10^{-6}
Substrate (b)	4.5×10^3	5.23×10^2	5.23×10^2	1.14×10^7	9.00×10^{-6}
Fluid, water (w)	9.99×10^2	4.43×10^3	4.17×10^3	2.15×10^9	3.03×10^{-4}

Table 3: Parameters describing the physical behavior of the materials constituting the thermophone systems investigated.

	λ [Pa·s]	μ [Pa·s]	λ_0 [Pa]	μ_0 [Pa]	κ [W·K^{-1}·m^{-1}]
Gas, air (g)	5.61×10^{-6}	1.68×10^{-5}	0	0	2.62×10^{-2}
Thermophone (s)	0	0	1.39×10^5	2.08×10^5	1.25
Substrate (b)	0	0	8.46×10^6	4.36×10^6	21.9
Fluid, water (w)	2.62×10^{-3}	1.14×10^{-3}	0	0	6.07×10^{-1}

Table 4: Other parameters describing the physical behavior of the materials constituting the thermophone systems investigated.

	x [m]	l_b [m]	l_g [m]	l_s [m]
Fig.34	$[5,\ 10] \times 10^{-2}$	0	0	1×10^{-6}
Fig.35	5×10^{-2}	0	0	1×10^{-6}
Fig.36	5×10^{-2}	0	0	1×10^{-6}
Fig.38	5×10^{-2}	∞	0	1×10^{-6}
Fig.40	5×10^{-2}	1×10^{-5}	0	1×10^{-6}
Fig.41	5×10^{-2}	∞	0	1×10^{-4}
Fig.42	5×10^{-2}	∞	0	$[1,\ 9,\ 81] \times 10^{-6}$
Fig.44	5×10^{-2}	$(1/27) \times 10^{-4}$	$(1/3) \times 10^{-4}$	1×10^{-6}
Fig.45	5×10^{-2}	∞	8×10^{-4}	1×10^{-7}
Fig.49	5×10^{-2}	0	$[0,\ 1/36,\ 1/12,\ 1/4,\ \infty] \times 10^{-4}$	1×10^{-6}
Fig.51	5×10^{-2}	0	$[0,\ 1/10] \times 10^{-4}$	1×10^{-6}
Fig.52	5×10^{-2}	0	$[1/16,\ 1/12,\ 1] \times 10^{-4}$	1×10^{-6}

Table 5: Specific geometrical parameters adopted in the analysis of different structures investigated. For each figure with SPL results, we clearly indicated the details defining the corresponding configuration. In all plots we assumed a thermophone surface $A = 4 \times 10^{-4} m^2$ and an input power $P_{in} = 1W$. The rate of heat loss per unit area of thermophone β_s is considered only in Fig.35 with the value $\beta_s = 28.9$ W/(m^{2}K). The viscosities λ and μ have been considered only in the results of Figs.36 and 51.

Thermophone in free field

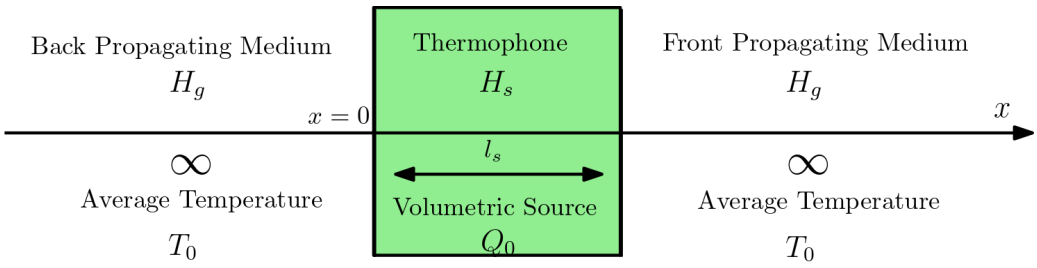

Figure 33: Schematic of a thermophone radiating in free field. The plane waves are symmetrically generated within the back and the front media.

One of the most widely used model is the so-called *piston based model* introduced by Arnold and Crandall [23] and successively improved by Daschewski *et al.* [40] and Xiao *et al.* [43] by introducing effect of a substrate, the heat stored in the thermophone and the rate of heat loss per unit area of the device (due to conduction, convection, and radiation). This model considers the thermophone radiating in free field from both sides, as shown in Fig.33. The sound generation is assumed to occur at the surfaces of the thermophone, in the so-called thermal layer, which is usually quite thin as specified in Eq.(154). In these models, the influence of the thermophone thickness l_s is considered through the HCPUA given by $C_{s,s} = \rho_s C_{p,s} l_s$. Lim *et al.* [78] also developed an improved model based on the previous assumptions but they described the thermoacoustic propagation with a real coupling between mechanical and thermal waves. In any case, since the order of magnitude of the acoustic wavenumber is much lower than the one of the thermal wavenumber, the results of Refs.[43] and [78] show good consistency. For comparison, the result of Lim *et al.* [78] is rewritten here as

$$p_{rms,NF} = \frac{P_{in}}{2\sqrt{2}A} \frac{\gamma_g - 1}{\left|\beta_s + \kappa_g \sqrt{\frac{i\omega}{\alpha_g}} + \frac{1}{2} i\omega C_{s,s}\right|} \sqrt{\frac{\omega}{\alpha_g}} \frac{\kappa_g}{C_0}, \tag{416}$$

where β_s is the rate of heat loss per unit area of thermophone ($W/(m^2K)$), which includes the influence of conduction, convection, and radiation. Moreover, $C_{s,s}$ is the thermophone HCPUA, κ_g is the thermal conductivity, α_g is the thermal diffusivity $\frac{\kappa}{\rho C_p}$ and γ_g is the ratio C_p/C_v of the propagation region (gas). In addition, A is the thermophone area, P_{in} is the input power and, finally, C_0 is the isentropic sound velocity.

In Fig.34 the result from Eq.(416) is compared to our model. Here, we adopted $\beta_s = 0$ and it can be seen that both models are consistent with each other from 1Hz to about 100kHz. The difference observed in high frequencies is explained by the fact that Eq.(416) (and most literature

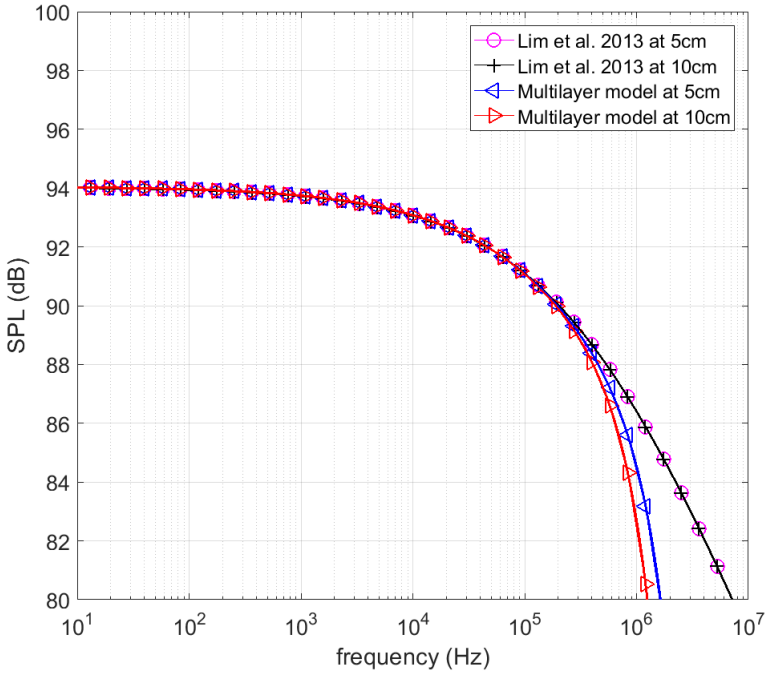

Figure 34: Frequency response of the thermophone in free field determined by means of the Lim *et al.* model [78] and our multilayer model. We plotted here the results for $\beta_s = 0$ and for two different observation distances.

models) uses a 0-th order approximation for the acoustic and thermal wavenumber, as explained in Section 2.2.1. If this approximation holds for a standard hearing frequency range (20 to 20kHz), when considered at very high frequencies it gives inaccurate results since the first order (and higher) terms become not negligible and should be taken into consideration (see Eqs.(155) for details).

In our model, where we consider the exact thermal and acoustic wavenumbers, it is interesting to remark that the high frequency drop depends on the distance between thermophone and observation point. As a matter of fact, the drop will occur at lower frequencies as this distance is increasing, limiting the high frequency efficiency of the thermophone for large distances. This behavior can be only observed with an accurate determination of the wavenumbers, as observed in Fig.34, where we plotted the frequency response at two different observation positions.

We further discuss the origin of the drop at high frequency, independently of the approximations adopted. As it is known, the sound generated by a thermophone occurs due to the fluctuation of heat in the air layer near the thermophone. The thickness of this active layer is related to the thermal wavenumber and is given by Eq.(154). It is then

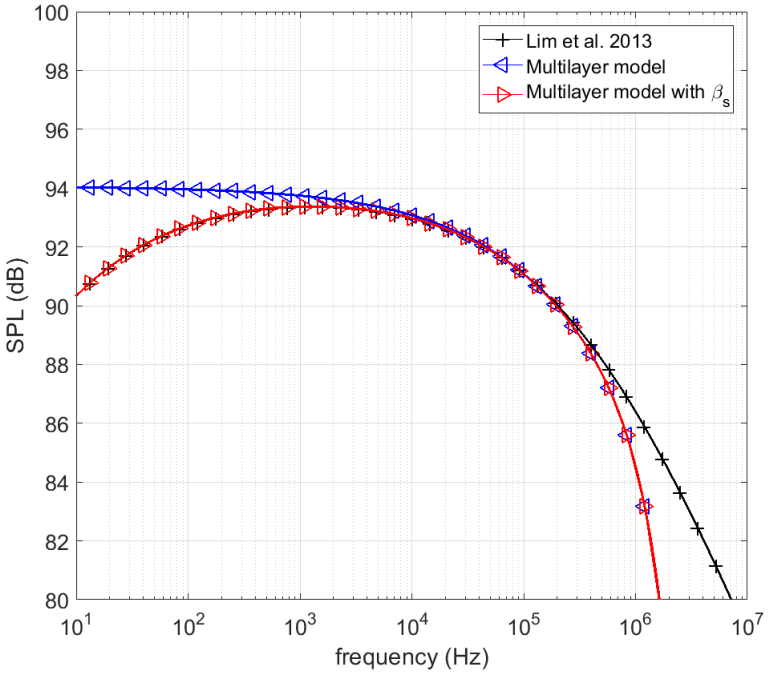

Figure 35: Frequency response of the thermophone in free field determined by means of the Lim *et al.* model [78] and our multilayer model. We plotted here the results for $\beta_s = 28.9$ and we also shown the response obtained through the multilayer model with $\beta_s = 0$ for comparison.

proportional to $1/\sqrt{\omega}$ whereas the acoustic wavelength is proportional to $1/\omega$. Since for low frequencies the thermal layer is much smaller than the acoustic wavelength, in this condition the sound is generated first in the thermal layer (a small fraction of the acoustic wavelength) and then propagated in the adjacent medium. This however stops to be true for high frequencies due to the different decreasing rate of each wavelength. We explain the behavior when the thermal layer is larger than the acoustic wavelength as follows. In this case, many acoustic wavelengths compose the thermal layer. Since the thermal wavelength is of the same order of the thermal layer, the spatial temperature variations (slower) are not able to follow the spatial pressure variation (faster) and the sound generation becomes less efficient, thus generating the observed drop in Fig.34 (both models).

Figure 35 shows the results for the same configuration of Fig.34 but now with a non zero coefficient β_s, taking into account the rate of heat loss per unit area of thermophone. It is seen that the mid and high frequency range doesn't change but at low frequencies there is a drop in the SPL. The heat loss has been implemented rigorously also in our model, by suitably modifying the continuity equation for the heat flux

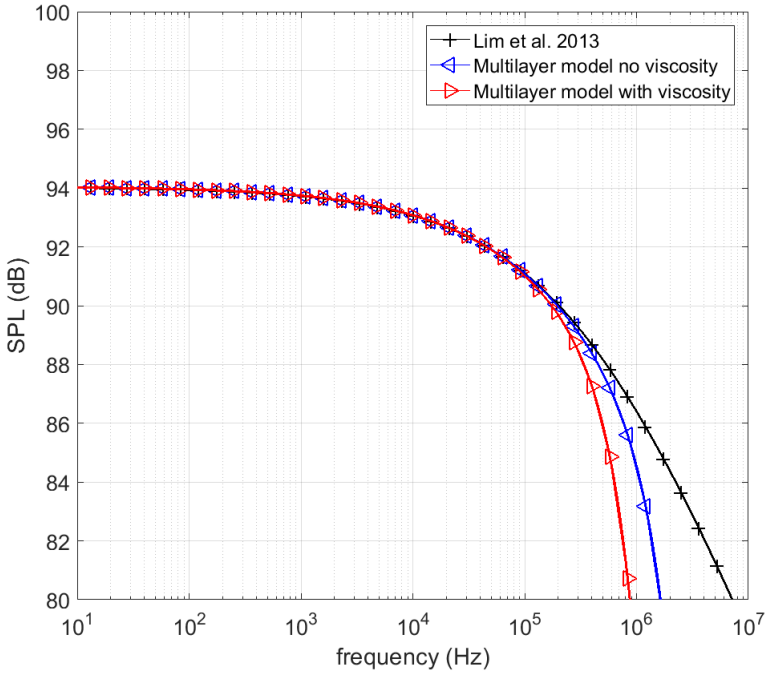

Figure 36: Frequency response of the thermophone in free field determined by means of the Lim *et al.* model [78] and our multilayer model. We plotted here the results for $\beta_s = 0$ at a distance of 5 cm, and we introduced the air viscosity in our model to show its effect at high frequency.

in Section 2.6.1. Papers which take β_s into account determined its value through experimental results [43, 76, 78]. The good agreement between our modified model and results from Lim *et al.* [78] is clearly shown in Fig.35.

Lastly, Fig.36 displays the results of our model with and without the air viscosity. It is seen that adding viscosity increases the high frequency drop rate. Since its influence is negligible for frequencies lower than 100kHz, the literature models often neglect it (except for Refs.[40, 79]).

Thermophone on substrate

Another important structure investigated in the literature consists in a thermophone layer directly placed on a substrate (without gap) and radiating in air, as shown in Fig.37. One model describing this system has been developed by Hu *et al.* [81]. This model is based on the balance equations earlier developed for describing the photoacoustic effect [30], and aims at reproducing the experimental results presented by Shinoda *et al.* [32]. This model takes the thickness of the thermophone into ac-

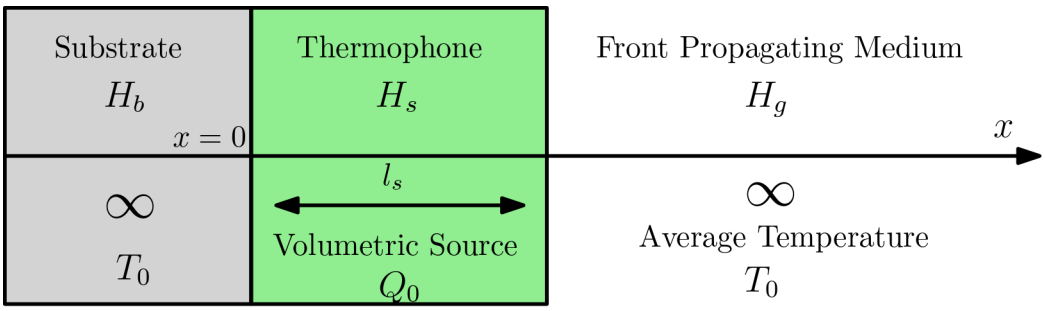

Figure 37: Schematic of a thermophone placed on a solid substrate on the left and radiating in free field on the right. The plane waves are non-symmetrically generated within the back and the front media.

count and consider the conservation of energy in the solids but neglect the propagation of the acoustic wave inside it. By using a surface input power P_{in}/A, the obtained pressure is [81]

$$p_{rms,NF} = \left| \frac{i d_t d_a k_g}{i d_a k_g (M\kappa_s\sigma_s + \kappa_g\sigma_g) - d_t\sigma_g(M\kappa_s\sigma_s + i\kappa_g k_g)} \times \left(e^{-\sigma_g x} - \frac{\sigma_g}{ik_g} e^{-ik_g x} \right) \frac{P_{in}}{A\sqrt{2}} \right|. \tag{417}$$

The use of a surface density power (instead of a volume density power as in other theories and in our model) is justified by the fact that this model is dedicated to the Shinoda *et al.* experiment, in which there is a 30nm aluminum film acting as the heat source. Most models are however considering that the whole thermophone is heating and so it is interesting to see how Hu's model holds with a volumetric source. By replacing the surface input power P_{in}/A with a volumetric source $\frac{P_{in}}{Al_s}\frac{1}{i\omega\rho_g C_{p,g}}$ and using the same assumptions of Hu's model, we obtained the volumetric counterpart of Eq.(417), as follows

$$p_{rms,NF} = \left| \frac{1}{i\omega l_s \rho_g C_{p,g}} \frac{\kappa_s\sigma_s}{\kappa_s\sigma_s - \kappa_b\sigma_b} \times \left(e^{\sigma_s l_s} \kappa_b\sigma_b(M-1) + M(\kappa_s\sigma_s - \kappa_b\sigma_b) \right) \times \frac{i d_t d_a k_g}{i d_a k_g (M\kappa_s\sigma_s + \kappa_g\sigma_g) - d_t\sigma_g(M\kappa_s\sigma_s + i\kappa_g k_g)} \times \left(e^{-\sigma_g x} - \frac{\sigma_g}{ik_g} e^{-ik_g x} \right) \frac{P_{in}}{A\sqrt{2}} \right|. \tag{418}$$

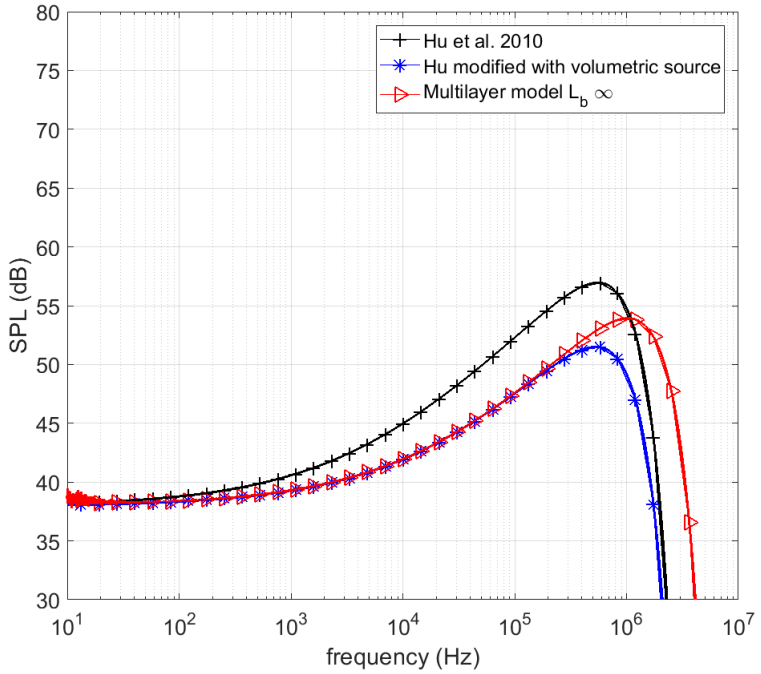

Figure 38: Frequency response of a thermophone in contact with a semi-infinite substrate on the left and propagating in air on the right (see the scheme in Fig.37). We compare the result of our multilayer model with Eq.(417) [81] and Eq.(418).

In Eqs.(417) and (418) the following definitions have been introduced following Ref.[81]

$$M = \frac{(\kappa_b\sigma_b + \kappa_s\sigma_s)e^{\sigma_s l_s} + (\kappa_b\sigma_b - \kappa_s\sigma_s)e^{-\sigma_s l_s}}{(\kappa_b\sigma_b + \kappa_s\sigma_s)e^{\sigma_s l_s} - (\kappa_b\sigma_b - \kappa_s\sigma_s)e^{-\sigma_s l_s}}, \tag{419}$$

$$d_t = \frac{i\omega\kappa_g - \sigma_g^2\alpha_g\kappa_g}{i\omega\alpha_g}, \tag{420}$$

$$d_a = \frac{i\omega\kappa_g + k_g^2\alpha_g\kappa_g}{i\omega\alpha_g}. \tag{421}$$

Here, the coefficients k and σ are the acoustic wavenumber and the thermal attenuation of each layer. The full derivation of this equation can be found in Appendix B.1.1.

The comparison of Eqs.(417) and (418) with our model, where we used a semi-infinite substrate as shown in Fig.37, can be found in Fig.38. It can be seen that there is a perfect match between Eq.(418) and our model for low and mid frequencies. For frequencies above 200kHz there is a discrepancy between the volumetric source version of Hu's model and our model. This is due to a difference in the acoustic wavenumber first order approximation. As a matter of fact, Eqs.(155) differ slightly

with Hu's solutions and this is only significant at very high frequencies. Indeed, if the wavenumbers used by Hu *et al.* are introduced in our model, there is a perfect agreement also at high frequencies. On the other hand, the case with a surface input power, described by Eq.(417), shows a higher SPL in the whole frequency range, as expected since there is no heat stored in the thermophone.

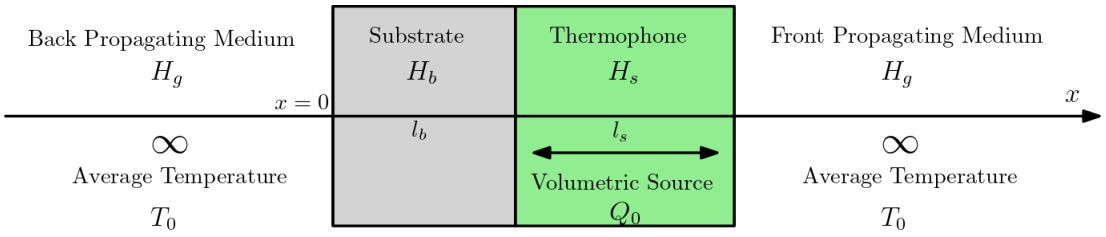

Figure 39: Schematic of a thermophone placed on a solid substrate of finite thickness on the left, and radiating in free field on the right. The plane waves are non-symmetrically generated within the back and the front media.

We consider now the case with a finite thickness of the substrate, as shown in Fig.39. This more elaborated structure can be studied through our multilayer model, and in Fig.40 a rise of SPL in the low frequency domain can be seen. In general, the presence of the substrate is useful for technological reasons, but it absorbs a large amount of heat and reduces therefore the thermophone output SPL, as seen in Fig.38. However, a small thickness of the substrate may help to ameliorate the performance. The observed SPL rise is due to the fact that since for lower frequencies the thermal penetration depth is larger, when the substrate is of a comparable order of magnitude, it will absorb less heat and so the thermophone is more efficient. The lower the frequency, the less impact the substrate has on the radiation and so the sound pressure may attain a free field radiation level. A more detailed analysis of the heat flux lost in the substrate can be found in Ref.[46].

To further investigate this configuration, we come back to the structure with infinite substrate shown in Fig.37, and we investigate the influence of the size of the thermophone. In Fig.41, we plotted our results with Eq.(416) (free field model), and with Eqs.(417) and (418). In this analysis, the thermophone is a hundred time thicker than before. First, it can be seen that the Hu *et al.* [81] model with a surface input power displays a significant rise in SPL. This rise is proportional to the thickness of the thermophone and is explained by the parameter M in Eq.(417). It approaches the value 1 for a surface input power, generating a flat frequency response in a given interval, as discussed in Ref.[81]. Indeed, concentrating the input power at the thermophone surface is more ef-

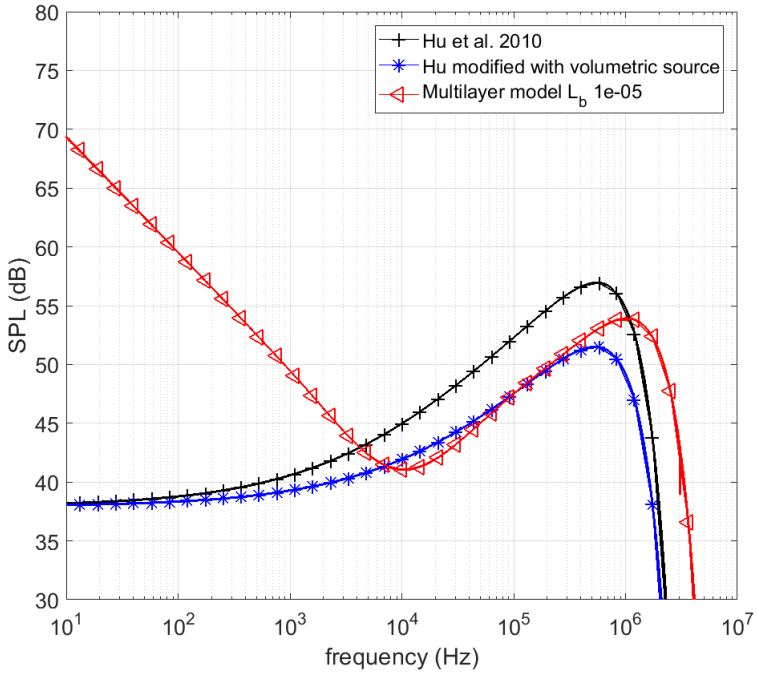

Figure 40: Frequency response of a thermophone placed on a substrate with finite thickness and radiating in air (see scheme in Fig.39). We compare the result of our multilayer model with Eq.(417) [81] and Eq.(418).

ficient than distributing the same power over the whole thermophone body, as already seen in Figs.38 and 40.

We consider now the case with a volumetric input power. Figure 41 displays that the model with a substrate is consistent with the decreasing response of the free field model for frequencies higher than 10kHz. This decreasing behavior is due to the rise of HCPUA and, therefore, to the heat stored in the sample. The fit between free field and substrate model is due to the size of the thermophone that is larger than the thermal penetration depth, thus leading to negligible influence of the substrate. It is interesting to show how the SPL of the system with increasing thermophone thickness changes moving from the case of Fig.38 to the one of Fig.41. This response evolution can be found in Fig.42, where three increasing values of l_s are considered and the results of our model are compared with Eq.(416), holding for the free field model. It is interesting to note that for increasing l_s the response of the multilayer model approaches asymptotically the response of the free field model, confirming the above discussion.

Lastly, anti-resonances around 1MHz can be seen in our model (Figs.41 and 42). These are mechanical anti-resonances occurring in the thermophone structure that can be analyzed through our model since we

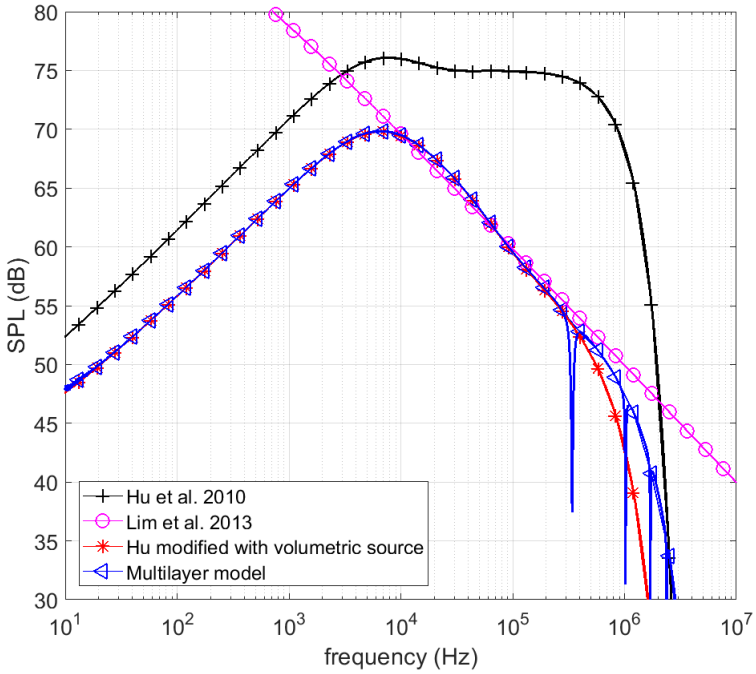

Figure 41: Frequency response of a thermophone in contact with a semi-infinite substrate on the left and propagating in air on the right (see the scheme in Fig.37). The thermophone is here a hundred time thicker than in previous plots. We compare the result of our multilayer model with Eq.(416) by Lim *et al.* [78], Eq.(417) by Hu *et al.* [81] and Eq.(418) (modification with volumetric source).

solve the complete set of wave equations in the solid layer. If these resonances/anti-resonance were mentioned in Brown *et al.* [74], they were never estimated before since they were supposed to occur at a frequency higher than the range of interest. These resonances can be attenuated by increasing the viscosity of the solid, and are influenced by the Young modulus of the thermophone as well.

Thermophone over a substrate with air gap

The most complicated structure investigated in the literature is obtained by adding a small air gap between the thermophone and the substrate, as shown in Fig.43. This kind of design was investigated by Vesterinen *et al.* [57] and by Tong *et al.* [72], in continuity with the free field modeling by Lim *et al.* [78]. Both articles consider the classical balance equations and the Tong's model also takes the heat loss into account. These models however do not consider explicitly the thermophone solid layer, which is implicitly described by the HCPUA factor. As a result of their

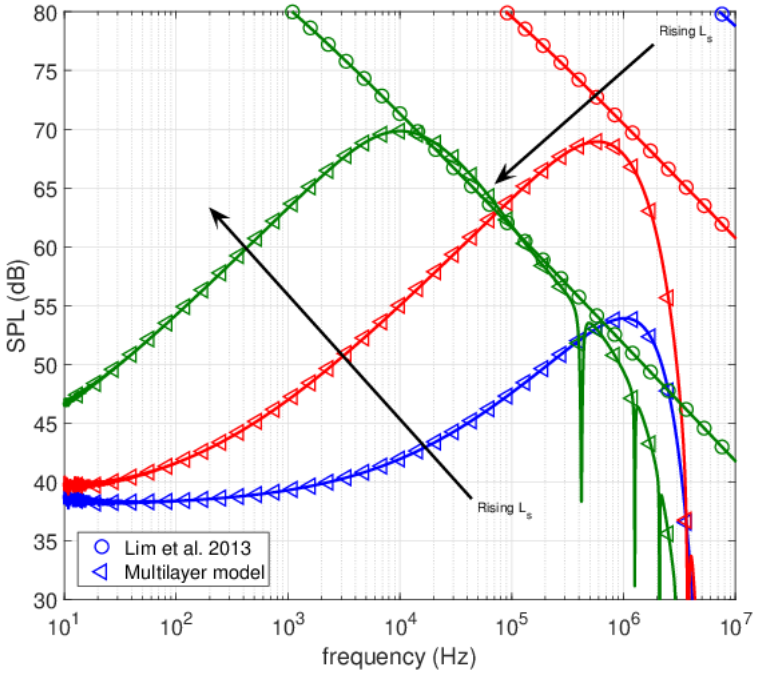

Figure 42: Frequency response of a thermophone with increasing thickness l_s in contact with a semi-infinite substrate on the left and propagating in air on the right (see the scheme in Fig.37). We compare the results of our multilayer model with Eq.(416), describing the free field thermophone [78].

calculations, assuming that there is a perfect sound reflection from the backing, Vesterinen *et al.* [57] determined an absolute maximum value for the sound pressure level of a thermophone as

$$p_{rms,NF,max} = \frac{P_{in} C_0}{\sqrt{2} A C_{p,g} T_0}. \tag{422}$$

Eq.(422) shows that the maximum sound pressure achievable for a given thermophone will only depend on the properties of the propagating medium. The input power or the ambient temperature can also be independently optimized. In order to see if this maximum pressure is achievable, an air gap between the thermophone and the substrate is added to our model and the results are compared with Tong's equation [72]

$$p_{rms,NF} = \left| \frac{C_0}{T_0 C_{p,g}} \frac{\overline{P_{in}}}{2\sqrt{2}A} \left[(\mathbf{R} - 1) e^{-\sigma_g l_g} + e^{-ik_g l_g} + 1 \right] e^{-ik_g x} \right|, \tag{423}$$

where

$$\overline{P_{in}} = \frac{-\sigma_g \kappa_g P_{in}}{(2\beta_s + i\omega C_{s,s})(1 + \mathbf{R} e^{-2\sigma_g l_g}) + 2\sigma_g \kappa_g}, \tag{424}$$

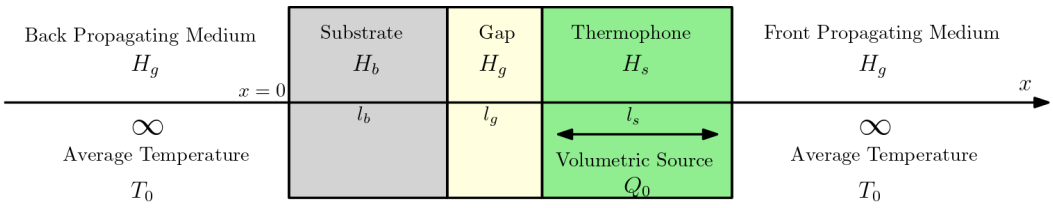

Figure 43: Schematic of a thermophone placed on a solid substrate of finite thickness on the left, and radiating in free field on the right. The plane waves are non-symmetrically generated within the back and the front media.

and

$$\mathbf{R} = \frac{\sqrt{\alpha_g} - \sqrt{\alpha_b}}{\sqrt{\alpha_g} + \sqrt{\alpha_b}}, \tag{425}$$

is the reflection coefficient of the thermal wave.

Figure 44 displays the comparison among our model, the Tong model, the Lim free field model and the Vesterinen maximal value. Here, the substrate is of finite size and the air gap is 0.033 mm wide. It is seen that at low frequencies there is a large difference between Tong's model and ours. In the mid range frequency there is good consistency between the models, and these results are close to the Vesterinen upper bound. Then, at high frequency, we observe a drop, which starts sooner in our model for the same reasons already explained in Section 3.1.1 in free field. The low frequency differences are due to the fact that the substrate has a finite size in our model and therefore is not as reflective as it is in Tong's model. It is important to remark that in the frequency range between 10kHz and 1MHz, the thermophone response is much larger than the free field level represented by the Lim *et al.* [78] result and exhibits a peak which is close to the Vesterinen upper bound. This behavior is due to the size of the air gap between thermophone and substrate. Indeed, we know that the thermal layer (in which the sound is generated) is larger for low frequencies than for high frequencies. Hence, if the air gap is not large enough, there will be heat loss in the substrate eventually leading to poorer SPL than in free field, as seen for frequencies below 1.5kHz. On the other hand, for frequencies generating a thermal layer similar to or smaller than the air gap, we have no heat loss in the substrate and it simply acts as a reflector, doubling the sound pressure, or equivalently, adding $20\log_{10}(2) = 6$dB to the SPL. This intensification can be seen above 10kHz. Furthermore, above 1MHz our model and the Tong's model display air gap anti-resonances leading to poorer SPL around these frequencies. These resonances occur before any mechanical resonance or anti-resonance within the thermophone layer and therefore they are more critical for the thermophone system design.

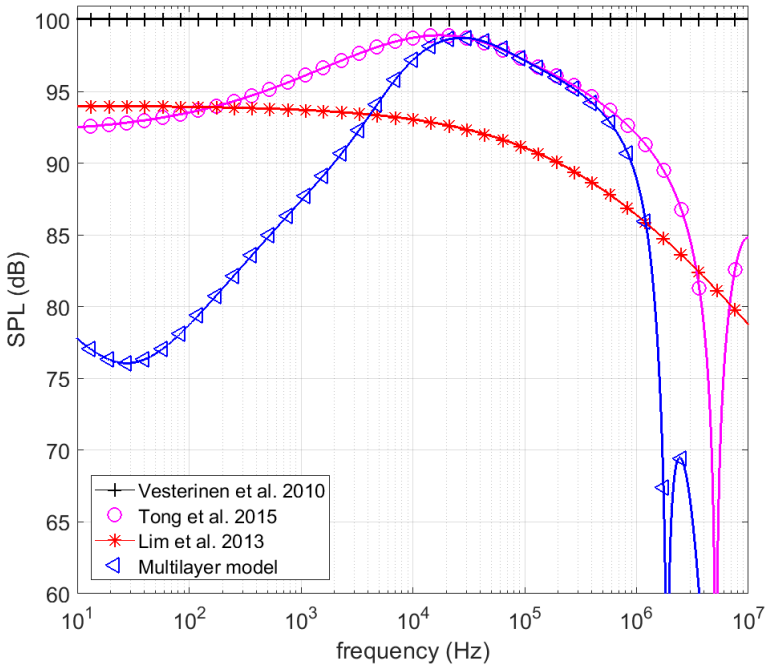

Figure 44: Frequency response of a thermophone placed over a substrate with an air gap, as shown in Fig.43. The result of the multilayer model can be compared with Eq.(423) (Tong *et al.* [72]). Moreover, we reported the result of the free field model given in Eq.(416) (Lim *et al.* [78]) and the Vesterinen *et al.* [57] upper bound reported in Eq.(422).

In Fig.45 the substrate is now infinitely large in our model and the air gap size is more than ten times larger ($l_g = 0.8$ mm). It is seen that from 200Hz to 10kHz there is less than 1dB difference between Vesterinen maximum SPL and Tong's model or ours. In this region, compared to the free field model, there is a 6dB improvement, which is consistent with a regular sound source with double sound pressure due to the backing reflection. Indeed, in this configuration the air gap is much larger than the thermal layer in the whole range from 200Hz to 10KHz and we have no heat loss in the substrate. It can be noticed that around 50Hz the results are above Vesterinen upper limit. This can be explained by the specific parameters acting as a second order filter with a typical underdamped response. The low frequency differences between Tong result and ours in Fig.45 are still due to a non perfect reflection from the substrate even though the infinite size improved it. To conclude, depending on the frequency range in which the thermophone is supposed to work, it is important to determine whether the air gap is useful to improve the sound pressure level compared to free field emission.

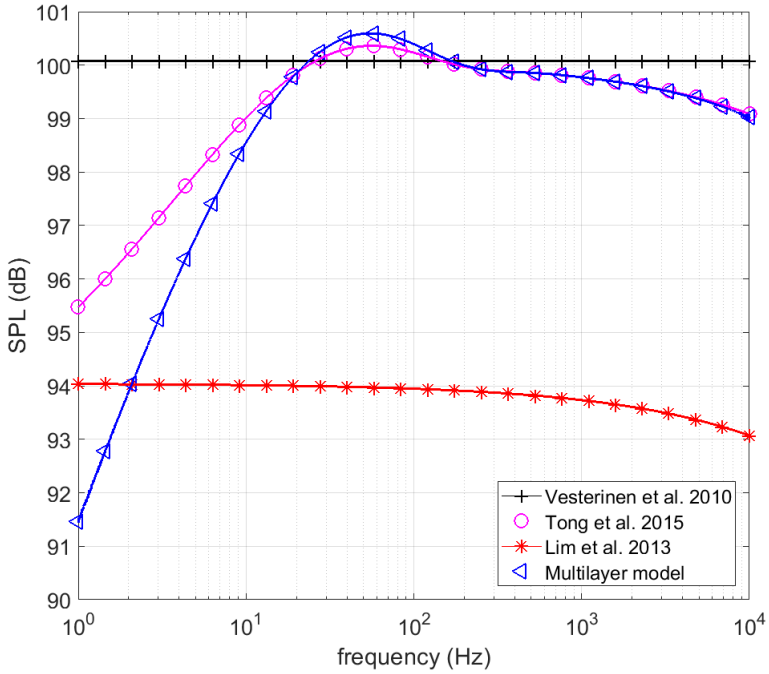

Figure 45: The same plots of Fig.44 for a structure shown in Fig.43, where the substrate is now infinitely large and the air gap size is more than ten times larger. In this case, our result and the Tong's model [72] achieve the SPL upper bound predicted by Vesterinen [57], corresponding to a 6dB improvement with respect to the Lim's free field model [78].

3.1.2 *Comparison with Literature's Experiments*

In this Section, in order to validate the model against real measurements, we compare the results of our approach with some recent experimental investigations [48, 63].

The first measurements concern the comparison between carbon multi-walled nanotubes (MWNT), providing the most attractive performance as thermoacoustic generator, and an alternative solution given by poly-acrylonitrile nanofibers (PAN) coated by indium-tin oxide (ITO) [48]. Indeed, the limited accessibility to large-size carbon MWNT sheets has promoted the research for alternative materials with interesting performances. In Fig.46 one can find the experimental results and the theoretical ones. The curves for the single-layer MWNT sheet correspond to a sample with surface 1.5×1.5 cm^2 and with an applied power of $P_{in} = 0.24$ W. On the other hand, the curves for the both-sides ITO-coated PAN sheet correspond to a sample with surface 1.2×1.5 cm^2 and with an applied power of $P_{in} = 0.29$ W. Both experimental results have been obtained at a distance of 3 cm from the thermophone surface [48].

We remark that the frequency responses shown in Fig.46 have been normalized for an input power of 1 W, in order to facilitate the comparison between the material performances.

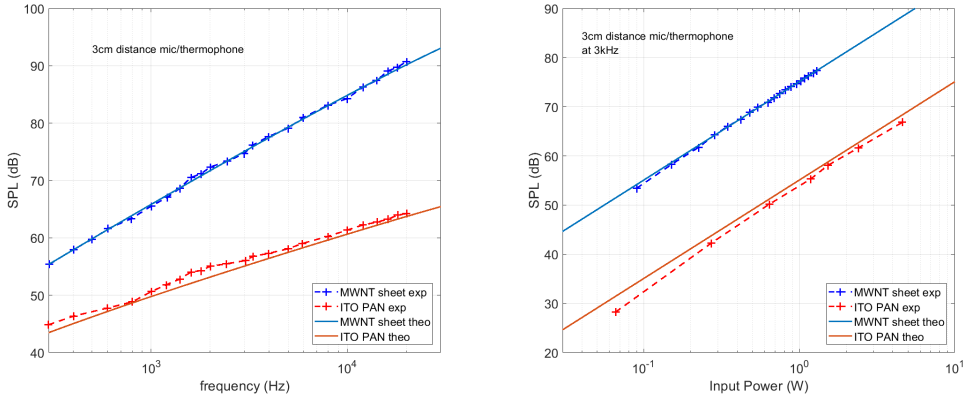

(a) (b)

Figure 46: Comparison between the thermoacoustic performances of carbon MWNT sheets and ITO-PAN sheets (experimental and theoretical results). Panel (a): frequency response of the two materials showing the behaviors SPL$\sim f^{1.0}$ for MWNT and SPL$\sim f^{0.53}$ for ITO-PAN (the plots correspond to a normalized power of 1W). Panel (b): SPL versus input power for the two materials.

The theoretical results shown in Fig.46 have been obtained with the free field model described in Section 3.1.1 in free field, where we introduced all the physical parameters given in Ref.[48]. For both the frequency response and the behavior of the SPL versus the input power, we observe a very good agreement between theory and experiments. Concerning the frequency response, the capacity of the model to represent the two different slopes SPL$\sim f^{1.0}$ for MWNT and SPL$\sim f^{0.53}$ for ITO-PAN proves that our approach is able to work with a HCPUA varying over several order of magnitude. Indeed, we have that HCPUA=13×10^{-3} $Jm^{-2}K$ for single-layer MWNT sheets and HCPUA=0.67 $Jm^{-2}K$ for ITO-coated PAN sheets. These values can be determined by observing that ρ_s =1 Kg/m^3, $C_{p,s}$=716 $JKg^{-1}K^{-1}$, l_s=18×10^{-6} m for the MWNT sheet and ρ_s =220 Kg/m^3, $C_{p,s}$=606 $JKg^{-1}K^{-1}$, l_s=5×10^{-6} m for the ITO-PAN sheets [48]. In addition, the linearity of the SPL-versus-power curves shows the linear behavior of the acoustic response in terms of the applied electric power, as implemented in the model.

We remark that the measurements presented in Fig.46 concern the acoustic far field response of the thermophone (distance of 3 cm from a thermophone with area 1.5×1.5 cm^2 or 1.2×1.5 cm^2). Therefore, in order to compare these far field measurements with our near field theo-

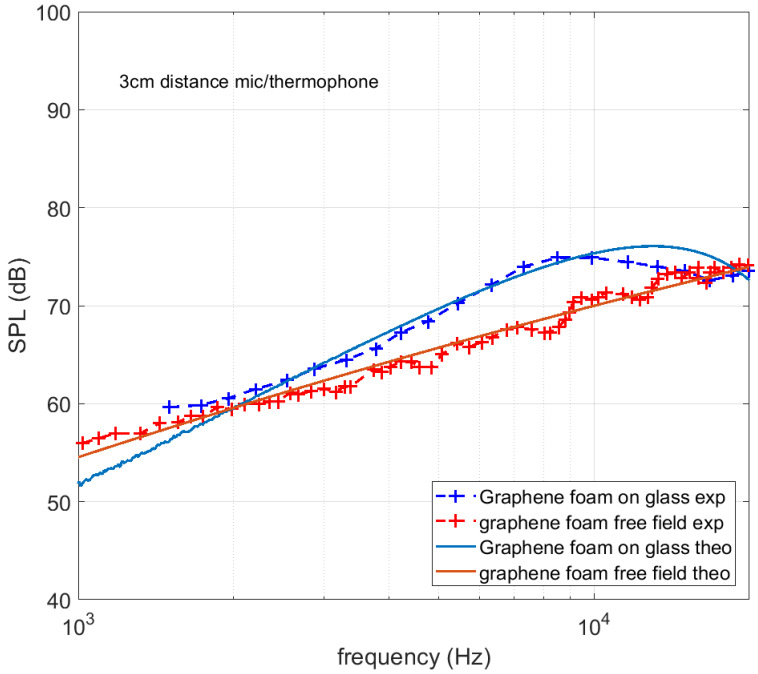

Figure 47: Experimental and theoretical frequency responses of FDGF thermophones. Both the free field case and the geometry with substrate have been considered. The free field case is well described by the relation SPL~ $f^{0.75}$, which can be compared with MWNT and ITO-PAN thermophones shown in Fig.46.

retical results, we have numerically implemented an acoustic diffraction calculation.

Hence, the theoretical curves in Fig.46 represents the results of the Rayleigh's second integral applied to the velocity field of our near field model as described in Section 2.7. In other words, our multilayer model is used to describe the thermoacoustic generation of waves (which is mostly wideband, as discussed in Section 3.1.1 in free field), whereas the diffraction theory is used to properly take into account the resulting acoustic propagation.

A second comparison with experimental measurements can be found in Fig.47. In this case we considered the results for the freeze dried graphene foam (FDGF) thermophone discussed in Ref.[63]. The FDGFs are particular graphene foams obtained with a specific procedure implemented to get uncollapsed structures, which are more efficient from the thermoacoustic point of view [63]. This material has been used as thermophone in free field and as thermophone located on a glass substrate (with a small gap). The acoustic measurements have been performed at a distance of 3cm for an applied power of $0.1W$. In Fig.47, one can find the experimental and theoretical results for both the free

field thermophone and the system with a glass substrate which has been obtained by combining the Rayleigh diffraction calculation with our near field model, as previously discussed. Again, we can observe a quite good agreement between theory and experiments. For the case of the thermophone located on the substrate we supposed a gap of 1 μm between FDGF and glass. For the implementation of the model we used the parameters declared in Ref.[63]. It is interesting to observe that the slope of the frequency response is accurately described by the expression SPL$\sim f^{0.75}$, representing an acoustic performance in-between single-layer MWNT sheets and ITO-coated PAN sheets, previously introduced. As a matter of fact, this slope corresponds to a HCPUA of $0.2 J m^{-2} K$, which is a value between $0.013 J m^{-2} K$ and $0.67 J m^{-2} K$, corresponding to MWNT and ITO-PAN, respectively. To conclude, the Rayleigh's second integral combined with the calculated velocity of our multilayer model proved to accurately reproduced real life measurements.

3.1.3 *Analysis of novel thermophone systems*

Two new configurations will now be studied using the multilayer model. The first case consists in a thermophone with (two or more) parallels generating layers, separated with air gaps. A simple case with only two generating layers, as seen in Fig.48, will be investigated by considering a fixed input power densities and the same thickness of both layers. The influence of the width of the air gap between the layers will then be examined, discussed and compared to the results of Aliev *et al.* [52] and those of Barnard *et al.* [128].

The second case will concern the sound generation in an underwater environment. The response of a one layer thermophone in an underwater free field geometry will be compared to the free field response in air. Afterward, based on an interpretation made by Aliev *et al.* [122], an hydrophobic behavior of the thermophone layer will be considered, where an air gap is assumed between the thermophone and the water, as shown in Fig.50. The results will be compared also with the Tong *et al.* theoretical model for encapsulated thermophones [132].

Multi generating layer thermophone

We analyze here the behavior of the system with two generating layers radiating symmetrically in air, as shown in Fig.48. Figure 49 displays the sound pressure level for two generating layers (each with thickness l_s and input power P_{in}), separated by an air gap of length l_g. For the

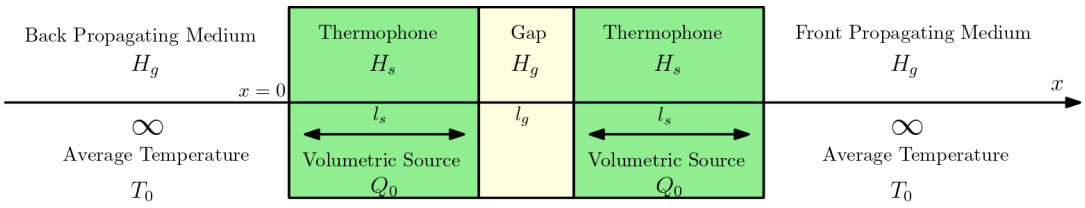

Figure 48: Schematic of a sound generation system composed of two thermophone layers placed in air, separated by an air gap, and radiating symmetrically in both directions.

sake of comparison, the free field response for a single generating layer is also plotted (with l_s and P_{in}). It is seen that for low frequencies there is a 6dB rise in sound pressure level regardless of the distance between the thermophone layers. This rise is justified by the fact that the pressure generated by two similar layers leads to double the pressure if the signals are in phase and if they can propagate without obstacles. It means that the samples are still close enough to prevent any effect of the phase difference between the sound generated by each layer and that they are acoustically transparent to one another. Furthermore, it could have been expected to see a drop in the low frequency region when the air gap is of the same order of magnitude as the thermal layer. Since the gap length does not influence this low frequency region, we deduce that there is no heat interference due to the thermal layers between each generator.

In the mid to high frequency region it is seen that the sound pressure region drops faster with a smaller gap length. The small and large gap curves are limiting cases which can be reproduced by adapting the free field model. For instance, if $l_g \to 0$, then the double layer system gets similar to a single layer with $2l_s$ and $2P_{in}$. This does not change the input power density S_0 but, since the thermophone is larger, the HCPUA gets larger and the high frequency drop is more significant. On the other hand, if the gap is large enough to cancel the thermal capacity interaction between the layers but still small enough to not create any significant phase difference, then the acoustic response is similar to that of a single layer thermophone with twice the input power (i.e., with l_s and $2P_{in}$).

The observed rise in the SPL with a multi layer thermophone concurs with the findings of Barnard *et al.* [128] and Aliev et al. [52]; however, to complete this picture, we added here the analysis of the influence of the air gap size. Although the same SPL level of this structure can be easily reproduced with a single layer thermophone by changing the input power, there is an important reason to adopt this double configuration. As explained by Aliev et al. [52], the maximum power density

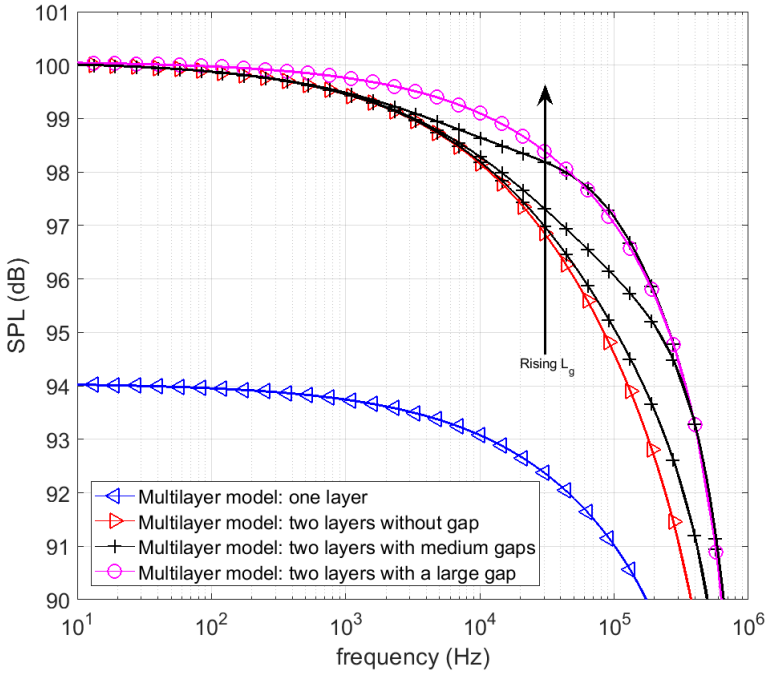

Figure 49: Frequency response of a thermophone system composed of two generating layers separated by a given air gap (see Fig.48 for details). We considered the case without gap $l_g = 0$, the case with medium gaps $l_g = 1/36, 1/12, 1/4 \times 10^{-4}$ m, and the case with a large gap $l_g = 1 \times 10^{-4}$ m (independent non-interacting layers). We can observe the effect of the air gap width and compare the result with the single layer thermophone system.

supplied to the thermophone must be limited to avoid the material failure. Of course, the simplest solution to improve the SPL without lowering the HCPUA is to increase the input power. However, the increase of the power density may generate material failure. Furthermore, the improvement of HCPUA is typically limited by the technological procedures adopted. Then, for a fixed thermophone geometry with a limited power density before failure, an interesting solution to improve the SPL is to use a multilayer geometry.

Underwater thermophone systems

The first investigations concerning underwater thermophone systems considered the encapsulation of the thermophone in a gas cavity [122, 132, 133]. This solution is useful to preserve the integrity of the thermophone material. However, the encapsulation can create resonances and therefore can limit the wide band frequency response. Consequently,

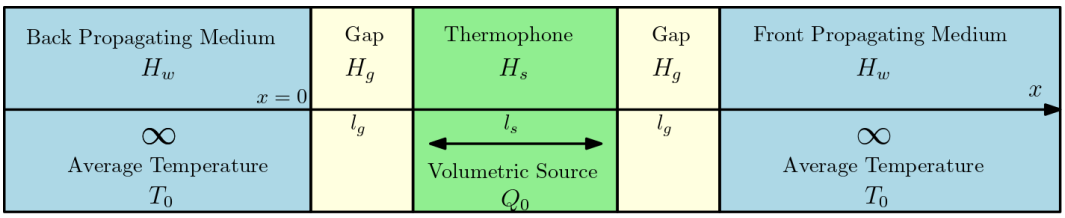

Figure 50: Schematic of a thermophone placed in water by means of two symmetric air gaps, and radiating symmetrically in both directions.

this configuration will not be investigated here since we prefer to analyze systems with a possibly wide band frequency response. Firstly, we study the emission of a simple thermophone in a free field underwater configuration. Then, we examine the underwater thermophone with two air layers generated by the hydrophobic behavior of the thermophone material.

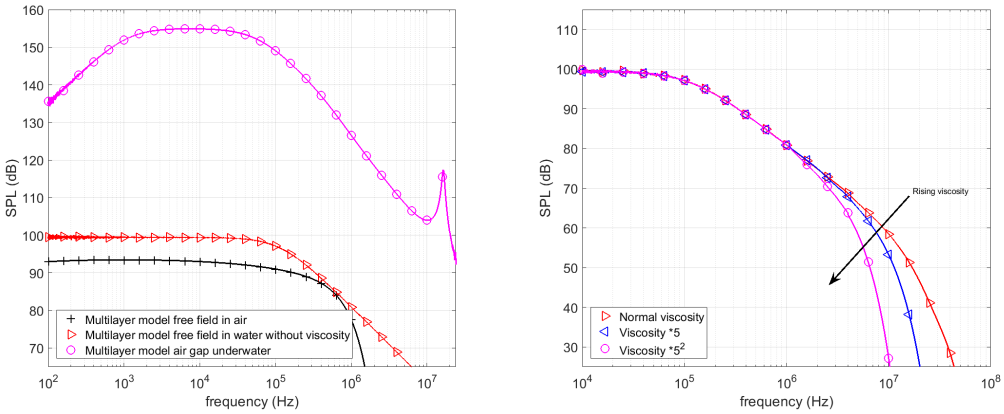

(a) (b)

Figure 51: Frequency response of a thermophone working underwater. Panel (a): we can compare the response of the underwater thermophone in free field without viscosity, the underwater thermophone with air gap (e.g. due to hydrophobicity as observed for carbon nanotubes), and finally, the thermophone working in air and in free field. Panel (b): response of the free field thermophone with the normal viscosity of water and two larger values of viscosity.

Figure 51 displays the free field response of the thermophone with and without viscosity in water, with viscosity in air, and the results of an hydrophobic model. We remember that in water the SPL is calculated with a pressure reference of 1µPa.

The low frequency behavior corresponds to a flat response for both air and water. On the other hand, the high frequency decrease starts at a lower frequency in the water and has a different slope rate (20

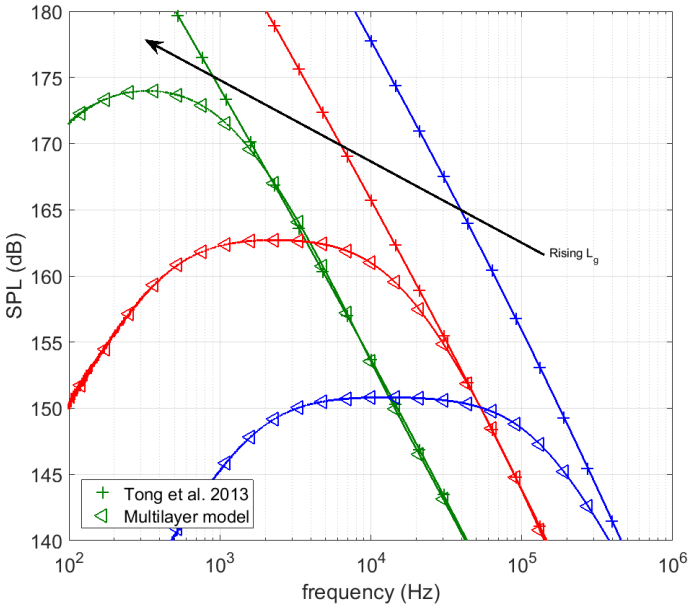

Figure 52: Frequency response for the underwater thermophone with symmetric air gaps. We can find the responses for three different air gap widths and we compare our results with those of Eq.(426), proposed by Tong *et al.* [132]. We underline the good agreement for the high-frequency behavior.

dB/dec, see Fig.51a). Those differences are mainly due to the change of parameters and reference pressure of the propagation medium. The individual parameters influence has not been further investigated here since other works have already done it considering various gases as propagation medium [70, 132]. The free field response in air is reported here mostly for reference. We now look at the differences in free field in water with different viscosity in Fig.51b. As expected, the frequency response shows a drop at a lower frequency if the viscosity is increased. The same behavior has been observed in air and shown in Fig.36. Importantly, we underline that in the numerical implementation of the model for the underwater case we cannot calculate the acoustic wavenumber k and the thermal attenuation σ through the approximated expressions in Eqs.(155), which are valid only for weak viscosity and weak thermal conductivity. Instead, we have to directly solve the fourth degree characteristic equation by numerical methods.

Aliev *et al.* [122], explained the high underwater efficiency of the carbon nanotubes thermophone through the hydrophobic behavior of the nanotubes. Therefore, we consider here a thin air layer between the thermophone and the water, as seen in Fig.50. The first result is shown in Fig.51, where an increase of 55dB can been observed with respect to the

free field response in water. Moreover, a resonance around 15MHz is also observed and is due to the air gap width between thermophone and water. Now, to better understand the band pass response for mid to low frequency, we can consider Fig.52, where the response of the system is shown as function of the air gap l_g (three different values of l_g have been adopted). Here, the equation elaborated by Tong *et al.* [132]

$$p_{rms,NF} = \left| \frac{1}{\sqrt{2}} \frac{P_{in}}{2A} (\gamma - 1) \sqrt{\frac{i\omega}{\alpha_g}} \frac{\kappa_g}{C_{0,g}} \frac{\frac{e^{k_g l_g}}{e^{2k_g l_g} - 1} \mathbf{T}\, e^{\frac{i\omega}{C_{0,w}}(l_g - x)}}{\beta_s + \kappa_g \sqrt{\frac{i\omega}{\alpha_g}} + \frac{i\omega}{2} C_{s,s}} \right|, \tag{426}$$

where $\mathbf{T}$ is the transmission coefficient

$$\mathbf{T} = \frac{2\rho_w C_{0,w}}{\rho_g C_{0,g} + \rho_w C_{0,w}}, \tag{427}$$

is also plotted for comparison. This equation was elaborated to describe an encapsulated thermophone with a perfectly rigid backing and with transmission through a window. Then, it has been adapted here to our hydrophobic behavior. Equation (426) assumes that the air gap is large enough so that there is no influence at the air/water interface due to the thermal layer. Figure 52 shows that, with different gaps, for a high enough frequency the multilayer model agrees with the Tong *et al.* model. The transition frequency, at which the two models start to concur, is the frequency for which the thermal layer becomes small enough to confine the entire sound generation in the air gap. The slope observed in the high frequency regime is then due to the transmission coefficient between two regions with a high impedance contrast. Below this high frequency regime there is a flat frequency response until a drop for low frequencies. This drop is due to the water on the other side of the thermophone, which acts as an imperfect reflecting substrate. To easily improve the sound generation in a direction, one can use a rigid backing on the other side, which creates a flatter frequency response at low frequencies. The SPL plateau observed for different values of l_g in Fig.52 is coming from a similar sound generation as the free field plateau response (see Fig.51). In this case, the air thermal layer oversteps the air-water interface, thus generating a sort of second active layer in the water region. Clearly, this couple of thermal layers is more efficient than the single thermal layer observed in the case without air gap. Lastly, it is seen that the overall SPL is increased at low frequency for smaller gap size, while diminishing the high frequency response. It means that the increasing of the gap induces a larger SPL in a frequency range which becomes narrower and more shifted towards the low frequencies. This leads us to believe that in order to improve the underwater sound generation we need either to generate the whole sound

in the air gap (and so have a large air gap) for low frequencies, or, to have a small air gap so that the thermal layer generates sound also at the air/water interface for higher frequencies. Since the width of the air gap strongly modifies the band pass frequency response of this system, a compromise between frequency range and produced SPL must be accepted, and l_g can be selected depending on the applications of interest. Finally, it has to be kept in mind that a low pass filter response could be achieved for a solid/air/thermophone/air/water design (rigid backing on one hand of the system).

Conclusions

In this Section, three classical thermophone configurations were analyzed and compared with other theoretical models from the literature. In particular, we studied a thermophone in free field, a thermophone deposited on a substrate and a thermophone over a substrate with an air gap in-between. The analysis has displayed good agreement between the presented model and other ones. It has been shown that in order to obtain the highest SPL in air, the thermophone over a substrate with an air gap design should be used. However, due to the size of the thermal length (in which sound is generated), it is important to leave a large enough air gap between thermophone and substrate to avoid any heat loss to the substrate specially at low frequencies (the lower the frequency, the longer the thermal length).

In order to validate the present approach, we also compared our results with experiments discussed in the recent literature. We compared the theory with the measurements carried out on three different thermophone materials, namely single-layer MWNT sheets, ITO-coated PAN sheets and FDGF sheets. The good agreement showed that the model is able to represent the behavior of systems with values of the heat capacity per unit area varying over several order of magnitude. Moreover, these materials have been used in different configurations, showing the capability of the model to represent the behavior of an arbitrary configuration.

In addition, we also discussed the behavior of two novel thermophone configurations, which can be adopted in air and underwater, respectively. In the first case, we investigated the possibility to create a generation device through two thermophone layers separated by a given air gap. This technique can be profitably used to reduce the density power, thus limiting possible thermophone damages, while increasing at the same time the sound pressure level due to coherent radiation. In the second case, we discussed the possible underwater use of

the thermophone. We analyzed the response of the underwater thermophone in free field and the response of the underwater thermophone with air gaps between generating layer and water. We showed that this last configuration, easily created thanks to the hydrophobicity of some nanomaterials, exhibits a very good efficiency and a pass band response which can be controlled by the air gap width.

The analysis will now be performed for cylindrical and spherical waves.

3.2 CYLINDRICAL AND SPHERICAL WAVES, ONE TEMPERATURE MODEL

In this section the multilayer cylindrical and spherical models created in Sections 2.3 and 2.4 are used and analysed. Those models are studied here together as it will be seen that they display similar results. The cylindrical or spherical geometry are non conventional shapes for thermophones at the macroscopique scale. Nonetheless, those geometries are worth being investigated as cylindrical shape analysis could be applied to the microstructure of porous thermophones for instance. Additionally, the spherical geometry is of interest since, if the radius of the sphere tends to zero it would correspond to a thermoacoustic monopole. As such, acoustical theory relative to monopoles could be applied assuming only a different input pressure generated from the monopole. This would allow for easy comparison with regular sound generator and facilitate thermoacoustic design.

Hence, despite having a very flexible multilayer model as for plane waves, this section will focus on three different cases which can be explained using Fig.53:

- a full cylinder or sphere ($R_b = 0$)
- a hollow cylinder or sphere (air at the core)
- a cylinder or sphere with substrate at the core

The full thermophone case will allow to estimate the radiation of an infinitely thin and long cylindrical thermophone as well as a monopole. The two other cases are motivated by the CVD method of fabrication of porous graphene. In graphene foams, the graphene is grown on a Nickel template which is then removed leaving the foam with hollow branches. See Section 4.1.1 for more details. The case with substrate at the core then represents a branch of foam before removal of the template while the hollow case represents branches after removal. Table 6 allows for an overview of the presented figures and their varying parameters. In all

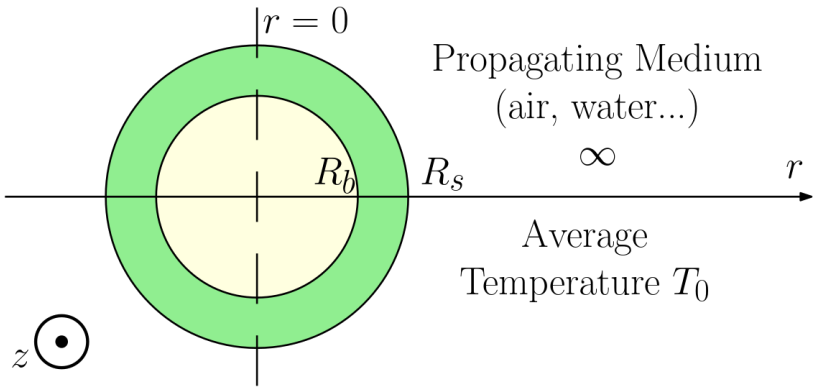

Figure 53: Schematic of the investigated models for cylindrical and spherical wave generation. The core of the thermophone (air or substrate) in light yellow has a radius R_b and the external radius of the thermophone layer (light green) is R_s

plots, the recording distance was fixed at $r_0 = 50 \times 10^{-6}$m, the input power is normalised at $P_{in} = 1W$, and the thermophone surface A was proportional to R_s^2. A was assumed to be the same for both cylindrical and spherical model in order to have a similar input power density and thus ease the comparison. The adequate modifications to the power density have been made whenever R_s was modified in both cylindrical and spherical models. The parameters used for the thermophone, air and substrate are similar to those seen in Table 3 and 4.

3.2.1 *Comparison with literature's models*

In order to exploit our multilayer model it must first be confronted to models from the literature. It was seen in Section 1.2 that very few models actually investigated cylindrical or spherical thermoacoustic sound generation. Furthermore, as previously said, no widely used thermophone have a cylindrical or a spherical macroscopic geometry. It is then not possible to compare experimental data from the literature to our model. The main investigation toward those geometries have been made by Hu *et al.* where they extended their plane wave geometry model [81] to spherical [83, 84] and then cylindrical waves [85]. Those models are based on the conservation equations and a *piston based model* for cylindrical shapes is also found in Tong *et al.* work in 2016 [87] which was then reused in his future work for thinline arrays [88]. Those models have been implemented and will be compared to the presented models of this work.

	Core	R_b [m]	R_s [m]
Fig.54a no losses		0	50×10^{-6}
Fig.54b with losses		0	50×10^{-6}
Fig.55a		0	50×10^{-6}
Fig.55b	Substrate	$R_s/3$	50×10^{-6}
Fig.56		0	$[100, 50, 5, 0.5] \times 10^{-6}$
Fig.57		0	50×10^{-6}
Fig.58	Air	$[9, 7, 5, 1, 0.1] \times R_s/10$	50×10^{-6}
Fig.59	Air	$R_s/3$	50×10^{-6}
Fig.60	Substrate	$[9, 7, 5, 3, 1] \times R_s/10$	50×10^{-6}
Fig.61	Substrate	$R_s/2$	$[100, 50, 25, 10] \times 10^{-6}$
Fig.62	Substrate	$R_s/3$	50×10^{-6}

Table 6: Specific geometrical parameters adopted in the analysis of different structures investigated. For each figure with SPL results we clearly indicated the details defining the corresponding configuration. In all plots we assumed a thermophone volume of $4/3\pi(R_s - R_b)^3$ m^2, an input power $P_{in} = 1W$ and a recording distance $r_0 = 50 \times 10^{-6}m$ from the generating surface.

Cylindrical model

In Fig.54 a full cylinder radiating in free field is compared to the models of Tong *et al.* [87] and Yin et Hu [85]. In his model, Tong *et al.* consider a uniformly heated cylindrical conductor and by doing so neglect the influence of the heat capacity of the thermophone. This is justified by the fact that in their future work Tong *et al.* investigate thinline arrays whose length are greatly larger than the radius of their cylinder. They only defined its radius to take into account determine the input power density in Eq.(5) [87]. In our model we also assumed a long cylinder compared to its radius to simplify the equations. Nonetheless, this dimension is of critical importance, not only for the input power density but also to the HCPUA and mechanical resonance determination. The final pressure equation of Tong *et al.* model is written in Eq.(10) as

$$p_g = DH_0^{(1)}(k_g r) + p_g^*, \tag{428}$$

with D a constant determined in Eq.(12) and p_g^* a particular solution found in Eq.(11) [87].

Regarding Yin et Hu model, it takes into account the thermal wave inside the solid but assumes that the input power is only distributed at the surface of the thermophone. This assumption was also observed

in Section 3.1.1 for plane waves and was justified when comparing the results with Shinoda *et al.* experiments [32]. However it does not holds for thick thermophones and a modified version of Hu *et al.* pressure equation with a volume density input power has to be derived similarly as in Eq.(418) for plane waves. It is finally found as

$$\begin{aligned} p_g =& \frac{\frac{Q_0}{i\omega\rho_s C_{p,s}}\kappa_s M_0 \sigma_s d_a d_t \left(k_g K_1(k_g R_s) K_0(\sigma_g r) - \sigma_g K_1(\sigma_g R_s) K_0(k_g r)\right)}{\left(d_a k_g K_1(k_g R_s)\left(\kappa_s M_0 \sigma_s K_0(\sigma_g R_s) - \kappa_g \sigma_g K_1(\sigma_g R_s)\right) + \right.} \\ & \left. -d_t \sigma_g K_1(\sigma_g R_s)\left(\kappa_s M_0 \sigma_s K_0(k_g R_s) - \kappa_g k_g K_1(k_g R_s)\right)\right), \\ =& p_{g,surface} \frac{Q_0}{i\omega\rho_s C_{p,s}} \kappa_s \sigma_s M_0, \end{aligned} \tag{429}$$

for volume density power. For simplicity this equation does not take into account a substrate. The full derivation of this equation and the definition of its parameters can be found in Appendix B.1.4.

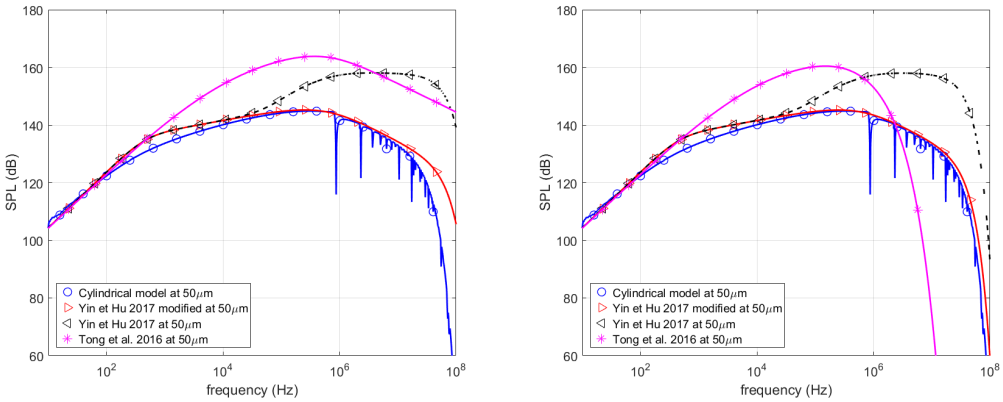

(a) (b)

Figure 54: Frequency spectrum of a full cylinder radiating in free field. The presented multilayer model is compared to the models of Tong *et al.* [87] and Yin et Hu [85]. The wavenumbers are estimated as in the literature at the order 0 in (a) and with a first order estimation in (b).

Figure 54a compares the frequency spectrum from the presented multilayer model for cylindrical wave with the literature. It is seen that there is a good agreement between the original Yin et Hu model with the presented model up to 20kHz. There is then an increase of SPL that reaches a plateau between 1 and 8Mhz before decreasing in the very high frequency range. This overestimation is due to the neglect of the thermal capacity of the thermophone in high frequency range. The power being supplied only on its surface, the energy stored by its heat capacity is then underestimated.

On the other hand, the modified Yin et Hu model with volume density power stay coherent with our model up to a a few mega hertz. After 3MHz both model observe a decreasing in SPL but at a higher rate in our case. This is due to the way the wavenumbers are calculated in Yin et Hu's model. Similarly as for plane wave, Yin et Hu used a 0^{th} order approximation for the thermal and acoustical wavenumbers. If the first order approximation defined in Eqs.(155) are used in Yin et Hu's model, the consistancy between both models reaches a few hundreds mega hertz as seen in Fig.54b. In the high frequency range it then necessary to take losses into account in the wavenumbers. More specifically thermal conduction losses.

Lastly it is seen that a small shift is seen between our model and the modified one around 1kHz. This is due to the chosen functions solutions of the temperature differential equations. In Eq.(269) the progressive and regressive waves function are defined with Hankel function of the first and second kind $H^{(1,2)}$ where Yin et Hu actually used modified Bessel function K. A better agreement between the simulated curves can be found in this frequency range if the modified Bessel functions are replaced by Hankel functions.

Regarding Tong *et al.* model in Fig.54a, the 20dB/dec increase in the low frequency ranges fits with our model but then due to the lack of consideration of the wave propagation in the thermophone as well as an assumed uniform heat distribution, there is an overestimation of SPL above 1kHz. In a similar fashion as for the surface density model of Yin et Hu, the thermal capacity of the thermophone is ignored in Tong *et al* making this model only valid for very thin thermophones or at very low frequency. Notably, a 0^{th} order approximation is used for the wavenumbers however, since the model is oversimplified, when a first order is used, the losses are then also overestimated as seen in Fig.54a.

It is worth discerning that there are no acoustic resonances due to size and shape of the thermophone in neither literature models. Only our multilayer model takes into account the acoustic propagation inside the solid, allowing us to determine antiresonances. Models in the literature neglected this influence as it was assumed to be in a frequency higher than the range of interest. The first antiresonance observed in our model is seen around 1MHz which is much higher than the human hearing range, making this assumption valid for most of the literature. Higher harmonics of the antiresonances are also observed and display variable intensities which are due to the chosen discretisation step of the simulation. All anti resonances should be of similar amplitude but the exact frequency might not fit with the chosen frequency step of the simulation.

Spherical model

In Fig.55a a full sphere radiating in free field is compared to the model of Hu *et al.* 2014 [84] and in Fig.55b a sphere with substrate as its core is considered and compared with Hu *et al.* model of 2012 [83]. As explained for plane and cylindrical waves, Hu *et al.* models assume a surface density energy input and so have to be modified in order to be comparable with our own. Assuming a volume density power input, the modified pressure equation for a full sphere becomes

$$\begin{aligned} p_g &= \frac{R_s}{r}\frac{d_a d_t k_g^+}{Z}(e^{-\sigma_g \Delta r} - \frac{\sigma_g^+}{k_g^+}e^{-k_g \Delta r})\frac{Q_0}{i\omega\rho_s C_{p,s}}\kappa_s \sigma_{s*}^-, \\ &= p_{g,surface}\frac{Q_0}{i\omega\rho_s C_{p,s}}\kappa_s \sigma_{s*}^-, \end{aligned} \tag{430}$$

and the one for a sphere with substrate at its core is

$$\begin{aligned} p_g &= \frac{d_a d_t k_g^+}{Z}(e^{-\sigma_g \Delta r} - \frac{\sigma_g^+}{k_g^+}e^{-\sigma_g \Delta r}) \\ &\quad \times \frac{\kappa_s \frac{Q_0}{i\omega\rho_s C_{p,s}}}{r}\left(R_s \sigma_{s*}^- + \frac{R_b \kappa_b \sigma_{b*}^-}{\kappa_b \sigma_{b*}^- - \kappa_s \sigma_s^-}\sigma_s (1-M) e^{\sigma_s \Delta R}\right), \\ &= \frac{p_{g,surface}^*}{r}\kappa_s \frac{Q_0}{i\omega\rho_s C_{p,s}}\left(R_s \sigma_{s*}^- + \frac{R_b \kappa_b \sigma_{b*}^-}{\kappa_b \sigma_{b*}^- - \kappa_s \sigma_s^-}\sigma_s (1-M) e^{\sigma_s \Delta R}\right). \end{aligned} \tag{431}$$

It is seen that Eq.(430) is equal to Eq.(431) with $M = 1$ and is of a similar form as Eq.(418). The detailed calculation of Eq.(430) and (431) as well as the definition of all parameters can be found in Appendix B.1.3 and B.1.2 respectively.

Similarly as for Fig.54a, Fig.55a displays a change of behavior between the original Hu *et al.* model with surface density power and the modified one with volume density power. The original version keeps increasing after 20kHz before reaching a plateau between 1 to 80MHz and then decreases. This is once again due to the neglect of the heat capacity of the thermophone by assuming a surface density power.

From 10kHz to 10MHz there is a good agreement between the modified model and our multilayer one. Above 10MHz the same issue as for plane and cylindrical waves is observed, where the 0^{th} order approximation of the wavenumbers in Hu *et al.* models prevent us from observing the same decrease. A perfect match is found if the wavenumbers are changed accordingly.

Below 10kHz, the observed slopes in both Hu *et al.* models and ours are different. This is explained by the chosen distance of recording. In Fig.55, the pressure is measured at $r_0 = 50\mu m$ distance. However, based

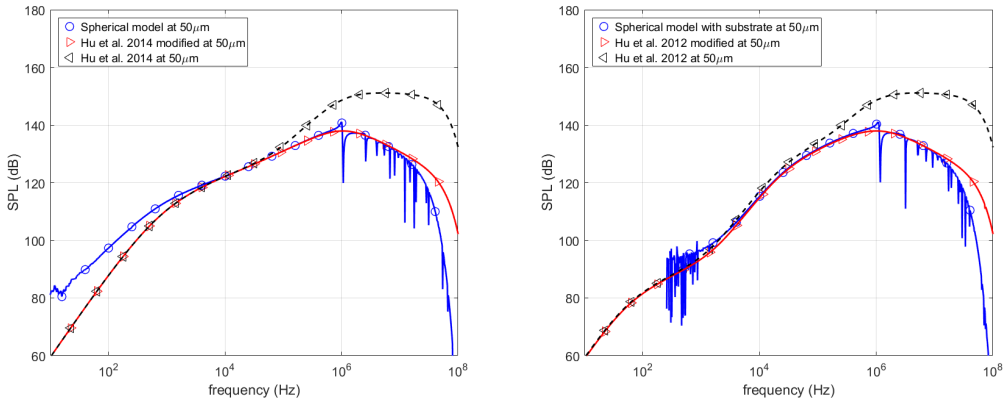

(a) (b)

Figure 55: Frequency spectrum of a full sphere (a) and a sphere with substrate at the core (b) radiating in free field. The presented multilayer model is compared to the model of Hu *et al.* of 2012 and 2014 for sphere with and without substrate respectively [83, 84].

on Eq.(154) the thermal layer L_{th} at 3kHz is about 50µm in air. It is known that L_{th} will be longer for lower frequency and so our recording distance is not far away enough of the "piston layer" to be accurate. In this low frequency range we are still inside the thermal layer in which the thermoacoustic process occurs leading to different result. This is made possible to observe only in our model as it is the most complex one, making little to no assumptions. In this particular case, Hu *et al.* model does not observe the thermal layer and assumes that the acoustic wave is already fully generated. This assumption is valid since most recording are made orders of magnitude away from the thermal layer. This theoretical recording distance r_0 was chosen to limit the numerical errors generated by our model for large distances. If r_0 is chosen further away, there is agreement between the models at low frequency but numerical errors can be seen in our model at high frequencies.

Now regarding Fig.55b, similar observations are made between the original and modified Hu *et al.* model at high frequencies. In fact, above 20kHz little to no differences can be made between the spectrums of the full sphere and the sphere with substrate. Below 20kHz, due to the small size of the substrate ($R_b = R_s/3$) thermal losses will occur where the thermal layer is longer than the thickness of the thermophone. As observed for plane waves, energy is lost in the substrate and results in this decrease in SPL. It is also seen that numerical errors appear at low frequency in our model, making Hu *et al.* model more robust and more adapted in this specific case.

Finally, like for plane and cylindrical wave, in both Fig.55 only our model display high frequency anti resonances. Thus making it the only adapted high frequency model for thick thermophones prone to resonances.

3.2.2 *Analysis of Novel Microscopic Geometries*

The validity of our multilayer model for cylindrical and spherical shapes has now been proven by being compared to other models from the literature. As previously explained, those geometries have been of little interest as most thermophones are assimilated to a plane surface in a macroscopic scale. In spite of that, it is of importance to investigate those geometries as thermophones are in a cylindrical shape at a microscopic scale. Additionally, acoustic theory based on monopole is very thorough and could be easily applied for thermophones if a monopole response is estimated. In the following section the three geometries of interest previously defined will be investigated and their defining parameters will be modified to assess their influence.

Filled Thermophone

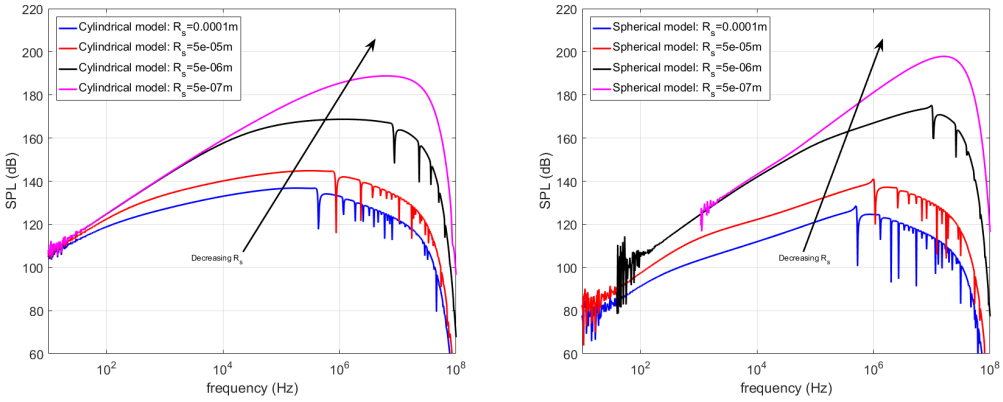

(a) (b)

Figure 56: Frequency spectrum of a full cylinder (a) and a full sphere (b) with various radius R_s.

Figs.56 show the frequency response of a full cylinder (a) and a full sphere (b) with various radius R_s. In Fig.56a reducing the radius of the cylinder increase the high frequency SPL. In fact, a 20dB/dec profile is observed from 10Hz to almost 1MHz for the smaller radius. This

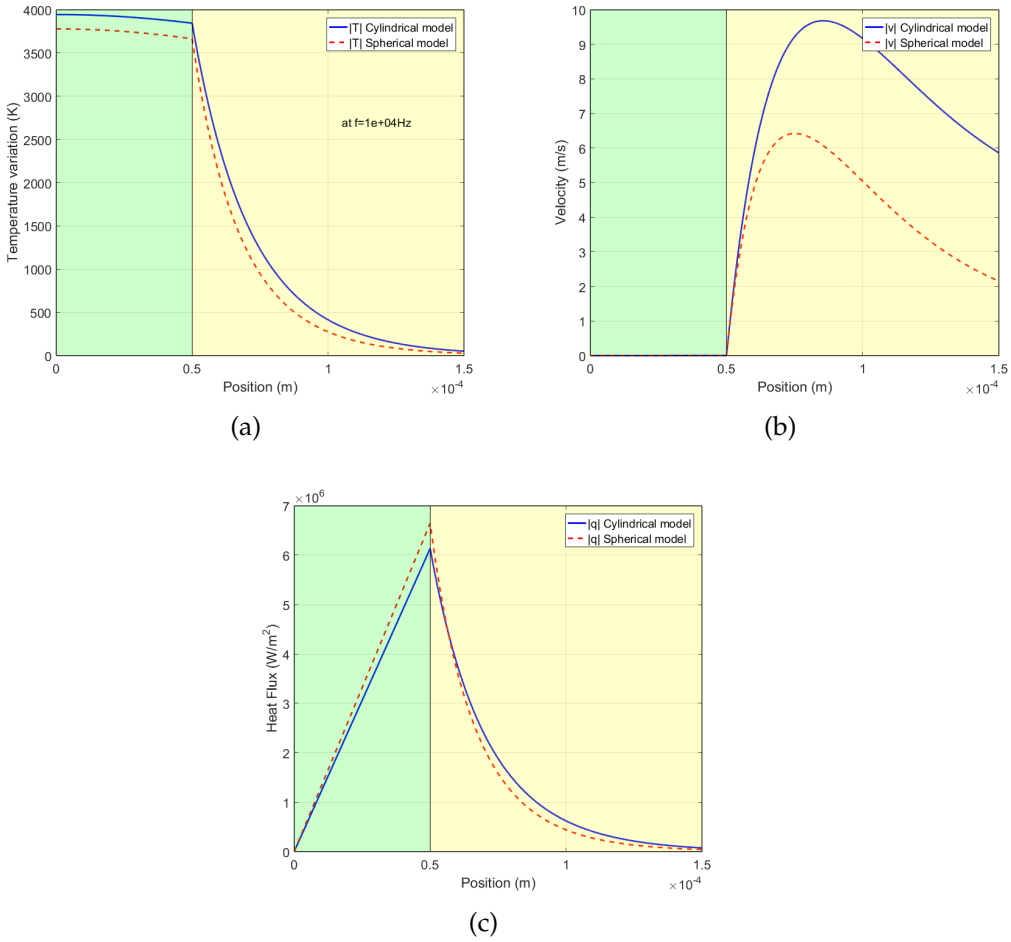

Figure 57: Temperature (a), particle velocity (b) and heat flux variations (c) in the near field for full cylindrical (continuous blue) and spherical (dashed red) thermophones. All curves show the absolute value of the corresponding complex quantities. Due to the symmetry of the geometries the center $r = 0$ of the thermophone (green region) is on the left. The yellow region correspond to the propagating air medium. Here at $f = 10\text{kHz}$.

increase could once again be attributed to the smaller HCPUA of the reduced radius. On the other hand, having a large radius seem to create flat frequency response in this frequency range which reminds us of the profile observed for plane wave. This is understood as if the cylinder becomes infinitely thick, it will be approximated as an infinitely flat surface at such distance r_0. Hence a similar frequency spectrum will be observed. It is also seen that the first observable antiresonance is at a lower frequency for thicker thermophone. For the smaller radius $R_s = 0.5\mu\text{m}$ the antiresonance is even higher than 100MHz. This behavior was expected as those mechanical resonances are directly proportional

to the size of the thermophone. This was also observed for plane waves in Section 3.1.1. Lastly it is important to remember that those plots are normalised with power but not power density. In other words, 1W was applied to all simulated cylinder but for smaller cylinder the actual power density was higher due to the reduced volume.

Fig.56b shares the same analysis as Fig.56a as it display very similar behavior. In order to facilitate comparison, a similar power density has been applied to both figures. In reality the power density of the cylinder should be lower due to its length. Nonetheless, having this in mind, it is observed that similar SPL levels are observed above 1MHz for both geometry. Below 1MHz, the frequency spectrum profile of the sphere display lower SPL than the cylinder. This could be explained by the fact that the surface of the cylinder in the z direction is closer to the observation point than for a sphere. Even though diffraction is not taken into account in those plots, the inherent shape (and thus mathematical solutions) of the thermophone could induce better low frequency radiations. Finally Fig.56 show that computational limitations are more easily reached for spherical geometry and for thin thermophones.

Figs.57 display the spatial behavior of the temperature, particle velocity and heat flux of a full cylinder and sphere at 10kHz from the center of the thermophone to twice the recording distance of the frequency spectrum plots. It is seen that both cylinder and sphere display very similar profiles. Notably, it is seen that at the center of the thermophone the temperature is the highest, the heat flux is canceled as it is directional and the velocity is null. At this frequency the thermal layer length is 26µm and can be seen in all figures but mostly in the velocity plot Fig.57b.

Hollow Thermophone

Figures 58 show the frequency response of hollowed cylinder and sphere with a fixed external radius and various internal radius. Air is assumed at the core of those thermophones. Fig.58a show that for a small internal radius relatively to the external one, the frequency spectrum is similar to the one of a full sphere. With increasing R_b, the heat capacity of the thermophone is reduced due to its thinner thickness. This leads to an increase in high frequency SPL while the low frequency range is not modified. Another observable change is the slight modification of the antiresonance frequency for large internal radius. New resonances due to the new geometry are also observed above 1MHz. However those changes are not as significant as the modification of the external radius previously observed for a full thermophone. Those changes in res-

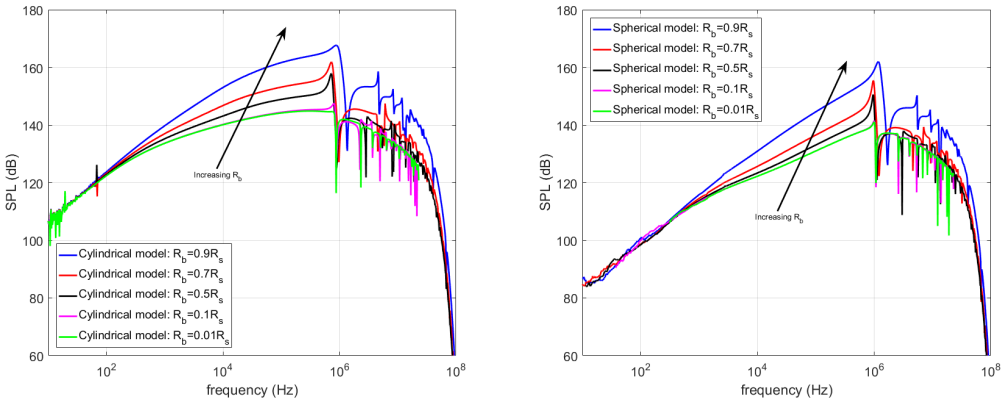

(a) (b)

Figure 58: Frequency spectrum of a hollow cylinder (a) and a hollow sphere (b) with a fixed external radius R_s and various internal radius Rb.

onances would not have been observable without the created multilayer model.

Identically as for a full thermophone, Fig.58b display similar behavior as Fig.58a. The same analysis can then be applied.

Figs.59 display the spatial behavior of the parameters at 10kHz in this new geometry for $R_b = R_s/3$. Similar behavior are observed for both cylinder and sphere. The temperature is maximum in the thermophone at R_b and the thermal layer is observed on the outer boundaries of R_s. The heat flux and the velocity are also canceled at $r = 0$. It is then not possible to observe the thermal layer from the inner radius as waves cancel one another.

Thermophone with substrate at core

Fig.60 display a similar geometry as before but instead of having air at the center of the thermophone, a substrate core is assumed. The frequency spectrum of a cylinder and spherical shape are found in Fig.60a and 60b respectively with varying inner diameter of substrate. Two main phenomenons are observable in Fig.60a. Firstly below 10kHz, it is seen that the thicker the core substrate is, the more losses are observed. Heat is dissipated in the substrate and this is even more pronounced at low frequency with large thermal layers. The cylinder with the thinner core has the highest SPL as it it closest to a full cylinder.

Secondly above 10kHz, since the thickness of the thermophone is reduced, its HCPUA is reduced as well and this increases its SPL at high frequencies (as seen for a hollow thermophone). Furthermore, when the

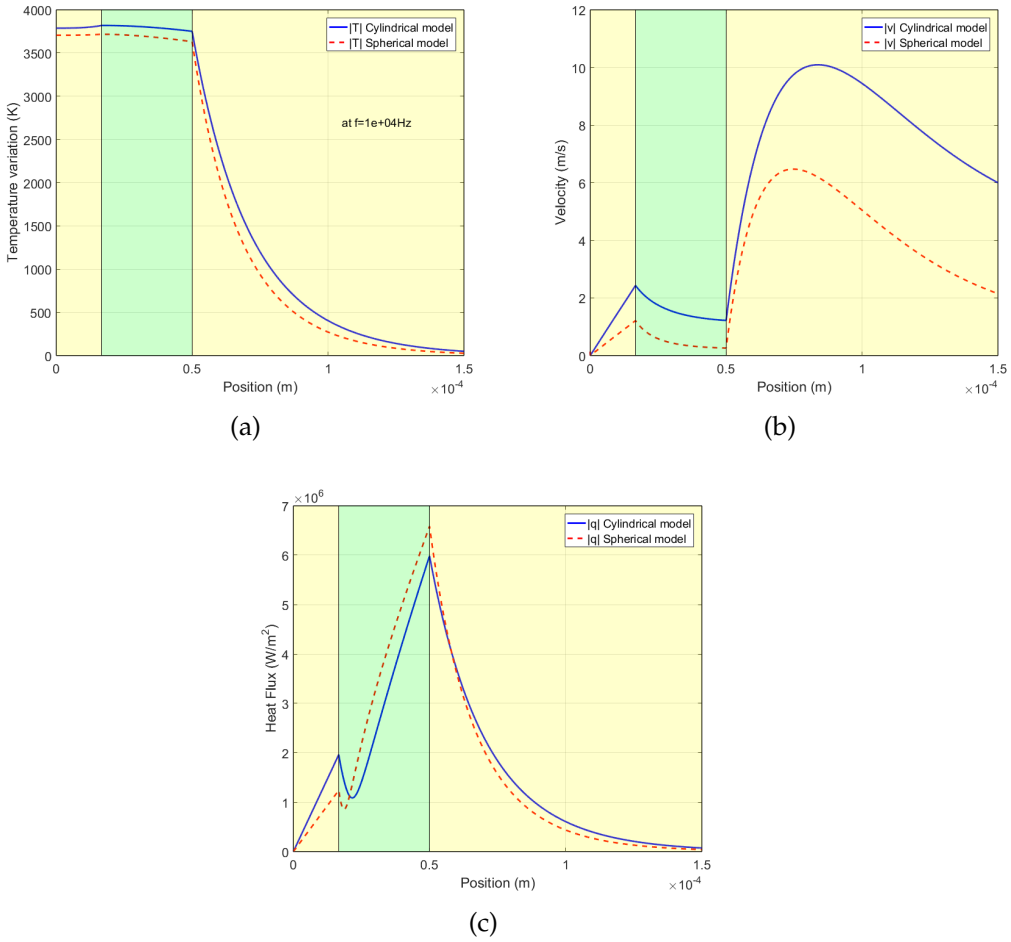

Figure 59: Temperature (a), particle velocity (b) and heat flux variations (c) in the near field for hollowed cylindrical (continuous blue) and spherical (dashed red) thermophones. All curves show the absolute value of the corresponding complex quantities. Due to the symmetry of the geometries the center $r = 0$ of the geometry (air, yellow region) is on the left. The green region correspond to the thermophone. Here at $f = 10\text{kHz}$.

thickness of the thermophone $R_s - R_b$ starts being in the same magnitude range as its thermal layer length, the influence of the substrate diminishes as observed for plane waves. This leads to the cylinder with the thicker substrate to radiate the most above 1MHz.

Additionally, the antiresonance of the thermophone is directly proportional on its size but also on its stiffness. Having a substrate at the core change the overall stiffness of the thermophone shifting the first antiresonance to a higher range.

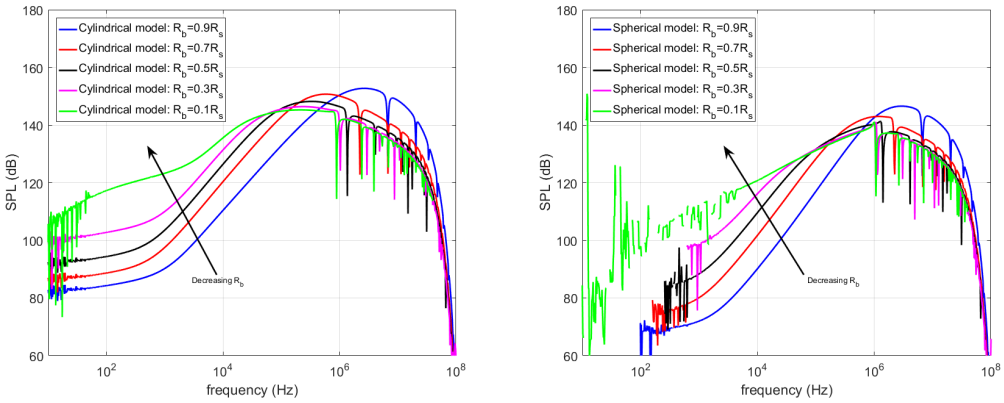

(a) (b)

Figure 60: Frequency spectrum of a cylinder (a) and a sphere (b) with a substrate core. The external radius R_s is fixed and the internal radius Rb changes.

Similar observation are made from Fig.60b but with greater difficulties as the numerical model is unstable at low frequencies, especially for thin core substrate.

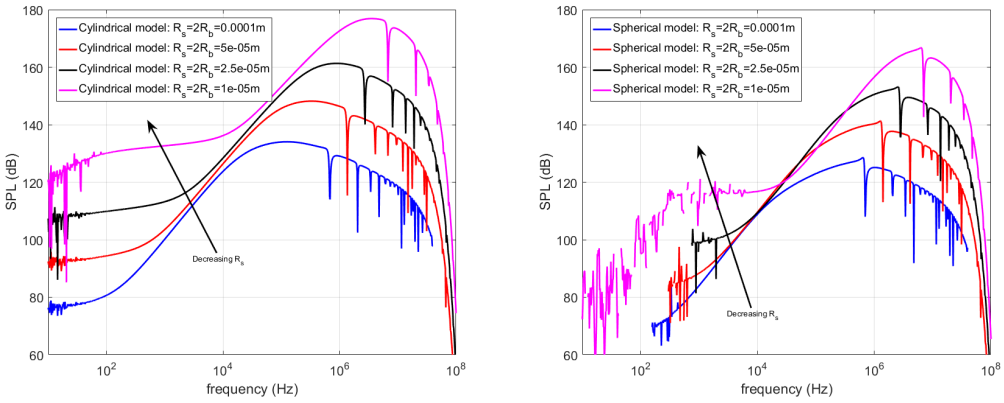

(a) (b)

Figure 61: Frequency spectrum of a cylinder (a) and a sphere (b) with a substrate core. The external radius R_s changes and the internal radius R_b is always half of the external one.

Figures 61 are complementary to Fig.60 as they show the same geometry but with a fixed ratio between inner and outer radius ($R_s = 2R_b$) and fluctuating outer radius. Across the whole frequency range the thinner thermophone has overall the best performance. Its low HCPUA due to its small size improve high frequency radiation. Its thin core of substrate also limit the losses at low frequencies. At last, the shift toward

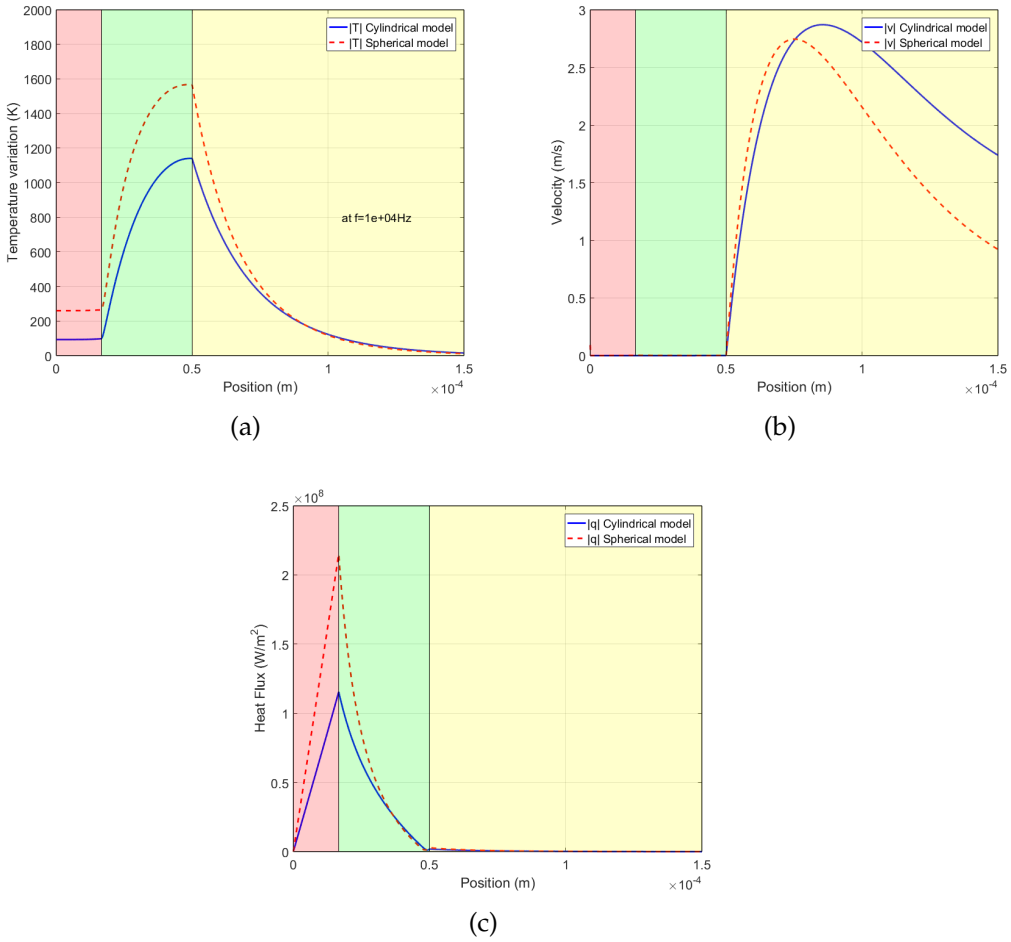

Figure 62: Temperature (a), particle velocity (b) and heat flux variations (c) in the near field for cylindrical (continuous blue) and spherical (dashed red) thermophones with a substrate core. All curves show the absolute value of the corresponding complex quantities. Due to the symmetry of the geometries the center $r = 0$ of the geometry (substrate, red region) is on the left. The green region correspond to the thermophone and the yellow region to the propagating air medium. Here at $f = 10\text{kHz}$.

high frequency of the first anti resonance of the solid for thicker radius is also clearly distinguishable.

The spatial behavior of the temperature, particle velocity and heat flux in this configuration is found in Fig.62. From Fig.62a it is seen that the temperature drops inside the substrate. The heat flux in Fig.62c is drawn to the substrate (stronger at R_b), as opposed to Fig.59 where the heat flux was at its maximum at the outer layer for the thermoacoustic generation. This leads to a smaller particle velocity and thus SPL in Fig.62b.

Conclusions

In Section 3.2.1 our multilayer cylindrical and spherical model were confronted to models from the literature. Very few models currently exist for cylindrical or spherical geometry of thermophone but our model proved to be coherent with those currently available. It has been proven once again to be able to fit different configurations (full thermophone or with core substrate), while still being the only one considering high order estimation of the wavenumber as well as mechanical resonances created by the bulk thermophones. It was seen in Section 3.1.1 that the multilayer models sometimes reached numerical limitations for plane waves due to the computational inverse of large singular matrices. Those limitations have been observed to be even more easily reached in the case of cylindrical and spherical geometries. The Bessel functions and complex exponential, solutions of the differential equation in those respective shapes, make the inverse matrix problem even more singular. Hence other models can be preferred in specific cases at distinct frequencies, where the assumptions made allow for a more robust system.

In Section 3.2.2 the influence on the shape of the cylindrical or spherical thermophone was analysed. Firstly, it was seen that across all geometries, cylindrical and spherical waves models have displayed similar results and the analysis are valid in both cases. Nonetheless, the cylindrical wave multilayer model proved to be more stable and less prone to numerical errors than its spherical counterpart. In a similar fashion as for plane waves, the thickness of the thermophone directly influence the thermophone HCPUA. Thinner thermophone are then privileged for high frequency radiation, although high power density has to be expected and could damage real samples. The use of a substrate at the core was proven to lead to thermal losses as expected.

All in all, a spherical monopole spectrum can be found using our model but might not be the most appropriate one as its multilayer flexibility prevents its easy implementation in those investigated simple cases (full, hollow or with a core substrate). Hu *et al.* simplified model might be more easily manipulated for monopole theoretical investigation [84]. Regarding microscopically shaped thermophone, the thickness has once again proven to be a decisive factor for HCPUA tuning. If the fabrication techniques of CNT might not allow easy changes in the thickness of the tube, CVD grown tubes could adapt the thickness of the branches with the growth time. At last, CVD based samples have to choose if they would rather keep the substrate for mechanical stability at the expense of thermoacoustic efficiency, or removing it at the risk of having hollow tubes with very high power density.

3.3 PLANE WAVE, TWO TEMPERATURES MODEL

In Section 2.5, a two temperature model for the thermo-acoustic sound generation has been elaborated. This model was motivated by the fact that most of the currently used thermophones are composed of non continuous materials. For instance, widely adopted structures are based on multi walled nanotubes (MWNT), arranged as sheets, forests, foams or sponges [48]. Those thermophones devices are therefore made of both air and nanotubes. Thus, the models based on a continuous homogeneous medium do not represent the real microstructure of these systems and neglect the interaction fluid/solid in the active region. As a matter of fact, in foam like thermophones a porosity of the active layer as large as 99% can be achieved, making the air component not negligible.

In the following, the thermo-acoustically generated temperatures, particle velocity and heat fluxes are analyzed as a function of the position x (one-dimensional modeling) at a frequency of 3kHz. This allows for a deeper understanding of the model and a better interpretation of the thermoacoustic generation phenomena in porous devices.

Additionally, measurements published in the literature will be compared to the theoretical response of our two temperature model (referred to as 2T model) and of the classical model based on a homogeneous and solid active layer (multilayer model for plane waves referred to as 1T model) [1]. The comparison will be discussed in two distinct sections, dealing with different thickness of the thermophone. Section 3.3.1 will investigate thin film thermophones with thickness of a few microns, and Section 3.3.1 foam like thermophones with thickness of hundreds of microns. The experimental data are taken from a recent investigation [48]. This Section provides frequency and power spectra of a wide variety of samples with a full description of the experimental setup. Thermal parameters of the samples were also measured and discussed. These data have been used in the theoretical models, making the comparison theory/experiment legitimate.

All of the presented theoretical results have been obtained using the parameters in Table 7 and Table 8. A specific discussion concerning the parameter g, which is the only new parameter introduced in this model, was made in Section 2.5.1. The 2T model and the classical 1T model [1], based on a single homogeneous active layer, have been implemented (see Fig.31). Both models have been adapted for acoustic diffraction as discussed in Section 2.7, by considering the size and the shape of the samples used in the experimental activity [48]. All results show the sound pressure level (SPL) in decibels (dB), as defined in Eq.(413). The results are shown at a distance of $3cm$ from the thermophone. The

frequency spectrum results are normalized with power and the power spectrum results are shown at 3kHz.

3.3.1 *Analysis*

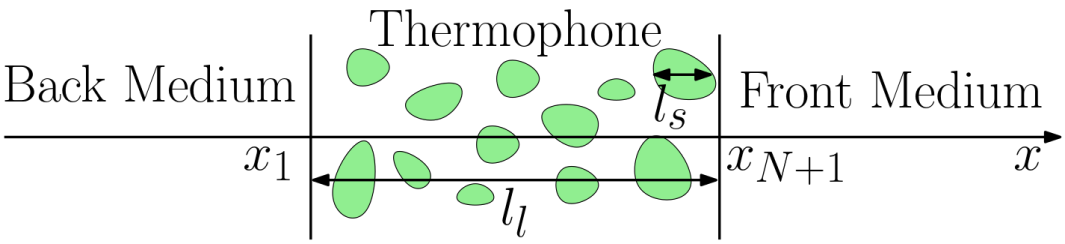

Figure 63: Schematic of a porous thermophone radiating in free field (symmetrically in back and front media). The thermophone layer has a width l_l and foam branches of average diameter l_s. The volumetric source Q_0 is supplied to the foam structure by Joule effect.

Here, the behavior of the main physical variables is shown by comparing a thick and a thin thermophone radiating in free field as seen in Fig.63. For the thick thermophone the parameters of the graphene sponge ($l_l = 800 \times 10^{-6}$m) are adopted, while for the thin one the parameters of the CNT sheet ($l_l = 18 \times 10^{-6}$m) are used. In Fig.64, one can find the temperatures, the particle velocity and heat fluxes as function of position x, calculated with the 1T and the 2T models for both the thick and thin thermophones at $f = 3$kHz. In this figure, the curves corresponding to the absolute value of the different complex quantities have been plotted. To better explain the behavior of the heat flux within the system, the real and imaginary parts of the heat fluxes in air and foam are shown as well in Fig.65. The input power is the same for all curves (1W) in Figs.64 and 65. The geometry considered is shown in Fig.32, where $N = 5$ is imposed to easily identify the pores/branches structure in the plots. Moreover, the diffraction procedure is not implemented to obtain the results of this spatial investigation since only the near field generation is of interest. Please note that the 1T model has been chosen to display results only outside the thermophone layer. If a behavioral response of the physical quantities can be calculated inside the solid layer in 1T, it would not reflect accurately the reality and be an overestimation of a bulk material. On the contrary, the 2T model allows for a more authentic analysis, also in the generating porous structure.

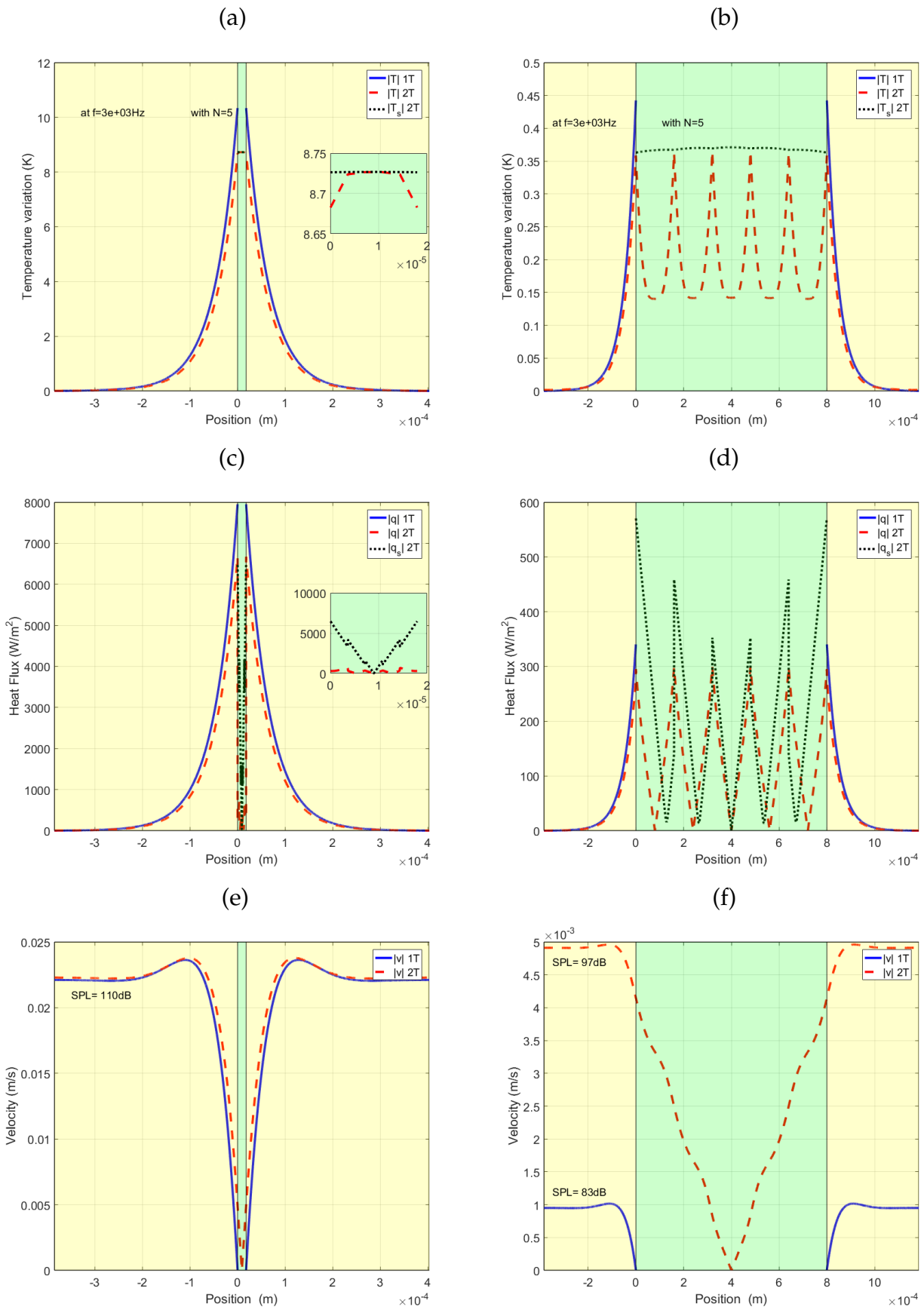

Figure 64: Near field temperature variations (a,b), heat flux (c,d) and particle velocity (e,f) for a thin (a,c,e) and thick (b,d,f) thermophone. All parameters are plotted only in air with the 1T model and in both air and solid with the 2T model. All curves show the absolute value of the corresponding complex quantities. The central region (green) represents the thermophone layer with both air and solid foam and the regions on the left and on the right (yellow) represent the air layers. The insets in (a) and (c) show a zoom within the generating layer.

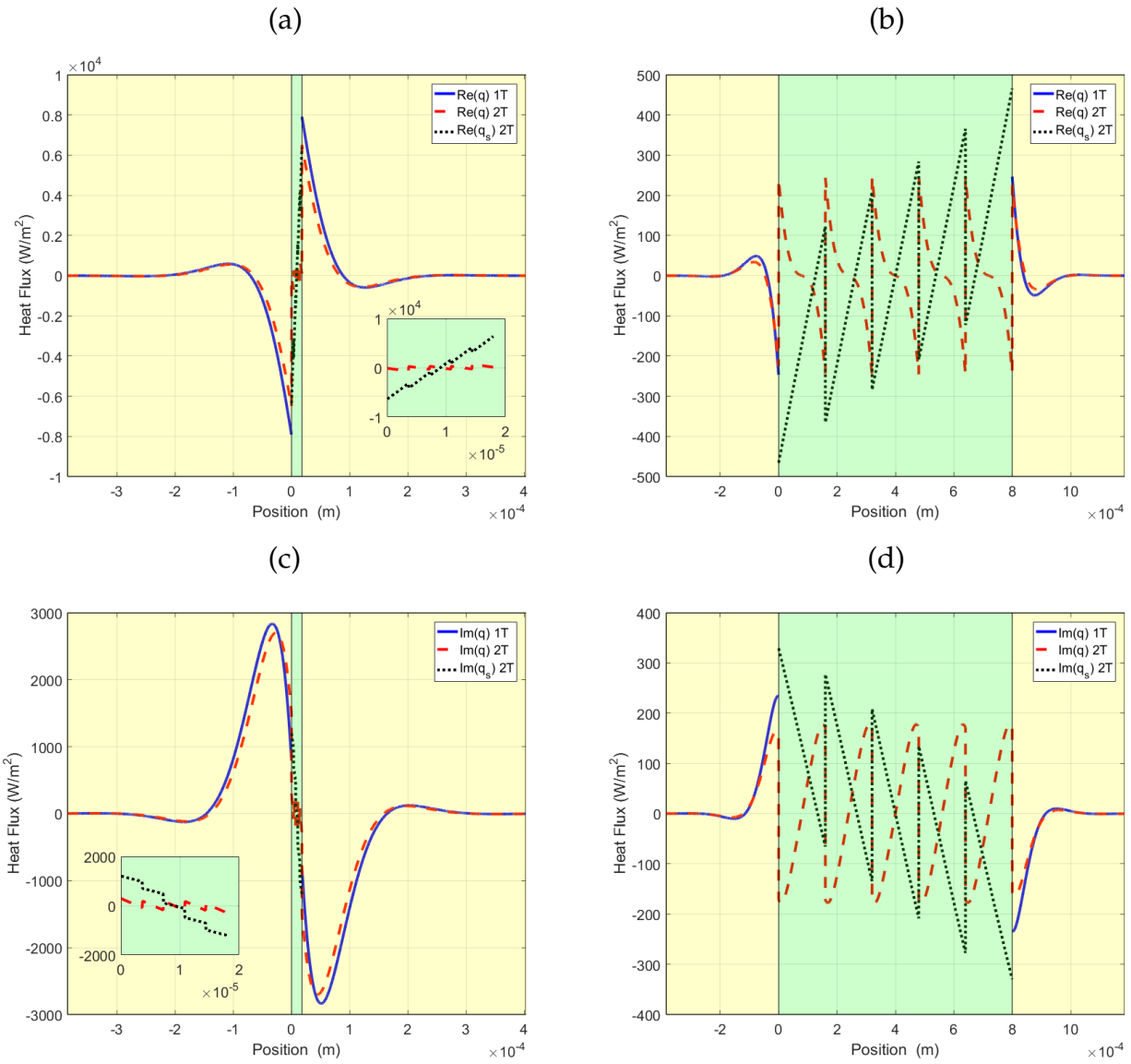

Figure 65: Real part (a,b) and imaginary part (c,d) of the heat flux for a thin (a,c) and a thick (b,d) thermophone. The quantities are plotted only in air with the 1T model and in both air and solid with the 2T model. The central region (green) represents the thermophone layer with both air and solid foam and the regions on the left and on the right (yellow) represent the air layers. The insets in (a) and (c) show a zoom within the generating layer.

Fig.64 (panels a and b) shows that despite a slightly higher value of the temperature on the edges of the thermophone for the 1T model, both thick and thin systems display the same behavior in air. The thermal active layer $\mathcal{L}_{th}$ can be seen in the vicinity of the thermophone and has the same length in all cases since it only depends on the frequency and the propagating medium (the higher the frequency the smaller the size of the generating layer). In the inset of Fig.64a, one can see that the temperatures inside the thin thermophone are almost constant and the branches providing the energy from the solid to the air in the 2T model are not distinguishable. On the other hand, for a thick thermophone one can find in Fig.64b the energy transmission near the branches, represented by the interfaces. Finally it is seen that, in the thick thermophone, the temperature of the solid is higher at the center of the thermophone and local maxima also exist in between two branches. Importantly, these evaluations of the temperatures within the thermophone layer (pores and branches) can be performed only with the proposed 2T model. These results are relevant for both analyzing the system and designing porous thermophones with specific features.

Fig.64 (panels c and d) show the heat fluxes in the considered structures. As before, the 1T model presents higher values of q at the edge of the thermophone than the 2T model, but the same order of magnitude and behavior are observed in both models. The thin thermophone displays an almost continuous increase of q inside the thermophone, from the centre to the external edges (2T model). However, for the thick thermophone, the heat flux transmission is seen in the air/foam structure and is characterised by a series of peaks. The sawtooth shape of the curves in Fig.64d is due to the fact that the absolute value of complex quantities is shown. To better understand the behavior of the heat fluxes in the structure, the real and imaginary parts of these quantities are represented in Fig.65, for both thin and thick thermophones. In the generating layer of the thin thermophone (panels a and c of Fig.65), the exchange of energy at the contact zones between air and foam can be only slightly appreciated. However, concerning the thick thermophone (panels b and d of Fig.65), one can clearly observe the jumps of the heat fluxes within the generating layer in both air and foam. These jumps represent the exchange of energy between air and foam and are described by Eqs.(365) and (366). It can be remarked that T in the air is not very different from T_s in the foam in the contact zones (see Fig.64b). Nevertheless, since the parameter g assume a quite large value, the product $g(T_s - T)$, characteristic of the two temperature model, is always finite and positive and it can be seen (in panels b and d of Fig.65) as the measure of the jumps in both q and q_s curves. Moreover, it is interesting to note that the jumps in q and q_s (both real and imaginary

parts) are always of the same extent but in opposite directions. It is perfectly coherent with the idea of energy exchanges, as introduced in Eqs.(365) and (366).

Fig.64 (panel e) shows that, for a thin thermophone, the particle velocity within the 1T and the 2T models is of the same magnitude leading to a similar radiated SPL of about 110dB in the vicinity of the thermophone. This is attributed to the fact that the density of branches is high enough for the temperature and the flux to be continuous in the thermophone leading the 2T model to perform similarly to the 1T one. On the other hand, in Fig.64 (panel f) it is seen that the particle velocity assumes different values for the 1T and the 2T models, leading to different radiated SPL of about 83 and 97dB, respectively. This difference is attributed to the non continuity of the thermophone layer in the 2T model, in opposition to the bulk solid layer in the 1T model. The improvement of the performances is clearly proportional to N. From the physical point of view, it means that the crucial factor to improve the performances is the total surface contact between air and foam branches within the porous generating layer. Clearly, this total surface increases with porosity but also depends on the real geometry of the microstructure (shape and connectivity of pores). The thick porous structure allows indeed to reduce the influence of the heat stored in the generating layer, thus improving the conversion of thermal energy in acoustic energy, e.g. the overall efficiency. This mechanism, properly implemented in the 2T model, corresponds to the actual behavior of real porous thermophones, as proved by the following comparisons with recent experiments.

In this section it was seen that for thin thermophones the 2T model performs similarly to the 1T model, but this is not the case with thicker and porous thermophones, where a sound generation difference of more than 10dB is observed. This proves that the modeling of the generating layer is of primary importance and that the thermoacoustic generation is intricately linked to its geometry (size, microstructure and so on). The theoretical model has therefore to be tuned to each thermophone geometry.

Thin film thermophones

Fig.66 (panels a and b) shows the frequency and the power response of a Carbon Nanotube Sheet (CNT sheet) and an Indium-Tin Oxyde coated Poly(acrylonitrile) Nanofibers sheet (ITO PAN). In both cases the diffraction procedure of Section 2.7 has been applied to the theoretical models. CNT sheets are considered as the most efficient thermophones currently available because of the very low heat capacity per unit area (HCPUA)

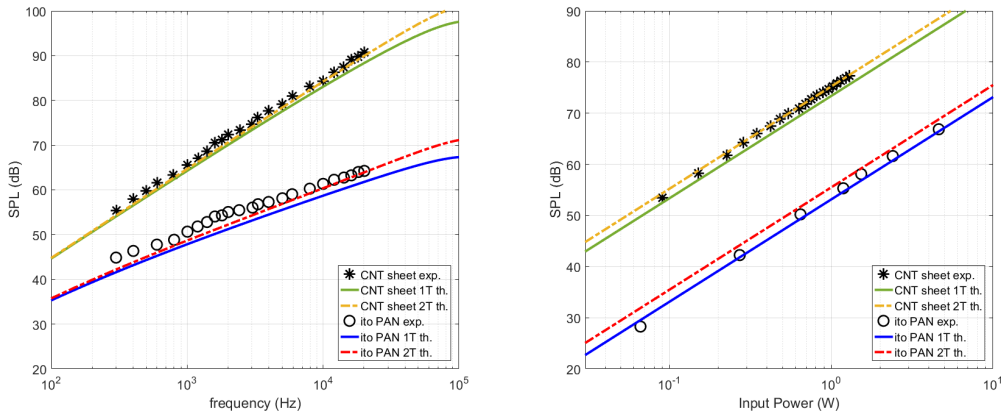

(a) (b)

Figure 66: Comparison of experimental [48] and theoretical responses of a CNT sheet and an ITO PAN thermophone working in free field at 3cm distance emission/reception. (a) Power normalized frequency response of the thinfilm thermophones. (b) SPL response of the thinfilm thermophones at 3kHz as a function of the input power. For the 2T model $N = 10$ has been adopted.

induced by their low density and low specific heat [48]. For this reason, CNT sheets are considered as the reference nanostructures for thermoacoustic heaters [48]. On the contrary, ITO PAN devices have a much higher density and therefore a higher HCPUA leading to a lower efficiency. This explains the different slopes seen in Fig.66a, where the CNT sheet response has a slope proportional to f^1 ($20dB/dec$), whereas the ITO PAN sheet has a slope closer to $f^{0.5}$ ($10dB/dec$) due to its higher HCPUA [1, 48]. This poorer efficiency is also seen in Fig.66b, where for a similar input power the ouput SPL is about 20dB higher for the CNT sheet. It is also seen that the power response slope is in both cases $20dB/dec$, meaning that the SPL output is directly proportional to the input P_{in} as previously recorded in theoretical and experimental literature [57]. In spite of the lower thermoacoustic performances, ITO PAN sheets are interesting materials for technological reasons. In fact, PAN polymers can be easily electrospun and coated with metals [48]. The ITO coating, in particular, is deposited by radio frequency sputtering and the final film is resistant to relatively high temperatures and quite transparent [48].

A good agreement of both 1T and 2T models is observed with the experimental data, for frequency and power spectra. This is attributed to the fact that the thickness of the thermophone is small enough so that the 2T approach does not add any significant value to the model. The thickness of the sample is still sufficiently small for the HCPUA to

be accurately evaluated by a continuous sheet through a 1T model. This however would stop to be true for thicker thermophones.

Finally, it can be noted that the output acoustic power for a spherical radiation on the CNT sheet can be estimated as $4\pi r^2 p_{rms}^2/\rho C_0 = 42 \times 10^{-9} W$. Here, the pressure at 1kHz is $p_{rms} = 10^{65/20} \times 20 \times 10^{-6} Pa$ and $r = 0.03m$ as the measurement was done at 3cm and not at the standard 1m distance. The pressure being normalized at 1W input power, this leads to an efficiency of about $4.2 \times 10^{-6}\%$, which is in the same range as reported in the literature [48].

Thick foam thermophones

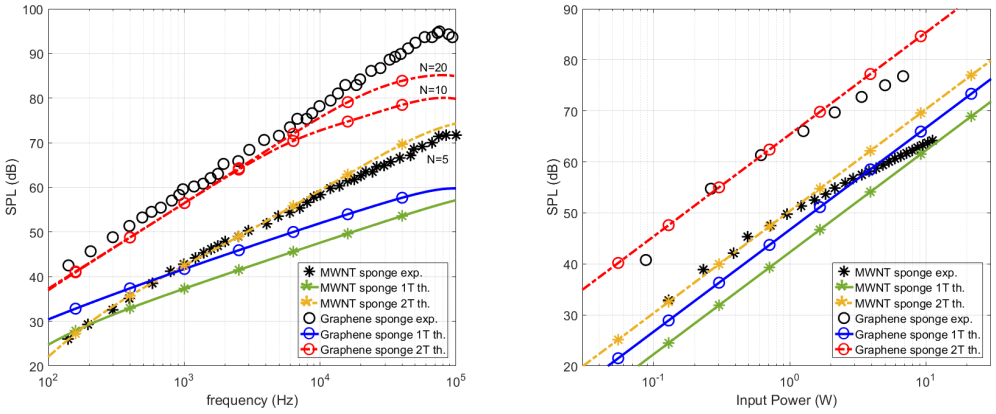

(a) (b)

Figure 67: Comparison of experimental [48] and theoretical responses of a MWNT sponge and a graphene sponge thermophones working in free field at 3cm distance emission/reception. (a) Power normalized frequency response of the foam thermophones. (b) SPL response of the foam thermophones at 3kHz as a function of the input power. For the graphene sponge, the theoretical curve is the same for $N = 10$ and $N = 20$. For the MWNT sponge $N = 5$ is adopted.

Fig.67 shows the measured responses of a MWNT sponge (0.1mm thick) and of a graphene sponge (0.8mm thick), together with the corresponding theoretical results. In both cases the diffraction procedure of Section 2.7 has been applied. These samples have a thickness one/two orders of magnitude larger than the previous ones and have a porosity within the range $95\% - 99\%$. The experimental frequency spectrum of the graphene sponge displays a slope proportional to f^1 (20dB/dec), meaning that the efficiency is preserved with respect to the thin film case. Indeed, even if the sample is rather thick, the HCPUA did not in-

crease significantly to reduce the thermophone performances. The high frequency decrease observed is simply due to the diffraction caused by the geometry of the sample. Now, concerning the MWNT sponge experimental frequency response, one observes that for low frequencies (below 1kHz) the slope is proportional to f^1 (20dB/dec), and for higher frequencies (between 1kHz and 100 kHz) the slope becomes proportional to about $f^{0.75}$ (15dB/dec). Indeed, at high frequency the effect of the HCPUA increases and, therefore, the thermoacoustic generation is coherently reduced [1]. Interestingly, the same effect exists also in the graphene sponge, but it is not observed here since it appears at higher frequencies because of the different physical parameters.

The important reason for introducing MWNT sponges is that MNWT networks generate an elastically compressible and flexible device [48]. Moreover, the MWNT sponges fabrication is simple and low-cost. On the other hand, the use of graphene sponges allows exploiting the exceptional properties of graphene, with a very large exchange surface due to the peculiar sponge geometry. The result is a three-dimensional cross-linked sponge with isotropic physical properties [48].

In Fig.67a, using the homogenized parameters of the thermophone shown in Table 8 [48], good agreement is found between the experiments and the 2T theoretical model for the MWNT sponge. A good agreement is also found for low frequencies between the graphene sponge and the 2T model. However, it is seen that for higher frequencies a larger number of interfaces has to be used to reproduce more accurately the experimental behavior. This is explained by the high surface density of the foam within the thermophone layer. Many interfaces need to be used to better represent the large amount of energy provided to the air for high frequencies. On the other hand, the 1T model displays a strongly different spectrum slope with respect to the experiments. This is due to the thickness of the sample. Indeed, the thermal interactions between the air and the thermophone microstructure are not integrated in the 1T model, since it assumes a thick continuous medium, thus artificially increasing the HCPUA. The sound generation inside the pores of the foam is not taken into account since the model is continuous and, therefore, more heat is assumed to be stored while it is actually dissipated in the pores air.

The power spectra of the thick samples are shown in Fig.67b, and display a different behavior with respect to the thin samples. At low input power, the SPL of the samples is proportional to P_{in} (20dB/dec) but for higher input power the spectrum is approximately proportional to $P_{in}^{0.75}$ (15dB/dec). This non linear behavior can be interpreted with an increase of the average static temperature inside the pores of the foam, and with a consequent efficiency reduction [48]. It is seen that

our model is not able to reproduce this behavior since the average temperature within the pores is fixed a priori.

Conclusions

A two temperature model for describing the thermo-acoustic generation of sound by thick foam thermophones has been elaborated in Section 2.5 and is here exploited.

The spatial distribution of the main physical variables were studied for both thick and thin thermophones. The results obtained through our two temperature model were compared with the classical model composed of a solid bulk generating layer. It was proven that the output SPL may be different between these models, depending on the thickness of the thermophone. For thin thermophone, 1T and 2T model give similar results but thicker thermophones lead to significant differences in the output SPL. These differences have been explained in terms of the specific features implemented in the two models and can be summarised by the over estimation of HCPUA of thick thermophone when using a 1T model. Afterward, the frequency and power spectra were compared with experimental results published in the recent literature [48]. The similar behaviors of the 1T and 2T models for thin thermophones were confirmed and both models were in quite good agreement with the experimental results. Thick thermophones were then investigated. While the 1T model was unable to accurately reproduce the experimental results, the 2T model displayed good agreement from the point of view of both frequency and power spectra. However, it could be further improved since it is unable to represent the losses due to the static temperature raise within the porous structure. It was pointed out that for complex foam like structures it is important to consider the so called homogenized parameters of the whole sample (solid plus air), which are different from the local parameters of a single foam branch.

In conclusion, the two temperatures model presented here appears to be a first step in modeling thick and nano- or micro-structured thermophone systems. The most important point introduced concerns the exchange of energy at any contact surface between air and solid foam. This feature better represents the reality of such systems and is able to reproduce experimental results, which were not understood on the basis of previous models.

	ρ [kg· m^{-3}]	C_p [J ·kg^{-1}·K^{-1}]	C_V [J ·kg^{-1}·K^{-1}]	B [Pa]	α_T [K^{-1}]	κ [W·K^{-1}·m^{-1}]
Gas, air	1.20	9.96×10^2	7.17×10^2	1.01×10^5	3.33×10^{-3}	26.2×10^{-3}

	λ [N·s·m^{-2}]	μ [N·s·m^{-2}]
Gas, air	16.82×10^{-6}	5.61×10^{-6}

Table 7: Parameters of the propagating medium (air).

	ρ_s [kg·m^{-3}]	$C_{V,s}$ [J ·kg^{-1}·K^{-1}]	B_s [Pa]	κ_s [W·K^{-1}·m^{-1}]	l_l [m]	l_s [m]	A [cm×cm]
CNT sheet	1	716	1.11×10^{11}	50	18×10^{-6}	10×10^{-9}	Square 1.5×1.5
ITO PAN	220	606	1.65×10^{11}	310	5×10^{-6}	450×10^{-9}	Square 1.2×1.5
MWNT sponge	30	716	1.11×10^{11}	100	100×10^{-6}	10×10^{-9}	Square 1×1
Graphene sponge	2.75	660	1.44×10^{8}	6.3	800×10^{-6}	5×10^{-9}	Circle d = 1.8

Table 8: Parameters of the thermophone materials used in the experiments and theoretical models [48].

Part IV

EXPERIMENTAL ANALYSIS

4

EXPERIMENTS

This chapter presents the most prominent results obtained experimentally over the past three years. The samples used in the presented results will be described but a more thorough list of all the samples used during this work is found in Appendix C.1. The focus of this section is on the acoustical radiation of thermophones. Additional characterisation results regarding the samples are found in Appendix C.2. It has to be noted that all presented figures display results that are normalised with distance (1m) and input power (1*W*) unless specified otherwise. Additionally, all samples used had their complex impedance measured with a spectrum analyser and which were observed to be constant up to 1MHz.

In first instance, the experiments performed in January and February 2020 in CINTRA Singapore with the PhD student Ngoh Zhi Lin are presented. The graphene foam sample referred as 3D-C is described from its fabrication process to its resulting microstructure. Its thermoacoustic properties are then investigated in regards of its density, geometry, support, pore density... and compared with our presented 2T model. This analysis is found in a recently published article [3].

Additional airborne acoustic analysis made at the IEMN in Lille with different samples are presented. Those complementary airborne experiments have been performed to try and push the limits of the standard acoustic setup used in the previous sections. The maximum airborne recording range was increased using a designed electronic system (reaching 200kHz) and was further increased using high frequency laser interferometry (measurements to the MHz range). Then a high frequency thermal camera recording which was able to show the rapid temperature variation of the foam are presented. Some preprocessing regarding the input signal has been performed to allow us to play complex musical signals using only audio AC amplifiers. Lastly some thoughts and experiments regarding underwater thermoacoustic measurements are discussed.

4.1 AIBORNE ACOUSTIC EXPERIMENTS PERFORMED IN CINTRA SINGAPORE

In this section, 3D-C is synthesized via thermal chemical vapor deposition and its microstructure and quality tested using Scanning Electron Microscopy and Raman spectroscopy respectively. Then, a two temperature model is used to predict the effects of numerous parameters: frequency, input power, sample size, connection area, connection path, pores per inch, thickness, compression as well as the addition of a backing on the acoustic performance and temperature of the sample. The experimental results presented in this section validate the predictions of the adopted two temperature model. The efficiency of 3D-C is then compared with results presented in other studies to understand how the presented 3D-C fared against ones from the literature as well as other carbon nanostructured materials.

4.1.1 *3D-C Fabrication, Characterisation and Experimental Setup*

Fabrication by CVD

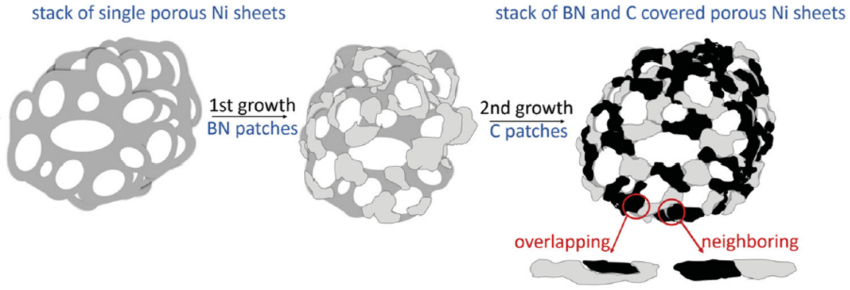

Figure 68: Chemical Vapor Deposition method for Boron-Nitrite and Carbon growth on a Nickel foam structure used by Loeblein *et al.* [59].

3D-C was synthesized following Ngoh *et al.*'s thermal chemical vapor deposition (TCVD) method [159]. A nickel foam template (Latech Scientific Supply Pte Ltd) was inserted into the middle of a split tube furnace before the system is ramped up to 1000°C under argon and hydrogen gas flow. After achieving the required temperature, the graphene precursor, methane gas, is flown into the system. After graphene growth is achieved, methane gas is switched off and the lid of the furnace is lifted for rapid air cooling. The graphene coated nickel template is then soaked in hydrochloric acid (HCl) at 85°C to chemically remove the sacrificial nickel template and obtain the final free-standing 3D-C. Figure

68 schematically explains the growth of Boron-Nitrite and Carbon on a Nickel foam structure used by Loeblein *et al.* [59].

Raman Spectroscopy

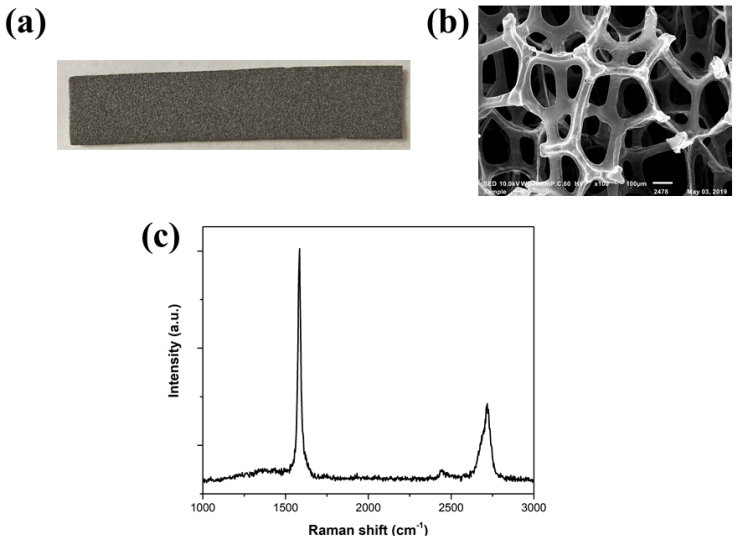

Figure 69: Chemical characterisation of 3D-C. (a) Visual image of 3D-C; (b) SEM micrograph of 3D-C; (c) Raman spectrum of 3D-C [3].

The microstructures of 3D-C were captured with the use of SEM (JEOL JSM-IT100). The crystallinity of 3D-C was determined using a Raman spectroscope (WITec CRM200 Raman, utilizing Nd:YAG 532 nm laser as excitation source). The SEM micrograph of the obtained free-standing 3D-C indicates that the microstructure of the synthesized 3D-C did not collapse and instead has similar microstructures as that of freeze-dried 3D-C synthesized by Fei *et al.* and Lee *et al.* [63, 129]. Raman spectroscopy was conducted on 3D-C to determine its crystallinity and the obtained spectrum can be seen in Fig.69c. Only 2 peaks appear at 1580cm^{-1} and 2705cm^{-1}, which represent the G and 2D peaks respectively, indicating the presence of graphene. The absence of the defect peak at 1350cm^{-1} indicates that the graphene present in 3D-C were of pristine quality [59, 63, 159–162].

Configuration of 3D-C samples

The synthesized 3D-C samples were adhered to the middle of the microscope glass slides (76.2 × 25.4 × 1.1mm, Sail brand) and customised acrylic holders with a 25 × 25 × 4mm hole in the middle (60 × 35 × 4mm,

Sample type	Front view	Back view
3D-C on microscope glass slide with **point** connection	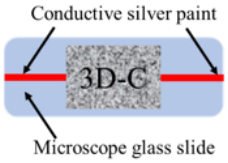	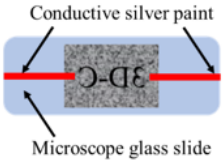
3D-C on microscope glass slide with **line** connection	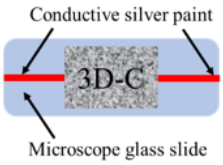	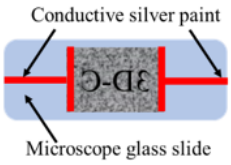
3D-C on microscope glass slide with **volume** connection	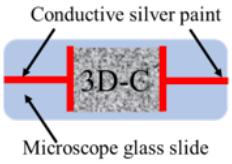	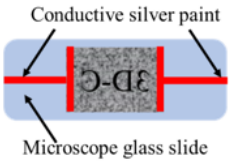
3D-C on microscope glass slide with **4** connection paths	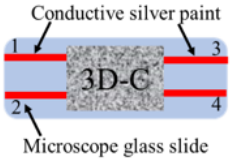	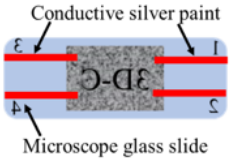
3D-C on customised acrylic holder slide with **point** connection	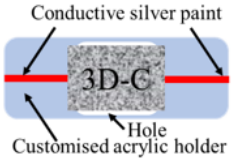	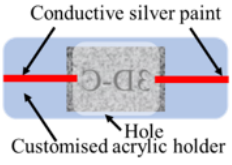

Figure 70: Schematics of how the various configurations of 3D-C are mounted on their respective backings.

Dama Trading Pte Ltd, Singapore) using conductive silver paint (Leitsilber 200 Silver Paint, Ted Pella, USA) as depicted in Fig.70.

Experimental setup

The acoustic performances of the mounted 3D-C samples were measured using the set-up in a non-anechoic room as seen in Fig.71. The lap-top used for data logging and parameter entry **1** is connected to the output generator module (Type 3160-A-022, Brüel & Kjær) **2**. The AC signal generated by the output generator is amplified by a power amplifier (Type 2735, Brüel & Kjær) **3**, and applied to the mounted 3D-C

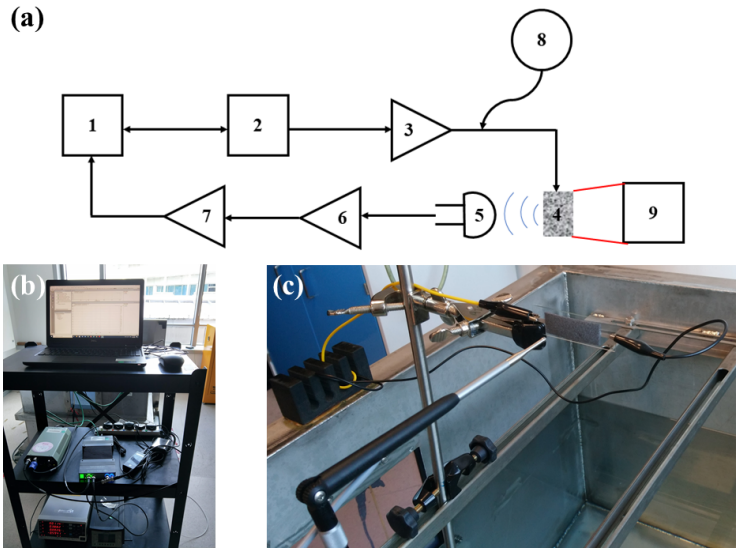

Figure 71: Set-up for measurement of 3D-C's acoustic performance. (a) Schematic diagram of set-up. Lap-top (1), output generator module (2), power amplifier (3), mounted 3D-C (4), microphone (5), microphone preamplifier (6), conditioning amplifier (7), power meter (8) and infrared thermal camera (9); (b) Visual images of circuitry set-up and; (c) Visual image of 3D-C mounted in set-up.

sample **4** via crocodile clips. The microphone (Type 4138, Brüel & Kjær) **5**, which is 3cm from the mounted 3D-C sample, receives the signal. This signal is amplified by the pre-amplifier (Type 2670, Brüel & Kjær) **6** and the conditioning amplifier (Type 2690, Brüel & Kjær) **7**. The amplified signal is feedbacked into the output generator to be relayed to the lap-top for data logging. The real-time power and temperature measurements when the system is in operation are captured by a power meter (PW335, Hioki) **8** and an infrared thermal camera (Ti480, Fluke) **9**.

The background noise of the room was captured to be ~ 25dB, except two broad peaks at 28kHz and 32kHz with sound pressure levels between 27 and 32dB (Fig.72a). All acoustic measurements made were significantly above background noise, indicating sufficient signal-to-noise ratio for it to be considered acoustic signals from the samples instead of background noise. The raw SPL of the $50 \times 20 \times 2$mm 3D-C mounted on a microscope glass slide with acoustic frequency of 10kHz and input power of 3*W* is as seen in Fig.72b.

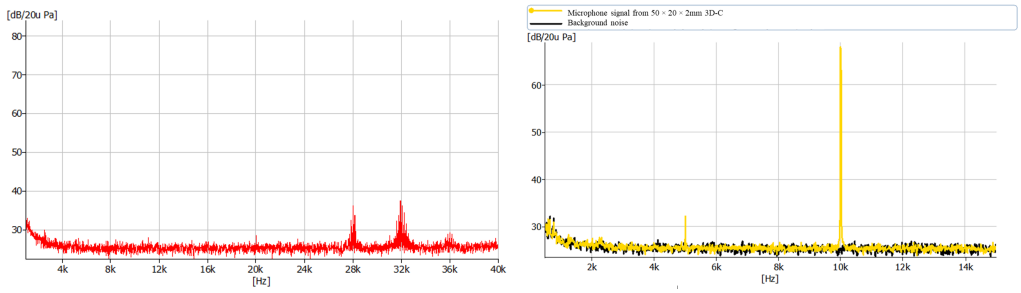

(a) (b)

Figure 72: (a) Captured background noise of non-anechoic chamber across the whole frequency range of interest. (b) Background noise and raw SPL of $50 \times 20 \times 2$mm 3D-C mounted on a microscope glass slide with acoustic frequency of 10kHz and input power of 3W in black and yellow respectively.

	ρ [kg· m^{-3}]	C_p [J ·kg^{-1}·K^{-1}]	C_V [J ·kg^{-1}·K^{-1}]	B [Pa]
Gas, air	1.20	9.96×10^2	7.17×10^2	1.01×10^5
Solid, 3D-C	3.0	660	660	1.44×10^8
	α_T [K^{-1}]	κ [W·K^{-1}·m^{-1}]	λ [N·s·m^{-2}]	μ [N·s·m^{-2}]
Gas, air	3.33×10^{-3}	26.2×10^{-3}	16.82×10^{-6}	5.61×10^{-6}
Solid, 3D-C	2.6×10^6	160	0	0

Table 9: Parameters of the propagating medium (air) and the solid (3D-C) used in the simulations.

Sample parameters

The geometries of the samples used and the physical parameters of the medium (air and 3D-C) are found in Tables 9, 10 and 11. The number N of discretized, regularly-spaced layers used in simulations is found in Tables 10 and 11. The number of layers used in simulations is approximately three times larger than the estimated one simply obtained by multiplying the thickness of the samples with the ppi data. As our model is one-dimensional and since the synthesized 3D-C has a very complex geometry with hollow branches, it is assumed that more energy is provided from 3D-C to the surrounding medium than that generated by the branches simply aligned in the propagation axis. This is indicated in our model by the additions of effective layers.

Figures	74, 75, 76, 84, 87	74, 80, 81	74	75, 76	75, 76	78
L_x (mm)	20	30	50	20	20	20
L_y (mm)	20	20	20	20	20	20
L_z (mm)	2	2	2	2	2	2
N (simulations)	28	28	28	x	x	x
Ppi	110	110	110	110	110	110
Connection (see Fig.70)	Point	Point	Point	Line	Volume	Across
DC Resistance (Ohm)	2.9	3.7	5.1	2.1	1.7	2.2

Table 10: Parameters of the samples used in the experiment with their equivalent number of layers N used in the simulations.

Figures	78	78	78	80	81	83	84
L_x (mm)	20	20	20	30	30	30	20
L_y (mm)	20	20	20	20	20	20	20
L_z (mm)	2	2	2	5	2	2	1
N (simulations)	x	x	x	70	28	x	28
Ppi	110	110	110	130	110	110	110
Connection (see Fig.70)	Diagonal	Same Side	All through	Point	Point	Point	Point
DC Resistance (Ohm)	2.5	2	1.7	1.8	1.1	3.8	3.7

Table 11: Parameters of the samples used in the experiment with their equivalent number of layers N used in the simulations.

4.1.2 *Analysis of Experiments done in CINTRA*

(a) (b)

Figure 73: Pictures from the exchange in CINTRA Singapore in January 2020. From left to Right on panel (a), Ms.Tan Dunlin, Ms.Ngoh Zhi Lin, Mr.Guiraud Pierre and Mr.Coquet Philippe. On panel (b) Zhi Lin and myself are performing experiments over the water tank.

The geometries of the samples used and the physical parameters of the medium (air and 3D-C) can be found in Tables 9, 10 and 11. All measurements were done with recording distances of 3cm to improve the signal to noise ratio but the reported SPL are normalized to a recording distance of 1m. All reported frequency spectrum measurements are also normalized with an input power of 1*W*. As indicated in the acoustic measurement set-up in Section 4.1.1, all measurements were made using only an alternating current (AC) signal generator. Without a DC supply, a thermophone will radiate at twice the generating its generating frequency. It is physically understood as, when an AC signal runs through the sample, the temperature is unable to have negative values, resulting in its variation being proportional to twice the frequency of the AC signal. Mathematically speaking, the sound pressure is proportional to the input power given by [142]

$$P_{input} = \frac{V_{input}^2}{R} = \frac{(V_{AC}\cos\omega t)^2}{R} = \frac{V_{AC}^2}{2R}(1+\cos 2\omega t). \tag{432}$$

Hence, the presented acoustic spectra correspond to the acoustical frequency, the first harmonics of the AC input. Power measurements and the associated recorded temperatures were obtained at an AC input frequency of 5kHz, which induces an acoustical wave at 10kHz.

Effect of Sample Size

Fig.74 shows the frequency and power spectrum of three of the samples with the same intrinsic parameters but of different sizes (see details in legend of Fig.74).

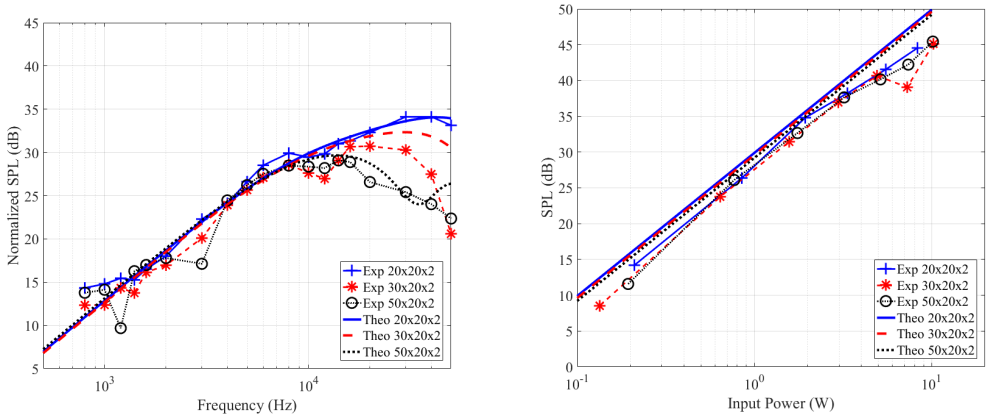

(a) (b)

Figure 74: (a) Acoustical frequency and, (b) power spectrum of 3D-C of different sizes in millimeter.

From Fig.74b, we deduce that the SPL and the input power exhibit a linear relationship, both experimentally and theoretically. Similarly, in Fig.74a there is a linear relationship (20dB/decade) between SPL and frequency from 1kHz to ~ 10kHz. This linear behaviour agrees with the thermoacoustic theory and the recent literature [43, 57, 71, 81]. In the higher frequency range, from ~ 10kHz to 50kHz, acoustic diffraction is observed. The longest sample has a lower anti resonance frequency, resulting in a decrease in SPL before the other samples. Since this classical acoustical result fits our theoretical curve, the assumption made in sub-Section 2.7 of considering a planar diffraction with the velocity taken at the limit of the thermal layer is then validated. Sample length affects the electrical DC resistance of the sample (Table 10, 11). Indeed, due to the longer path which the electrical current has to go through (L_x in Tables 10, 11), longer samples display higher DC resistance. This however does not influence the overall SPL of the sample as both frequency and power spectra are in the same range for the three sample with different size. Since thermophones are driven by thermal power and not electrical potential, different DC resistances can create impedance matching issues with the interfacing hardware but will not change the acoustic radiation once normalized. However, it was also observed that for the same input power, the temperature was the lowest for the longest sample. This is due to the increased surface area which the sample has,

allowing thermal energy to dissipate into the surrounding medium at a faster rate. With increased heat dissipation, the observed temperatures are lower.

Effect of Connections

Connection Area

Figures 75 and 76 show the results for samples of similar parameters and dimensions but with a difference in the way the connection was made. As seen in Fig.70, the point connection consists of just a dot of silver on the centre of the edges of 3D-C, the line connection has conductive silver paint following the edges of the 3D-C, and the volume connection has conductive silver paint dripped directly on 3D-C to completely coat the thickness of 3D-C.

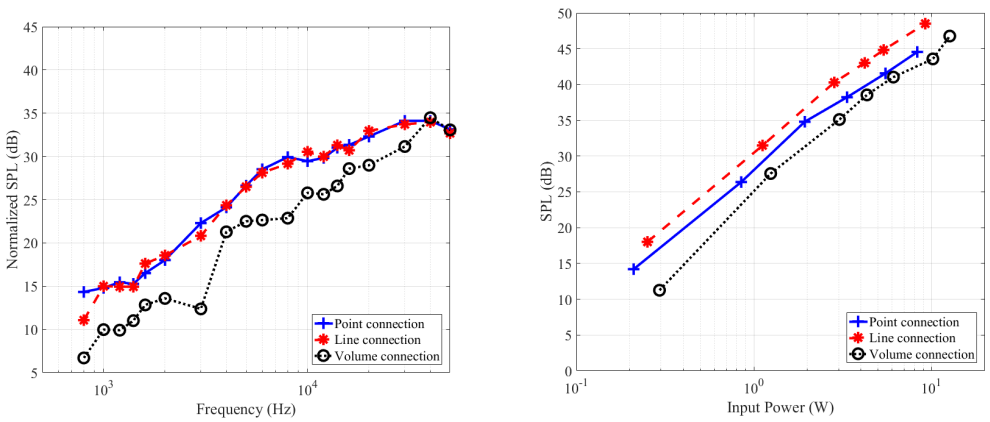

(a) (b)

Figure 75: (a) Acoustical frequency and, (b) power spectrum of samples of the same size but with different silver paste connections, see Fig.70.

In the frequency spectrum of Fig.75a, the point and line connection display similar results unlike the volume connection, which performs on average 5dB lower across the whole frequency range. The thermal camera image in Fig.77 shows that the silver paste is not heated, thus preventing the thermoacoustic process from happening on the edges of 3D-C. This resulted in a thermal energy loss, consequently decreasing its acoustical performance. The differences are not as pronounced in Fig.75b but it is seen that for a fixed input power the volume connection displays the lowest SPL. Unlike in Fig.75a, it is seen that the line connection performs 2dB higher than the point connection in Fig.75b. This could be attributed to measurements errors in either Fig.75a or 75b

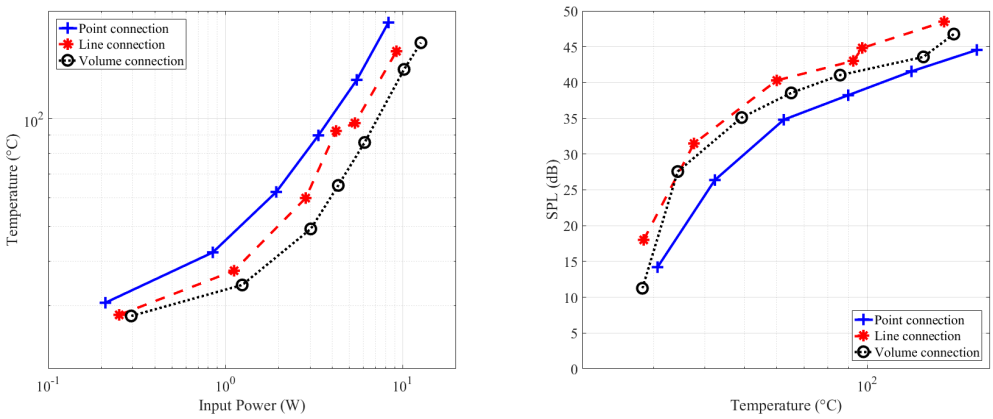

(a) (b)

Figure 76: Temperature dependence of the samples with different silver paste connections. (a) Relationship between temperature and input power and, (b) relationship between SPL and temperature.

but would lead to think that the line connection is more efficient than the point one.

In Fig.76a, the thermal behaviour of 3D-C with increasing power is shown. Above 1*W* of input power, the temperature increases linearly with input power, as also observed in the literature [48]. At low input power below 2*W*, the temperatures of the samples are similar to the temperature of the surrounding air medium, and no conclusion can be drawn on the linear relationship between the input power and temperature. More low power measurements have to be performed with different experimental conditions to be sure of the linearity between temperature and input power at all power levels. Fig.76a shows that at the same input power, the point connection has a higher temperature than the line connection, which also has a higher temperature than the volume connection. Increased electrical contact surface with the sample decreases the power density in these regions, diminishing the hot point temperature. In Fig.76b, the SPL is plotted against temperature. Although the normalized SPL of the point connection is 5dB higher than the volume connection in Fig.75a, the volume connection performed better in absolute SPL values relative to temperature in Fig.76b.

In other words, Fig.75a indicates that the line or point connection are equally as efficient, and both perform better than the volume connection, as indicated in Fig.75b as well. However, Fig.76a and 76b show that the point connection is performing worse in terms of temperature than the others and is hence more likely to decompose prior to the other samples when a high input power is channelled into the sample. Hence, the better power repartition of the sample connected via line connection

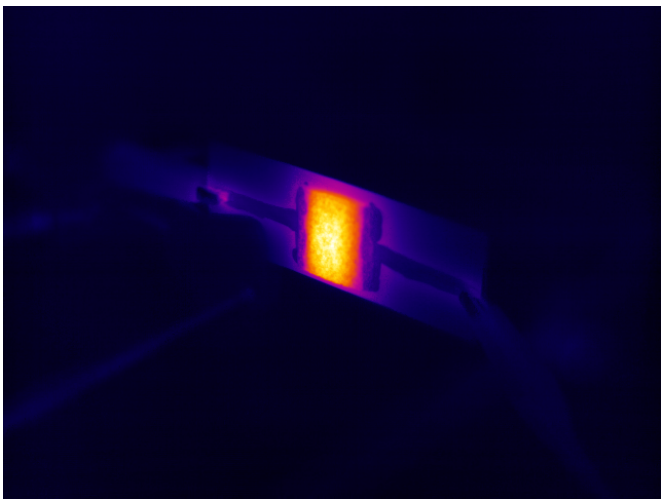

Figure 77: Thermal image of 3D-C with volume connection with 3.3W power input at an acoustical frequency of 10kHz.

inflicts less heat damages when a high input power is injected into the sample, indicating its better resilience to high input power.

Connection Path

In Fig.78, a single sample with four different connection points is investigated. The electrical path used changed for each measurement. Following the schematic of the sample seen in Fig.70, the paths investigated are 1-3 (across), 1-4 (diagonal), 1-2 (same side) and 12-34 (all through).

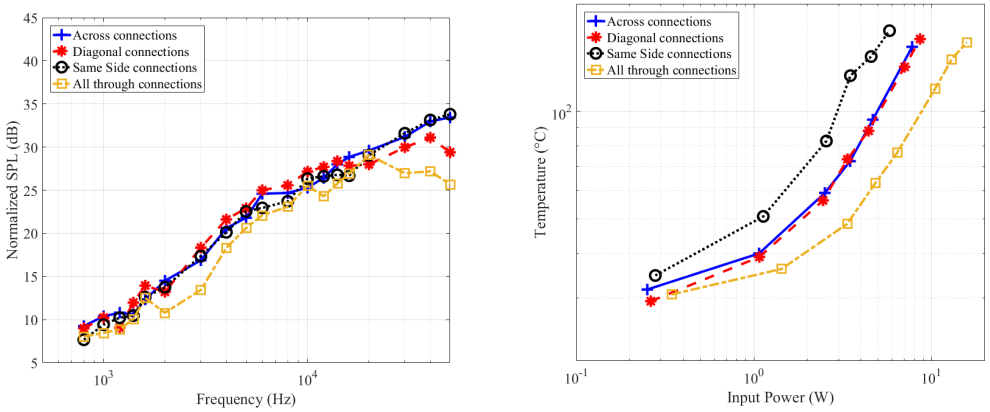

(a) (b)

Figure 78: (a) Acoustical frequency spectrum and (b) temperature variations of one sample with different electrical connection paths.

As expected, changes in the path also lead to changes in the DC resistance as seen in Tables 10, 11. The DC resistance of the path taken is directly proportional to the travel distance in 3D-C between the electrical contacts and their surface areas. Shorter paths have lower DC resistance, and increased contact surface results in lower DC resistance as well (Table 10, 11). Thermal images in Fig.79 show that the temperature hot spots follow the least resistive path and that the temperature is most uniform only when the current is more uniformly distributed throughout the sample ("all through" connection).

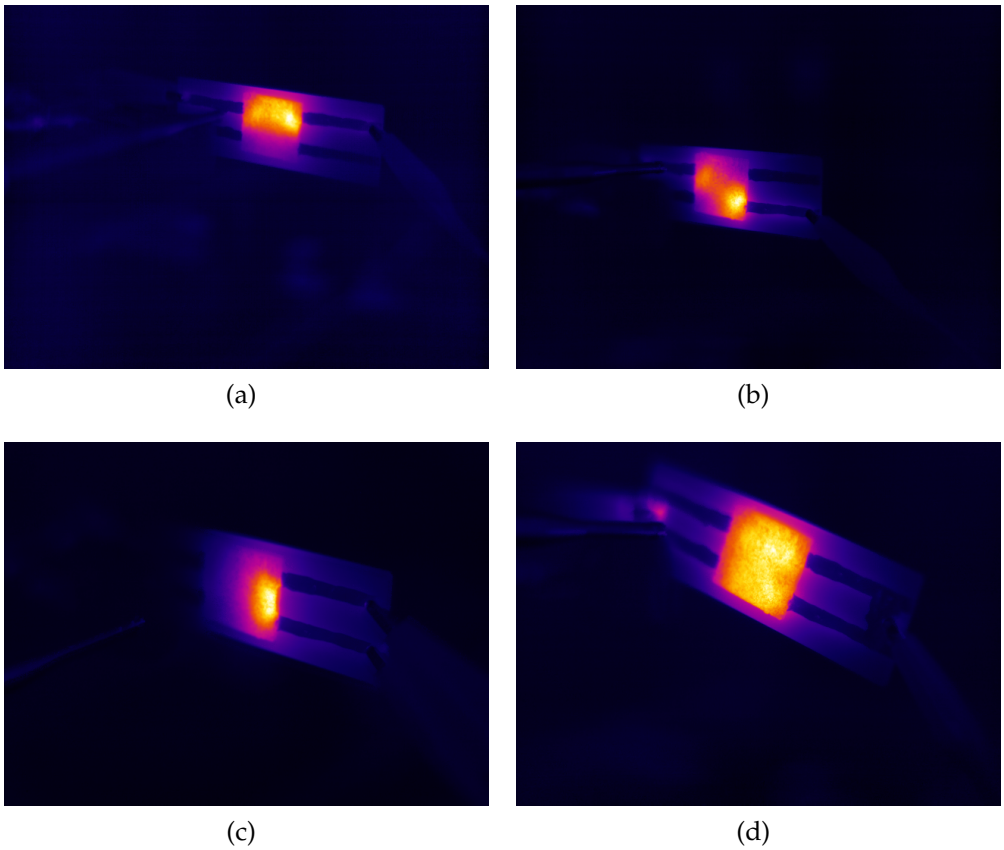

(a) (b)

(c) (d)

Figure 79: Thermal images of the sample with multiple connections (a) across (b) diagonal (c) same side (d) all through.

Fig.78a shows that at frequencies below 20kHz, the samples' SPL have a linear relationship with the frequency. Despite the hot spots being located at the electrical connections, it is expected that high thermal conductivity of the samples would cause the entire 3D-C material to radiate. A single sample would then display similar normalized SPL regardless of the electrical path chosen, which is confirmed by the consistent spectra of Fig.78a up to 20kHz. At frequencies above 20kHz, acoustic diffraction phenomena appear for all connection paths. If the entirety of 3D-C was radiating equally, the frequency spectra would be similar across

the whole frequency range. However, these acoustic diffractions indicate that the acoustic radiation of the thermophone is dependent on the least resistive path. Due to the non-uniform distribution of energy, the entirety of 3D-C was not used to its maximum potential. Paradoxically, using the 3D-C in its "most efficient" configuration (uniform energy distribution) will create acoustic diffraction at lower frequencies due to the use of a longer radiating surface. This is seen in Fig.79d with the "all through" path.

Comparing the results in Fig.78b, the sample with the least resistive path (shortest travel distance, across connection) has a higher power density concentration. Hence, for a fixed input power, the temperature of the sample's hot spot will be higher than in a more distributed configuration (all through connection). The connection utilizing the most of the sample's surface and having a high connecting surface would hence have the highest power resilience. Connection "all through" is then recommended and concurs with the line connection analysis from the previous sub-section for samples with varying connection types (Fig.75a).

Effect of physical parameters variation of 3D-C

Various physical parameters, namely the pore per inch (ppi), thickness and density of 3D-C, were varied and their influence on the acoustics performance investigated.

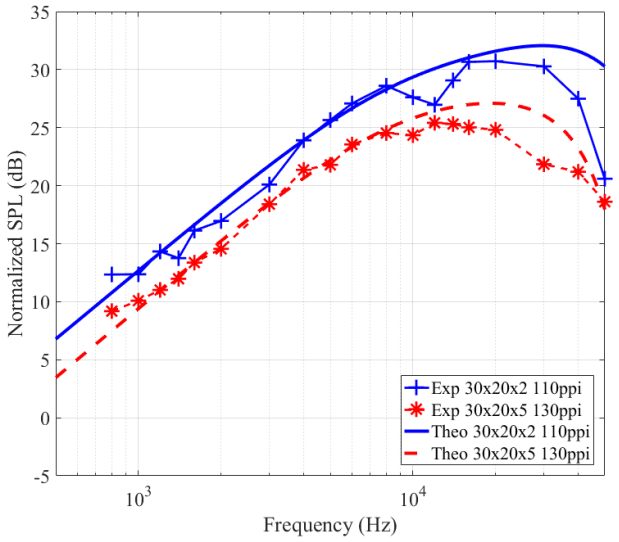

Figure 80: Acoustical frequency spectrum of samples with different thickness and ppi.

Figure 80 compares a regular sample 2mm thick with 110 ppi and a thicker 5mm sample with 130 ppi. In their associated theoretical models, despite the difference in ppi, the change of thickness lead to the use of a similar number of layers per millimeter in both cases (Table 10, 11). Across the whole frequency range, there is a difference of ~ 3 dB between the samples. This difference attributed to the slightly differing microstructures of each piece of 3D-C, resulting in differences in efficiency. The specific surface area has been changed in the theoretical model to tune the power density to the results (1.4 times higher than with 110 ppi). Above 20kHz, the diffraction differs slightly in the experimental results but a strong anti-resonance is observed in the model. This is explained by the higher thickness of the 130 ppi sample and the regularly spaced layers in the foam considered in the model. When each layer radiates acoustically coherent sound waves, each layer would add up coherently with a slight delay

$$\sum_{n=0}^{N} \cos\left(kx_0 + nk\frac{L_z}{N}\right) = \cos\left(kx_0 + k\frac{N}{2}\frac{L_z}{N}\right)\frac{\sin\left((N+1)\frac{k}{2}\frac{L_z}{N}\right)}{\sin\left(\frac{k}{2}\frac{L_z}{N}\right)}. \quad (433)$$

Anti-resonances then occur at every frequency with k as an integer

$$f = \frac{C_0}{L_z\frac{N+1}{N}}k = \frac{343}{5\times10^{-3}\frac{71}{70}} = 6.76\times10^4 \text{ Hz}, \quad (434)$$

as observed in Fig.80 with $k = 1$. Other than high frequency diffractions caused by the difference in thicknesses and hence number of radiating layers, both samples perform similarly acoustically. However, the 130 ppi sample cools approximately twice as fast as the 110 ppi sample. Videos found in Supporting Information (Videos S1 and S2 in supplementary information of the third article [3]) show that the cooling process of the sample was improved with higher ppi. The increase in ppi resulted in an additional increase in the number of pores in the 3D-C, allowing air to circulate more freely in the material, increasing the rate of cooling by thermal conduction towards the surrounding air.

Figures 81 compares two samples with different densities. Unlike the previous samples, the 3ρ sample had a longer growth time of graphene, leading to thicker branches and a material with three times the density. HCPUA is considered the most important parameter in the global efficiency of thermophones [35, 78], which can be written as $\rho C_p l$ with l the thickness of the radiating surface. To achieve optimum thermoacoustic radiation, HCPUA has to be as low as possible. Increasing the density of the thermophone would then diminish its acoustical performance. Fig.81a shows both experimental frequency spectra, and a drop

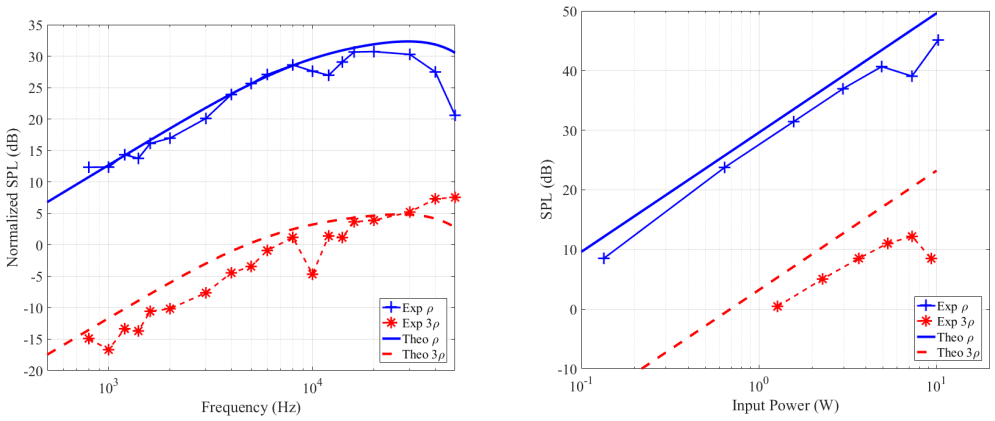

(a) (b)

Figure 81: (a) Acoustical frequency and, (b) power spectrum of 3D-C with different densities

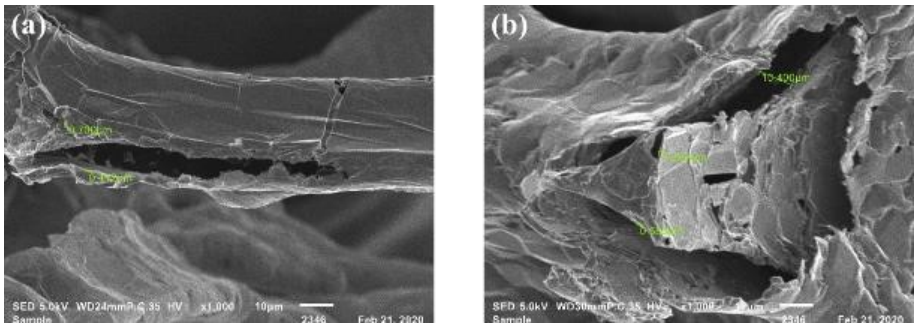

Figure 82: SEM micrographs of 3D-C taken up close. (a) SEM micrograph of a sample with density ρ; (b) SEM micrograph of a sample with density 3ρ [3].

of 25dB is observed across the whole frequency range for the 3ρ sample. The trends of both curves are similar and the theoretical model fits both curves. This fit was obtained by increasing the theoretical HCPUA value by a factor of ~ 27. This is justified by the higher measured density, increased thickness of the branches (Fig.82) and the proportional increase of the specific heat. The power spectrum as seen in Fig.81b displays the same behaviour as Fig.81a. The SPL is reduced by 25 to 30dB in the 3ρ sample and the increase of HCPUA allows a good fit between theoretical predictions and experimental results. The few dB differences between theory and experiments of Fig.81b can be explained by the local experimental reduction of the SPL at 10kHz seen in Fig.81b.

Improvement of sound pressure level

Next, we investigate a method to improve sound generation in 3D-C based on well-known acoustical results and new experiments on the 3D-C structure.

Addition of backing

In a general acoustic context, when a monopole is placed on a reflecting surface, a coherent reflection from the backing will double the emitted sound pressure, thus causing a 6dB increase in the SPL. In theoretical thermoacoustic models, it has been shown that if a thermophone is directly in contact with its backing, some thermal losses will occur. Part of the thermal energy used for the acoustic generation will be lost by thermal conduction in the backing [1, 40, 76, 81]. To prevent this, it is crucial to leave a large enough air gap between the sample and the backing. This air gap should be longer than the thermal layer in which the thermoacoustic generation occurs. It is also important to remember that the thermal layer is inversely proportional to the square root of the frequency, see Eq.(154). For instance, in air, the thermal layer length is about $\sim 260\mu m$ at 100Hz and so $\sim 26\mu m$ at 10kHz. It is then interesting to note that the size of the pores in 3D-C is a few hundred microns, which means that the pore is large enough for the acoustic generation to occur inside of it.

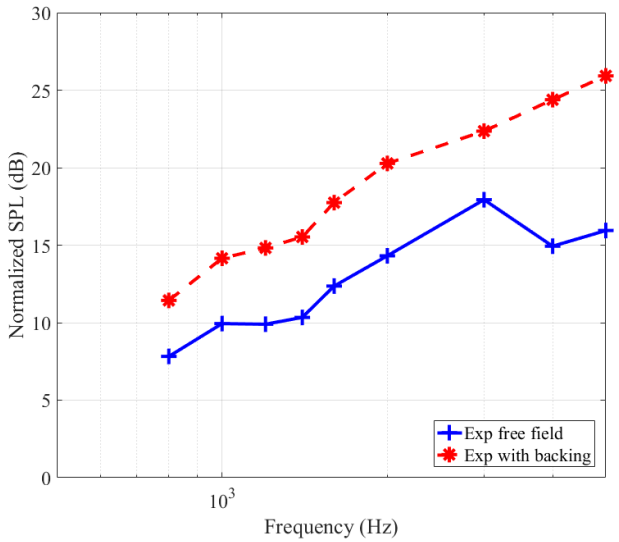

Figure 83: Acoustical frequency spectra of 3D-C radiating in free field and with an acoustical backing.

In Fig.83, a sample radiating in free field was recorded, and then an acrylic backing was added 4mm behind one side of 3D-C for com-

parison. As predicted by acoustical theory, the SPL increased by 6dB below 5kHz. Above 5kHz (not shown here), acoustic diffraction caused by the size and thickness of the backing can be observed but is not discussed here as it is a standard acoustic result not related to thermoacoustics. The thermophone performance can hence be improved by 6dB by the simple addition of a backing. Nevertheless, this backing has to be placed at a controlled distance: close enough for coherent reflections but at least several hundred microns away from the sample in order to avoid undesired losses by thermal conduction.

Compression of 3D-C Material

The two temperature model proposed in Guiraud *et al.* 2019 [2] indicated that one method to improve the high frequency radiation of a foam thermophone with a fixed thickness was to increase the number of discretized layers. This would increase the contact surface area between 3D-C and the surrounding air, improving the energy transfer between the two media. One way to investigate this property experimentally would be to compare samples with the same thickness and porosity but with a different layer density, a lower ppi.

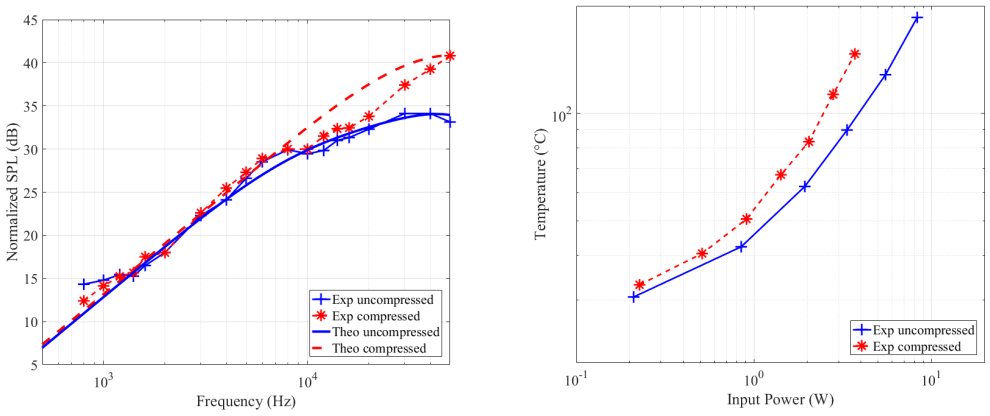

(a) (b)

Figure 84: (a) Acoustic frequency spectra and (b) temperature dependence of 3D-C before and after mechanical compression, the thickness being 2mm and 1mm respectively as seen in Tables 10, 11

In Fig.80, the increased thickness compensated the increase in ppi, the number of layers per millimetres did not change (Tables 10, 11). Another way would be to mechanically compress a sample in order to reduce its thickness while preserving its structure, thus artificially increasing the layer density more significantly. This would also allow for better comparison if the internal structure of 3D-C is fully preserved af-

ter compression. The experimental results of this method are presented in Fig.84 and are compared with theoretical results in which the number of layers N is the same in both cases but the thickness reduced, as seen in Tables 10, 11. Figure 84a shows that at frequencies below 10kHz, the sample acoustically performs similarly before and after compression, indicating that the internal structure of the sample was preserved during the compression. This is also proven by the SEM micrograph of the compressed 3D-C in Fig.85.

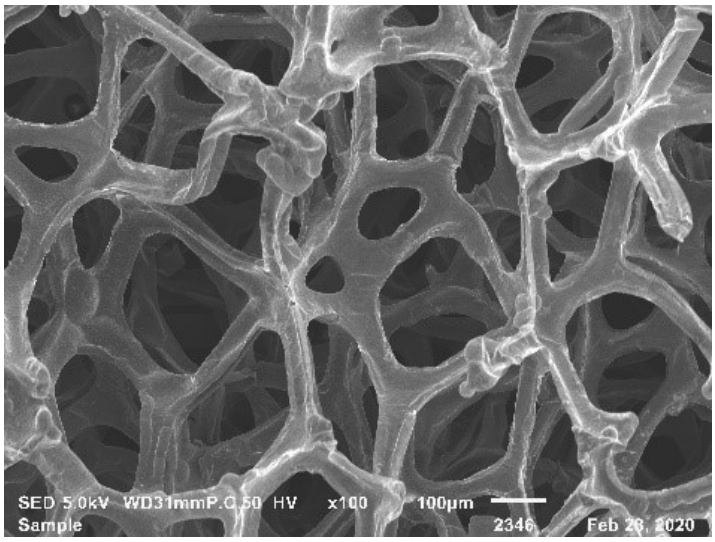

Figure 85: SEM micrograph of compressed 3D-C.

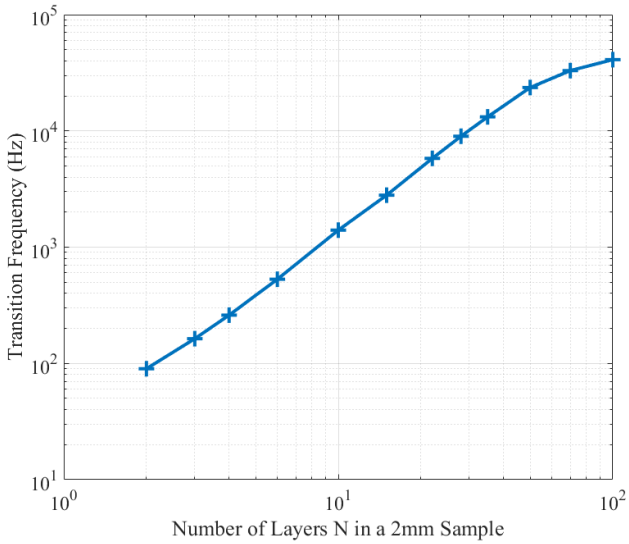

Figure 86: Transitional frequency depending on the theoretical number of layers in a 2mm sample.

Above 10kHz, the maximum SPL of the compressed sample is 6dB higher than the maximum SPL of the uncompressed one. The good agreement with the experimental curves confirms that all branches in 3D-C were radiating and that the ppi had been artificially increased by a factor of 2. Considering the theoretical data but ignoring high frequency acoustic diffraction, it is observed that by increasing the number of discretized layers, the SPL is linearly proportional to the acoustic frequency up to a higher frequency (slope of 20dB/decade up to 40kHz). On the other hand, when there is insufficient energy transferred to the air (not enough layers), the SPL would be proportional to the square root of the frequency (10dB/decade increase for the uncompressed sample from 10k to 40kHz). For practical design of a thermophone device at a designated frequency, it would be interesting to know the minimum number of layers required for maximum efficiency. Due to the complex matrix form of the two temperature model, it is challenging to analytically determine the frequency in which this change of behavior will occur (from 20 to 10dB/dec) based on the number of layers. A numerical trend can however be observed in Fig.86.

Lastly, Fig.84b shows that the temperature will be higher in the compressed sample for the same input power. This is easily explained as the compression scales down the pore size and thus reduces the cooling effect of the air. The heat dissipates less easily and the temperature rises.

Comparison with literature results

Table 12: Comparison of different 3D-C synthesized via TCVD in the literature. The normalized SPL at 1m and 1W is measured at 1kHz

Thermophone	Substrate	SPL (dB) at 1kHz	Reference
		36	Maximum from Vesterinen [57], See Eq.(435)
Freeze Dried 3D-C	Glass	25	Fei 2015 [63]
Freeze Dried 3D-C	Free-standing	25	Lee 2018 [129]
Natural Dried 3D-C	Glass	15	This work
Natural Dried 3D-C	Glass	12	Fei 2015 [63]

Table 12 compares the thermoacoustic response of 3D-C synthesized from literature methods [63, 129]. Firstly, minimal research has been conducted on 3D-C due to it being discovered in 2011 [160], which

is more than 5 years later than CNTs [163]and graphene [164]. Thus, this leaves room for more thorough understanding of 3D-C geometry. Assuming that the heat capacity of the thermophone is negligible, a maximum value for the pressure generated by thermoacoustics was estimated in the literature as found in Eq.(422) and is here rewritten [48, 57]

$$p_{rms} = \frac{f}{2\sqrt{2}C_p T_0}\frac{1}{r}P_{in}. \tag{435}$$

Eq.(435) depends only on parameters of the propagating medium and was added in Table 12 as a comparison, assuming sound propagation in air. Table 12 shows that 3D-C presented in this paper performed 10dB lower than its freeze-dried counterpart from literature, which had been observed in Fei *et al.* work [63]. However, the naturally dried 3D-C used by Fei *et al.* performs 3dB lower than the presented foam. This is attributed to the improvement made to the TCVD technique, which is reflected in the pristine quality of the 3D-C as seen in the Raman spectroscopy with the absence of the defect peak at $1350cm^{-1}$ (Fig. 3c). Overall 3D-C does not reach the maximum theoretical performance for thermophones and different structures like CNTs have been shown to display higher SPL compared to 3D-C. For instance, at 5kHz, 3D-C is a thousand times less efficient than the theoretical maximum from Eq.(435), which is also a thousand times less efficient than a traditional loudspeaker. Additionally, while 3D-C is not as efficient as CNTs, its internal structure allows for a better cooling during operation, rendering it less vulnerable to damage caused by overheating.

Eq.(435) is a maximum that was determined based on the assumption of ideal physical properties of a thermophone and not on its geometry. It would be interesting to utilize 3D-C with such flexible synthesis methods to investigate more complex and potentially more efficient thermophones. Unlike CNTs which require the tedious extraction of its strands from its synthesized forest webs [165], 3D-C's simple synthesis method make it a thermophone worth investigating and improving due to its mass manufacturing capabilities [166].

In Fig.87, the uncompressed 3D-C used in Fig.84 is compared with thermophones tested by Aliev *et al.* 2015 [48]. In Fig.87a, 3D-C performs similarly as Indium Tin Oxide coated PolyAcrylonitrile Nanofibers (ITO PAN), Multi Walled Carbon Nanotube (MWNT) forest and MWNT sponge, but is 10 to 20dB below the performances of gold coated PAN, Graphene sponge (GS) and Carbon Nanotube (CNT) Sheet, commonly agreed to be one of the most efficient thermophones currently available. This is confirmed by the proximity of the CNT sheet curve with the theoretical optimal pressure of Eq.(435).

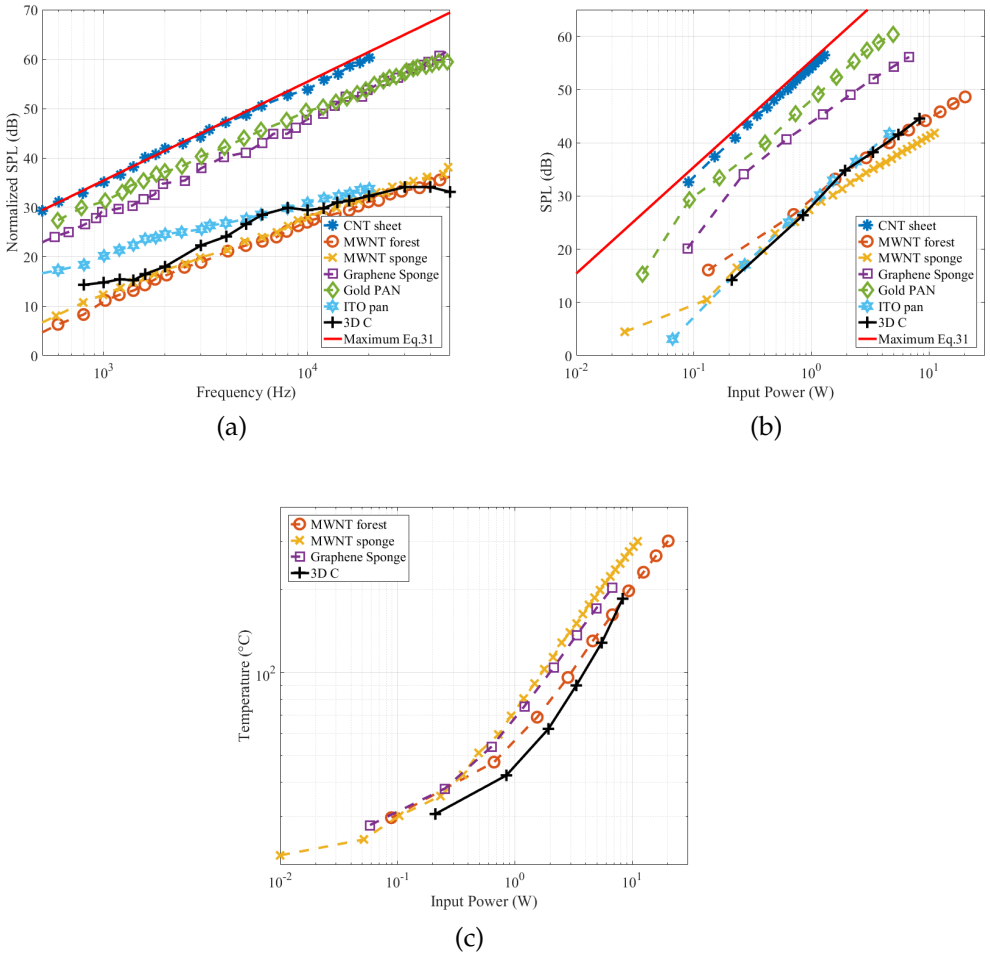

Figure 87: (a) Acoustic frequency, (b) power input and (c) temperature spectra comparison of uncompressed 3D-C in Fig.84 with reported literature values.

Similar observations are drawn from Fig.87b, where the power spectrum are plotted, with the information provided by Aliev *et al.* 2015 [48] adapted to be compared with our measurements based on our frequency spectra results. It is interesting to realize that the two temperature model also has been positively confronted to Aliev's data in Guiraud *et al.* 2019 [2]. The data used in the model for 3D-C and GS are very similar, with the main difference being that the theoretical specific surface area of 3D-C is 10 times higher than GS, resulting in a proportionally higher power density in GS. This is corroborated by Fig.87c in which the temperatures of the samples are investigated. The temperature of Aliev's sample are 10° to 40°C hotter than the 3D-C. The very high porosity of 3D-C improves the cooling properties of the sample

making it less likely to break down due to high temperature induced by high input power.

Comparing 3D-C with GS at the same temperature, there is a ratio of two between the input powers. This difference would only explain a difference of 6dB between the frequency spectra curves and is not equal to the ratio of 10 in the simulation. This difference could be attributed to thermal losses in the 3D-C packaging, inherent sample properties' differences wrongly defined in the model, or the different 3D geometries. A more thorough analysis should be conducted to define an optimal geometry for a thermophone to further improve the efficiency of such devices.

For instance, the acoustical efficiency for a spherical radiation can be written as

$$\nu = \frac{4\pi r^2 p_{rms}^2}{\rho C_0}. \tag{436}$$

The presented frequency spectrum plots being normalized at 1m and 1W, a 10dB difference is equivalent to a loss in efficiency by a factor of 10. At 5kHz our 3D-C efficiency is 5.6×10^{-7}%, while a regular loudspeaker has an efficiency ranging from 0.5% to 4%. Even CNT sheets which are among the most efficient thermophones have efficiency of only 1×10^{-4}% [48]. Thermophones still must be improved before being able to compete in the market with commercial loudspeakers for audio purposes.

Conclusion

3D-C with varying parameters were synthesized and the acoustic performances studied and compared to theoretical models and experiments from the literature [2, 48, 63, 129]. Results show that there is good fitting between the theoretical models and the experimental data. Namely the effect of electrical input frequency, input power, material size, area of electrical connection, path of electrical connections, material density, material ppi and the presence of a backing on the acoustical performance of the samples were investigated. This study provides insights on how 3D-C should be used for efficient thermoacoustic effect, from the synthesis, to the packaging, depending on the frequency range of interest. Furthermore, it was shown that the real time hot point temperatures were good indicators of when the sample would decompose.

Despite its small size, the high porosity and pristine graphene quality of 3D-C allowed it to exhibit excellent acoustical performance. Its unique geometry also allowed for more rapid cooling as compared to other carbon nanostructured materials in literature. With a sufficiently

large air gap between 3D-C and its backing, the addition of an acoustical backing improved the sample's acoustical performance. The electrical contact surface should be as large as possible with electrical paths which allow electrical current to pass through the entire sample for efficient use of the entire material and optimum heat resilience. In this study, a line connection showed to have the best acoustical and thermal performance.

It is within the author's knowledge that measurements of very low power input (below a few hundred milli-Watts) has not been investigated in depth, as most power spectra in the literature are displayed in a linear fashion [35, 48, 127]. More "low power" measurements have to be performed with different experimental conditions to confirm the linearity between temperature and input power at all power levels. While 3D-C is able to produce complex sound (music) with only AC signals using a pre-processing method [143] (see Section 4.3.2 and Video S3 in supplementary information of the third article [3]), more studies have to be done to improve its efficiency before it can compete with regular loudspeakers in the market of audible acoustic generation. Utilization of 3D-C's flexible synthesis could be a way to improve the efficiency by geometrical means. Another idea to further exploit would be to use thermophones mainly for high frequency applications (3D-C was tested up to 150kHz and other thermophones up to a few MHz [40]) in order to utilize the linearly increasing efficiency of thermophones with frequency [57, 140].

4.2 AIRBORNE ACOUSTIC EXPERIMENTS PERFORMED AT THE IEMN

We shall now present additional airborne measurements done in the course of this work at the IEMN. Different samples than just 3D-C are used and airborne experiments' limitations are pushed. 3D-C will be compared with other samples that are found from online suppliers across the hearing range. An electronic board will then be designed to allow recordings up to 200kHz in air before a laser interferometry experiment is put into place to permit measurements up to a few MHz in air.

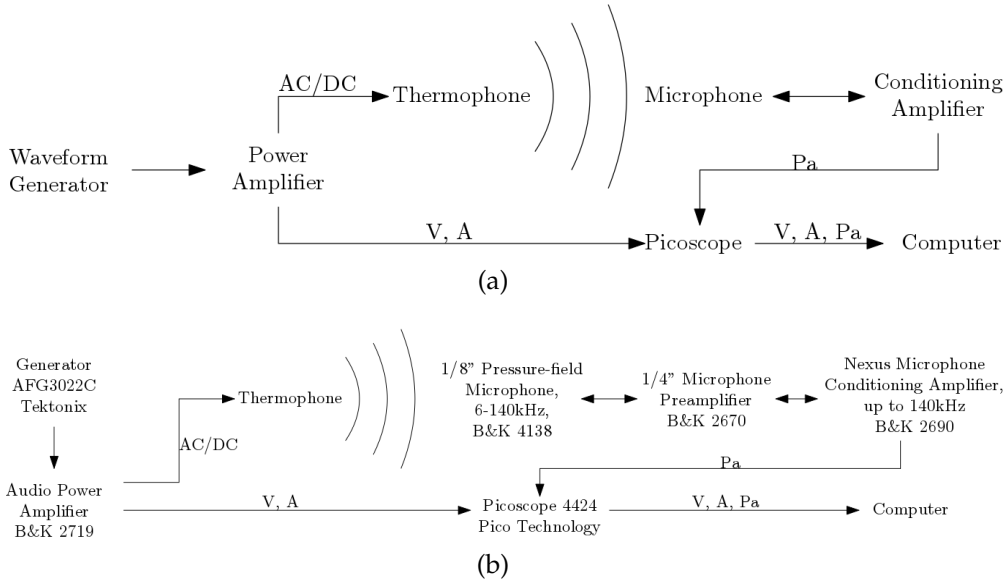

Figure 88: Airborne acoustical setup for hearing range measurement (20Hz to 20kHz). The schematic of the setup is found in (a) and the corresponding real devices used are found in (b)

4.2.1 *Experimental Setup and Measurements up to* 20kHz

Experimental Setup

The experimental setup most wildly used throughout this thesis is described in Fig.88a. The input signal fed to the thermophone is driven by a waveform generator and an amplifier. The signal received by the microphone is then recorded with a picoscope which also controls the input voltage and tension delivered to the thermophone, allowing us to easily regulate the input power. The impedance of the samples is not mentioned as all presented plots are normalised with the simultaneously recorded input power. The details of the hardware used is found in Fig.88b. Notably, if the B&K Microphone can record up to 140kHz, the amplifier is an audio one and so is not reliable above 20kHz. Hence the presented results in this section are only up to 20kHz.

Samples and Supports

A full list of the samples that have been used throughout the thesis is found in Appendix C.1. This contains pictures and details about the type of material, the type of supports, their size and their resistance measured using different methods. This section will only mention the samples used in the following analysis and noted with Roman numbers.

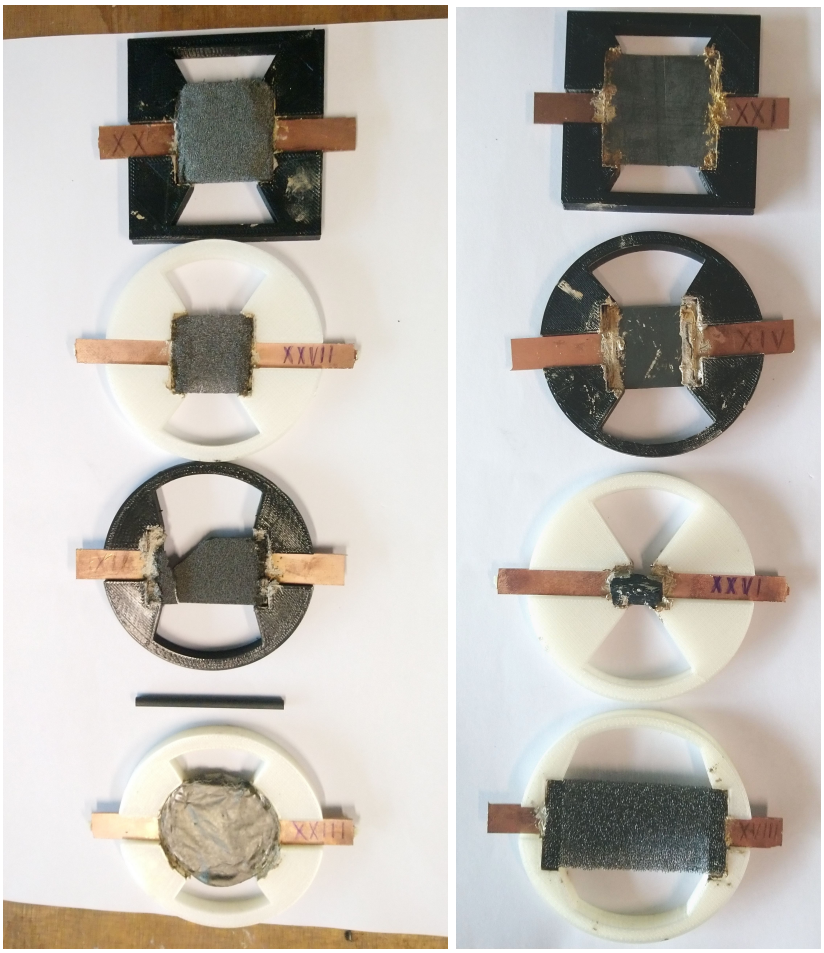

(a) (b)

Figure 89: Pictures of the samples used in the following analysis displayed in the same order as Fig.90a from top to bottom. Respectively: 110 ppi carbon foam (XX), 100ppi graphene foam (XXVII), 100ppi carbon (XI), graphite tube, graphene film super paper (XXIII) in (a) and Flexible graphite film (XX), rigid graphite film (XIV), self supporting multiwalled CNT (XXVI), vitreous carbon foam (XVIII) in (b).

Figures 89 show pictures of the supports and thermophones used in the following analysis. They are arranged following the display order of Fig.90 from most to least efficient. Our goal here to provide some insight of the thermoacoustic capacities of some carbon based materials available in the market but not designed for thermoacoustics. All samples are glued with silver paste on a copper board which is mounted on a 3D printed plastic support designed using Onshape and printed inhouse.

In order of efficiency, samples XX, XXVII and XI are all foam samples made of carbon provided by our partners or bought to *ACS Materials*.

There is then a carbon tube, a graphene sheet super paper (XXIII), a flexible graphene film (XXI), a rigid graphene film (XIV), a self supporting multiwall CNT (XXVI) and lastly a vitreous carbon foam (XVIII). All those samples have been bought to the supplier *Goodfellow*.

Results and analysis

Comparison of multiple samples from various suppliers

We here compare samples found from technological suppliers, namely *ACS materials* and *Goodfellow*. The frequency spectrum are seen in Fig.90a and the power spectrum in Fig.90b. The acoustic antiresonance at 15kHz is caused by the supports and will not be discussed as it is not relevant for this work. Firstly it can be noticed that all samples do not perform as well as samples made and used in CINTRA which displayed 15dB at 1kHz for instance which is 30dB higher than a vitreous carbon foam seen in Fig.90a (XVIII). However, due to the similar structure of vitreous carbon foam compared with 3D-C and despite their low efficiency, it can be noted that all of the experiments done in Section 4.1.2 have also been performed with them. The associated analysis is then also valid for those sample as all behaviors concurred even with with a lower efficiency (higher HCPUA).

It is important to recall that all those sample were chosen because of their carbon based structure but were not created with a thermoacoustic purpose in mind. Nonetheless it is seen that the carbon foam from *ACS Material* do perform better. Their thin microstructure and their quality graphene make them the most similar to CINTRA's 3D-C. Most other samples, either had a poor thermal conductivity or a too high thermal capacity thus affecting the HCPUA. It can be observed by looking at the different slope in the frequency spectrum. For instance in Fig.90a the vitreous carbon display an almost flat frequency response.

In Fig.90b all samples display a linear increase with frequency as expected. A slight decrease at high input power of the sample XI could be attributed to the static thermal raise inside the pores of the foam as explained in Section 3.3.1.

Lastly it is seen in Fig.91 that some samples like the multi wall CNT store way more energy that the other samples. This might indicate again a higher heat capacity than needed. Its frequency slope in Fig.90a being in between the carbon foam and the vitreous carbon, this would corroborate this explanation. It is also seen that the 110ppi sample has the highest SPL per temperature in Fig.91b. As explained with CINTRA's samples, its high ppi increases its cooling ability and thus is less prone to overheating.

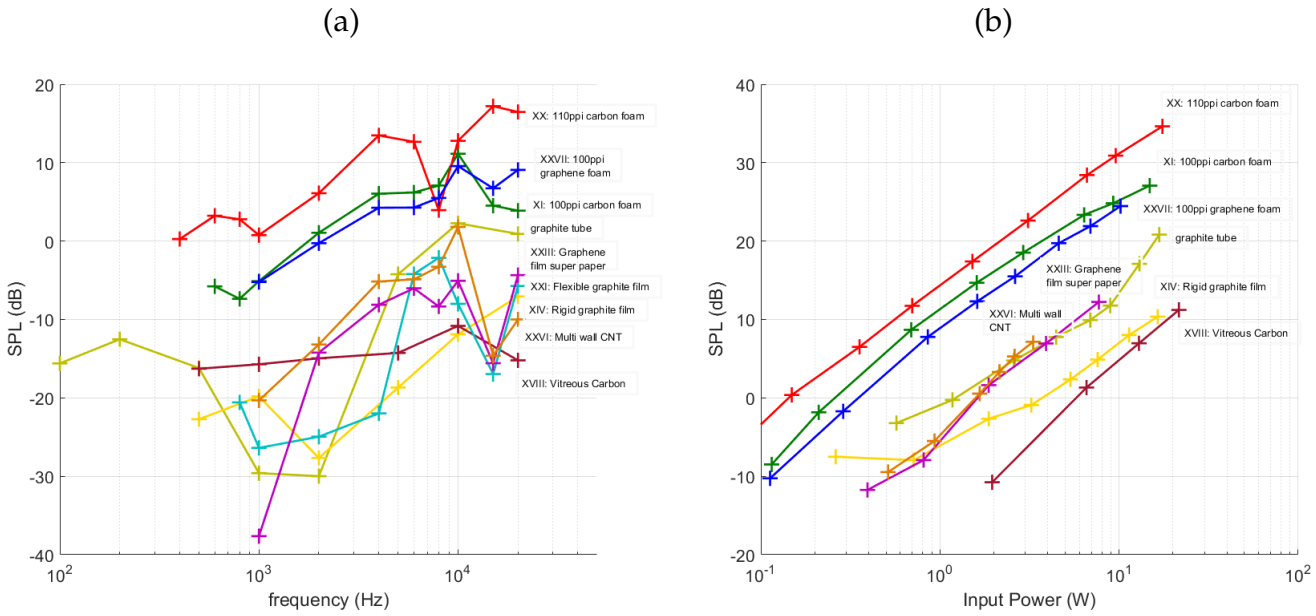

Figure 90: Temperature dependence of different carbon based samples from online suppliers. (a) Relationship between temperature and input power and, (b) relationship between SPL and temperature.

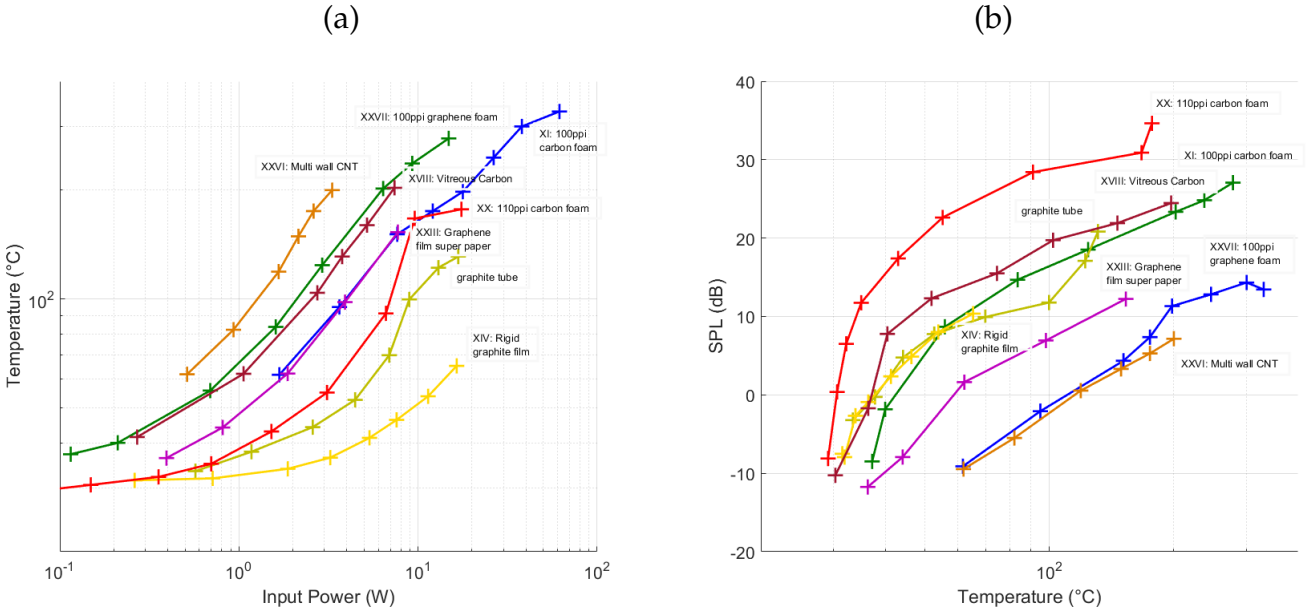

Figure 91: Frequency (a) and power spectrum (b) of different carbon based samples from online suppliers.

Experimentally it can be noted that the graphite tube, though displaying relatively weak temperature in the thermal camera in Fig.91a, had a high heat capacity due to its thickness and was very hot after a recording thus preventing manipulation with it for some time in between measurements. A very sharp increase in SPL starting at 2kHz is also seen in Fig.90a. It is attributed to its cylindrical shape. Below 2kHz mostly noise is recorded and the cylindrical shape creates a different acoustic radiation no longer proportional to f as for an ideal plane wave but an higher order. This would explains this sharp increase as seen in Section 3.2.1. Its weak radiation prevented further investigations.

Some other samples not shown here had a very high resistance and restricted us from supplying a high enough power to record a thermoacoustic effect. The sample XXV for instance is made of graphene aerogel was expected to present high thermoacoustic capabilities [48, 49, 73]. Some difference in the structure or the experimental setup potentially raised the impedance and must have prevented us to observe the desired phenomenon.

Comparison of same type samples

An emphasis is now be made regarding the discrepancies of efficiency across similar samples. Figure 92 display the frequency and power spectrum of measurements done with *ACS materials* graphene foam samples. They are similar material mounted on similar supports, thus explaining the antiresonance at 4kHz and the similar spectrum. Nonetheless, despite those similarities, a range of up to 10dB differences can be seen between samples. The complex process of fabrication and the non regular microstructure between foams will create such discrepancies. Additionally, their brittleness makes them hard to manipulate and makes the electrical connection process also difficult to perfectly reproduce thus adding to creating those differences. This should be kept in mind while doing any experiments with similarly prepared samples and expecting similar results.

4.2.2 *Experimental Setup and Measurements up to* 200kHz

It was seen that measurements up to 20kHz can easily be done using an audio amplifier. This was made possible as the average resistance of all samples is very low (less than 5Ω, see table 15) and audio amplifier are meant to work with low impedance drivers. This section aims to make use of the high frequency range of the microphone (−1dB at 140kHz and −3dB at 200kHz). The challenges, solutions and results of this endeavor are here presented.

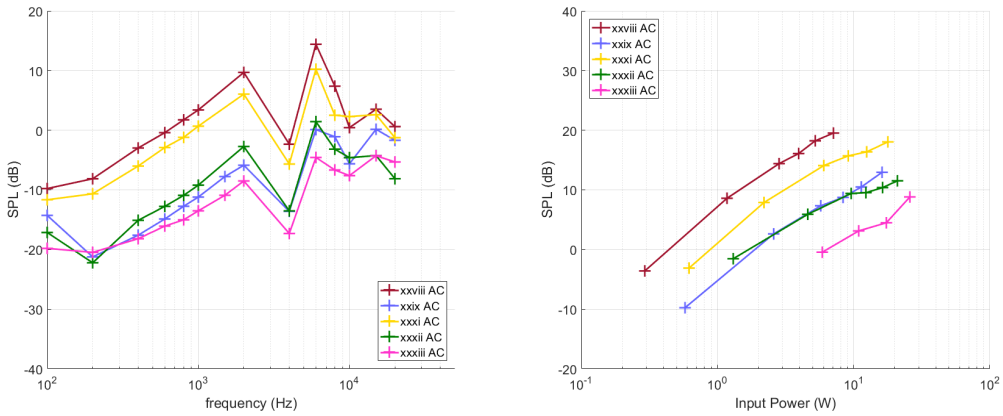

(a) (b)

Figure 92: Frequency (a) and power spectrum at 5kHz (b) of similar carbon based foams from *ACS Materials* on similar supports.

Experimental Setup

In order to make use of the high recording range of the microphone, a high voltage amplifier (3MHz) with a high slew rate (2000V/µs) Falco WMA-300 [167] was considered to replace the B&K amplifier. However, the Falco amplifier was meant to work with a standard input impedance of 50Ω. The thermophone low impedance created an impedance mismatch that had to be corrected. Furthermore, due to the low efficiency of the samples available at the time and of thermophones in general, it is needed to be able to supply a high input power. The impedance mismatch added to the high output current needed compelled us to investigate a different method.

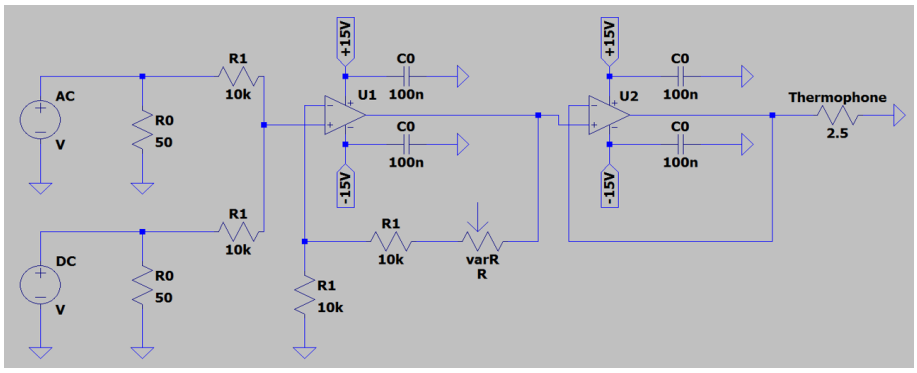

Figure 93: Electrical schematic of the summing amplifier with impedance matching network. The summing amplifier AOP is a LF356N. An OPA549 is used for impedance matching.

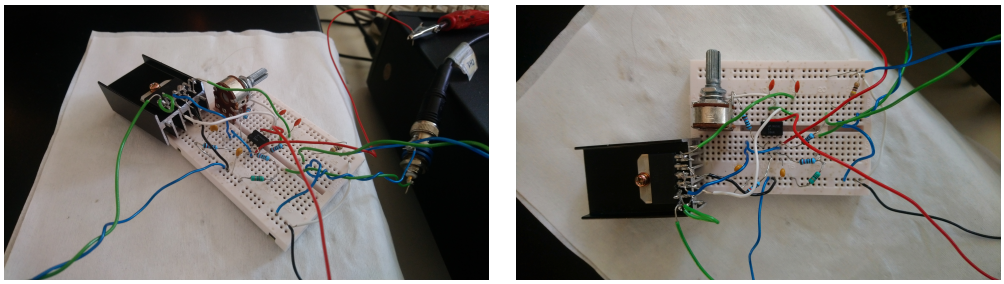

(a) (b)

Figure 94: Pictures of the amplifier network board

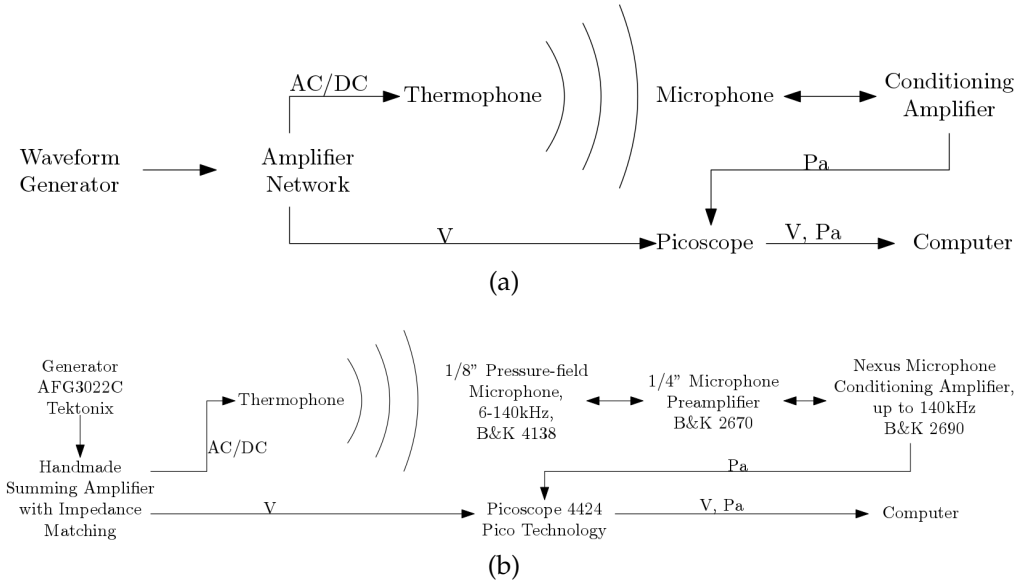

Figure 95: Airborne acoustical setup for extended hearing range measurement (20Hz to 200kHz). The schematic of the setup is found in (a) and the corresponding real devices used are found in (b)

A handmade summing amplifier was designed in order to be able to supply an AC/DC signal to the thermophone. The LF356N AOP was chosen because of its convenient gain-bandwith product (5MHz) and slew rate (9V/µs). A higher gain-bandwith product would have allowed us to have more amplification but at the cost of lower slew rate or lower maximum output current. The ideal AOP would have needed a high gain-bandwidth product, a high slew rate and a high maximum output current. As it does not exist the LF356N was chosen. This summing amplifier network was coupled to an impedance matching network. The AOP needed in this case had to be able to deliver high output power, to have a slew rate high enough to follow the high frequencies, as well as a high enough gain-bandwith product to not deteriorate the signal at high frequencies. The AOP OPA549 was chosen and mounted on a radiator

to prevent overheating. Its characteristic are 0.9MHz of gain-bandwith, 9V/µs of slew rate and 10/8 A maximum current output AC/DC. The electrical schematic of the whole network is seen in Fig.93 and picture are seen in Fig.94

The resulting acoustical setup used for measurements up to 200kHz in air with the microphone is found in Fig.95. It has to be noted that the new thermophone amplifier does not allow a control of the current simultaneously as the voltage. It was experimentally observed that when damaged (overheating, mechanical manipulation errors...) the resistance of the samples could variate. Furthermore, depending on the electrical connections used, variation could also been observed from one measurement to another. Those changes are only of a few Ohms but since thermophones natural impedance are very low and that they are power driven, the choice of resistance can highly influence the normalised results. In the following graphs the legend indicates the resistance which was used to normalise the figures based on Table 15.

Results and Analysis

Figure 96 display frequency spectrum results made with the regular 20kHz experimental setup and the new one going to 200kHz. Good agreement is seen between the measurement with both experimental setups and a maximum of 5dB difference is observed with the sample XXXII.

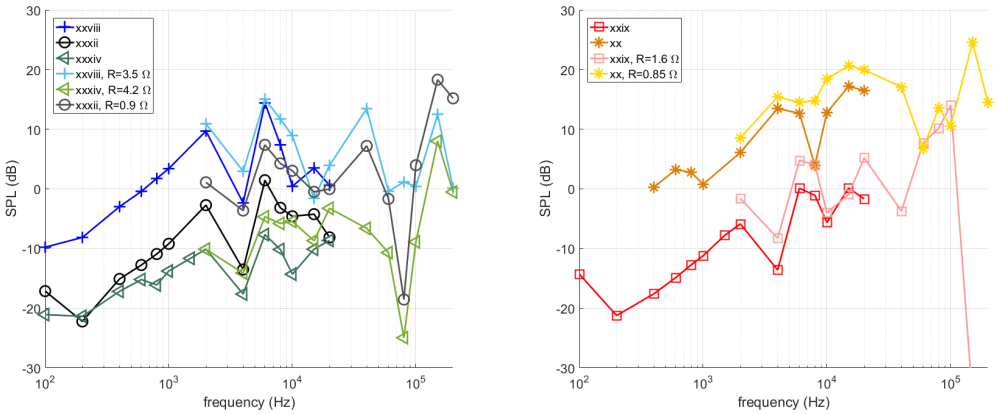

(a) (b)

Figure 96: Comparison of acoustic recording of same samples with different experimental setup, one up to 20kHz and the other up to 200kHz. Samples XXVIII, XXXII, XXXIV in (a) and XXIX and XX in (b).

As explained while describing the experimental setup, the main recording difference between the measurements up to 200kHz and the previous one up to 20kHz is that we are not able to record the current supplied to the thermophone. The resistance is estimated from measurements (multimeter, spectrum analyser and previous measurements, see Table 15) and then used to deduce the input power for normalisation purposes. As a consequence, some over or under estimation can occur and lead to those differences. This highlights the importance of accurate impedance measurements as thermophones are power driven. The resistance used in each case is seen in the legend of Fig.96. Otherwise, acoustical resonances are observed but overall thermoacoustic radiation is proven up to 200kHz. By rigorously designing the support, thermophones could be used for accurate high frequency transducers.

4.2.3 *Interferometry: Measurements up to* 1MHz

Proof of effective radiation up to 200kHz has been made. We will now try to prove the effective radiation of thermophones up to 1MHz in air. This has been done before mainly by Daschewski and al.[40, 167] and displayed a frequency spectrum up to 1MHz and a sharp associated impulse response. This ultrasound radiation will now be proven for graphene foam thermophones.

Experimental Setup

In order to measure up to 1MHz acoustic measurements in air, a vibrometer laser is focused on a light membrane. The sound will induce vibration in the light membrane which will be measured by the vibrometer. This displacement is then used to deduce the pressure and the SPL [168, 169]. The experimental setup is seen in Fig.97a and the hardware used in Fig.97b. At this stage the limiting parameter is the amplifier network as the impedance matching network AOP gain-bandwith ratio is 0.9MHz. Otherwise nothing theoreticaly prevent measurements up to a higher frequency.

Results

In Fig.98a the recorded signal is compared to the background noise recorded by the frequency analyser. It is seen that the SPL level reaches the background noise around 1MHz. Hence, in addition to improving the amplifier network, the sample should also be more efficient for higher frequency measurements.

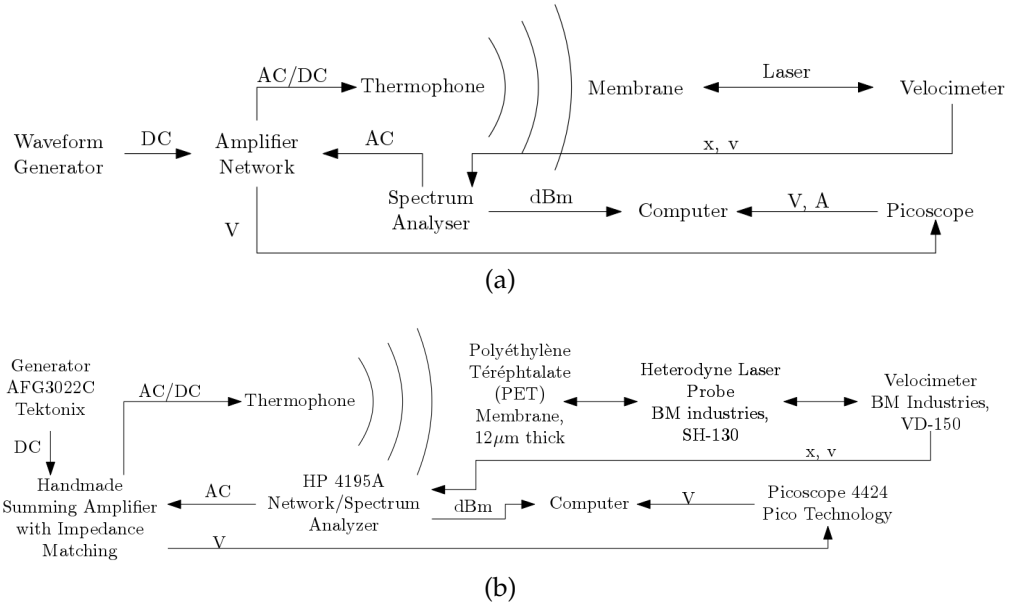

Figure 97: Airborne acoustical setup for ultrasonic measurement (up to a few MHz). The schematic of the setup is found in (a) and the corresponding real devices used are found in (b)

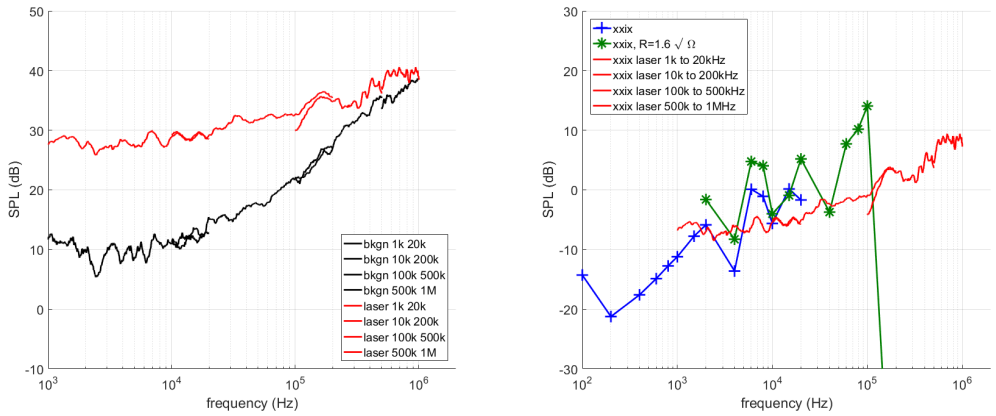

Figure 98: (a) Recorded SPL of sample XXIX by laser interferometry and its associated background noise. The measurements were performed with various frequency range to allow a better resolution and to lower the noise. (b) Comparison of frequency spectrum of sample XXIX with all three acoustical setup.

The SPL is then normalised and compared to the previous measurements methods. Despite the very different recording methods and having once again estimated the resistance for normalisation purposes there is a good consistency between measurements. This proves the effective sound generation of carbon foam up to 1MHz. It can be noted that

this method could be used for ultrasonic recordings underwater with a similar setup [170].

Conclusion

In this section different samples from various suppliers and have been tested in IEMN. Despite having no predestined used in thermoacoustic use they all displayed some thermoacoustics capabilities. However, their higher resistance, higher thermal capacities and lower thermal conductivity than graphene foam made by CINTRA made them less efficient and of a lower interest.

High frequency airborne acoustic measurements issues have been raised and solved with different experimental setup presented. In a nutshell, measurements in the hearing range were done with an audio amplifier but a summing amplifier setup coupled with an impedance matching electrical system had to be used for measurements up to 200kHz. Lastly an interferometry laser experimental setup was put into place and proved the effective radiation of carbon foam up to 1MHz.

4.3 ADDITIONAL AIRBORNE MEASUREMENTS FROM THE IEMN

This section presents additional experiments performed at the IEMN. As previously mentioned, other experiments can also be found in Appendix C.2. For instance, DSC or AFM measurements [171] were performed but are not mentioned here as they do not provide any relevant insight. The interested reader is encouraged to read it if a more thorough understanding of what could be done with a foam thermophone is desired. Nevertheless, the experiments presented in this sections are diverse and are a first step toward future different use and investigation regarding thermophones. A high frequency thermal camera is here used to observe the temperature variations inside a branch of 3D-C. The influence of the supplied input power on the spectral sound quality is then investigated, and music is played on the samples using only an audio amplifier. Lastly, a discussion is engaged regarding the use of thermophones for underwater generation.

4.3.1 *High Frequency Thermal Camera*

In this section, a high frequency thermal camera was used to qualitatively observe the high frequency temperature variation of a thermophone. The goal of this experiment was to observe the temperature variation of a single branch of a foam. Figure 99 show pictures of the high frequency thermal camera in the IEMN.

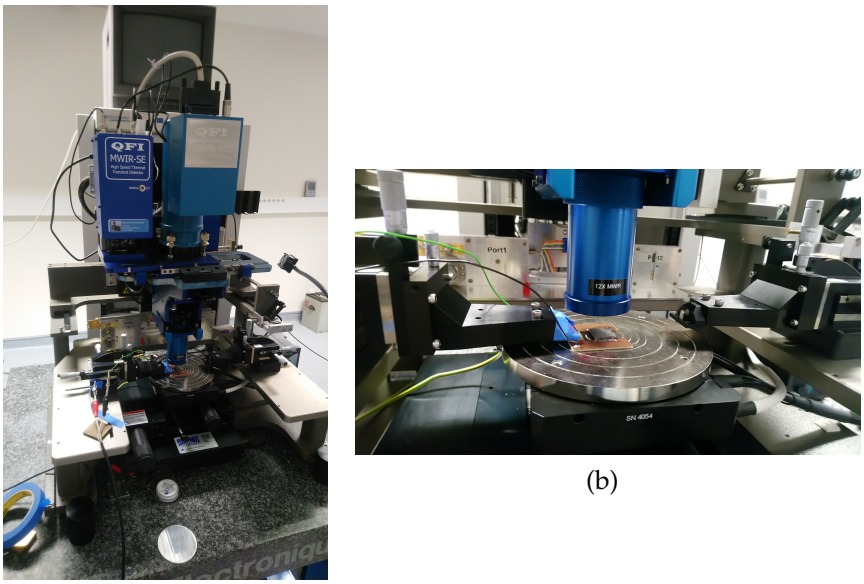

(a) (b)

Figure 99: (a) Picture of the high frequency thermal camera at the IEMN. (b) Zoomed imaged of the thermal camera under operation with 3D-C.

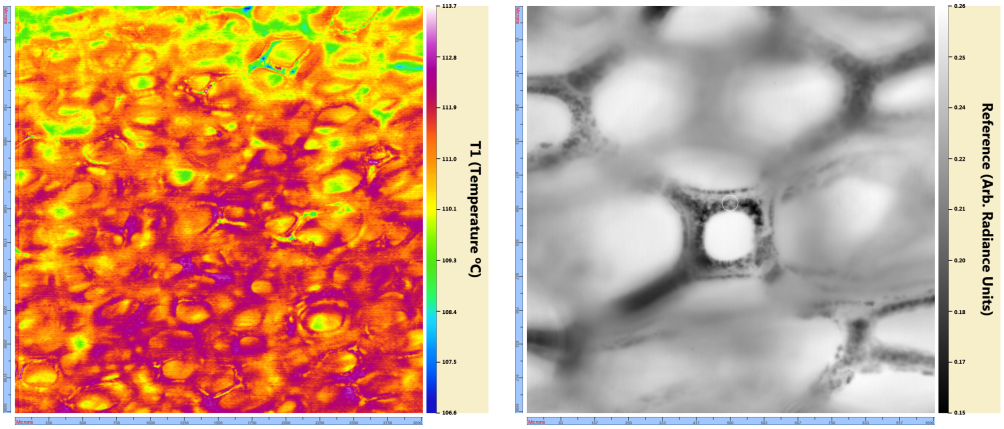

(a) (b)

Figure 100: (a) 3×3mm thermal image of 3D-C under operation. (b) 1×1mm image on which a circle of diameter 40μm on the branch represent the point in which the temperature is recorded at high rate.

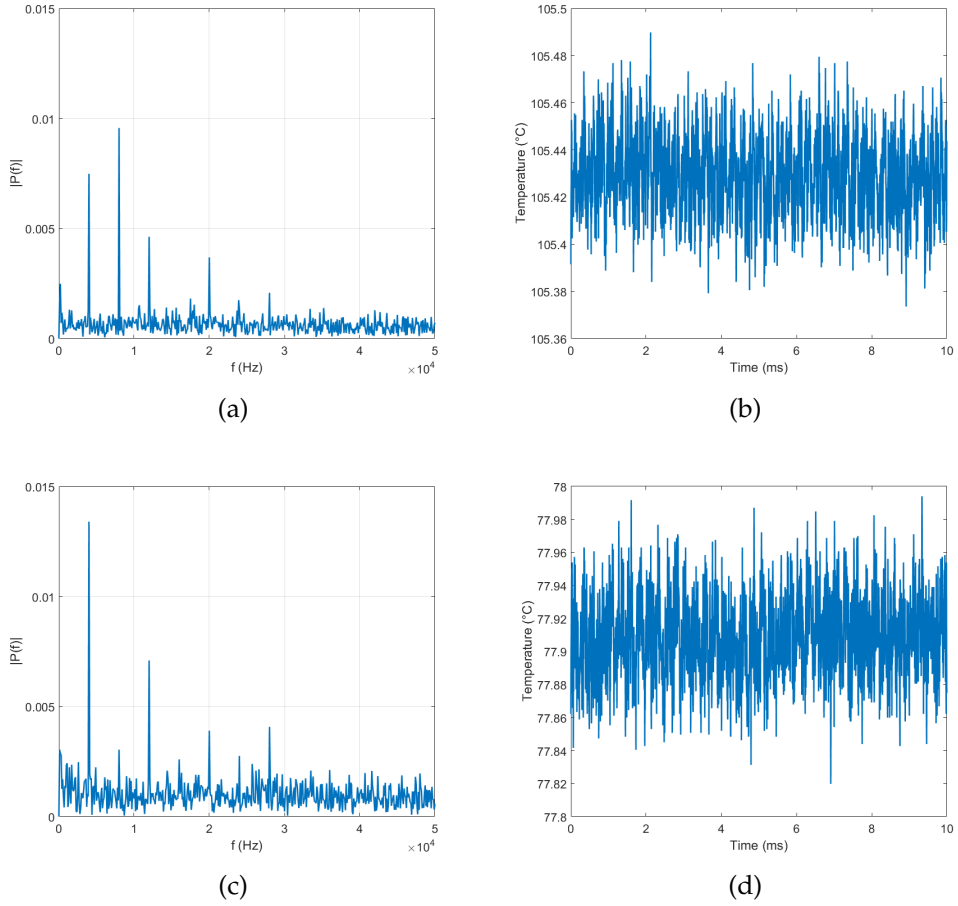

Figure 101: Spectral ((a) and (c)) and temporal ((b) and (d)) recording of the temperature in the centered pixel of Fig.100b in different mode of operation of 3D-C. A 4kHz AC electrical signal is supplied in (a), (b) and a DC signal is added in (c), (d)

In order to have accurate measurements the camera needs to heat the observed samples up to a certain temperature using the platform on which the sample is place. However due to the support necessary for the foam to work and the fact that it is a complex porous system this calibration could not be made. Hence the presented results are only qualitative ones.

The observed macroscopic thermal 3×3mm image of the thermal camera is seen in Fig.100a. A zoom is then made to observe a 1×1mm window and the focus of a pixel of a 40µm pixel is made on one of the branches, as observed at the center of Fig.100b.

The results are seen in Fig.101. Two different input signal are used, a single AC signal at 4kHz and an ACDC signal at 4kHz as well. When only AC signal is feed to the sample, the variation of temperature are strongest at 2f as theoretically expected in Fig.101a. However the fun-

damental and uneven harmonics appear as well. Those might be due to some non linear behavior of the experimental setup as it was not observed as sharply during acoustic measurements. Now feeding an ACDC signal to the sample, the variation of temperature are strongest at the fundamental but uneven harmonic are still observed in Fig.101c and at a different intensity than before. Due to the limited amount of time this experiment was performed, it is hard to conclude whether it is due to a non linear behavior of the electrical supply or a non linear behavior of the thermoacoustic process that is not yet understood. Nonetheless, it was proven that it is possible to observe the variation of temperature in a single branch of thermophone.

4.3.2 *Various Input Signals*

In order to try and improve the acoustic sound generation, some variations on the electrical signal delivered to the thermophones have been performed. Briefly we can mention that high frequency modulation tests have been performed and proved to be effective despite a higher input power strain on the sample. Additionally, a novel spectral analysis with AC input signal has been implemented. The parameters, spectral flatness measures (SFM), total harmonic distortion (THD) spectral centroid (SC) and spectral spread (SS) were calculated as

$$\mathrm{SFM} = \frac{\sum_n a_n^{\frac{1}{n}}}{\sum_n \frac{a_n}{n}}, \tag{437}$$

$$\mathrm{THD} = \frac{\sqrt{\sum_{n=2}^{N} a_n^2}}{\sqrt{\sum_{n=1}^{N} a_n^2}}, \tag{438}$$

$$\mathrm{SC} = \frac{\sum_n a_n f_n}{a_n}, \tag{439}$$

$$\mathrm{SS} = \frac{\sum_n a_n (f_n - \mathrm{SC})^2}{\sum_n a_n}, \tag{440}$$

with a_n the amplitude of the n harmonic f_n. SFM and THD of thermophones proved to be high (from 30 to 90%) and to increase with frequency. The results presented in Appendix C.2.5, Fig.117 and 118 are quite disparate depending on the support used and so make it hard to draw a meaningful conclusion. On the contrary, SC and SS display more consistent results. For instance, the SC was found at the second harmonic (three times the desired acoustic fundamental) across the whole frequency range regardless of samples. Similarly, SS is consistently found at $3f^2$ with f the fundamental. Still, caution is advised in

the interpretation as strong harmonics are needed for the calculation of those spectral parameters and due to the low performance of most sample the results should be repeated and improved before being definitive. As mentioned in Section 1.3.4, an extensive literature review has already been performed regarding various input signals and THD analysis [137, 138, 140], hence why those experiments have not been deepened.

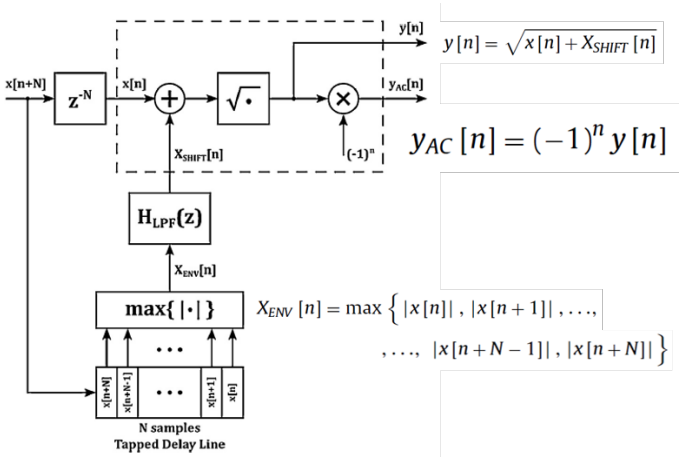

Figure 102: Block diagram of the pre processing used to be able to playback complex signals with only the use of a AC amplifier [143].

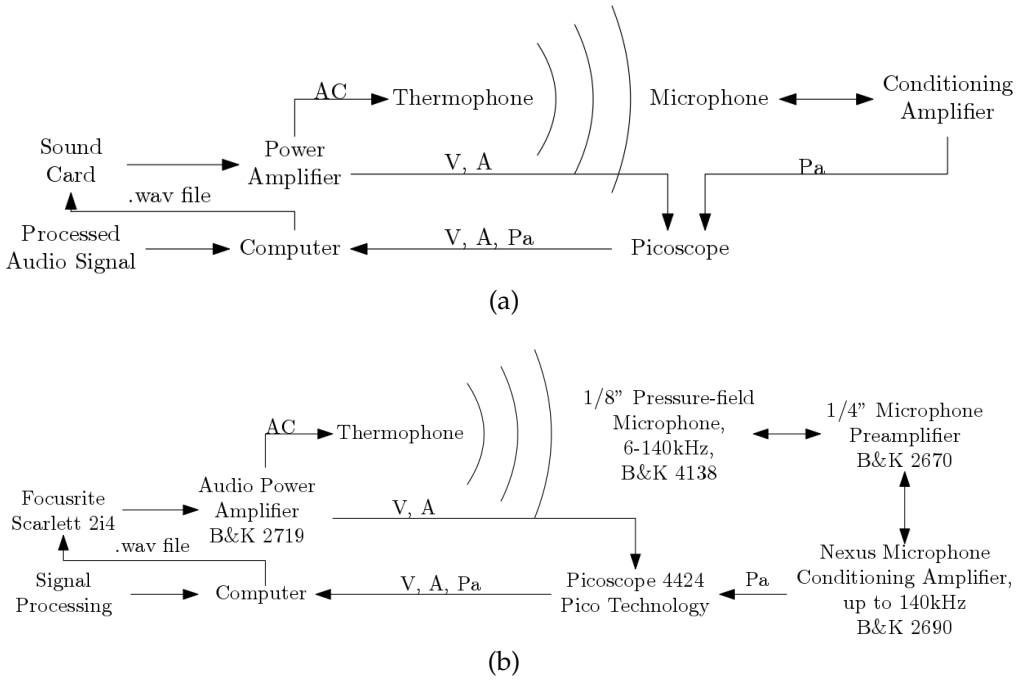

Figure 103: Airborne acoustical setup for musical measurement. The schematic of the setup is found in (a) and the corresponding real devices used are found in (b)

An experiment based on a recently published paper by La Torraca 2019 [143] describes a pre processing implementation that allows thermophone to play complex signals using only an AC generator. In fact, as previously explained in order to play complex signals a DC component was necessary in order for acoustic thermophone output to be coherent with the input electrical frequency. This implementation would allow thermophone to be easily used with commonly available AC audio amplifier. The block diagram describing this predistortion is found in Fig.102 and was implemented in Matlab. The experimental setup is found in Fig.103 and different *.wav* signals of various genre have been played. Qualitatively speaking, human speech was accurately reproduced and was understandable despite the supposedly high THD. For music, one the main issue is that the signals loudness are meant to be tension driven for traditional loudspeakers. Hence, when the music went from a quiet part to a louder one it increased the input power and put the sample at risk of overheating. All in all a *punk rock* song was privileged during testing as the heavily compressed signal allowed for an overall more stable input power throughout the song. Since music reproduction was not a main goal of the thesis, pre processing experiments were not continued. The idea of using a compressed signal to keep the input power constant during the whole listening session should nonetheless be remembered for future investigation.

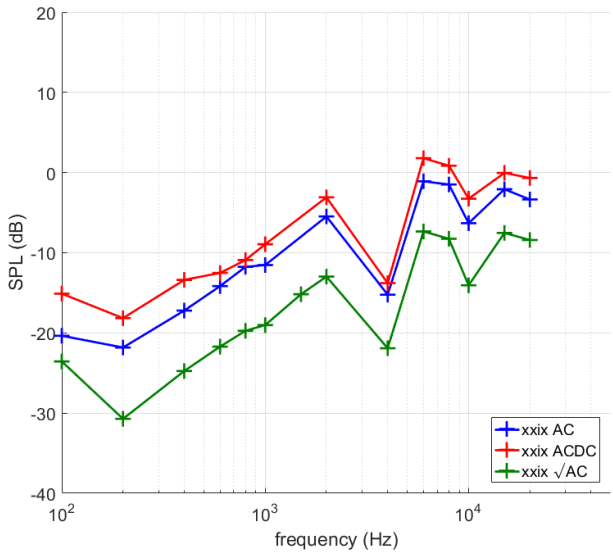

Figure 104: Comparison of SPL of the same sample with different method of input power.

A normalised frequency spectrum of a single thermophone driven with different input power is found in Fig.104. Only AC, ACDC and the $\sqrt{}$AC signal defined by Fig.102 are used. As expected from the literature,

it is seen that the ACDC signal is more efficient than a single AC signal. The $\sqrt{}$AC input signal is less efficient than traditional AC or ACDC input but can be more easily used with audio amplifier.

4.3.3 *Underwater Measurements*

One of the goal of this work was to evaluate the technical capabilities of thermophone for acoustic radiation underwater. Section 1.3.1 detailed the state of the art of underwater thermophone. In a nutshell, thermophone are encapsulated and while the flexible design and lightweight is still used, the hard casing of the samples create a resonance preventing the use of the wide band and high frequency radiation process. The goal is then to make 3D-C able to radiate underwater without obtaining those resonances and while keeping the frequency spectrum specific to thermophones

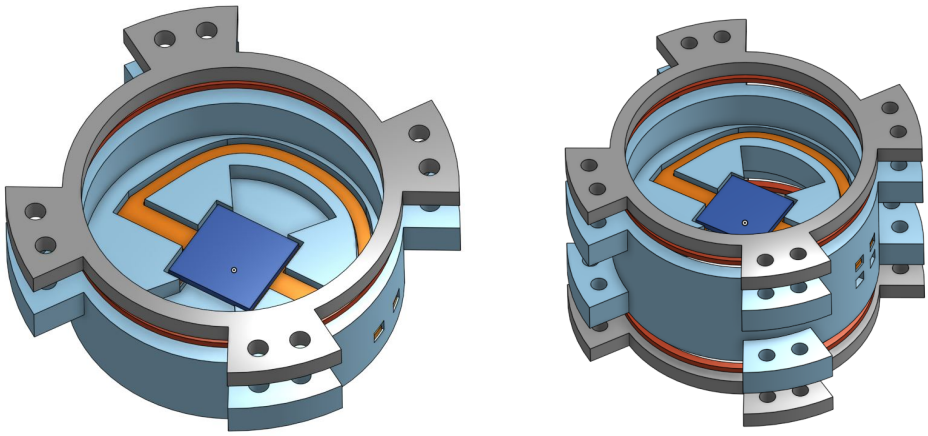

(a) (b)

Figure 105: 3D CAO model from Onshape of a one (a) or two sides (b) underwater support. Shapes in dark blue represent the sample, in orange the copper board, in red the rubber joint and in light blue and in grey the 3D printed support.

It can be seen in Fig.109b in Annexe C.2.1 that 3D-C does not resist underwater, hence the encapsulation is also necessary in our case even considering the potential hydrophobicity of carbon. Nonetheless the encapsulation is desired to be as soft as possible to avoid hard resonances. Another condition would be for the encapsulation to be able to protect the sample in air and under pressure. Lastly, it was desired to be able to easily use the encapsulation support for recording in air and underwater to ease the comparison. A 3D design was created in or-

der to solve those specific concerns as seen in Fig.105. More specifically Fig.105a use a backing to improve the radiation in one direction and Fig.105b is symmetrical without backing to radiate in both directions. A thin lid (PET membrane 12µm thick for instance) would be place between the support (in light blue) and the top (light grey). A rubber joint laser cutted (red) would be placed in between to assure the sealing. The sample (dark blue) would be connected on copper boards which would be connected to wired coming from the holes on the side of the support. Those holes would be sealed with a glue gun.

Those supports were 3D printed and tested for water proofing without success. In fact, even a high density of 3D printing would not allow the support to be entirely water proof for a long period of time. A coating could be used on the support to help in this regards as well as the use of specialised 3D printers. The design of those support were stopped as it was agreed that our partner CINTRA would handle this part of the experimental investigation.

Experiments were planned in a large water tank in Sofia Antipolis at Thales Underwater System in March 2020 with the partner CINTRA. They were canceled due to the COVID-19 outbreak. The only tests performed were done in CINTRA in January 2020 in a small water tank seen in Fig.73b. The SPL was about 26dB higher than in air which corresponds to the difference in the reference pressure used (20µPa in air and 1µPa underwater). However, the hard casing of 3D-C used by CINTRA and the small sized tank created many resonances making the results hard to exploit. Nonetheless, sound was recorded underwater proving the concept with 3D-C.

Conclusions

Throughout this chapter, the thermoacoustic capabilities of thermophones and more specifically 3D-C have been extensively investigated. Section 4.1 presented various experiments made with 3D-C, in partnership with CINTRA Singapore and the PhD student Ngoh Zhi Lin. Notably, aside from some specific experiments related to the foam like structure of 3D-C (compression, 2T model comparison...), the resulting analysis can in fact be used to understand any thermophones. This analysis provides insight on how to manipulate and use thermophones in an optimal way. For instance, it is advised to have a large electrical connection to avoid overheating or to use a backing at a distance to increase SPL.

Section 4.2 then presented complementary comparison made in IEMN with thermophone found from online suppliers. Their lower efficiency prevented groundbreaking results but showed a coherent analysis with

3D-C samples. Using those samples, airborne measurements challenges have been raised (microphone limitations, impedance matching issues...) and were solved, thus allowing recording up to 200kHz using electronics and up to 1MHz using laser interferometry.

Lastly some novel experiments performed in IEMN have been presented in Section 4.3. The high frequency temperature variations of a single branch of a foam have been recorded, music have been played using only an audio amplifier and underwater sound radiation concerns have been raised along with proposed solutions (mainly a new encapsulation design, presented with a soft sealing).

Additional characterisation experiments also performed in IEMN are found in Appendix C.2 such as density measurements which prove the instability of 3D-C underwater without protection. DSC measurements have been tried without success due to the lightweight of 3D-C. Finally, a 3D microtomography of the foam structure is also presented and AFM experiments to try and observe the thermal layer in which the sound is generated are described.

CONCLUSION

In this work a thorough historical review of the literature of thermoacoustics and more specifically thermophones is found in Chapter 1. The theoretical models for multilayer continuous medium for plane waves, cylindrical waves and spherical waves generation as well as an innovative 2T model are found in Chapter 2. Validation and analysis of those theoretical models is found in Chapter 3 which provides a deep understanding of the thermoacoustic radiation phenomenon. Lastly, experiments with various thermophones but mostly carbon based foam made by CINTRA Singapore are described and analysed in Chapter 4.

Regarding the theoretical models, the 1T multilayer model for plane waves permits to have a real flexibility in the design of thermophones never reached before in the literature. This single model being able to reproduced most configurations used in various published models. Its cylindrical and spherical multilayers models counterpart provide a similar advantage but of a lower interest. It was seen that those geometries are mostly found at the microscale and the need for a complex multilayer model is not as clearly established. Nonetheless, those models are the first to take the propagation in the solid into account and to consider the viscosity of the media. Thus providing insights on internal resonances never seen before. As for the 2T model, it was proven to provide a better representation of the thermoacoustic radiation of thick foam like materials as it does not overestimate HCPUA with the added thickness. This idea of simultaneous existence of both solid an fluid was never before applied to thermoacoustic generation.

The resulting study concurs with various theoretical and experimental analysis from the literature, where thermophones are used in a number of different configurations. By doing so, it helped increase the understanding of thermophones and how to improve them (analysis of geometry, design, parameters...). Novel situations were also investigated using the flexibility of our models. The influence of the thickness of the hydrophobic layer on a sample underwater was studied for instance, which could be later confronted with real life measurements.

Furthermore, airborne measurements have proven the effective sound generation of carbon foams up to 1MHz using various experimental setups. Difficulties in the handling of such samples have been raised (support, connection, experimental setup...) and could be used as a guideline for future experimental users. All things considered, foam like ge-

ometry present the very interesting property of having a high specific surface area, allowing a large contact surface to avoid overheating and to permit the generation of the thermoacoustic effect on a large scale. In spite of that, as of today its performances does not reach the theoretical maximum efficiency attained only by CNT forests. The improvement made on the structure does not compensate for the low efficiency of the sample. However, it is hoped that this thesis could raise awareness regarding the interest of creating novel structures with a thermoacoustic purpose in mind, in the hope to improve sound generation from thermophones.

As for the perspectives, it would be relevant in the near future to further reflect on how to improve thermoacoustic underwater generation and to investigate a soft encapsulation design that best preserves their wideband properties. Additionally the use of an AFM seems the most promising way to record what is thermally happening at a microscale of the thermophone and to measure what is theoretically expected. It has already been briefly tested with CNT [171] but it should be improved and tested with 3D-C and other samples as well. From an application point of view, other potential research leads could be to integrate thermophones within a loudspeaker to help high frequency radiations. Otherwise, the flexible geometry could help in the design of new patterns for sound transducers (to create an acoustic vortex for acoustical tweezers for instance). Reconfigurable arrays of arbitrary distributed sound sources could also be easily designed and tested to be locally excited, with or without delay, using photothermoacoustics.

All in all, thermophones are promising alternative for sound generation. While their current low efficiencies prevent them from replacing commercial loudspeakers, their non-mechanical sound generation mechanism induces a wide frequency band of operating range. In addition, their lightweight, flexible design, small size and low cost of production make them a novel alternative for sonar applications or ultrasonic transducers. Particularly, 3D-C has an advantage over CNTs for large scale manufacturing as CNTs require a tedious process of using a nanomanipulator to acquire its strands from CNT forests [165]. The ability of 3D-C and thermophone at large to emit sound thermoacoustically is hence worth investigating.

Part V

APPENDIX

A

THEORETICAL APPENDIX

A.1 CONTINUUM MEDIUM MECHANICS AND BALANCE EQUATIONS

The balance equations used to describe the thermoacoustic process will be here build from scratch. This whole section constructs the basis on which the theoretical model are based on. The interested reader should read this appendix before Section 2.

A.1.1 *Lagrangian and Eulerian Formalisms*

The motion of a region of a material is described with respect to a reference configuration $\Omega_0 \subset \mathbb{R}^3$. During the motion, the region is deformed to $\Omega_t \subset \mathbb{R}^3$, when t is time. The current coordinates $\vec{x}$ are therefore written in terms of the reference coordinate $\vec{X}$ as

$$\vec{X} \in \Omega_0 \rightarrow \vec{x} = F_t(\vec{X}) \in \Omega_t, \tag{441}$$

where F_t is a map (function) for anytime t. The couple $(\vec{X}, t)$ is named Lagrangian coordinates, while the couple $(\vec{x}, t)$ is named Eulerian coordinates. The inverse of Eq.(441) can be written as

$$\vec{x} \in \Omega_t \rightarrow \vec{X} = F_t^{-1}(\vec{x}) \in \Omega_0. \tag{442}$$

The deformation between current and reference configurations is described through the deformation gradient

$$\hat{F}_t(\vec{X}, t) = \vec{\nabla}_{\vec{X}} \vec{F_t}(\vec{X}, t), \tag{443}$$

$$\text{or} \qquad F_{i,k} = \frac{\partial x_i}{\partial X_k} \quad \forall i, k.$$

We can also define the deformation gradient of the inverse function

$$\hat{G}_t(\vec{x}, t) = \vec{\nabla}_{\vec{x}} \vec{F_t}^{-1}(\vec{x}, t), \tag{444}$$

$$\text{or} \qquad G_{k,i} = \frac{\partial X_k}{\partial x_i} \quad \forall i, k.$$

We assume that the determinants of $\hat{G}$ and $\hat{F}$ exist at each point and are positive. The physical significance of these assumption is that the material of the body cannot penetrate itself, and that material occupying a finite non-zero volume in the reference configuration cannot be compressed to a point or expanded to infinite volume during the motion.

Of course, $\hat{G}$ and $\hat{F}$ are related by the relations $\hat{G}(F_t(\vec{X}), t) = \hat{F}^{-1}(\vec{X}, t)$ and $\hat{F}(F_t^{-1}(\vec{x}), t) = \hat{G}^{-1}(\vec{x}, t)$.

The velocity and acceleration fields, $\vec{v}$ and $\vec{a}$ respectively, describing the particle starting at $\vec{X}$, are given by (Lagrangian description):

$$\vec{v}(\vec{X}, t) = \frac{\partial \vec{x}}{\partial t}(\vec{X}, t), \tag{445}$$

$$\vec{a}(\vec{X}, t) = \frac{\partial^2 \vec{x}}{\partial t^2}(\vec{X}, t). \tag{446}$$

When we consider the Eulerian variables we get

$$\vec{v}(\vec{x}, t) = \frac{\partial \vec{x}}{\partial t}(F_t^{-1}(\vec{x}), t), \tag{447}$$

$$\vec{a}(\vec{x}, t) = \frac{\partial^2 \vec{x}}{\partial t^2}(F_t^{-1}(\vec{x}), t). \tag{448}$$

Any scalar, vector or tensor field can be regarded as a function of $(\vec{X}, t)$ or $(\vec{x}, t)$ when the motion $\vec{x} = F_t(\vec{X}, t)$ is given. If we have $\phi(\vec{x}, t)$ a random field, we can also write

$$\Phi(\vec{X}, t) = \phi(F_t(\vec{X}), t), \tag{449}$$

where ϕ is the Eulerian field and Φ is the Lagrangian one. The derivative leads to

$$\frac{\partial \Phi}{\partial t} = \frac{\partial \phi}{\partial t} + \frac{\partial \phi}{\partial \vec{x}} \cdot \frac{\partial \vec{x}}{\partial t} = \frac{\partial \phi}{\partial t} + \frac{\partial \phi}{\partial \vec{x}} \cdot \vec{v}. \tag{450}$$

Often, we use the same symbol for Φ and ϕ and we assume two different symbols for the derivatives. In particular we define $\dot{\phi} = \frac{\partial \Phi}{\partial t}$, also written $\dot{\phi} = \frac{d\phi}{dt}$, for the Lagrangian or material derivative and $\frac{\partial \phi}{\partial t}$ for the Eulerian or Spatial derivative. Eq.(450) can then be rewritten

$$\dot{\phi} = \frac{\partial \phi}{\partial t} + \frac{\partial \phi}{\partial \vec{x}} \cdot \vec{v}. \tag{451}$$

It is also useful to define the velocity gradient

$$\hat{L} = \frac{\partial \vec{v}}{\partial \vec{x}}, \tag{452}$$

with components $L_{i,j} = \frac{\partial v_i}{\partial x_j}$.

It satisfies the relation

$$\dot{\hat{F}} = \hat{L}\hat{F}, \tag{453}$$

which can be proved as follows

$$\begin{aligned}\dot{\hat{F}} &= \frac{\partial}{\partial t}\frac{\partial}{\partial \vec{X}}F_t(\vec{X}),\\ &= \frac{\partial}{\partial \vec{X}}\frac{\partial}{\partial t}F_t(\vec{X}),\\ &= \frac{\partial \vec{v}}{\partial \vec{X}},\\ &= \frac{\partial \vec{v}}{\partial \vec{x}}\frac{\partial \vec{x}}{\partial \vec{X}},\\ &= \hat{L}\hat{F}.\end{aligned}$$

Eq.(453) can be inverted like

$$\frac{d\hat{F}^{-1}}{dt} = -\hat{G}\hat{L}, \tag{454}$$

This holds true since, with $\hat{F}^{-1}\hat{F} = \hat{I}$, we have $\frac{d}{dt}(\hat{F}^{-1}\hat{F}) = 0$ or $\frac{d\hat{F}^{-1}}{dt}\hat{F} + \hat{F}^{-1}\frac{d\hat{F}}{dt} = 0$, from which $(\frac{d\hat{F}^{-1}}{dt}) = -\hat{F}^{-1}\frac{d\hat{F}}{dt}\hat{F}^{-1}$ and so we can write

$$\begin{aligned}\frac{d\hat{F}^{-1}}{dt} &= -\hat{F}^{-1}\frac{d\hat{F}}{dt}\hat{F}^{-1},\\ &= -\hat{F}^{-1}\hat{L}\hat{F}\hat{F}^{-1},\\ &= -\hat{F}^{-1}\hat{L},\\ &= -\hat{G}\hat{L}.\end{aligned}$$

Here we clearly written the differential operator d/dt in order to avoid the possible unclear interpretation originated by the combination with the inverse matrix operation.

A.1.2 *Reynolds Theorem*

We consider a subset $P_t \subset \Omega_t$, which is the time deformed version of $P_0 \subset \Omega_0$. We describe a property useful to calculate the time derivative of an arbitrary volume integral. We consider a scalar field ϕ and we obtain

$$\frac{d}{dt}\int_{P_t}\phi d\vec{x} = \frac{d}{dt}\int_{P_0}\phi J d\vec{X}, \tag{455}$$

where $J = \det(\frac{\partial \vec{x}}{\partial \vec{X}}) = \det(\hat{F})$.

We elaborate Eq.(455) as

$$\frac{d}{dt}\int_{P_t}\phi d\vec{x} = \int_{P_0}\frac{d}{dt}(\phi J)d\vec{X} = \int_{P_0}(\dot{\phi}J + \phi\dot{J})d\vec{X}, \tag{456}$$

where $\dot{\phi}$ and $\dot{J}$ are material derivatives. $\dot{J}$ can be calculated as

$$\frac{d}{dt}\det F = \det \hat{F}\,\mathrm{tr}(\dot{\hat{F}}\hat{F}^{-1}). \tag{457}$$

From Eq.(453) we get $\dot{\hat{F}}\hat{F}^{-1} = \hat{L}$ so

$$\dot{J} = J\,\mathrm{tr}(\hat{L}) = J\vec{\nabla}_{\vec{x}}\cdot\vec{v}. \tag{458}$$

Therefore

$$\begin{aligned}\frac{d}{dt}\int_{P_t}\phi\,d\vec{x} &= \int_{P_0}(\dot{\phi}+\phi\vec{\nabla}_{\vec{x}}\cdot\vec{v})J\,d\vec{X},\\ &= \int_{P_t}(\dot{\phi}+\phi\vec{\nabla}_{\vec{x}}\cdot\vec{v})\,d\vec{x}.\end{aligned} \tag{459}$$

Since $\dot{\phi} = \frac{\partial\phi}{\partial t} + \frac{\partial\phi}{\partial\vec{x}}\cdot\vec{v}$ we have

$$\frac{d}{dt}\int_{P_t}\phi\,d\vec{x} = \int_{P_t}\left(\frac{\partial\phi}{\partial t} + \frac{\partial\phi}{\partial\vec{x}}\cdot\vec{v} + \phi\vec{\nabla}_{\vec{x}}\cdot\vec{v}\right)d\vec{x}. \tag{460}$$

Finally

$$\frac{d}{dt}\int_{P_t}\phi\,d\vec{x} = \int_{P_t}\left[\frac{\partial\phi}{\partial t} + \vec{\nabla}_{\vec{x}}\cdot(\phi\vec{v})\right]d\vec{x}. \tag{461}$$

Reynolds Theorem, Transport Theorem

This property is the so called Reynolds theorem or transport theorem. If $\phi = 1$ we obtain

$$\frac{d}{dt}\int_{P_t}\phi\,d\vec{x} = \int_{P_t}\vec{\nabla}_{\vec{x}}\cdot\vec{v}\,d\vec{x}. \tag{462}$$

A.1.3 *Stress*

In continuum mechanics two systems of force acting on a given region must be considered:

- **The body forces**: They depend on the external fields acting on P_t and are defined as $d\vec{F}_v = \vec{b}(\vec{x})d\vec{x}$ being $d\vec{F}_v$ the force on the volume $d\vec{x}$ centered at $\vec{x}$. The quantity $\vec{b}(\vec{x})$ is a body force density.
- **The surface forces**: They describe the interaction between neighboring portion of deformable bodies. they are the subject of the present section.

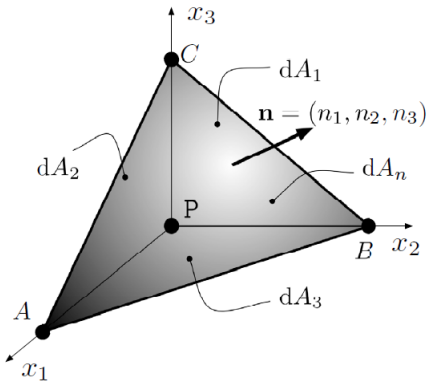

Figure 106: Cauchy tetrahedron on a generic point P

Surface forces are defined as $d\vec{F}_s = \vec{f}(\vec{x}, \vec{n}, t)dS$ where:

- $d\vec{F}_s$ is the force applied by the region where the unit vector $\vec{n}$ is directed toward the other region
- $\vec{x}$ is the point where the surface dS with normal unit vector $\vec{n}$ is located
- $\vec{f}$ is a density of force for unit of area
- t is the time

The Cauchy theorem (1827) states that

$$\vec{f}(\vec{x}, \vec{n}, t) = \hat{T}(\vec{x}, t)\vec{n}, \tag{463}$$

where $\hat{T}$ is the so called Cauchy stress tensor. Eq.(463) is proven by considering a tetrahedron ABCP as seen in Fig.106 with $P \equiv \vec{x}$, $\vec{n} \perp \overline{ABC}$, $||\vec{n}|| = 1$, $\vec{e_i} \parallel \vec{x_i}$ and $||\vec{e_i}|| = 1$.

The Newton equation for the motion of the material within ABCP is given by $\vec{b}dV + \vec{f}_n dA_n + \vec{f}_1 dA_1 + \vec{f}_2 dA_2 + \vec{f}_3 dA_3 = \rho\vec{a}dV$ where $\vec{f}_1$, $\vec{f}_2$, $\vec{f}_3$ and $\vec{f}_n$ are the forces acting on dA_1, dA_2, dA_3, and dA_n respectively, $\vec{a}$ is the acceleration and dV is the volume. We have that

$$\begin{cases} \vec{f}_n = \vec{f}(\vec{n}, \vec{x}, t) \\ \vec{f}_k = \vec{f}(-\vec{e}_k, \vec{x}, t) \quad \forall k = 1, 2, 3 \end{cases} \tag{464}$$

and that $dA_i = n_i dA_n$. Also $dV = \frac{1}{3} dA_n dh$ where $dh = \text{dist}(P, dA_n)$.

From now on we will use for simplicity the Einstein notation that implies the summation over a set of indexed terms. Using this notation

Einstein notation

here with the sum over j, we obtain

$$\vec{f}(\vec{n},\vec{x},t)+\vec{f}(-\vec{e}_j,\vec{x},t)n_j+\frac{1}{3}\vec{b}dh=\frac{1}{3}\rho\vec{a}dh. \tag{465}$$

If $dh\to 0$ we get

$$\vec{f}(\vec{n},\vec{x},t)=-\vec{f}(-\vec{e}_j,\vec{x},t)n_j. \tag{466}$$

If $\vec{n}=\vec{e}_i$ we simply obtain an equivalent to the third law for the surface force

$$\vec{f}(\vec{e}_i,\vec{x},t)=-\vec{f}(-\vec{e}_i,\vec{x},t). \tag{467}$$

Eq.(467) can then be substituted to Eq.(466) giving

$$\vec{f}(\vec{n},\vec{x},t)=\vec{f}(\vec{e}_j,\vec{x},t)n_j. \tag{468}$$

This shows that the surface force $\vec{f}$ on a given plane is determined by the three surface forces on the three coordinate plane. This can be expressed in components as

$$f_i(\vec{n},\vec{x},t)=\vec{f}(\vec{e}_j,\vec{x},t)\cdot\vec{e}_i n_j=T_{ij}n_j, \tag{469}$$

where

$$T_{ij}=\vec{f}(\vec{e}_j,\vec{x},t)\cdot\vec{e}_i, \tag{470}$$

Stress Tensor

is the stress tensor. It represents the pressure applied on the j-th surface along the i-th direction.

A.1.4 *Continuity Equation*

The continuity equation is the first balance equation of continuum mechanics. It concerns the conservation of mass. With ρ the density of the material, the total mass within P_t is

$$n(P_t)=\int_{P_t}\rho(\vec{x},t)d\vec{x}. \tag{471}$$

The mass conservation implies

$$\frac{d}{dt}\int_{P_t}\rho(\vec{x},t)d\vec{x}=0. \tag{472}$$

By using the transport theorem we get

$$\int_{P_t}(\dot{\rho}+\rho\vec{\nabla}_{\vec{x}}\cdot\vec{v})d\vec{x}=\int_{P_t}(\frac{\partial\rho}{\partial t}+\vec{\nabla}_{\vec{x}}\cdot(\rho\vec{v}))d\vec{x}=0. \tag{473}$$

We have therefore two forms of the continuity equations

Continuity Equation

$$\dot{\rho} + \rho\vec{\nabla}_{\vec{x}} \cdot \vec{v} = 0, \tag{474}$$

$$\frac{\partial \rho}{\partial t} + \vec{\nabla}_{\vec{x}} \cdot (\rho\vec{v}) = 0. \tag{475}$$

Eq.(474) being in the Lagrangian description of the continuity equation and Eq.(475) being the Eulerian one.

It is important to observe the validity of the property

$$\begin{aligned}\frac{d}{dt}\int_{P_t} \rho\psi d\vec{x} &= \int_{P_t} (\dot{\rho}\psi + \rho\dot{\psi} + \rho\psi\vec{\nabla}_{\vec{x}} \cdot \vec{v}) d\vec{x}, \\ &= \int_{P_t} (-\rho\psi\vec{\nabla}_{\vec{x}} \cdot \vec{v} + \rho\dot{\psi} + \rho\psi\vec{\nabla}_{\vec{x}} \cdot \vec{v}) d\vec{x}, \\ &= \int_{P_t} \rho\dot{\psi} d\vec{x}, \end{aligned} \tag{476}$$

for any field ψ thanks to Eq.(474). It means that in $\frac{d}{dt}\int_{P_t} \rho\psi d\vec{x}$ the time derivatives can be applied directly to the function ψ (as a Lagrangian derivative).

A.1.5 *Linear Momentum Balance*

We know that the resultant of the external forces is equal to the rate of change of the total linear momentum of the system

$$\frac{d\vec{P}}{dt} = \vec{F}. \tag{477}$$

For the region P_t we have

$$\frac{d}{dt}\int_{P_t} \rho\vec{v} d\vec{x} = \int_{\partial P_t} \hat{T}\vec{n} dS + \int_{P_t} \vec{b} d\vec{x}, \tag{478}$$

when we decomposed the external forces in surfaces forces and body forces. The property shown in Eq.(476) and the divergence theorem

Divergence Theorem

$$\int_{\partial P_t} \hat{T}\vec{n} dS = \int_{P_t} \vec{\nabla}_{\vec{x}} \cdot \hat{T} d\vec{x}, \tag{479}$$

deliver

$$\int_{P_t} \rho\dot{\vec{v}} d\vec{x} = \int_{P_t} \vec{\nabla}_{\vec{x}} \cdot \hat{T} d\vec{x} + \int_{P_t} \vec{b} d\vec{x}. \tag{480}$$

Since P_t is arbitrary we must have

$$\vec{\nabla}_{\vec{x}} \cdot \hat{T} + \vec{b} = \rho \dot{\vec{v}}. \tag{481}$$

In component we get

$$\frac{\partial T_{ji}}{\partial x_i} + b_j = \rho \dot{v}_j. \tag{482}$$

Since $\dot{\vec{v}} = \frac{\partial \vec{v}}{\partial t} + \frac{\partial \vec{v}}{\partial \vec{x}} \cdot \vec{v}$ we can write Eq.(481) in the explicit Eulerian form

$$\rho \frac{\partial \vec{v}}{\partial t} + \rho \frac{\partial \vec{v}}{\partial \vec{x}} \cdot \vec{v} = \vec{\nabla}_{\vec{x}} \cdot \hat{T} + \vec{b}, \tag{483}$$

Linear Momentum Balance

being the linear momentum balance.

A.1.6 *Angular Momentum Balance*

By taking moments about a fixed point, we can show that the resultant moment of the external forces $\vec{M}$ is equal to the rate of change of the total angular momentum $\vec{L}$

$$\frac{d\vec{L}}{dt} = \vec{M}, \tag{484}$$

or when applied to the region P_t

$$\frac{d}{dt} \int_{P_t} \vec{x} \wedge \rho \vec{v} \, d\vec{x} = \int_{\partial P_t} \vec{x} \wedge (\hat{T}\vec{n}) \, dS + \int_{P_t} \vec{x} \wedge \vec{b} \, d\vec{x}, \tag{485}$$

or

$$\frac{d}{dt} \int_{P_t} x_h \rho v_k \eta_{hkj} \vec{e}_j \, d\vec{x} = \int_{\partial P_t} x_h T_{kp} n_p \eta_{hkj} \vec{e}_j \, dS + \int_{P_t} x_h b_k \eta_{hkj} \vec{e}_j \, d\vec{x}, \tag{486}$$

with η_{hkj} being the Levi-Civita symbol. By applying the divergence theorem,

$$\int_{P_t} x_h \rho \dot{v}_k \eta_{hkj} \vec{e}_j \, d\vec{x} = \int_{P_t} \frac{\partial}{\partial x_p}(x_h T_{kp}) \eta_{hkj} \vec{e}_j \, d\vec{x} + \int_{P_t} x_h b_k \eta_{hkj} \vec{e}_j \, d\vec{x}. \tag{487}$$

We now simplify knowing $\frac{\partial x_h}{\partial x_p} = \delta_{hp}$ (δ being the Kronecker symbol)

$$\int_{P_t} x_h \rho \dot{v}_k \eta_{hkj} \vec{e}_j \, d\vec{x} = \int_{P_t} \left[T_{kh} + x_h \frac{\partial T_{kp}}{\partial x_p} \right] \eta_{hkj} \vec{e}_j \, d\vec{x} + \int_{P_t} x_h b_k \eta_{hkj} \vec{e}_j \, d\vec{x}. \tag{488}$$

Finally

$$\int_{P_t} \left[x_h \left(\rho \dot{v}_k - \frac{\partial T_{kp}}{\partial x_p} - b_k \right) - T_{kh} \right] \eta_{hkj} \vec{e}_j \, d\vec{x} = 0. \tag{489}$$

By using the balance of linear momentum we obtain $\int_{P_t} T_{kh} \eta_{hkj} \vec{e}_j \, d\vec{x} = 0$ or equivalently $T_{kh} \eta_{hkj} = 0 \; \forall j$. This finally leads to

$$T_{ij} = T_{ji}. \tag{490}$$

Angular Momentum Balance

The symmetry of the Cauchy Stress Tensor $\hat{T}$ represents the balance of angular momentum.

A.1.7 *Energy Balance*

From the linear momentum balance in the form of Eq.(482) multiplied by v_j we get

$$\rho v_j \dot{v}_j = v_j \frac{\partial T_{ji}}{\partial x_i} + b_j v_j, \tag{491}$$

and

$$\rho v_j \dot{v}_j = \frac{\partial}{\partial x_i}(v_j T_{ji}) - \frac{\partial v_j}{\partial x_i} T_{ji} + b_j v_j. \tag{492}$$

Let us decomposed $L_{ji} = \frac{\partial v_j}{\partial x_i}$ in symmetric and antisymmetric part $L_{ji} = D_{ji} + W_{ji}$ with $D_{ji} = \frac{1}{2}(L_{ji} + L_{ij})$ and $W_{ji} = \frac{1}{2}(L_{ji} - L_{ij})$.

We have that $L_{ji} T_{ji} = D_{ji} T_j + W_{ji} T_j$ where $W_{ji} T_{ji} = 0$ since $\hat{W}$ is antisymmetric. Indeed, $W_{ji} T_{ji} = W_{ji} T_{ij}$ due to Cauchy symmetry of T_{ij}, and $= -W_{ij} T_{ij}$ due to the antisymmetry of W_{ij}, then $= -W_{ji} T_{ji}$ by changing the order of the indexes. This leads to $W_{ji} T_{ji} = -W_{ji} T_{ji} = 0$. By integrating Eq.(492) over P_t and using the decomposition of the velocity gradient stated above, we get

$$\int_{P_t} \frac{\partial}{\partial x_i}(v_j T_{ji}) d\vec{x} + \int_{P_t} b_j v_j d\vec{x} = \int_{P_t} T_{ji} D_{ji} d\vec{x} + \int_{P_t} \rho v_j \dot{v}_j d\vec{x}, \tag{493}$$

and by using the transport and divergence theorems we finally obtain

$$\frac{d}{dt} \int_{P_t} \frac{1}{2} \rho v^2 dV + \int_{P_t} T_{ji} D_{ji} dV = \int_{\partial P_t} v_j T_{ji} n_i dS + \int_{P_t} b_j v_j dV. \tag{494}$$

Global Balance of Mechanical Energies

Eq.(494) represents the global balance of purely mechanical energies. The left hand side can be viewed as the rate of change of the total mechanical energy $\frac{d\kappa}{dt} + \frac{d\upsilon}{dt}$ with κ being the kinetic energy and υ the potential energy. The right hand side can be considered as the total power

entering the region P_t (velocity time force over surface and volume). This conceptual scheme is correct from a purely mechanical point of view however the more general energy balance must consider the thermal processes occurring in the real materials.

In this more general context, the potential mechanical energy should be substituted with the interned energy (considering all energy stored in the region P_t but for the macroscopic kinetic energy κ) and the power entering the system should also consider the heat supplied to P_t. The new balance can be written as follows

$$\frac{d}{dt}\int_{P_t}\rho(e+\frac{1}{2}v^2)dV=\int_{\partial P_t}v_jT_{ji}n_i\,dS+\int_{P_t}b_jv_j\,dV-\int_{\partial P_t}q_jn_j\,dS+\int_{P_t}Q_0\,dV, \tag{495}$$

the first two terms on the right hand side being associated to the mechanical power. Here e is the internal energy density or specific internal energy [$J.kg^{-1}$], $\vec{q}\cdot\vec{n}$ is the heat flowing out of the surface ∂P_t [$W.m^{-2}$] and Q_0 is the heat density supplied to P_t [$W.m^{-3}$].

This equation can be elaborated to obtain a local form

$$\begin{aligned}\int_{P_t}\rho(\dot{e}+v_j\dot{v}_j)dV&=\int_{P_t}\left[\frac{\partial}{\partial x_i}(v_jT_{ji})+b_jv_j-\frac{\partial q_j}{\partial x_j}+Q_0\right]dV,\\&=\int_{P_t}\left[D_{ji}T_{ji}+v_j\frac{\partial T_{ji}}{\partial x_i}-\frac{\partial q_j}{\partial x_j}+b_jv_j+Q_0\right]dV.\end{aligned} \tag{496}$$

Or equivalently

$$\int_{P_t}\rho\dot{e}dV=\int_{P_t}\left[D_{ji}T_{ji}+v_j(\frac{\partial T_{ji}}{\partial x_i}+b_j-\rho\dot{v}_j)-\frac{\partial q_j}{\partial x_j}+Q_0\right]dV. \tag{497}$$

By using the balance of the linear momentum, with : being the Frobenius inner product (here used for only real components), we get

$$\rho\dot{e}=T_{ji}D_{ji}-\frac{\partial q_j}{\partial x_j}+Q_0, \tag{498}$$

$$\text{or}\qquad \rho\dot{e}=\hat{T}:\hat{D}-\vec{\nabla}\cdot\vec{q}+Q_0. \tag{499}$$

Energy Balance Equation

This is the most general energy balance for a continuum medium, when e is the internal energy density as defined in classical thermodynamics.

A.1.8 *Entropy Balance*

From classical thermodynamics, we know that for quasi-static or reversible transformation we have $dQ = TdS \Leftrightarrow dS = \frac{dQ}{T}$, where dQ represents the heat quantity exchanged, T the temperature and S the entropy. In this case the first principle can be written as

$$dE = dQ + dL = TdS + dL, \tag{500}$$

where E is the total internal energy and L is the macroscopic work done on the system. For arbitrarily evolving or irreversible transformation we have $dS \geqslant \frac{dS}{T}$, which represents the second principle. It can be alternatively stated by writing

$$dS = \frac{dQ}{T} + \Sigma_s \tag{501}$$

where Σ_s represent the entropy production with $\Sigma_s \geqslant 0$. For the continuum medium we introduce the entropy density s for unit of mass $[J/(K.kg)]$ and the entropy production density σ_s for unit of volume and time $[J/(K.m^3.s)]$. We can then write

$$\frac{d}{dt}\int_{P_t} \rho s \, dV = \int_{\partial P_t} -\frac{\vec{q}\cdot\vec{n}}{T} \, dS + \int_{P_t} \frac{Q_0}{T} \, dV + \int_{P_t} \sigma_s \, dV. \tag{502}$$

While the first term in the right hand side represents the heat entering the region P_t due to the heat flux $\vec{q}$, the second term represent the heat entering P_t because of the heat density Q_0 locally supplied. The sum of these two terms corresponds to the first term in the right hand side of Eq.(501). Eq.(502) is then completely equivalent to Eq.(501). Transport and divergence theorems then lead to

$$\int_{P_t} \rho \dot{s} \, dV = \int_{P_t} -\vec{\nabla}\cdot(\frac{\vec{q}}{T}) \, dV + \int_{P_t} \frac{Q_0}{T} \, dV + \int_{P_t} \sigma_s \, dV. \tag{503}$$

In local form we get

$$\rho \dot{s} = -\vec{\nabla}\cdot(\frac{\vec{q}}{T}) + \frac{Q_0}{T} + \sigma_s, \quad \sigma_s \geqslant 0. \tag{504}$$

Entropy Balance Equation

The balance equations needed for the description of the thermoacoustic principle have been laid down. The reader who wanted to understand the creation of those equation can now go back to Section 2. The following sections A.2 and A.3 bring insights on some general properties of the entropy production terms.

A.2 ENTROPY PRODUCTION

In general the entropy production can be written in the bilinear form

$$\sigma_s = \sum_i J_i X_i \geqslant 0, \tag{505}$$

where J_i and W_i can be scalars, vectors or tensors. The quantities X_i are the gradients within the systems and the J_i are their effects. The linear response is described by

$$J_i = \sum_j L_{ij} X_j, \tag{506}$$

and the entropy production becomes

$$\sigma_s = \sum_i \sum_j L_{ij} X_i X_j \ \geqslant 0, \tag{507}$$

where L_{ij} must be positive definite.

There are two main properties of coefficients L_{ij}: the Curie principle and the Onsager reciprocity relation.

A.2.1 *Curie Principle (1894)*

The fluxes J_i and the fixed X_j of different tensor order can not be coupled in an isotropic medium. If we consider for example vectors and tensor of order two (matrices), their coupling can be realized only by tensor of order three, which are zero for isotropic symmetry. In general all tensors L_{ij} must have the symmetry properties of the specific crystal symmetry of the anisotropic medium considered. For this reason, an isotropic fluid heat transfer cannot be coupled to viscosity.

A.2.2 *Onsager Reciprocity Relations (1931)*

We always have

$$L_{ij} = L_{ji}. \tag{508}$$

It means that the couplings between different dissipative processes are always reciprocal. The proof of this statement can be done within statistical mechanics.

A.3 TENSORS

A.3.1 *Constitutive Equation*

Because of the symmetry of $\hat{T}$, the elastic stress-strain relation is defined by six relations of the form $T_{ij} = f(\{\epsilon_{ij}\})$ which are uniquely solvable for each different component of the strain. A thermo-elastic material is one whose state of stress depends on the present strain and on the temperature (or entropy). In what follows we shall always assume that the temperature (or entropy) is constant so that, effectively, we have a pure stress-strain relationship.

For most materials the response is linear if the strain is small. This corresponds to the generalized Hooke's law which has the following general form

$$T_{ij} = \mathcal{C}_{ijkh}\epsilon_{kh}, \tag{509}$$

where $\mathcal{C}_{ijkh}$ are constants (for homogeneous materials). Eq.(509) is of general validity, including all possible crystalline symmetries or, in other words, any kind of anisotropy. The fourth-rank tensor (with 81 components) of the elastic constants satisfies the following symmetry rules:

- Symmetry in the first pair of indices: since $T_{ij} = T_{ji}$ we have

$$\mathcal{C}_{ijkh} = \mathcal{C}_{jikh}. \tag{510}$$

- Symmetry in the last pair of indices: since $\epsilon_{kh} = \epsilon_{hk}$ we have

$$\mathcal{C}_{ijkh} = \mathcal{C}_{ijhk}. \tag{511}$$

- Symmetry between the first pair and the last pair of indices:

$$\mathcal{C}_{ijkh} = \mathcal{C}_{khij}. \tag{512}$$

This last result is easily proved if we suppose that an elastic energy density $U = U(\hat{\epsilon})$ exists, being dependent only on the state of strain. From the energy density we derive the constitutive relation $T_{ij} = \frac{\partial U(\hat{\epsilon})}{\partial \epsilon_{ij}}$ (just think about the case of the one-dimensional harmonic spring, where $U = \frac{1}{2}kx^2$ and $F = kx$). Drawing a comparison between the energy based constitutive relation $T_{ij} = \frac{\partial U(\hat{\epsilon})}{\partial \epsilon_{ij}}$ and Eq.(509) we simply obtain

$$\mathcal{C}_{ijkh} = \frac{\partial T_{ij}}{\partial \epsilon_{kh}} = \frac{\partial^2 U(\hat{\epsilon})}{\partial \epsilon_{kh}\partial \epsilon_{ij}}. \tag{513}$$

The symmetry of the second order derivative directly leads to Eq.(512).

According to the above universal symmetry properties, $\mathcal{C}_{ijkh}$ has at most 21 independent components. Further reductions of the number of independent elastic constants depend upon the possible crystalline symmetry of the material body.

The linear relation can be written in tensor compact form $\hat{T} = \hat{\mathcal{C}}\hat{\epsilon}$, where the elastic tensor $\hat{\mathcal{C}}$ is called *stiffness tensor*. We also introduce the inverse relation $\hat{\epsilon} = \hat{\mathcal{D}}\,\hat{T}$ with $\hat{\mathcal{D}} = \hat{\mathcal{C}}^{-1}$. The new tensor $\hat{\mathcal{D}}$ is called *compliance tensor*.

A.3.2 *The Isotropic and Homogeneous Elastic Body*

The paradigmatic system investigated by elasticity theory is the linear, isotropic and homogeneous medium. The homogeneity property implies that the elastic behavior of the medium is the same in all its points: the stiffness and the compliance tensors are constant everywhere in the medium. The isotropy property implies that the mechanical response does not depend on the direction considered: stiffness or compliance tensors are invariant under arbitrary rotations. For a linear, isotropic and homogeneous body we will prove that only two elastic moduli are independent. They are typically called Lamé coefficients and they are referred to as μ (shear modulus) and λ, respectively. Alternatively, we may use the Young modulus E and the Poisson ratio ν. A bulk modulus B can be used as well.

Let us now derive the constitutive equation for a linear, isotropic and homogeneous elastic body. Because the stress tensor $\hat{T}$ is symmetric, we can select a suitable reference frame where $\hat{T}$ is diagonal. In this reference frame we refer to $\hat{T}^*$ as the diagonal representation of $\hat{T}$, where the only components different from zero are T^*_{11}, T^*_{22} and T^*_{33}. To begin we consider the case of a uniaxial traction, i.e., an elongation, along the x_1 axis, which means $T^*_{11} \neq 0$, $T^*_{22} = 0$ and $T^*_{33} = 0$. For most materials the experimental observation shows that the body will be elongated along the direction x_1, while it shrinks in the plane (x_2, x_3). We can formalize this response by writing the linear relations

$$\begin{aligned}
\epsilon^*_{11} &= +\frac{1}{E}T^*_{11},\\
\epsilon^*_{22} &= -\frac{\nu}{E}T^*_{11},\\
\epsilon^*_{33} &= -\frac{\nu}{E}T^*_{11},\\
\epsilon^*_{12} &= \epsilon^*_{23} = \epsilon^*_{31} = 0.
\end{aligned} \tag{514}$$

The Young modulus E describes the length variation along the direction x_1 while the Poisson ratio ν describes the contractions in the two per-

pendicular directions. Of course, in these conditions we can not observe shear deformations.

When the diagonal stress $\hat{T}^*$ assumes triaxial character Eq.(514) can be easily generalized as

$$\begin{aligned}
\epsilon^*_{11} &= \frac{1}{E}\left[T^*_{11} - \nu\left(T^*_{22} + T^*_{33}\right)\right], \\
\epsilon^*_{22} &= \frac{1}{E}\left[T^*_{22} - \nu\left(T^*_{11} + T^*_{33}\right)\right], \\
\epsilon^*_{33} &= \frac{1}{E}\left[T^*_{33} - \nu\left(T^*_{22} + T^*_{11}\right)\right], \\
\epsilon^*_{12} &= \epsilon^*_{23} = \epsilon^*_{31} = 0.
\end{aligned} \tag{515}$$

The constitutive relations given in Eq.(515) are valid only in the reference frame where the stress tensor is diagonal. We remark that Eq.(515) can be written in the following more compact form

$$\hat{\epsilon}^* = \frac{1}{E}\left[(1+\nu)\hat{T}^* - \nu\hat{I}\ \mathrm{tr}\left(\hat{T}^*\right)\right]. \tag{516}$$

If we make an arbitrary change of reference frame by means of a rotation matrix $\hat{R}$, the stress tensor $\hat{T}^*$ is transformed into $\hat{T}$ and the strain tensor $\hat{\epsilon}^*$ is transformed into $\hat{\epsilon}$ ($\hat{\epsilon} = \hat{R}^T\hat{\epsilon}^*\hat{R}$ and $\hat{T} = \hat{R}^T\hat{T}^*\hat{R}$). By means of such transformations, we obtain the isotropic constitutive equation in an arbitrary reference frame in the form

$$\hat{\epsilon} = \frac{1}{E}\left[(1+\nu)\hat{T} - \nu\hat{I}\ \mathrm{tr}\left(\hat{T}\right)\right]. \tag{517}$$

This is in fact the constitutive equation of a linear, isotropic and homogeneous elastic material. Eq.(517) can be inverted, thus obtaining the stress tensor in terms of the strain tensor

$$\hat{T} = \frac{E}{1+\nu}\hat{\epsilon} + \frac{\nu E}{(1+\nu)(1-2\nu)}\hat{I}\ \mathrm{tr}\left(\hat{\epsilon}\right). \tag{518}$$

We now introduce the Lamé coefficients μ_0 and λ_0 defined by the following relations

$$\mu_0 = \frac{E}{2(1+\nu)}, \qquad \lambda_0 = \frac{\nu E}{(1+\nu)(1-2\nu)}, \tag{519}$$

which, inserted into Eq.(518), provide the constitutive equation in its most popular form

$$\hat{T} = 2\mu_0\hat{\epsilon} + \lambda_0\hat{I}\ \mathrm{tr}(\hat{\epsilon}). \tag{520}$$

Similarly, Eq.(517) can be also written in terms of the Lamé coefficients

$$\hat{\epsilon} = \frac{1}{2\mu_0}\hat{T} - \frac{\lambda}{2\mu_0(2\mu_0+3\lambda_0)}\hat{I}\ \mathrm{tr}(\hat{T}). \tag{521}$$

In order to introduce the bulk modulus B, we consider an hydrostatic stress described by the tensor

$$\hat{T} = \begin{bmatrix} \sigma & 0 & 0 \\ 0 & \sigma & 0 \\ 0 & 0 & \sigma \end{bmatrix}. \tag{522}$$

By means of Eq.(521) we easily obtain the corresponding state of strain

$$\hat{\epsilon} = \frac{1}{3}\frac{1}{\lambda_0 + \frac{2}{3}\mu_0}\sigma\hat{I}. \tag{523}$$

This simple result allows us to define the bulk modulus B as

$$B = \lambda_0 + \frac{2}{3}\mu_0. \tag{524}$$

Therefore, the stress-strain relation in hydrostatic condition can be summarized as $\hat{\epsilon} = \frac{1}{3B}\sigma\hat{I}$ where σ represents the (scalar) pressure applied to the system. The further relation $\mathrm{tr}(\hat{\epsilon}) = \frac{\sigma}{B}$ has an important physical interpretation: it describes the local volumetric variation under the assumption of hydrostatic stress.

Table 13: Relations among the different elastic moduli.

	(λ_0, μ_0)	(B, μ_0)	(μ_0, ν)	(E, ν)	(E, μ_0)
λ_0		$B - \frac{2}{3}\mu_0$	$\frac{2\mu_0\nu}{1-2\nu}$	$\frac{\nu E}{(1+\nu)(1-2\nu)}$	$\frac{\mu_0(E-2\mu_0)}{3\mu_0-E}$
μ_0				$\frac{E}{2(1+\nu)}$	
B	$\frac{3\lambda_0+2\mu_0}{3}$		$\frac{2\mu_0(1+\nu)}{3(1-2\nu)}$	$\frac{E}{3(1-2\nu)}$	$\frac{E\mu_0}{3(3\mu_0-E)}$
E	$\frac{\mu_0(3\lambda_0+2\mu_0)}{\lambda_0+\mu_0}$	$\frac{9B\mu_0}{3B+\mu_0}$	$2(1+\nu)\mu_0$		
ν	$\frac{\lambda_0}{2(\lambda_0+\mu_0)}$	$\frac{3B-2\mu_0}{2(3B+\mu_0)}$			$\frac{E-2\mu_0}{2\mu_0}$

To conclude, we observe that the stress-strain relation (Hooke's law) for an isotropic elastic medium can be written in terms of any two independent material constants, chosen in the set $\lambda_0, \mu_0, B, E, \nu$. In Table 13 one can find all the possible conversions among the above defined elastic moduli. The elastic moduli E, λ_0, μ_0 and B are measured in Pa while the Poisson ratio ν is dimensionless being defined as a ratio between deformations.

A.4 POLAR DECOMPOSITION THEORY PROOF

We prove the Cauchy polar decomposition theorem by introducing the right Cauchy tensor $\hat{C} = \hat{F}^T\hat{F}$, for which $\hat{C}^{-1} = \hat{G}\hat{G}^T$ and $d\vec{x} \cdot d\vec{y} = d\vec{X} \cdot \hat{C} d\vec{Y}$. $\hat{C}$ is symmetric since

$$(\hat{F}^T\hat{F})^T = \hat{F}^T[\hat{F}^T]^T = \hat{F}^T\hat{F}, \tag{525}$$

and it is also positive definite as proved by

$$\vec{w}^T\hat{F}^T\hat{F}\vec{w} = (\hat{F}\vec{w})^T(\hat{F}\vec{w}) = \|\hat{F}\vec{w}\| \geqslant 0, \quad \forall\vec{w} \tag{526}$$

$\hat{C}$ can be then diagonalized with real eigenvalues $\hat{F}^T\hat{F} = \hat{O}^{-1}\hat{\Delta}\hat{O}$ with $\hat{\Delta}$ diagonal and $\hat{O}$ orthogonal. We define

$$\hat{U} = \sqrt{\hat{C}} = \sqrt{\hat{F}^T\hat{F}} = \sqrt{\hat{O}^{-1}\hat{\Delta}\hat{O}} = \hat{O}^{-1}\sqrt{\hat{\Delta}}\hat{O}, \tag{527}$$

which is justified by the fact

$$(\hat{O}^{-1}\sqrt{\hat{\Delta}}\hat{O})^2 = \hat{O}^{-1}\sqrt{\hat{\Delta}}\hat{O}\hat{O}^{-1}\sqrt{\hat{\Delta}}\hat{O} = \hat{O}^{-1}\hat{\Delta}\hat{O}. \tag{528}$$

Here $\sqrt{\hat{\Delta}} = \text{diag}\,(\sqrt{\Delta_i})$ if $\hat{\Delta} = \text{diag}\,(\Delta_i)$. This prove that $\hat{U}$ is also definite positive. Now we define $\hat{R} = \hat{F}\hat{U}^{-1}$ and we prove its orthogonality

$$\hat{R}^T\hat{R} = (\hat{U}^{-1})^T\hat{F}^T\hat{F}\hat{U}^{-1} = (\hat{U}^{-1})^T\hat{U}^2\hat{U}^{-1} = \hat{I}. \tag{529}$$

This conclude the proof of the first polar decomposition.

We also prove its uniqueness. We suppose that two decompositions $\hat{F} = \hat{R}\hat{U} = \hat{R}^*\hat{U}^*$ exists. It follows that $\hat{F}^T\hat{F} = \hat{U}^2 = \hat{U}^{*2}$ from which $\hat{U} = \hat{U}^*$ and then $\hat{R} = \hat{R}^*$. The second decomposition can be obtained with $\hat{V} = \sqrt{\hat{F}\hat{F}^T} = \sqrt{\hat{B}}$, where $\hat{B} = \hat{F}\hat{F}^T$ is the so-called left Cauchy tensor satisfying $\hat{B}^{-1} = \hat{G}^T G$ and $d\vec{X}d\vec{Y} = d\hat{x} \cdot \hat{B}^{-1} d\vec{y}$, with $\hat{R}' = \hat{V}^{-1}\hat{F}$. To conclude we verify that $\hat{R}' = \hat{R}$. Since $\hat{R}'\hat{R}'^T = \hat{I}$ we have that $\hat{F} = \hat{V}\hat{R}' = \hat{R}'\hat{R}'^T\hat{V}\hat{R}'$. The unicity of the decomposition $\hat{F} = \hat{R}\hat{U}$ allows us to affirm that $\hat{R}' = \hat{R}$ and $\hat{U} = \hat{R}^T\hat{V}\hat{R}$. This complete the proof of the Cauchy theorem.

A.5 CHANGE OF COORDINATES

In this section the different mathematical operators will be explicitly written in different coordinates systems, namely the cylindrical $(\vec{e_r}, \vec{e_\theta}, \vec{e_z})$, and spherical $(\vec{e_r}, \vec{e_\theta}, \vec{e_\phi})$ ones.

A.5.1 *Cylindrical Coordinates*

- $\vec{\nabla} p$

Knowing that

$$\vec{r} = x\vec{e_x} + y\vec{e_y}, \tag{530}$$

$$\text{and} \quad r = \sqrt{x^2 + y^2}, \tag{531}$$

$$\text{then} \quad \frac{\partial r}{\partial x} = \frac{x}{r}. \tag{532}$$

This leads to

$$\frac{\partial p}{\partial x} = \frac{\partial p}{\partial r}\frac{\partial r}{\partial x} = \frac{\partial p}{\partial r}\frac{x}{r}, \tag{533}$$

and then

$$\vec{\nabla} p = \frac{\vec{r}}{r}\frac{\partial p}{\partial r}. \tag{534}$$

- $\vec{\nabla}.\vec{v}$

In a straightforward manner

$$\begin{aligned}
\vec{\nabla}.\vec{v} &= \vec{\nabla}.(\frac{\vec{r}}{r}v(r)), \\
&= \frac{\partial}{\partial x}(\frac{x}{r}v) + \frac{\partial}{\partial y}(\frac{y}{r}v), \\
&= \frac{r - x\frac{x}{r}}{r^2}v + (\frac{x}{r})^2\frac{\partial v}{\partial r} + \frac{r - y\frac{y}{r}}{r^2}v + (\frac{y}{r})^2\frac{\partial v}{\partial r}, \\
&= \frac{r^2 - x^2 + r^2 - y^2}{r^3}v + \frac{x^2 + y^2}{r^2}\frac{\partial v}{\partial r},
\end{aligned} \tag{535}$$

hence

$$\vec{\nabla}.\vec{v} = \frac{1}{r}v + \frac{\partial v}{\partial r}. \tag{536}$$

- $\vec{\nabla}(\vec{\nabla}.\vec{v})$

The equation is investigated along the x axis before generalizing with ∇. Hence

$$\begin{aligned}\frac{\partial}{\partial x}(\vec{\nabla}.\vec{v}) &= \frac{\partial}{\partial x}(\frac{1}{r})v + \frac{1}{r}\frac{\partial v}{\partial x} + \frac{\partial^2 v}{\partial r^2}\frac{x}{r},\\ &= \frac{\partial}{\partial r}(\frac{1}{r})\frac{x}{r}v + \frac{1}{r}\frac{\partial v}{\partial r}\frac{x}{r} + \frac{\partial^2 v}{\partial r^2}\frac{x}{r},\\ &= \frac{-x}{r^3}v + \frac{x}{r^2}\frac{\partial v}{\partial r} + \frac{x}{r}\frac{\partial^2 v}{\partial r^2},\end{aligned}$$

leads to

$$\vec{\nabla}(\vec{\nabla}.\vec{v}) = \frac{\vec{r}}{r}\left(-\frac{1}{r^2}v + \frac{1}{r}\frac{\partial v}{\partial r} + \frac{\partial^2 v}{\partial r^2}\right) = \frac{\vec{r}}{r}\frac{\partial}{\partial r}\left(\frac{1}{r}\frac{\partial}{\partial r}(rv)\right). \tag{537}$$

- $\nabla^2\vec{v}$

$\nabla^2\vec{v}$ can be decomposed along the Cartesian coordinates as

$$\nabla^2\vec{v} = \nabla^2 v_x\vec{e_x} + \nabla^2 v_y\vec{e_y} + \nabla^2 v_z\vec{e_z}, \tag{538}$$

with $v_z = 0$, $v_x = \frac{x}{r}v(r)$ and $v_y = \frac{y}{r}v(r)$. The equation is investigated along the x axis before generalizing with ∇. Using Eq.(532) we have

$$\begin{cases}\frac{\partial v_x}{\partial x} = \frac{r^2-x^2}{r^3}v + \frac{x^2}{r^2}\frac{\partial v}{\partial r},\\ \frac{\partial v_x}{\partial y} = x\frac{\partial}{\partial r}(\frac{1}{r})\frac{\partial r}{\partial y}v + x\frac{1}{r}\frac{\partial v}{\partial r}\frac{\partial r}{\partial y} = -\frac{xy}{r^3}v + \frac{xy}{r^2}\frac{\partial v}{\partial r}.\end{cases} \tag{539}$$

Using Eq.(539) we can now deduce the second derivatives

$$\begin{aligned}\frac{\partial^2 v_x}{\partial x^2} =& \frac{\partial}{\partial x}(\frac{r^2-x^2}{r^3})v + \frac{r^2-x^2}{r^3}\frac{\partial v}{\partial r}\frac{x}{r} + \frac{\partial}{\partial x}(\frac{x^2}{r^2})\frac{\partial v}{\partial r} + \frac{x^2}{r^2}\frac{\partial^2 v}{\partial r^2}\frac{x}{r},\\ =& \frac{(2r\frac{\partial r}{\partial x} - 2x)r^3 - (r^2-x^2)3r^2\frac{\partial r}{\partial x}}{r^6}v + \frac{r^2-x^2}{r^3}\frac{x}{r}\frac{\partial v}{\partial r} +\\ &+ \frac{2x^2 - x^2 2r\frac{\partial r}{\partial x}}{r^4}\frac{\partial v}{\partial r} + \frac{x^3}{r^3}\frac{\partial^2 v}{\partial r^2},\\ =& -\frac{3(r^2-x^2)rx}{r^6}v + \frac{(r^2-x^2)x + 2x(r^3-x^2)}{r^4}\frac{\partial v}{\partial r} + \frac{x^3}{r^3}\frac{\partial^2 v}{\partial r^2},\\ =& -\frac{3(r^2-x^2)x}{r^5}v + \frac{3(r^2-x^2)x}{r^4}\frac{\partial v}{\partial r} + \frac{x^3}{r^3}\frac{\partial^2 v}{\partial r^2},\end{aligned} \tag{540}$$

and

$$\begin{aligned}\frac{\partial^2 v_x}{\partial y^2} &= x\frac{\partial}{\partial y}(\frac{y}{r^3}v + \frac{y}{r^2}\frac{\partial v}{\partial r}),\\ &= x\left[-\frac{r^3 - y3y^2\frac{y}{r}}{r^6}v - \frac{y}{r^3}\frac{\partial v}{\partial r}\frac{y}{r} + \frac{r^2 - y2r\frac{y}{r}}{r^4}\frac{\partial v}{\partial r} + \frac{y}{r^2}\frac{\partial^2 v}{\partial r^2}\right],\\ &= x\left[-\frac{r^2 - 3y^2}{r^5} + \frac{r^2 - 3y^2}{r^4}\frac{\partial v}{\partial r} + \frac{y^2}{r^3}\frac{\partial^2 v}{\partial r^2}\right]. \end{aligned} \tag{541}$$

This leads to

$$\begin{aligned}\nabla^2 v_x &= \frac{\partial^2 v_x}{\partial x^2} + \frac{\partial^2 v_x}{\partial y^2},\\ &= -\frac{x}{r^5}(3r^2 - 3x^2 + r^2 - 3y^2)v + \frac{x}{r^4}(3r^2 - 3x^2 + r^2 - 3y^2)\frac{\partial v}{\partial r} + x\frac{x^2 + y^2}{r^3}\frac{\partial^2 v}{\partial r^2},\\ &= \frac{x}{r}\left(-\frac{1}{r^2}v + \frac{1}{r}\frac{\partial v}{\partial r} + \frac{\partial^2 v}{\partial r^2}\right). \end{aligned} \tag{542}$$

Similarly it can be proven that

$$\nabla^2 v_y = \frac{y}{r}\left(-\frac{1}{r^2}v + \frac{1}{r}\frac{\partial v}{\partial r} + \frac{\partial^2 v}{\partial r^2}\right), \tag{543}$$

leading to

$$\nabla^2 \vec{v} = \frac{\vec{r}}{r}\left(-\frac{1}{r^2}v + \frac{1}{r}\frac{\partial v}{\partial r} + \frac{\partial^2 v}{\partial r^2}\right) = \frac{\vec{r}}{r}\frac{\partial}{\partial r}\left(\frac{1}{r}\frac{\partial}{\partial r}(rv)\right). \tag{544}$$

- $\nabla^2 T$

The equation is investigated along the x axis before generalizing with ∇. Hence

$$\begin{aligned}\frac{\partial T}{\partial x} &= \frac{\partial T}{\partial r}\frac{x}{r},\\ \frac{\partial^2 T}{\partial x^2} &= \frac{\partial}{\partial r}(\frac{x}{r})\frac{\partial T}{\partial r} + \frac{x}{r}\frac{\partial^2 T}{\partial r^2}\frac{x}{r},\\ &= \frac{r^2 - x^2}{r^3}\frac{\partial T}{\partial r} + \frac{x^2}{r^2}\frac{\partial^2 T}{\partial r^2},\end{aligned}$$

leads to

$$\begin{aligned}\nabla^2 T &= \frac{r^2 - x^2 + r^2 - y^2}{r^3}\frac{\partial T}{\partial r} + \frac{x^2 + y^2}{r^2}\frac{\partial^2 T}{\partial r^2},\\ &= \frac{1}{r}\frac{\partial T}{\partial r} + \frac{\partial^2 T}{\partial r^2},\\ &= \frac{1}{r}\frac{\partial}{\partial r}(r\frac{\partial T}{\partial r}). \end{aligned} \tag{545}$$

A.5.2 *Spherical Coordinates*

- $\vec{\nabla} p$

Knowing that

$$\vec{r} = x\vec{e_x} + y\vec{e_y} + z\vec{e_z}, \tag{546}$$

$$\text{and} \quad r = \sqrt{x^2 + y^2 + z^2}, \tag{547}$$

$$\text{then} \quad \frac{\partial r}{\partial x} = \frac{x}{r}. \tag{548}$$

This leads to

$$\frac{\partial p}{\partial x} = \frac{\partial p}{\partial r}\frac{\partial r}{\partial x} = \frac{\partial p}{\partial r}\frac{x}{r}, \tag{549}$$

and then

$$\vec{\nabla} p = \frac{\vec{r}}{r}\frac{\partial p}{\partial r}. \tag{550}$$

- $\vec{\nabla}.\vec{v}$

In a straightforward manner

$$\begin{aligned}
\vec{\nabla}.\vec{v} &= \vec{\nabla}.(\frac{\vec{r}}{r}v(r)), \\
&= \frac{\partial}{\partial x}(\frac{x}{r}v) + \frac{\partial}{\partial y}(\frac{y}{r}v) + \frac{\partial}{\partial z}(\frac{z}{r}v), \\
&= \frac{r - x\frac{x}{r}}{r^2}v + (\frac{x}{r})^2\frac{\partial v}{\partial r} + \frac{r - y\frac{y}{r}}{r^2}v + (\frac{y}{r})^2\frac{\partial v}{\partial r} + \frac{r - z\frac{z}{r}}{r^2}v + (\frac{z}{r})^2\frac{\partial v}{\partial r}, \\
&= \frac{r^2 - x^2 + r^2 - y^2 + r^2 - z^2}{r^3}v + \frac{x^2 + y^2 + z^2}{r^2}\frac{\partial v}{\partial r},
\end{aligned}$$

hence

$$\vec{\nabla}.\vec{v} = \frac{2}{r}v + \frac{\partial v}{\partial r}. \tag{551}$$

- $\vec{\nabla}(\vec{\nabla}.\vec{v})$

The equation is investigated along the x axis before generalizing with ∇. Hence

$$\begin{aligned}
\frac{\partial}{\partial x}(\vec{\nabla}.\vec{v}) &= \frac{\partial}{\partial x}(\frac{2}{r})v + \frac{2}{r}\frac{\partial v}{\partial x} + \frac{\partial^2 v}{\partial r^2}\frac{x}{r}, \\
&= \frac{\partial}{\partial r}(\frac{2}{r})\frac{x}{r}v + \frac{2}{r}\frac{\partial v}{\partial r}\frac{x}{r} + \frac{\partial^2 v}{\partial r^2}\frac{x}{r}, \\
&= \frac{-2x}{r^3}v + \frac{2x}{r^2}\frac{\partial v}{\partial r} + \frac{x}{r}\frac{\partial^2 v}{\partial r^2},
\end{aligned}$$

leads to

$$\vec{\nabla}(\vec{\nabla}.\vec{v}) = \frac{\vec{r}}{r}\left(-\frac{2}{r^2}v + \frac{2}{r}\frac{\partial v}{\partial r} + \frac{\partial^2 v}{\partial r^2}\right) = \frac{\vec{r}}{r}\frac{\partial}{\partial r}\left(\frac{1}{r^2}\frac{\partial}{\partial r}(r^2 v)\right). \tag{552}$$

- $\nabla^2\vec{v}$

$\nabla^2\vec{v}$ can be decomposed along the Cartesian coordinates as

$$\nabla^2\vec{v} = \nabla^2 v_x\vec{e_x} + \nabla^2 v_y\vec{e_y} + \nabla^2 v_z\vec{e_z}, \tag{553}$$

with $v_x = \frac{x}{r}v(r)$, $v_y = \frac{y}{r}v(r)$ and $v_z = \frac{z}{r}v(r)$. The equation is investigated along the x axis before generalizing with ∇. Using Eq.(532) we have for $k, l \in \{x, y, z\}$

$$\begin{cases} \frac{\partial v_k}{\partial k} = \frac{r^2-k^2}{r^3}v + \frac{k^2}{r^2}\frac{\partial v}{\partial r}, \\ \frac{\partial v_k}{\partial l} = k\frac{\partial}{\partial r}(\frac{1}{r})\frac{\partial r}{\partial l}v + k\frac{1}{r}\frac{\partial v}{\partial r}\frac{\partial r}{\partial l} = -\frac{kl}{r^3}v + \frac{kl}{r^2}\frac{\partial v}{\partial r}. \end{cases} \tag{554}$$

Using Eq.(554) we can now have the second derivatives

$$\begin{cases} \frac{\partial^2 v_k}{\partial k^2} = -\frac{3(r^2-k^2)k}{r^5}v + \frac{3(r^2-k^2)k}{r^4}\frac{\partial v}{\partial r} + \frac{k^3}{r^3}\frac{\partial^2 v}{\partial r^2}, \\ \frac{\partial^2 v_k}{\partial l^2} = k\left[-\frac{r^2-3l^2}{r^5} + \frac{r^2-3l^2}{r^4}\frac{\partial v}{\partial r} + \frac{l^2}{r^3}\frac{\partial^2 v}{\partial r^2}\right]. \end{cases} \tag{555}$$

This leads to

$$\begin{aligned} \nabla^2 v_x =& \frac{\partial^2 v_x}{\partial x^2} + \frac{\partial^2 v_x}{\partial y^2} + \frac{\partial^2 v_x}{\partial z^2}, \\ =& -\frac{x}{r^5}(3r^2 - 3x^2 + r^2 - 3y^2 + r^2 - z^2)v + \\ & \frac{x}{r^4}(3r^2 - 3x^2 + r^2 - 3y^2 + r^2 - 3z^2)\frac{\partial v}{\partial r} + \\ & x\frac{x^2+y^2+z^2}{r^3}\frac{\partial^2 v}{\partial r^2}, \\ =& \frac{x}{r}\left(-\frac{2}{r^2}v + \frac{2}{r}\frac{\partial v}{\partial r} + \frac{\partial^2 v}{\partial r^2}\right). \end{aligned} \tag{556}$$

Similarly it can be proven that

$$\nabla^2 v_k = \frac{k}{r}\left(-\frac{2}{r^2}v + \frac{2}{r}\frac{\partial v}{\partial r} + \frac{\partial^2 v}{\partial r^2}\right), \tag{557}$$

leading to

$$\nabla^2\vec{v} = \frac{\vec{r}}{r}\left(-\frac{2}{r^2}v + \frac{2}{r}\frac{\partial v}{\partial r} + \frac{\partial^2 v}{\partial r^2}\right) = \frac{\vec{r}}{r}\frac{\partial}{\partial r}\left(\frac{1}{r^2}\frac{\partial}{\partial r}(r^2 v)\right). \tag{558}$$

- $\nabla^2 T$

The equation is investigated along the x axis before generalizing with ∇. Hence

$$\begin{aligned}\frac{\partial T}{\partial x} &= \frac{\partial T}{\partial r}\frac{x}{r},\\ \frac{\partial^2 T}{\partial x^2} &= \frac{\partial}{\partial r}(\frac{x}{r})\frac{\partial T}{\partial r} + \frac{x}{r}\frac{\partial^2 T}{\partial r^2}\frac{x}{r},\\ &= \frac{r^2 - x^2}{r^3}\frac{\partial T}{\partial r} + \frac{x^2}{r^2}\frac{\partial^2 T}{\partial r^2},\end{aligned}$$

leads to

$$\begin{aligned}\nabla^2 T &= \frac{r^2 - x^2 + r^2 - y^2 + r^2 - z^2}{r^3}\frac{\partial T}{\partial r} + \frac{x^2 + y^2 + z^2}{r^2}\frac{\partial^2 T}{\partial r^2},\\ &= \frac{2}{r}\frac{\partial T}{\partial r} + \frac{\partial^2 T}{\partial r^2},\\ &= \frac{1}{r^2}\frac{\partial}{\partial r}(r^2\frac{\partial T}{\partial r}).\end{aligned} \tag{559}$$

A.6 NON HOMOGENEOUS SECOND ORDER DIFFERENTIAL EQUATION

Considering a non homogeneous second order differential equation

$$af''(x) + bf'(x) + cf(x) = g(x), \tag{560}$$

with a, b, c constants and f, g functions. Assuming that the solution to the homogeneous equation associated to Eq.(560) can be written

$$f(x) = C_1 f_1(x) + C_2 f_2(x), \tag{561}$$

with C_i constants and f_i known functions.

The particular solution of equation Eq.(560) is looked for of the form

$$f(x) = C_1(x) f_1(x) + C_2(x) f_2(x), \tag{562}$$

with C_i now unknown functions. By differentiating Eq.(562) we have

$$\begin{aligned}af'' + bf' + cf =& a(C_1'' f_1 + 2C_1' f_1' + C_1 f_1'' + C_2'' f_2 + 2C_2' f_2' + C_2 f_2'') +\\ & b(C_1' f_1 + C_1 f_1' + C_2' f_2 + C_2 f_2') +\\ & c(C_1 f1 + C_2 f_2),\end{aligned}$$

and using Eq.(561)

$$a\left(\frac{d}{dx}(C_1' f_1 + C_2' f_2) + (C_1' f_1' + C_2' f_2')\right) + b(C_1' f_1 + C_2' f_2) = g. \tag{563}$$

Since we are looking for only one solution to this equation with two unknown we can choose to add a reasonable condition on the functions C_i. Choosing that the first derivative of C_i are also a solution to the homogeneous equation, the final system of equation now becomes

$$\begin{cases} C_1' f_1 + C_2' f_2 = 0 \\ C_1' f_1' + C_2' f_2' = \frac{g}{a}. \end{cases} \tag{564}$$

Knowing that f_i form a base for all the solutions of the homogeneous equation associated to Eq.(560), the Wronskian

$$\begin{vmatrix} f_1 & f_2 \\ f_1' & f_2' \end{vmatrix} \neq 0, \tag{565}$$

and so the system of equations Eq.(564) only admits one solution for C_1 and C_2 which, with Eq.(562), are a particular solution of equation Eq.(560).

B

MODIFIED LITERATURE MODELS

B.1 HU AND YIN MODIFIED MODELS

In this section, the modified pressure equations of the models of Hu *et al.* of 2010 [81], 2012 [83], 2014 [84] and Yin *et al.* 2017 [85] are derived. In those models the energy input is provided only on the surface of the thermophone. This was justified for the comparison with Shinoda et al [32] for plane waves but does not hold in most geometry. In the models created in this thesis the input source is distributed through the whole volume and not only on its surface. Hence for comparison the models cited above are then modified to reflect those changes. This means that there is no added term in the continuity of heat flux at the surface of the thermophone and that a term S_s is added in the temperature equation in the solid. More specifically

$$S_s = S\frac{\alpha_s}{i\omega} = \frac{Q_0}{\kappa_s}\frac{\alpha_s}{i\omega} = \frac{Q_0}{i\omega\rho_s C_{p,s}}. \tag{566}$$

B.1.1 *Hu et al. 2010*

We here modified Hu *et al.* model from 2010 for planar waves [81]. The investigated parameters in Eqs.(3a) to (3c) are rewritten

$$p_g = d_t(A_g e^{\sigma_g x} + B_g e^{-\sigma_s x}) + d_a(C_g e^{ik_g x} + D_g e^{-ik_g x}), \tag{567}$$
$$T_g = A_g e^{\sigma_g x} + B_g e^{-\sigma_s x} + C_g e^{ik_g x} + D_g e^{-ik_g x}, \tag{568}$$
$$T_s = A_s e^{\sigma_s x} + B_s e^{-\sigma_s x} + S_s, \tag{569}$$
$$T_b = A_b e^{\sigma_b x} + B_b e^{-\sigma_b x}. \tag{570}$$

The boundary condition in Eq.(5a) to (5e) (continuity of parameters and solid surface) are also re written as

$$T_b = T_s, \qquad x = -L_s \tag{571}$$
$$\kappa_b\frac{\partial T_b}{\partial x} = \kappa_s\frac{\partial T_s}{\partial x}, \qquad x = -L_s \tag{572}$$
$$T_s = T_g, \qquad x = 0 \tag{573}$$
$$\kappa_s\frac{\partial T_s}{\partial x} = \kappa_g\frac{\partial T_g}{\partial x}, \qquad x = 0 \tag{574}$$
$$\frac{\partial p_g}{\partial x} = 0. \qquad x = 0 \tag{575}$$

Additionally, the non reflection conditions lead to $A_g = C_g = B_b = 0$. Equation (571) becomes

$$A_b e^{\sigma_b L_s} = A_s e^{\sigma_s x} + B_s e^{-\sigma_s x} + S_s. \tag{576}$$

Injected in Eq.(572) we have

$$\begin{aligned}
&\kappa_b\sigma_b A_b e^{\sigma_b L_s} = \kappa_s\sigma_s A_s e^{-\sigma_s L_s} - \kappa_s\sigma_s B_s e^{\sigma_s L_s},\\
&\kappa_b\sigma_b (A_s e^{\sigma_s L_s} + B_s e^{\sigma_s L_s} + S_s) = \kappa_s\sigma_s A_s e^{-\sigma_s L_s} - \kappa_s\sigma_s B_s e^{\sigma_s L_s},\\
&A_s e^{-\sigma_s L_s}(\kappa_b\sigma_b - \kappa_s\sigma_s) = B_s e^{\sigma_s L_s}(-\kappa_s\sigma_s - \kappa_b\sigma_b) - S_s\kappa_b\sigma_b,\\
&A_s = B_s e^{2\sigma_s L_s}\frac{\kappa_s\sigma_s + \kappa_b\sigma_b}{\kappa_s\sigma_s - \kappa_b\sigma_b} + e^{\sigma_s L_s} S_s \frac{\kappa_b\sigma_b}{\kappa_s\sigma_s - \kappa_b\sigma_b}.
\end{aligned} \tag{577}$$

Similarly Eq.(575) gives

$$\begin{aligned}
&-d_t\sigma_g B_g - d_a i k_g D_g = 0,\\
&B_g = -\frac{d_a}{d_t}\frac{ik_g}{\sigma_g} D_g.
\end{aligned} \tag{578}$$

Equations (573) and (574) are written

$$A_s + B_s + S_s = B_g + D_g, \tag{579}$$

and

$$\kappa_s\sigma_s A_s - \kappa_s\sigma_s B_s = -\kappa_g\sigma_g B_g - ik_g\kappa_g D_g. \tag{580}$$

We can then rewrite Eqs.(580) and (579) respectively as

$$\left(e^{2\sigma_s L_s}\frac{\kappa_s\sigma_s + \kappa_b\sigma_b}{\kappa_s\sigma_s - \kappa_b\sigma_b} + 1\right) B_s + S_s\left(e^{\sigma_s L_s}\frac{\kappa_b\sigma_b}{\kappa_s\sigma_s - \kappa_b\sigma_b} + 1\right) = \frac{d_t\sigma_g - i d_a k_g}{d_t\sigma_g} D_g, \tag{581}$$

and

$$\kappa_s\sigma_s\left(e^{2\sigma_s L_s}\frac{\kappa_s\sigma_s + \kappa_b\sigma_b}{\kappa_s\sigma_s - \kappa_b\sigma_b} - 1\right) B_s + e^{\sigma_s L_s} S_s \frac{\kappa_s\sigma_s\kappa_b\sigma_b}{\kappa_s\sigma_s - \kappa_b\sigma_b} = ik_g\kappa_g\frac{d_a - d_t}{d_t} D_g. \tag{582}$$

This leads to

$$\begin{aligned}
B_s =& \frac{d_t\sigma_g - i d_a k_g}{d_t\sigma_g}\frac{\kappa_s\sigma_s - \kappa_b\sigma_b}{e^{2\sigma_s L_s}(\kappa_s\sigma_s + \kappa_b\sigma_b) + \kappa_s\sigma_s - \kappa_b\sigma_b} D_g\\
&- \left(1 + \frac{e^{\sigma_s L_s}\kappa_b\sigma_b}{\kappa_s\sigma_s - \kappa_b\sigma_b}\right)\frac{\kappa_s\sigma_s - \kappa_b\sigma_b}{e^{2\sigma_s L_s}(\kappa_s\sigma_s + \kappa_b\sigma_b) + \kappa_s\sigma_s - \kappa_b\sigma_b} S_s,\\
B_s =& \frac{d_t\sigma_g - i d_a k_g}{d_t\sigma_g}\frac{\kappa_s\sigma_s - \kappa_b\sigma_b}{e^{2\sigma_s L_s}(\kappa_s\sigma_s + \kappa_b\sigma_b) + \kappa_s\sigma_s - \kappa_b\sigma_b} D_g\\
&- \frac{\kappa_s\sigma_s - \kappa_b\sigma_b + e^{\sigma_s L_s}\kappa_b\sigma_b}{e^{2\sigma_s L_s}(\kappa_s\sigma_s + \kappa_b\sigma_b) + \kappa_s\sigma_s - \kappa_b\sigma_b} S_s.
\end{aligned} \tag{583}$$

Finally

$$\begin{aligned}
&\kappa_s\sigma_s\frac{e^{2\sigma_s L_s}(\kappa_s\sigma_s+\kappa_b\sigma_b)-\kappa_s\sigma_s+\kappa_b\sigma_b}{\kappa_s\sigma_s-\kappa_b\sigma_b}\\
&\times\left(\frac{d_t\sigma_g-ik_g d_a}{d_t\sigma_g}\frac{\kappa_s\sigma_s-\kappa_b\sigma_b}{e^{2\sigma_s L_s}(\kappa_s\sigma_s+\kappa_b\sigma_b)+\kappa_s\sigma_s-\kappa_b\sigma_s}D_g\right.\\
&\left.-\frac{\kappa_s\sigma_s-\kappa_b\sigma_b+e^{\sigma_s L_s}\kappa_b\sigma_b}{e^{2\sigma_s L_s}(\kappa_s\sigma_s+\kappa_b\sigma_b)+\kappa_s\sigma_s-\kappa_b\sigma_b}S_s\right)\\
&+\frac{e^{\sigma_s L_s}\kappa_s\sigma_s\kappa_b\sigma_b}{\kappa_s\sigma_s-\kappa_b\sigma_b}S_s=ik_g\kappa_g\frac{d_a-d_t}{d_t}D_g, \qquad (584)\\
&\left(\kappa_s\sigma_s\frac{e^{2\sigma_s L_s}(\kappa_s\sigma_s+\kappa_b\sigma_b)-\kappa_s\sigma_s+\kappa_b\sigma_b}{e^{2\sigma_s L_s}(\kappa_s\sigma_s+\kappa_b\sigma_b)+\kappa_s\sigma_s-\kappa_b\sigma_b}\frac{d_t\sigma_g-ik_g d_a}{d_t\sigma_g}-ik_g\kappa_g\sigma_g\frac{d_a-d_t}{d_t\sigma_g}\right)D_g\\
&=S_s\left(-\frac{e^{\sigma_s L_s}\kappa_s\sigma_s\kappa_b\sigma_b}{\kappa_s\sigma_s-\kappa_b\sigma_b}\right.\\
&\left.+\kappa_s\sigma_s\frac{e^{2\sigma_s L_s}(\kappa_s\sigma_s+\kappa_b\sigma_b)-\kappa_s\sigma_s+\kappa_b\sigma_b}{e^{2\sigma_s L_s}(\kappa_s\sigma_s+\kappa_b\sigma_b)+\kappa_s\sigma_s-\kappa_b\sigma_b}\frac{\kappa_s\sigma_s-\kappa_b\sigma_b+e^{\sigma_s L_s}\kappa_b\sigma_b}{\kappa_s\sigma_s-\kappa_b\sigma_b}\right), \qquad (585)\\
&\left(\frac{\kappa_s\sigma_s M}{d_t\sigma_g}(d_t\sigma_g-ik_g d_a)-\frac{ik_g\kappa_g\sigma_g(d_a-d_t)}{d_t\sigma_g}\right)D_g\\
&=S_s\left(-\frac{e^{\sigma_s L_s}\kappa_s\sigma_s\kappa_b\sigma_b}{\kappa_s\sigma_s-\kappa_b\sigma_b}+\frac{\kappa_s\sigma_s M}{\kappa_s\sigma_s-\kappa_b\sigma_b}(\kappa_s\sigma_s-\kappa_b\sigma_b+e^{\sigma_s L_s}\kappa_b\sigma_b)\right), \qquad (586)
\end{aligned}$$

and

$$\begin{aligned}
D_g=&S_s\frac{d_t\sigma_g(-e^{\sigma_s L_s}\kappa_b\sigma_b+M(\kappa_s\sigma_s-\kappa_b\sigma_b+e^{\sigma_s L_s}\kappa_b\sigma_b))}{M\kappa_s\sigma_s(d_t\sigma_g-ik_g d_a)-ik_g\kappa_g\sigma_g(d_a-d_t)}\frac{\kappa_s\sigma_s}{\kappa_s\sigma_s-\kappa_b\sigma_b},\\
D_g=&S_s\frac{d_t\sigma_g(e^{\sigma_s L_s}\kappa_b\sigma_b(M-1)+M(\kappa_s\sigma_s-\kappa_b\sigma_b))}{M\kappa_s\sigma_s(d_t\sigma_g-ik_g d_a)-ik_g\kappa_g\sigma_g(d_a-d_t)}\frac{\kappa_s\sigma_s}{\kappa_s\sigma_s-\kappa_b\sigma_b},\\
D_g=&S_s\frac{-d_t\sigma_g(e^{\sigma_s L_s}\kappa_b\sigma_b(M-1)+M(\kappa_s\sigma_s-\kappa_b\sigma_b))}{ik_g d_a(M\kappa_s\sigma_s+\kappa_g\sigma_g)-d_t\sigma_g(M\kappa_s\sigma_s+ik_g\kappa_g)}\frac{\kappa_s\sigma_s}{\kappa_s\sigma_s-\kappa_b\sigma_b}. \qquad (587)
\end{aligned}$$

We are now able to rewrite the pressure for plane waves radiation, in a similar fashion as Eq.(6a)

$$\begin{aligned}
p_g=&S_s\frac{\kappa_s\sigma_s}{\kappa_s\sigma_s-\kappa_b\sigma_b}(e^{\sigma_s L_s}\kappa_b\sigma_b(M-1)+M(\kappa_s\sigma_s-\kappa_b\sigma_b))\\
&\times\frac{d_a d_t ik_g}{ik_g d_a(M\kappa_s\sigma_s+\kappa_g\sigma_g)-d_t\sigma_g(M\kappa_s\sigma_s+ik_g\kappa_g)}(e^{-\sigma_g x}-\frac{\sigma_g}{ik_g}e^{-ik_g x}),\\
=&p_{g,surface}S_s\frac{\kappa_s\sigma_s}{\kappa_s\sigma_s-\kappa_b\sigma_b}(e^{\sigma_s L_s}\kappa_b\sigma_b(M-1)+M(\kappa_s\sigma_s-\kappa_b\sigma_b)). \qquad (588)
\end{aligned}$$

B.1.2 *Hu 2012*

We here modified Hu *et al.* model from 2012 for spherical waves [83]. Using the notation $p_i^* = rp_i$ and $T_i^* = rT_i$ as in the article, the investigated parameters Eq.(8a) to (8d) are rewritten as

$$p_g^* = d_t(A_g e^{\sigma_g r} + B_g e^{-\sigma_s r}) + d_a(C_g e^{k_g r} + D_g e^{-k_g r}), \tag{589}$$
$$T_g^* = A_g e^{\sigma_g r} + B_g e^{-\sigma_s r} + C_g e^{k_g r} + D_g e^{-k_g r}, \tag{590}$$
$$T_s^* = A_s e^{\sigma_s r} + B_s e^{-\sigma_s r} + rS_s, \tag{591}$$
$$T_b^* = A_b e^{\sigma_b r} + B_b e^{-\sigma_b r}. \tag{592}$$

The boundary condition in Eqs.(6a) to (6h) are now written as

$$\frac{dp_g^*}{dr} - \frac{p_g^*}{r} = 0, \qquad r = R_s \tag{593}$$
$$\kappa_s\left(\frac{dT_s^*}{dr} - \frac{T_s^*}{r}\right) = \kappa_g\left(\frac{dT_g^*}{dr} - \frac{T_g^*}{r}\right), \qquad r = R_s \tag{594}$$
$$T_s^* = T_g^*, \qquad r = R_s \tag{595}$$
$$\kappa_s\left(\frac{dT_s^*}{dr} - \frac{T_s^*}{r}\right) = \kappa_b\left(\frac{dT_b^*}{dr} - \frac{T_b^*}{r}\right), \qquad r = R_b \tag{596}$$
$$T_s^* = T_b^*, \qquad r = R_b \tag{597}$$
$$\frac{dT_b^*}{dr} - \frac{T_b^*}{r} = 0, \qquad r = 0 \tag{598}$$
$$T_g^* \to 0, \qquad r \to \infty \tag{599}$$
$$p_g^* \to 0. \qquad r \to \infty \tag{600}$$

The non reflection condition in Eqs.(599) and (600) gives $A_g = C_g = 0$ and the to avoid discontinuity at $r = 0$, Eq.(598) gives $A_b = -B_b$. Equation (593) is written

$$\begin{aligned} &d_t B_g e^{-\sigma_g R_s}\left(-\frac{1}{R_s} - \sigma_g\right) + d_a D_g e^{-k_g R_s}\left(-\frac{1}{R_s} - k_g\right) = 0, \\ &B_g = -\frac{d_a}{d_t} e^{R_s(\sigma_s - k_g)} \frac{\frac{1}{R_s} + k_g}{\frac{1}{R_s} + \sigma_g} D_g, \\ &B_g = -\frac{d_a}{d_t} e^{R_s(\sigma_g - k_g)} \frac{k_g^+}{\sigma_g^+} D_g. \end{aligned} \tag{601}$$

It is then used in Eq.(597) as

$$\begin{aligned} &A_s e^{\sigma_s R_b} + B_s e^{-\sigma_s R_b} + S_s R_b = A_b(e^{\sigma_b R_b} - e^{-\sigma_b R_b}), \\ &A_b = \frac{1}{e^{\sigma_b R_b} - e^{-\sigma_b R_b}}(A_s e^{\sigma_s R_b} + B_s e^{-\sigma_s R_b} + S_s R_b). \end{aligned} \tag{602}$$

Equation (596), the right hand side term (RHS) is

$$\begin{aligned}
\text{RHS} =& \kappa_b(e^{\sigma_b R_b}(\sigma_b - \frac{1}{R_b}) + e^{-\sigma_b R_b}(\sigma_b + \frac{1}{R_b}))A_b,\\
=& \kappa_b(e^{\sigma_b R_b}(\sigma_b - \frac{1}{R_b}) + e^{-\sigma_b R_b}(\sigma_b + \frac{1}{R_b}))\frac{A_s e^{\sigma_s R_b} + B_s e^{-\sigma_s R_b} + S_s R_b}{e^{\sigma_s R_b} - e^{-\sigma_b R_b}},\\
=& \kappa_b(\sigma_b \frac{e^{\sigma_b R_b} + e^{-\sigma_b R_b}}{e^{\sigma_b R_b} - e^{-\sigma_b R_b}} - \frac{1}{R_b})(A_s e^{\sigma_s R_b} + B_s e^{-\sigma_s R_b} + S_s R_b),\\
=& \kappa_b \sigma_{b*}^-(A_s e^{\sigma_s R_b} + B_s e^{-\sigma_s R_b} + S_s R_b),
\end{aligned}$$

and so

$$\begin{aligned}
&\kappa_s(A_s e^{\sigma_s R_b}(\sigma_s - \frac{1}{R_b}) + B_s e^{-\sigma_s R_b}(-\sigma_s - \frac{1}{R_b})) = \kappa_b \sigma_{b*}^-(A_s e^{\sigma_s R_b} + B_s e^{-\sigma_s R_b} + S_s R_b),\\
&\kappa_s(A_s e^{\sigma_s R_b}\sigma_s^- - B_s e^{-\sigma_s R_b}\sigma_s^+) = \kappa_b \sigma_{b*}^-(A_s e^{\sigma_s R_b} + B_s e^{-\sigma_s R_b} + S_s R_b),\\
&A_s e^{\sigma_s R_b}(\kappa_s \sigma_s^- - \kappa_b \sigma_{b*}^-) = B_s e^{-\sigma_s R_b}(\kappa_s \sigma_s^+ + \kappa_b \sigma_{b*}^-) + S_s R_b \kappa_b \sigma_{b*}^-,\\
&A_s = B_s e^{-2\sigma_s R_b}\frac{\kappa_s \sigma_s^+ + \kappa_b \sigma_{b*}^-}{\kappa_s \sigma_s^+ - \kappa_b \sigma_{b*}^-} + S_s \frac{R_b \kappa_b \sigma_{b*}^-}{\kappa_s \sigma_s^+ - \kappa_b \sigma_{b*}^-} e^{-\sigma_s R_b}. \qquad (603)
\end{aligned}$$

This leads in Eq.(595) to

$$\begin{aligned}
D_g(e^{-k_g R_s} - e^{-k_g R_s}\frac{d_a}{d_t}\frac{k_g^+}{\sigma_g^+}) &= A_s e^{\sigma_s R_s} + B_s e^{-\sigma_s R_s} + R_s S_s,\\
D_g e^{-k_g R_s}(1 - \frac{d_a}{d_t}\frac{k_g^+}{\sigma_g^+}) &= B_s(e^{-\sigma_s R_s} + e^{\sigma_s(R_s - 2R_b)}\frac{\kappa_s \sigma_s^+ + \kappa_b \sigma_{b*}^-}{\kappa_s \sigma_s^- - \kappa_b \sigma_{b*}^-})\\
&\quad + S_s(R_s + \frac{R_b \kappa_b \sigma_{s*}^-}{\kappa_s \sigma_s^- - \kappa_b \sigma_{b*}^-} e^{\sigma_s(R_s - R_b)}).
\end{aligned} \qquad (604)$$

Lastly the terms of Eq.(594) are now

$$\begin{aligned}
\text{LHS} =& \kappa_g(B_g(-\sigma_g - \frac{1}{R_s})e^{-\sigma_g R_s} + D_g(-k_g - \frac{1}{R_s})e^{-k_g R_s}),\\
=& D_g e^{-k_g R_s}(\sigma_g^+ \frac{d_a}{d_t}\frac{k_g^+}{\sigma_g^+} - k_g^+)\kappa_g,
\end{aligned} \qquad (605)$$

and

$$\begin{aligned}
\text{RHS} =& \kappa_s(A_s(\sigma_s - \frac{1}{R_s})e^{\sigma_s R_s} + B_s(-\sigma_s - \frac{1}{R_s})e^{-\sigma_s R_s}),\\
=& B_s(\kappa_s \sigma_{ss}^- e^{\sigma_s(R_s - 2R_b)}\frac{X}{-Y} - \kappa_s \sigma_{ss}^+ e^{-\sigma_s R s})\\
&+ S_s\left(\frac{R_b \kappa_b \sigma_{b*}^-}{\kappa_b \sigma_s^- - \kappa_b \sigma_{b*}^-}\kappa_s \sigma_{ss}^- e^{\sigma_s(R_s - R_b)}\right),\\
=& D_g e^{-k_g R_s}(1 - \frac{d_a}{d_t}\frac{k_g^+}{\sigma_g^+})\kappa_s \sigma_{s*}^- - S^*,
\end{aligned} \qquad (606)$$

with $X = \kappa_s\sigma_s^+ + \kappa_b\sigma_{b*}^-$ and $-Y = \kappa_s\sigma_s^- - \kappa_b\sigma_{b*}^-$ as well as

$$\begin{aligned}
&\frac{e^{-\sigma_s R_s}(\kappa_s\sigma_{ss}^- e^{2\sigma_s\Delta R}\frac{X}{-Y} - \kappa_s\sigma_{ss}^+)}{e^{-\sigma_s R_s}(1 + e^{2\sigma_s\Delta_R}\frac{X}{-Y})},\\
=&\frac{e^{\sigma_s\Delta R}(\kappa_s(\sigma_s - \frac{1}{R_s})e^{\sigma_s\Delta R}X + \kappa_s(\sigma_s + \frac{1}{R_s})e^{-\sigma_s\Delta R}Y)}{e^{\sigma_s\Delta R}(Xe^{\sigma_s\Delta R} - Ye^{-\sigma_s\Delta R})},\\
=&\kappa_s\left(\frac{\sigma_s(Xe^{\sigma_s\Delta R} + Ye^{-\sigma_s\Delta R})}{Xe^{\sigma_s\Delta R} - Ye^{-\sigma_s\Delta R}} - \frac{1}{R_s}\right),\\
=&\kappa_s(\sigma_s M - \frac{1}{R_s}),\\
=&\kappa_s\sigma_{s*}^-,
\end{aligned} \tag{607}$$

and

$$\begin{aligned}
-S^* =&S_s\left(-\frac{R_b\kappa_b\sigma_{b*}^-}{\kappa_b\sigma_{b*}^- - \kappa_s\sigma_s^-}e^{\sigma_s\Delta R}\kappa_s\sigma_{ss}^- - \kappa_s\sigma_{s*}^-\left(R_s - \frac{R_b\kappa_b\sigma_{b*}^-}{\kappa_b\sigma_{b*}^- - \kappa_s\sigma_s^-}e^{\sigma_s\Delta R}\right)\right),\\
=&S_s\left(-R_s\kappa_s\sigma_{s*}^- - \kappa_s e^{\sigma_s\Delta R}\frac{R_b\kappa_b\sigma_{b*}^-}{\kappa_b\sigma_{b*}^- - \kappa_s\sigma_s^-}(\sigma_{ss}^- - \sigma_{s*}^-)\right),\\
=&\kappa_s S_s\left(-R_s\sigma_{s*}^- - \frac{R_b\kappa_b\sigma_{b*}^-}{\kappa_b\sigma_{b*}^- - \kappa_s\sigma_s^-}\sigma_s(1-M)e^{\sigma_s\Delta R}\right).
\end{aligned} \tag{608}$$

We then have

$$\begin{aligned}
\frac{-S^*}{D_g} =&\kappa_g e^{-k_g R_s}(\frac{d_a}{d_t}\frac{k_g^+}{\sigma_g^+}\sigma_g^+ - k_g^+) - \kappa_s\sigma_{s*}^- e^{-k_g R_s}(1 - \frac{d_a}{d_t}\frac{k_g^+}{\sigma_g^+}),\\
=&e^{-k_g R_s}\left(\frac{\kappa_g d_a\sigma_g^+ k_g^+ - \kappa_g k_g^+ d_t\sigma_g^+ - \kappa_s\sigma_{s*}^- d_t\sigma_g^+ + \kappa_s\sigma_{s*}^- d_a k_g^+}{d_t\sigma_g^+}\right),\\
=&e^{-k_g R_s}\left(\frac{d_a k_g^+(\kappa_s\sigma_{s*}^- + \kappa_g\sigma_g^+) - d_t\sigma_g^+(\kappa_s\sigma_{s*}^- + \kappa_g k_g^+)}{d_t\sigma_g^+}\right),\\
=&e^{-k_g R_s}\left(\frac{Z}{d_t\sigma_g^+}\right).
\end{aligned} \tag{609}$$

We are now able to rewrite the pressure for spherical waves radiation, in a similar fashion as Eq.(10a)

$$\begin{aligned}
p_g = \frac{p_g^*}{r} =& B_g \frac{d_t}{r} e^{-\sigma_g r} + D_g \frac{d_a}{r} e^{-k_g r}, \\
=& \frac{D_g}{r} \left(-d_a \frac{k_g^+}{\sigma_g^+} e^{R_s(\sigma_g - k_g)} e^{-\sigma_g r} + d_a e^{-k_g r} \right), \\
=& \frac{-S^*}{r} \frac{d_a d_t \sigma_g^+}{Z} (-\frac{k_g^+}{\sigma_g^+} e^{-\sigma_g \Delta r} + e^{-k_g \Delta r}), \\
=& \frac{d_a d_t k_g^+}{Z} (e^{-\sigma_g \Delta r} - \frac{\sigma_g^+}{k_g^+} e^{-\sigma_g \Delta r}) \\
& \times \frac{\kappa_s S_s}{r} \left(R_s \sigma_{s*}^- + \frac{R_b \kappa_b \sigma_{b*}^-}{\kappa_b \sigma_{b*}^- - \kappa_s \sigma_s^-} \sigma_s (1 - M) e^{\sigma_s \Delta R} \right), \\
=& p_{g,surface}^* \frac{\kappa_s S_s}{r} \left(R_s \sigma_{s*}^- + \frac{R_b \kappa_b \sigma_{b*}^-}{\kappa_b \sigma_{b*}^- - \kappa_s \sigma_s^-} \sigma_s (1 - M) e^{\sigma_s \Delta R} \right).
\end{aligned} \tag{610}$$

B.1.3 *Hu 2014*

Hu *et al.* in 2014 simplified their 2012 spherical model by removing the substrate in the center of the sphere [84]. The resulting pressure equation could then be induced from the previous section but is here proven again to help the understanding. As in the article, the investigated parameters Eq.(4a) to (4c) are rewritten as

$$p_g = \frac{d_t}{r}(A_g e^{\sigma_g r} + B_g e^{-\sigma_s r}) + \frac{d_a}{r}(C_g e^{k_g r} + D_g e^{-k_g r}), \tag{611}$$

$$T_g = \frac{A_g}{r} e^{\sigma_g r} + \frac{B_g}{r} e^{-\sigma_s r} + \frac{C_g}{r} e^{k_g r} + \frac{D_g}{r} e^{-k_g r}, \tag{612}$$

$$T_s = \frac{A_s}{r} e^{\sigma_s r} + \frac{B_s}{r} e^{-\sigma_s r} + S_s. \tag{613}$$

The boundary conditions of Eq.(6a) to (6f) are now written as

$$\frac{dp_g}{dr} = 0, \qquad r = R_s \tag{614}$$

$$\kappa_s \frac{dT_s}{dr} = \kappa_g \frac{dT_g}{dr}, \qquad r = R_s \tag{615}$$

$$T_s = T_g, \qquad r = R_s \tag{616}$$

$$\frac{dT_s}{dr} = 0, \qquad r = 0 \tag{617}$$

$$T_g \to 0, \qquad r \to \infty \tag{618}$$

$$p_g \to 0. \qquad r \to \infty \tag{619}$$

The non reflection condition in Eqs.(618) and (619) gives $A_g = C_g = 0$ and to avoid discontinuity at $r = 0$, Eq.(617) gives $A_s = -B_s$. Equation (614) is written

$$\begin{aligned}
&B_g \frac{d_t}{R_s} e^{-\sigma_g R_s}(-\sigma_g - \frac{1}{R_s}) + D_g \frac{d_a}{R_s} e^{-k_g R_s}(-k_g - \frac{1}{R_s}) = 0,\\
&B_g = -\frac{d_a}{d_t}\frac{k_g^+}{\sigma_g^+} e^{-(k_g-\sigma_g)R_s} D_g.
\end{aligned} \tag{620}$$

Hence Eq.(616) gives

$$\begin{aligned}
&\frac{D_g}{R_s} e^{-k_g R_s}(1 - \frac{d_a}{d_t}\frac{k_g^+}{\sigma_g^+}) = \frac{A_s}{R_s}(e^{\sigma_s R_s} - e^{-\sigma_s R_s}) + S_s,\\
&A_s = D_g e^{-k_g R_s}\frac{1 - \frac{d_a}{d_t}\frac{k_g^+}{\sigma_g^+}}{e^{\sigma_s R_s} - e^{-\sigma_s R_s}} - S_s \frac{R_s}{e^{\sigma_s R_s} - e^{-\sigma_s R_s}}.
\end{aligned} \tag{621}$$

The terms of Eq.(615) are now

$$\begin{aligned}
\text{LHS} =& \kappa_s \frac{A_s}{R_s}((\sigma_s - \frac{1}{R_s})e^{\sigma_s R_s} + e^{-\sigma_s R_s}(\sigma_s + \frac{1}{R_s})),\\
=& \kappa_s \frac{A_s}{R_s}(\sigma_s(e^{\sigma_s R_s} + e^{-\sigma_s R_s}) - \frac{1}{R_s}(e^{\sigma_s R_s} - e^{-\sigma_s R_s})),\\
=& \kappa_s \frac{D_g}{R_s} e^{-k_g R_s}(1 - \frac{d_a}{d_t}\frac{k_g^+}{\sigma_g^+})\left(\sigma_s \frac{e^{\sigma_s R_s} + e^{-\sigma_s R_s}}{e^{\sigma_s R_s} - e^{-\sigma_s R_s}} - \frac{1}{R_s}\right)\\
&- S_s \kappa_s \left(\sigma_s \frac{e^{\sigma_s R_s} + e^{-\sigma_s R_s}}{e^{\sigma_s R_s} - e^{-\sigma_s R_s}} - \frac{1}{R_s}\right),\\
=& \kappa_s \frac{D_g}{R_s} e^{-k_g R_s}(1 - \frac{d_a}{d_t}\frac{k_g^+}{\sigma_g^+})\sigma_{s*}^- - S_s \kappa_s \sigma_{s*}^-,
\end{aligned} \tag{622}$$

and

$$\text{RHS} = \kappa_g \frac{D_g}{R_s} e^{-k_g R_s}((-k_g - \frac{1}{R_s}) + (\sigma_g + \frac{1}{R_s})\frac{d_a}{d_t}\frac{k_g^+}{\sigma_g^+}), \tag{623}$$

which leads to

$$\begin{aligned}
&\kappa_s \frac{D_g}{R_s} e^{-k_g R_s}(1 - \frac{d_a}{d_t}\frac{k_g^+}{\sigma_g^+})\sigma_{s*}^- - S_s \kappa_s \sigma_{s*}^- = \kappa_g \frac{D_g}{R_s} e^{-k_g R_s}(\sigma_g^+ \frac{d_a}{d_t}\frac{k_g^+}{\sigma_g^+} - k_g^+),\\
&D_g = \frac{S_s \kappa_s \sigma_{s*}^- d_t \sigma_g^+ R_s e^{k_g R_s}}{\sigma_{s*}^-(\kappa_s d_t \sigma_g^+ - \kappa_s d_a k_g^+) - \sigma_g^+ d_a k_g^+ \kappa_g + d_t \sigma_g^+ \kappa_g k_g^+},\\
&D_g = \frac{S_s \kappa_s \sigma_{s*}^- d_t \sigma_g^+ R_s e^{k_g R_s}}{-d_a k_g^+(\kappa_g \sigma_g^+ + \kappa_s \sigma_{s*}^-) + d_t \sigma_g^+(\kappa_g k_g^+ + \kappa_s \sigma_{s*}^-)},\\
&D_g = \frac{S_s \kappa_s \sigma_{s*}^- d_t \sigma_g^+}{-Z} R_s e^{k_g R_s}.
\end{aligned} \tag{624}$$

We are now able to rewrite the pressure for spherical waves radiation, in a similar fashion as Eq.(7) as

$$\begin{aligned}
p_g =& \left(\frac{d_a}{r}e^{-k_g r} - \frac{d_a}{r}e^{-(k_g-\sigma_s)R_s}\frac{k_g^+}{\sigma_g^+}e^{-\sigma_g r}\right)\frac{S_s\kappa_s\sigma_{s*}^- d_t\sigma_g^+}{-Z}R_s e^{k_g R_s},\\
=&\frac{R_s}{r}\frac{d_a d_t\sigma_g^+}{-Z}(e^{-k_g\Delta r} - \frac{k_g^+}{\sigma_g^+}e^{-\sigma_g\Delta r})S_s\kappa_s\sigma_{s*}^-,\\
=&\frac{R_s}{r}\frac{d_a d_t k_g^+}{Z}(e^{-\sigma_g\Delta r} - \frac{\sigma_g^+}{k_g^+}e^{-k_g\Delta r})S_s\kappa_s\sigma_{s*}^-,\\
=&p_{g,surface}S_s\kappa_s\sigma_{s*}^-. \qquad (625)
\end{aligned}$$

Notably, this is a similar equation as Eq.(610) with $M = 1$.

B.1.4 *Yin 2017*

Yin et Hu in 2017 have again modified their model for cylindrical waves. Here we once more adapt it for volumic input power and we consider for simplicity no substrate but just a thermophone in a cylindrical shape. The investigated parameters in Eqs.(5a,b,c) [85] are rewritten as

$$\begin{aligned}
p_g =& d_t B_g K_0(\sigma_g r) + d_a D_g K_0(k_g r), \qquad (626)\\
T_g =& B_g K_0(\sigma_g r) + D_g K_0(k_g r), \qquad (627)\\
T_s =& A_s J_0(\sigma_s r) + B_s Y_0(\sigma_s r) + S_s. \qquad (628)
\end{aligned}$$

Here the non reflection conditions leading to $A_g = C_g = 0$ have already been used. The other boundary conditions of Eq.(4a,b,c) and (4f) [85] are then

$$\begin{aligned}
\frac{dp_g}{dr} =& 0, && r = R_s \qquad (629)\\
\kappa_s\frac{dT_s}{dr} =& \kappa_g\frac{dT_g}{dr}, && r = R_s \qquad (630)\\
T_s =& T_g, && r = R_s \qquad (631)\\
\frac{dT_s}{dr} =& 0, && r = 0 \qquad (632)
\end{aligned}$$

with Eq.(632) leading to $B_s = 0$. Equation (629) is written as

$$\begin{aligned}
&- d_t B_g\sigma_g K_1(\sigma_g R_s) - d_a D_g k_g K_1(k_g R_s) = 0,\\
&B_g = -\frac{d_a}{d_t}\frac{k_g}{\sigma_g}\frac{K_1(k_g R_s)}{K_1(\sigma_s R_s)}D_g, \qquad (633)
\end{aligned}$$

leading in Eq.(631) to

$$A_s J_0(\sigma_s R_s) + S_s = D_g \left(K_0(k_g R_s) - \frac{d_a}{d_t} \frac{k_g}{\sigma_g} \frac{K_1(k_g R_s)}{K_1(\sigma_g R_s)} K_0(\sigma_g R_s) \right),$$
$$A_s = \frac{D_g}{J_0(\sigma_s R_s)} \left(K_0(k_g R_s) - \frac{d_a}{d_t} \frac{k_g}{\sigma_g} \frac{K_1(k_g R_s)}{K_1(\sigma_g R_s)} K_0(\sigma_g R_s) \right) - \frac{S_s}{J_0(\sigma_s R_s)}. \tag{634}$$

The terms of Eq.(630) become

$$\begin{aligned} \text{LHS} =& -\kappa_s A_s \sigma_s J_1(\sigma_s R_s), \\ =& -D_g \kappa_s \sigma_s M_0 \left(K_0(k_g R_s) - \frac{d_a}{d_t} \frac{k_g}{\sigma_g} \frac{K_1(k_g R_s)}{K_1(\sigma_g R_s)} K_0(\sigma_g R_s) \right) + \kappa_s \sigma_s S_s M_0, \end{aligned} \tag{635}$$

with $M_0 = \frac{J_1(\sigma_s R_s)}{J_0(\sigma_s R_s)}$, and

$$\begin{aligned} \text{RHS} =& -\kappa_g B_g \sigma_g K_1(\sigma_g R_s) - \kappa_g D_g K_1(k_g R_s), \\ =& \kappa_g D_g \left(-k_g K_1(k_g R_s) + \sigma_g K_1(\sigma_g R_s) \frac{d_a}{d_t} \frac{k_g}{\sigma_g} \frac{K_1(k_g R_s)}{K_1(\sigma_g R_s)} \right), \\ =& -\kappa_g k_g D_g K_1(k_g R_s)(1 - \frac{d_a}{d_t}). \end{aligned} \tag{636}$$

Hence

$$\frac{D_g}{S_s} = \frac{M_0 \kappa_s \sigma_s}{\kappa_s \sigma_s M_0 \left(K_0(k_g R_s) - \frac{d_a}{d_t} \frac{k_g}{\sigma_g} \frac{K_1(k_g R_s)}{K_1(\sigma_g R_s)} K_0(\sigma_g R_s) \right) - \kappa_g k_g D_g K_1(k_g R_s)(1 - \frac{d_a}{d_t})}. \tag{637}$$

We are now able to rewrite the pressure for cylindrical waves radiation without sustrate, in a similar fashion as Eq.(7b) as

$$\begin{aligned} p_g =& D_g \left(d_a K_0(k_g r) - d_t \frac{d_a}{d_t} \frac{k_g}{\sigma_g} \frac{K_1(k_g R_s)}{K_1(\sigma_g R_s)} K_0(\sigma_g r) \right), \\ =& \frac{S_s \kappa_s M_0 \sigma_s \left(d_a K_0(k_g r) - d_a \frac{k_g}{\sigma_g} \frac{K_1(k_g R_s)}{K_1(\sigma_g R_s)} K_0(\sigma_g r) \right)}{\kappa_s \sigma_s M_0 \left(K_0(k_g R_s) - \frac{d_a}{d_t} \frac{k_g}{\sigma_g} \frac{K_1(k_g R_s)}{K_1(\sigma_g R_s)} K_0(\sigma_g R_s) \right) - \kappa_g k_g D_g K_1(k_g R_s)(1 - \frac{d_a}{d_t})}, \\ =& \frac{S_s \kappa_s M_0 \sigma_s d_a d_t \left(\sigma_g K_1(\sigma_g R_s) K_0(k_g r) - k_g K_1(k_g R_s) K_0(\sigma_g r) \right)}{\left(\kappa_s M_0 \sigma_s \left(d_t \sigma_g K_1(\sigma_g R_s) K_0(k_g R_s) - d_a k_g K_1(k_g R_s) K_0(\sigma_g R_s) \right) + \right.} \\ & \left. + \kappa_g k_g \sigma_g K_1(k_g R_s) K_1(\sigma_g R_s)(d_a - d_t) \right), \\ =& \frac{S_s \kappa_s M_0 \sigma_s d_a d_t \left(k_g K_1(k_g R_s) K_0(\sigma_g r) - \sigma_g K_1(\sigma_g R_s) K_0(k_g r) \right)}{\left(d_a k_g K_1(k_g R_s) \left(\kappa_s M_0 \sigma_s K_0(\sigma_g R_s) - \kappa_g \sigma_g K_1(\sigma_g R_s) \right) + \right.} \\ & \left. - d_t \sigma_g K_1(\sigma_g R_s) \left(\kappa_s M_0 \sigma_s K_0(k_g R_s) - \kappa_g k_g K_1(k_g R_s) \right) \right), \\ =& p_{g,surface} S_s \kappa_s \sigma_s M_0. \end{aligned} \tag{638}$$

C

EXPERIMENTAL APPENDIX

C.1 SAMPLES' LIST

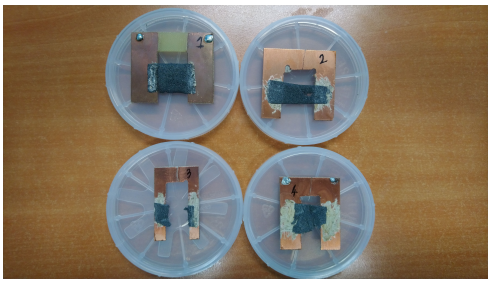

(a) Old 1 to 4

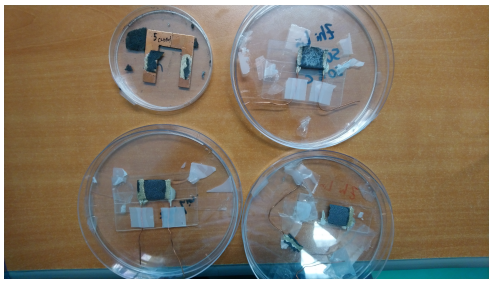

(b) Old 5 and Old Zhi Lin 1 to 3

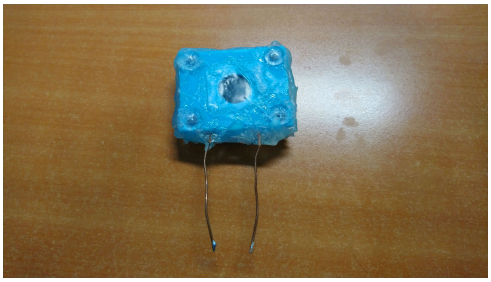

(c) Old Zhi Lin 4

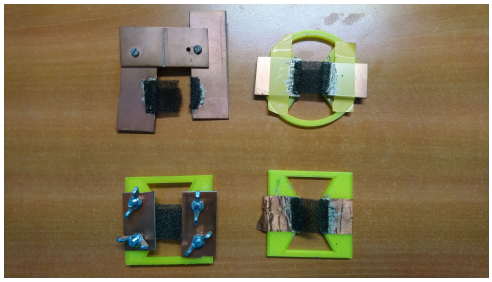

(d) Old test 1 to 4

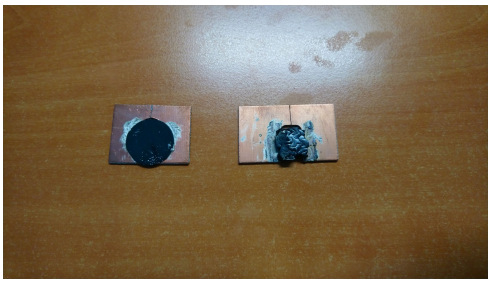

(e) Old Djamila 1 et 2

Figure 107: Old samples used during the first 6 months of the thesis

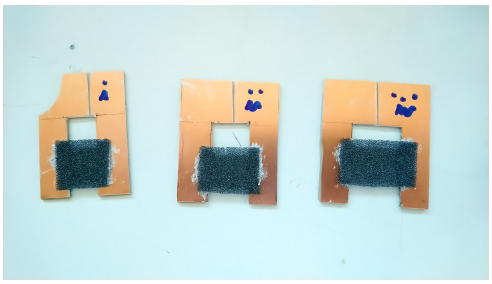

(a) I to III

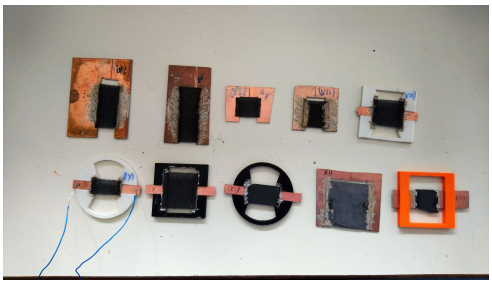

(b) IV to XIII

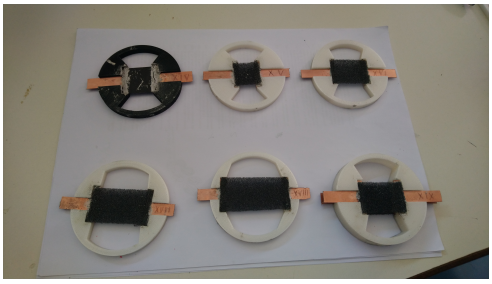

(c) XIV to XIX

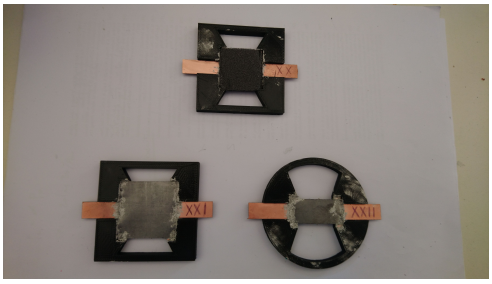

(d) XX to XXII

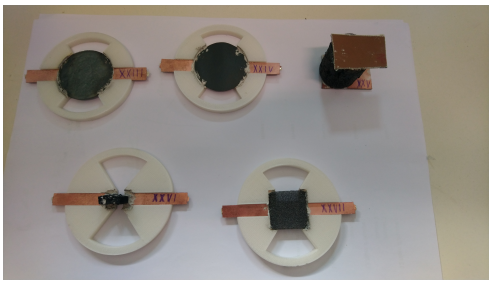

(e) XXIII to XXVII

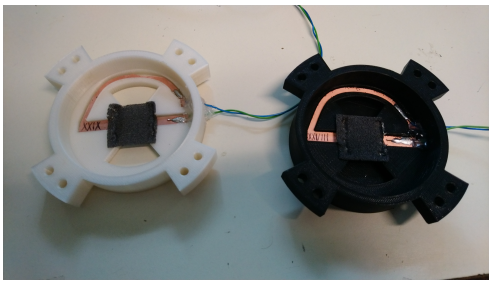

(f) XXVIII to XXIX

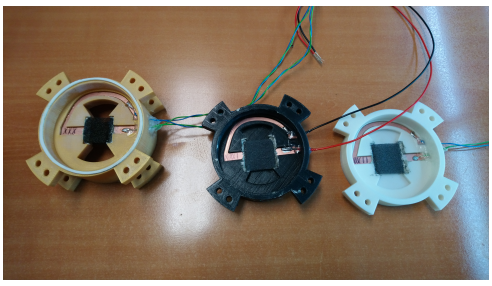

(g) XXX to XXXII

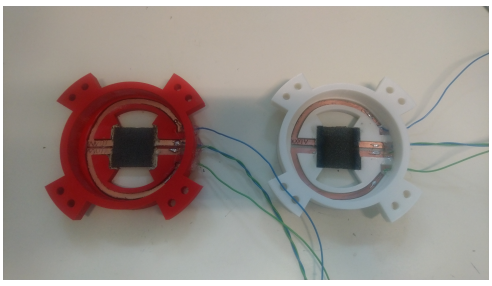

(h) XXXIII to XXXIV

Figure 108: All samples available at the IEMN

Sample Number	Sample type	Support type	Sample size (mm)
Old 1	Graphene foam CINTRA	Copper	30x20
Old 2	Graphene foam CINTRA	Copper	40x15
Old 3	Graphene foam CINTRA	Copper	25x15
Old 4	Graphene foam CINTRA	Copper	20x20
Old 5	25BN75C foam CINTRA	Copper	35x20
Zhi Lin 1	100C	Rod on glass	25x20
Zhi Lin 2	100C	Rod on glass	30x20
Zhi Lin 3	50BN50C	Rod on glass	25x20
Zhi Lin 4	Graphene foam CINTRA	Rod in plastic filling	25x20
Old Test 1	Vitreous carbon	Copper	35x25
Old Test 2	Vitreous carbon	Copper on plastic	25x25
Old Test 3	Vitreous carbon	Copper on plastic	30x25
Old Test 4	Vitreous carbon	Scotch Copper on plastic	25x25
Djamila 1	3D carbon structure	Copper	13x13
Djamila 2	Carbon sheet structure	Copper	$d = 20$
I	Vitreous carbon	Copper	25x25
II	Vitreous carbon	Copper	30x25
III	Vitreous carbon	Copper	40x25
IV	Vitreous carbon	Copper	25x50
V	Vitreous carbon	Copper	25x65
VI	Vitreous carbon	Copper	30x25
VII	Vitreous carbon	Copper	25x30
VIII	Vitreous carbon	Plastic: square	35x30
IX	Vitreous carbon	Plastic: circle	35x15
X	Vitreous carbon	Plastic: square	40x40
XI	Carbone foam 100ppi	Plastic: circle	40x20
XII	Flexible Graphite Sheet	Copper	50x50
XIII	Rigid Graphite Sheet	Plastic: square	25x25
tube (bonus)	Hollow Graphite tube	Crocodile clips	$d_{in} = 1.6$, $d_{out} = 3.2$, $h = 50$
XIV	Rigid Graphite Sheet	Plastic: circle	25x25
XV	Vitreous carbon	Plastic: circle	23x23
XVI	Vitreous carbon	Plastic: circle	35x25
XVII	Vitreous carbon	Plastic: circle	45x25
XVIII	Vitreous carbon	Plastic: circle	55x25
XIX	Vitreous carbon	Plastic: circle, double	35x25
XX	Carbon foam 110ppi	Plastic: square	30x30
XXI	Flexible Graphite Sheet	Plastic: square	35x35

XXII	Flexible Graphite Sheet	Plastic: circle	35x15
XXIII	Graphene sheet super paper	Plastic: circle	$d = 40$
XXIV	Graphene oxide sheet super paper	Plastic: circle	$d = 40$
XXV	Graphene aerogel	Copper	$h = 30$, $d = 30$
XXVI	Self Supporting Multiwalled CNT	Plastic: circle	15x5x12
XXVII	Graphene foam ACS	Plastic: circle	25x25
XXVIII	Graphene foam ACS	Simple Underwater design (backing)	25x25
XXIX	Graphene foam ACS	Simple Underwater design	25x25
XXX	Vitrous carbon	Simple Underwater design	25x25
XXXI	Graphene foam ACS	Simple Underwater design (backing)	30x30
XXXII	Graphene foam ACS	Simple Underwater (closer backing)	30x30
XXXIII	Graphene foam ACS	Simple Underwater, double wiring	30x30
XXXIV	Vitrous Carbon	Simple Underwater, double wiring	30x30

Sample Number	R (multimetre) Ohm	R (analyser) Ohm	R (recorded) Ohm
I	9.2	10	
II	11	11	
III	9.2	9.6	
IV	3.4	3.4	2.8
V	2.5	2.6	2.2
VI	6.5	6.3	
VII	3.6	3.6	3
VIII	6.3	6.9	4.3
IX	12,1 copper 14,5 wires	21	7.4
X	4.1	4(?)	
XI			2.3
XII	2	0.18	0.53
XIII	0.5	0.15	0.44
tube	unstable, from 20 to 1		0.5
XIV	0.2	0.16	0.45
XV	3.5		2.8
XVI	4.9	9.7	4.6 then 7.8
XVII	6.5	10.4	5.5
XVIII	8.7	12.4	7.3
XIX	6,8a 6b 3,4ab	10a 11b 5,2ab	3
XX	0.6	0.65	0.85
XXI	0.2	0.2	0.48
XXII	0.2	0.25	0.48
XXIII	28.4	60	5.7
XXIV	6,3M		
XXV	3,5k		
XXVI	0.8	0.77	1
XXVII	1.3	1050	1.5
XXVIII	5.2	5.3	3.5
XXIX	2.1	2.7	1.6
XXX	7,9a 8,3b 4ab	6a 7,3b 3,3,ab	
XXXI	2.5		2.1
XXXII	1.6	1.1	0.9
XXXIII	1,6 average (cf CR)	1,8 average (cf plot)	1.3
XXXIV	6 average (cf CR)	6 average (cf plot)	4.2

C.2 IEMN CHARACTERISATION

In this section experimental characterisation done at the IEMN of 3D-C samples provided by CINTRA during the first year of the PhD are presented. Those experiments are not displayed in the core of this thesis as the results did not provide satisfactory results. Furthermore, issues in the shipment of new samples did not allow us to repeat those experiments in a suitable way. Nonetheless, those characterisations are still presented here as they reflect some points of concerns regarding manipulation of 3D-C. They also contain insight on what could be done to improve those measurements.

C.2.1 *Density Measurements*

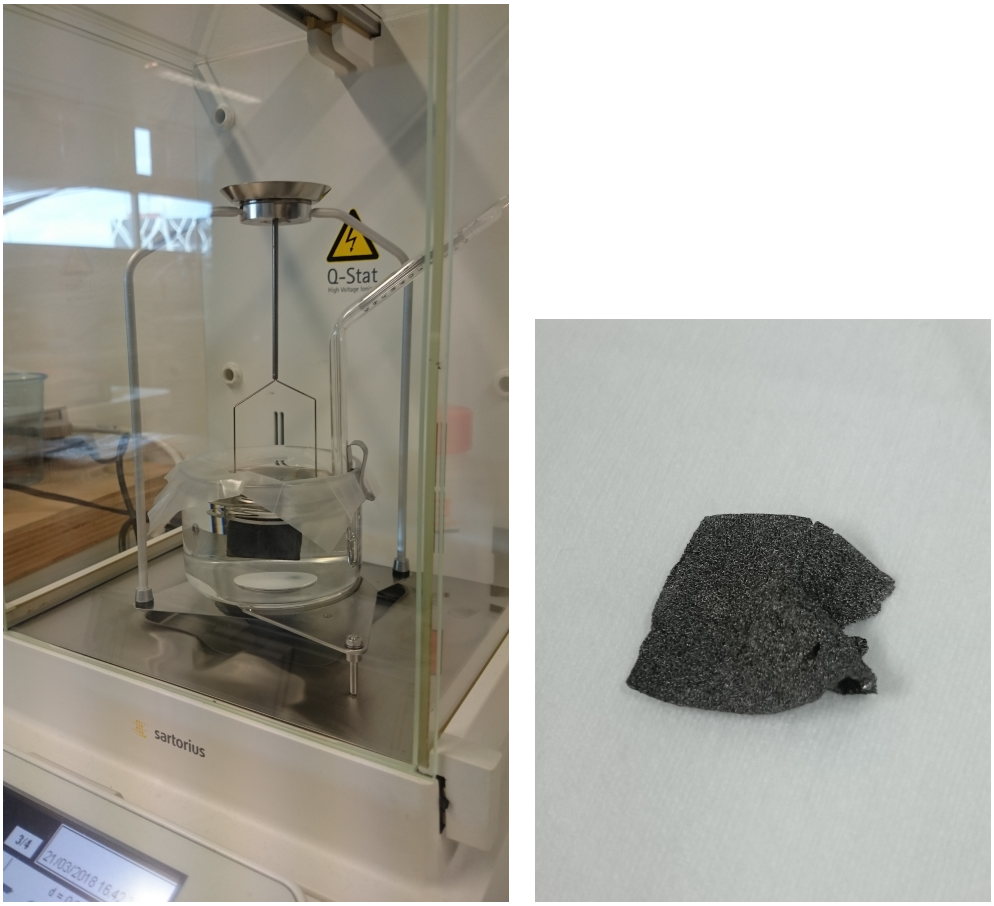

(a) (b)

Figure 109: Densimeter experimental setup: (a) 3D-C sample immersed for Archimede's force measurement; (b) shape of 3D-C after immersion in a liquid.

One of the main parameter of interest in all theoretical model is the density of the thermophone. As explained in Section 3.3 it is important to distinguish the global and specific density. The specific density is attributed to the material in which the branches of the foam are made, whereas the global density is attributed to the averaged density of the whole foam. If the density of the carbon and graphite is known from the literature and the global density could be easily deduced by averaging the volume of the foam as a parallelepiped, a densimeter seen in Fig.109a has been used in order to try and obtain a more accurate value.

The working principle is that a scale weight the sample in air and then immersed in a uniform liquid of known density. Using Archimede's law it is then possible to deduce the exact volume of the sample and then infer its density. The experiment has been performed in distilled water and in ethanol (lower density than water). In both cases the 3D-C sample started floating before slowly sinking. In Fig.109a 3D-C is actually seen to be in a vertical position as it is slowly going down. The hydrophobic behavior of 3D-C [122] is assumed to gradually give way to water that fills up the pores and eventually the hollow branches of the foam as well. This causes the sample to sink and prevents an accurate measure of weight. The global density measured by assuming parallelepiped shape was then used in future endeavours.

Additionally it is seen in Fig.109b that after a prolonged immersion 3D-C became twisted and more brittle. This is a similar behavior as observed by Aliev *et al.* in 2010 with CNT [122]. It lead him to consider enclosing the CNT for underwater radiation which is also the favored solution of this work.

C.2.2 *DSC Measurements*

In the course of this work a differential scanning calorimetry (DSC) instrument from the IEMN seen in Fig.110 was repaired and used to try and determine the specific heat of the carbon composing 3D-C foam samples. Samples had to be powdered and fed to the crucible seen in Fig.110b. A few grams were needed to have reliable results and the lightweight of 3D-C proved to be challenging. A fair number of samples were crushed to reach a decent load and even then the minimum weight was not reach. Nonetheless, after calibration of the DSC measurement were tried without success. After multiple attempts it was decided to use values from the literature. A guide regarding the use of the DSC was written is now used by new PhD students.

(a) (b)

Figure 110: Pictures of the DSC device in IEMN (a) with a zoom on the crucible insert section (b)

C.2.3 *Microtomography*

In order to have a precise model of 3D-C internal structure, experiments with a microtomographe seen in Fig.111 were performed. An X ray tomography is done at 360° and a 3D reconstruction of the sample is made in every point of space based on the absorption coefficient of the material. The results from a 3D-C sample mounted on glass are seen in Fig.112. The glass support and the silver paste used for the electrical connection are seen in the image but the graphene foam part is invisible. Its very low thickness, density and atomic number makes it very difficult to see with X rays.

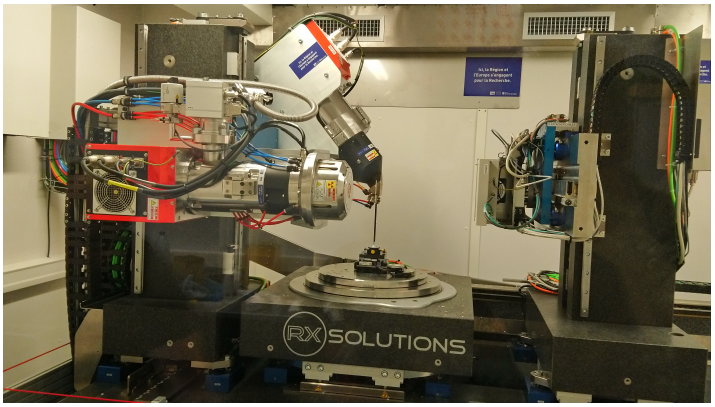

Figure 111: Picture of the Microtomographe on the Univ. Lille Campus

The idea to use microtomography was latter tried again to map the nickel structure on which the graphene is grown. The results provided by the PhD student Hubert Romain are seen in Fig.113 and are currently used in M.Hubert COMSOL simulations.

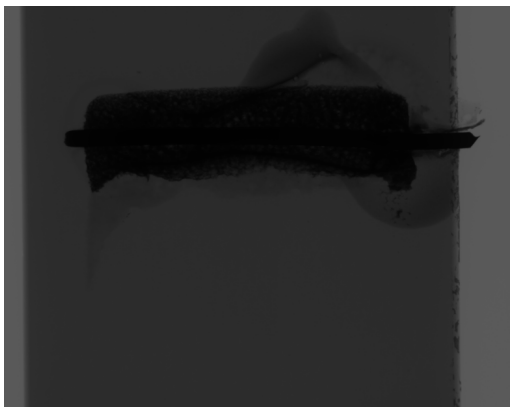

Figure 112: Microtomographie of 3D-C. The silver paste is visible on the top and the glass backing as well in the background but the Carbon foam is invisible.

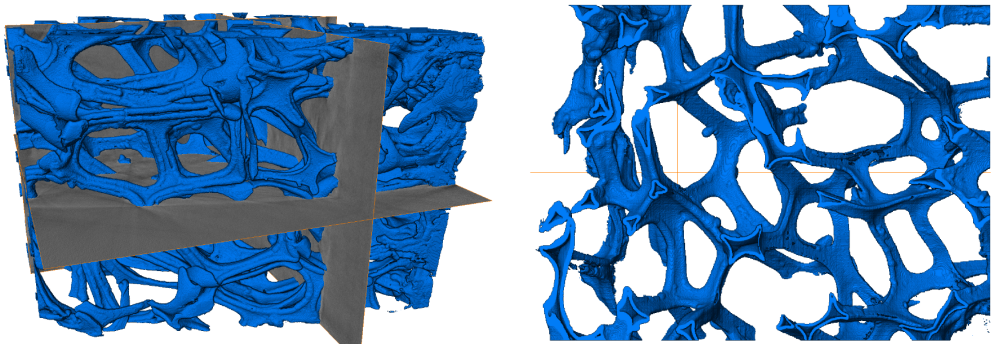

(a) (b)

Figure 113: Microtomographie reconstruction of the Nickel structure used for carbon growth. Complete reconstruction (a) and zoomed view (b). Courtesy of Romain Hubert with N. Limodin, T. Rougelot and J. Hosdez, ISIS4D – In Situ Innovative Set-Ups under X-ray microtomography.

C.2.4 *AFM Measurements*

IEMN possess multiple atomic force microscopy (AFM) instruments and some early analysis on 3D-C have been performed with it. An AFM seen in Fig.114 uses a cantilever for a point by point analysis of a surface. The most common use is a topographical analysis of a surface as well as measurement of different mechanical parameters (viscoelasticity, stiffness... etc). Local electrical conductivity measurements can also be performed as well as some thermal analysis where the cantilever is used as a thermometer. The latest mode being of greater interest for thermophones. Using a foam geometry is challenging for an AFM as flat surfaces are privileged for AFM measurements. Additionally the

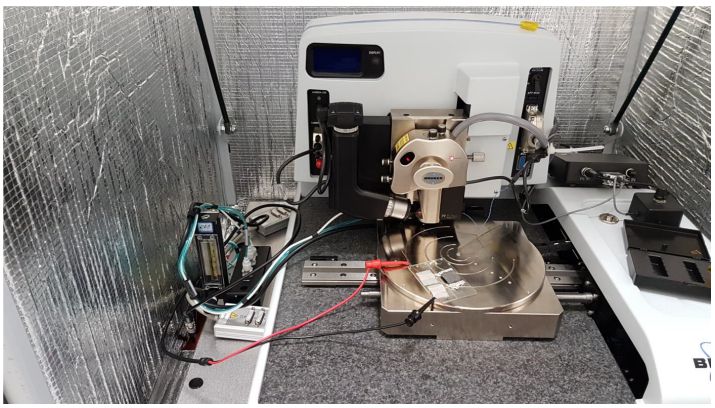

Figure 114: Picture of the AFM device available at the IEMN

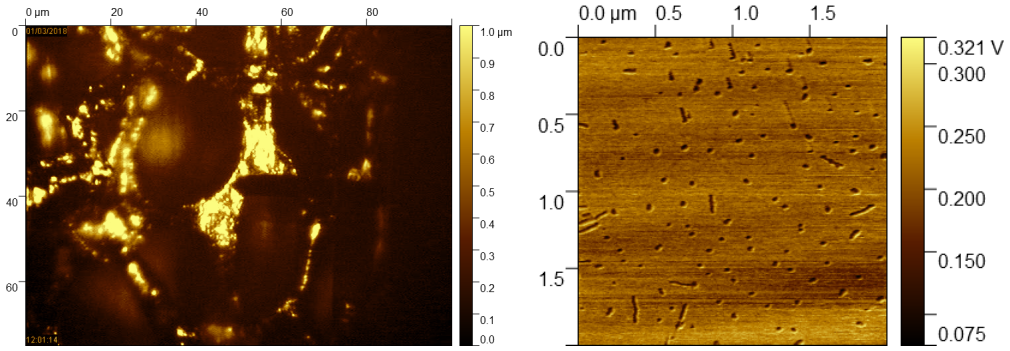

(a) (b)

Figure 115: Picture of the positioning of the AFM cantilever (a) and the resulting picture of adherence measurement on the surface of a branch (b)

cantilever can not reach branches at the center of the foam at the risk of damaging the ones at the tops. It can be noted that AFM measurements with thermophone have only been made with CNT samples [171] leaving room for improvement and further analysis.

An image of the positioning of the cantilever on a branch of the foam is seen in Fig.115a and the resulting topographical image is in Fig.115b. The small dots are assimilated to the center of growth of carbon. This was confirmed by a tomography image of 100×100nm where the overlapping graphene between two growth center created rifts that would disassociate the cantilever with the surface. This problem was also encountered when trying to measure local electrical conductivity of 3D-C. Eventually results were obtained and displayed a behavior close to a metal. Those measurements are not presented here as they are only qualitative and are limited by the tunnel effect.

Lastly the cantilever was used as a thermometer to try and measure the thermal layer in which the sound is generated. Sound was gener-

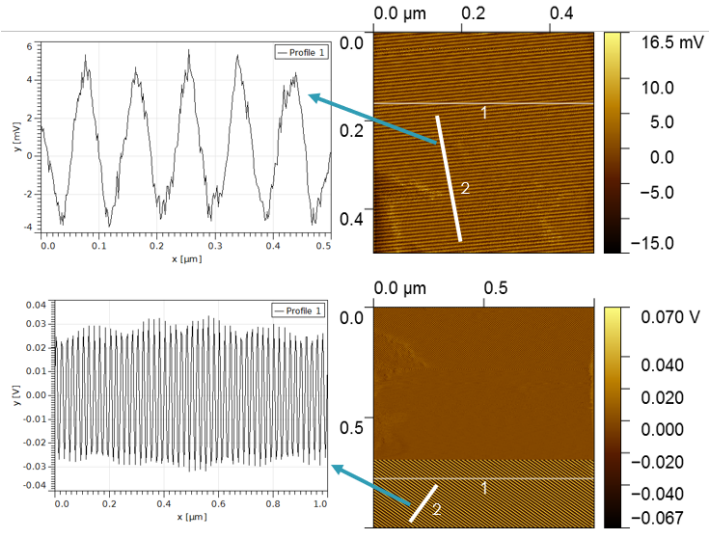

Figure 116: Experimental thermal measurement of the AFM cantilever as it approches the surface of the foam under operation

ated by the 3D-C and the cantilever was slowly approaching the surface. The lightweight of the cantilever added to the close space of the measurements made the cantilever oscillate with the generated sound. This prevented accurate temperature measurements but allowed for the determination of the acoustic frequency based on the oscillating frequency of the cantilever as seen in Fig.116. Due to the COVID-19 as well as a lack of adequate samples, this experiment was not reproduced despite improvement in the thermal stability of the IEMN AFM. Nonetheless, we strongly recommend the reader to further improve this experiment as it could provide good insights and experimental validation of the thermal layer never before measured.

C.2.5 *Spectral Analysis Plots*

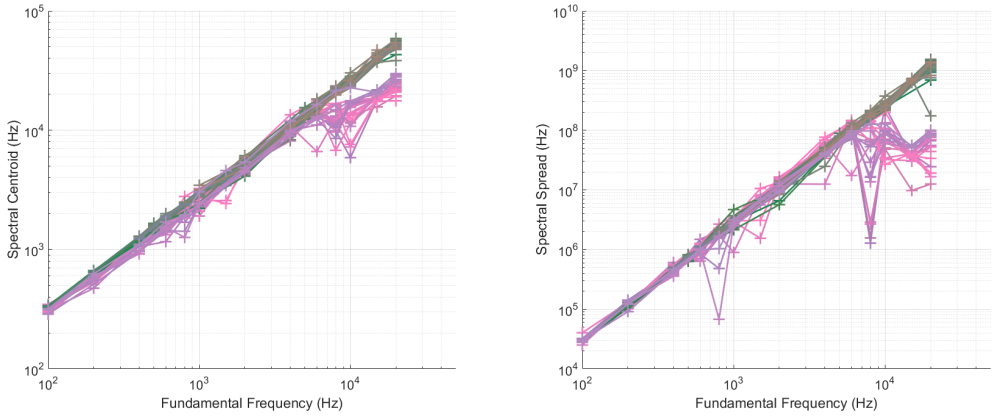

(a) (b)

Figure 117: Spectral Centroid (a) and Spectral Spread (b) of all the measured samples. The curves in shades of pink and green use AC and ACDC input power respectively.

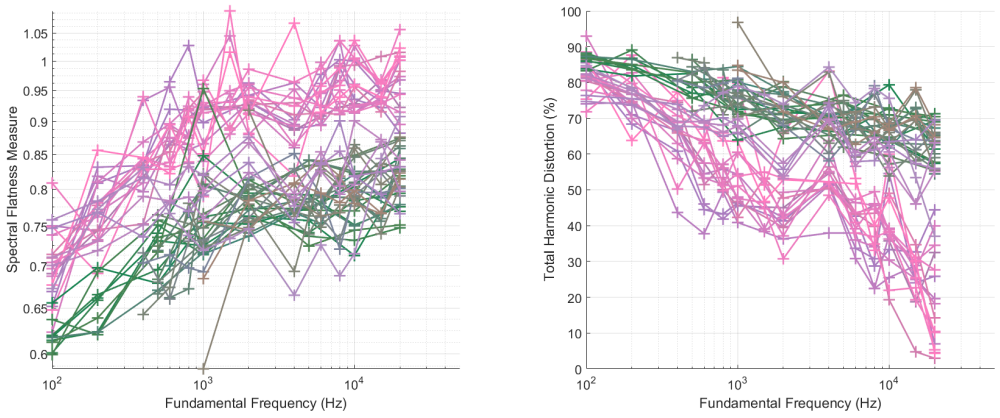

(a) (b)

Figure 118: Spectral Flatness Measure (a) and Total Harmonic Distortion (b) of all the measured samples. The curves in shades of pink and green use AC and ACDC input power respectively.

BIBLIOGRAPHY

[1] P. Guiraud, S. Giordano, O. Bou-Matar, P. Pernod, and R. Lardat. "Multilayer modeling of thermoacoustic sound generation for thermophone analysis and design." In: *Journal of Sound and Vibration* 455 (2019). ISSN: 10958568. DOI: 10.1016/j.jsv.2019.05.001.

[2] Pierre Guiraud, Stefano Giordano, Olivier Bou Matar, Philippe Pernod, and Raphael Lardat. "Two temperature model for thermoacoustic sound generation in thick porous thermophones." In: *Journal of Applied Physics* 126.16 (Oct. 2019). ISSN: 10897550. DOI: 10.1063/1.5121395.

[3] Zhi Lin Ngoh, Pierre Guiraud, Dunlin Tan, Stefano Giordano, Olivier Bou-Matar, Edwin Hang Tong Teo, Philippe Pernod, Philippe Coquet, and Raphael Lardat. "Experimental characterization of three-dimensional Graphene's thermoacoustic response and its theoretical modelling." In: *Carbon* (2020). ISSN: 0008-6223. DOI: https://doi.org/10.1016/j.carbon.2020.06.045. URL: http://www.sciencedirect.com/science/article/pii/S000862232030614X.

[4] Daisuke Noda and Yuki Ueda. "A thermoacoustic oscillator powered by vaporized water and ethanol." In: *American Journal of Physics* 81.2 (Feb. 2013), pp. 124–126. DOI: 10.1119/1.4766940.

[5] B. Higgins. "On the Sound Produced by a Current of Hydrogen gas passing through a tube." In: *Journal of the Natural Philosophy, Chemistry and the Arts* 1 (1802), pp. 129–131.

[6] C. Sondhauss. "Ueber die Schallschwingungen der luft in erhitzen glasröhren und in gedeckten pfiefen von ungleicher weite." In: *Annalen der Physik* 155 (1850), pp. 1–34.

[7] P.L. Rijke. "On the vibration of the air in a tube open at both ends." In: *Philosophical Magazine* 17 (1859), pp. 419–422.

[8] G. W. Swift. "Thermoacoustic engines." In: *Journal of the Acoustical Society of America* 84.4 (1988), pp. 1145–1180. ISSN: NA. DOI: 10.1121/1.396617.

[9] Nathanael Mayo. "Advancements in thermophones: sound generation from nanoscopic heaters." In: *Acoustics Today* (2018).

[10] A.S. Herschel. "Vibrations of air produced by heat." In: *Nature* 10 (1874), pp. 233–235. DOI: 10.1038/010233a0.

[11] H. Helmholtz. *Die Lehre von den Tonempfindungen als Physiologische Grundlage Für die Theorie der Musik*. 1863.

[12] Jennifer Groundwater. *Alexander Graham Bell: The Spirit of Innovation*. Ed. by Calgary: Altitude Publishing. 2005, p. 31. ISBN: 1-55439-006-0.

[13] J.W.S Rayleig. *The theory of sound. Volume 2*. Macmillan and Co. London, 1878.

[14] T. Weisendanger. "The Thermophone." In: *Scientific American Supplement* 148 (1878), p. 2353.

[15] William Henry Preece. "On some thermal effects of electric currents." In: *Proceedings of the Royal Society of London* 30 (1880), pp. 408–411. URL: http://rspl.royalsocietypublishing.org/.

[16] A.G. Bell and C.S. Tainter. "On the Production and reproduction of speech by light." In: *American Journal of Science* 20 (1880), pp. 305–324.

[17] W.H. Preece. "On the conversion of radiant energy into sonorous vibrations." In: *Proceedings of the Royal Society of London* 31 (1881), pp. 506–520.

[18] E. Mercadier. "Sur la radiophonie." In: *Journal de Physique Théorique et Appliquée* 10.1 (1881), pp. 53–68. ISSN: 0368-3893. DOI: 10.1051/jphystap:018810010005300.

[19] E. Mercadier. "Sur la radiophonie (3e mémoire)." In: *Journal de Physique Théorique et Appliquée* 10.1 (1881), pp. 234–241. ISSN: 0368-3893. DOI: 10.1051/jphystap:0188100100023401.

[20] E. Mercadier. "Sur la radiophonie (2e mémoire)." In: *Journal de Physique Théorique et Appliquée* 10.1 (1881), pp. 147–154. ISSN: 0368-3893. DOI: 10.1051/jphystap:0188100100014701.

[21] Srirang Manohar and Daniel Razansky. "Photoacoustics: a historical review." In: *Advances in Optics and Photonics* 8.4 (Dec. 2016), p. 586. ISSN: 1943-8206. DOI: 10.1364/aop.8.000586.

[22] de Lange P. "On Thermophones." In: *Proceedings of the Royal Society of London* 91 (1915), p. 239. URL: http://rspa.royalsocietypublishing.org/.

[23] H.D. Arnold and I.B Crandall. "The Thermophone as a Precision Source of Sound." In: *Physical Review* 10 (1917), pp. 22–38. DOI: https://doi.org/10.1103/PhysRev.10.22.

[24] E.C. Wente. "A Condenser Transmitter as a Uniformly Sensitive Instrument for the Absolute Measurement of Sound Intensity." In: *Physical Review* 10 (1917), pp. 39–63. DOI: https://doi.org/10.1103/PhysRev.10.39.

[25] Edward C. Wente. "The Thermophone." In: *Physical Review* 19 (1922), pp. 333–345. DOI: https://doi.org/10.1103/PhysRev.19.333.

[26] L.J. Sivian. "Absolute Calibration of Condenser Transmitters." In: *Bell Systems Technical Journal* 10 (1931), pp. 96–115.

[27] Stuart Ballantine. "Technique of Microphone Calibration." In: *The Journal of the Acoustical Society of America* 3.3 (Jan. 1932), pp. 319–360. DOI: 10.1121/1.1915566.

[28] Henry A Fairbank, William M Fairbank, and C T Lane. "The Thermophone as a Source of Sound in Liquid Helium and Liquid Hydrogen." In: *The Journal of the Acoustical Society of America* 19.19 (1947), pp. 475–3. DOI: 10.1121/1.1916506. URL: http://dx.doi.org/10.1121/1.1916506.

[29] Leon Trilling. "On Thermally Induced Sound Fields." In: *Journal of the Acoustical Society of America* 27.3 (1955), pp. 425–431. ISSN: NA. DOI: 10.1121/1.1907920.

[30] F. Alan McDonald and Grover C. Jr Wetsel. "Generalized theory of the photoacoustic effect." In: *Journal of Applied Physics* 49.2313 (1978). DOI: 10.1063/1.325116.

[31] Paul Riety. "Retour sur la Théorie du Thermophone à Feuilles d'Or." In: *Cahiers d'Acoustique* 70 (1955).

[32] H Shinoda, T Nakajima, K Ueno, and N Koshida. "Thermally induced ultrasonic emission from porous silicon." In: *Letters to Nature* (1999).

[33] Takashi Kihara, Toshihiro Harada, Masahiro Kato, Kiyoshi Nakano, Osamu Murakami, Takefumi Kikusui, and Nobuyoshi Koshida. "Reproduction of mouse-pup ultrasonic vocalizations by nanocrystalline silicon thermoacoustic emitter." In: *Applied Physics Letters* 88.4 (2006), pp. 1–3. ISSN: 00036951. DOI: 10.1063/1.2168498.

[34] Tian He, Xie Dan, Yang Yi, Ren Tian-Ling, Wang Yu-Fend, Zhou Chang-Jian, Peng Ping-Gang, Wang Li-Gang, and Liu Li-Tian. "Transparent, flexible, ultrathin sound source devices using Indium Tin oxide films." In: *Applied Physics Letters* (2011). DOI: 10.1063/1.3617462.

[35] He Tian et al. "Graphene-on-paper sound source devices." In: *ACS Nano* (2011). ISSN: 19360851. DOI: 10.1021/nn2009535.

[36] Ji Won Suk, Karen Kirk, Yufeng Hao, Neal A. Hall, and Rodney S. Ruoff. "Thermoacoustic sound generation from monolayer graphene for transparent and flexible sound sources." In: *Advanced Materials* (2012). ISSN: 09359648. DOI: 10.1002/adma.201201782.

[37] Yoshiki Nakajima and Takehiro Sugimoto. "Flexible Sound Generator Based on Thermoacoustic Effect." In: *Sensors* (2012). DOI: 10.1109/ICSENS.2012.6411099.

[38] G Chitnis, A Kim, S H Song, A M Jessop, J S Bolton, and B Ziaie. "A Thermophone On Porous Polymeric Substrate." In: *Applied Physics Letters* 101 (2012). DOI: 10.1063/1.4737005.

[39] Nobuyoshi Koshida, Daihei Hippo, Masamitsu Mori, Hiroshi Yanazawa, Hiroyuki Shinoda, and Toshikazu Shimada. "Characteristics of thermally induced acoustic emission from nanoporous silicon device under full digital operation." In: *Applied Physics Letters* 102.12 (Mar. 2013). ISSN: 00036951. DOI: 10.1063/1.4798517.

[40] M. Daschewski, R. Boehm, J. Prager, M. Kreutzbruck, and A. Harrer. "Physics of thermo-acoustic sound generation." In: *Journal of Applied Physics* (2013). ISSN: 00218979. DOI: 10.1063/1.4821121.

[41] Ming Shan Tsai, Ko Kang Yang, Sy Hann Chen, Chen Ching Ting, and I. Min Jiang. "Fabrication of efficient thermoacoustic device with an interdigitated-like electrode on indium tin oxide glass." In: *Japanese Journal of Applied Physics* (2016). ISSN: 13474065. DOI: 10.7567/JJAP.55.106702.

[42] Zihan Zhang, He Tian, Peng Lv, Yi Yang, Qiuyun Yang, Shaolin Yang, Guanzhong Wang, and Tianling Ren. "High-performance sound source devices based on graphene woven fabrics." In: *Applied Physics Letters* (2017). ISSN: 00036951. DOI: 10.1063/1.4977706.

[43] Lin Xiao et al. "Flexible, stretchable, transparent carbon nanotube thin film loudspeakers." In: *Nano Letters* (2008). ISSN: 15306984. DOI: 10.1021/nl802750z.

[44] A.O. Niskanen, J. Hassel, M. Tikander, P. Maijala, L. Grönberg, and Helistö. "Suspended metal wire array as a thermoacoustic sound source." In: *Applied Physics Letters* (2009). DOI: 10.1063/1.3249770.

[45] He Tian et al. "Flexible, ultrathin, and transparent sound-emitting devices using silver nanowires film." In: *Applied Physics Letters* (2011). DOI: 10.1063/1.3671332.

[46] Paolo La Torraca, Marco Bobinger, Maurizio Servadio, Paolo Pavan, Markus Becherer, Paolo Lugli, and Luca Larcher. "On the Frequency Response of Nanostructured Thermoacoustic Loudspeakers." In: *MDPI Nanomaterials* (2018). DOI: 10.3390/nano8100833. URL: www.mdpi.com/journal/nanomaterials.

[47] Rajen Dutta, Brian Albee, Wytze E. Van Der Veer, Taylor Harville, Keith C. Donovan, Dimitri Papamoschou, and Reginald M. Penner. "Gold nanowire thermophones." In: *Journal of Physical Chemistry C* (2014). ISSN: 19327455. DOI: 10.1021/jp504195v.

[48] Ali E. Aliev, Nathanael K. Mayo, Monica Jung De Andrade, Raquel O. Robles, Shaoli Fang, Ray H. Baughman, Mei Zhang, Yongsheng Chen, Jae Ah Lee, and Seon Jeong Kim. "Alternative nanostructures for thermophones." In: *ACS Nano* (2015). ISSN: 1936086X. DOI: 10.1021/nn507117a.

[49] Ali E. Aliev, Sahila Perananthan, and John P. Ferraris. "Carbonized Electrospun Nanofiber Sheets for Thermophones." In: *ACS Applied Materials and Interfaces* (2016). ISSN: 19448252. DOI: 10.1021/acsami.6b08717.

[50] Mikhail E. Kozlov, Carter S. Haines, Jiyoung Oh, Marcio D. Lima, and Shaoli Fang. "Sound of carbon nanotube assemblies." In: *Journal of Applied Physics* 106.124311 (2009). DOI: 10.1063/1.3272691.

[51] Katsunori Suzuki, Shingo Sakakibara, Morihiro Okada, Yoichiro Neo, Hidenori Mimura, Yoku Inoue, and Toshihiro Murata. "Study of carbon-nanotube web thermoacoustic loud speakers." In: *Japanese Journal of Applied Physics*. 2011. DOI: 10.1143/JJAP.50.01BJ10.

[52] Ali E. Aliev, Nathanael K. Mayo, Ray H. Baughman, Dragan Avirovik, Shashank Priya, Michael R Zarnetske, and John B. Blottman. "Thermal management of thermoacoustic sound projectors using a free standing carbon nanotube aerogel sheet as a heat source." In: *Nanotechnology* 25.405704 (2014). DOI: 10.1088/0957.

[53] Mahsa Asgarisabet and Andrew Barnard. "Multi-Physics Simulation of Ultra-Lightweight Carbon Nanotube Speakers." In: *SAE International Journal of Materials and Manufacturing* 10.3 (June 2017). ISSN: 1946-3987. DOI: 10.4271/2017-01-1816.

[54] Dante Ahn and Seung Eon Ahn. "Thermoacoustic properties of multi-wall carbon nanotube sheet for loudspeaker application." In: *Materials Letters* 263 (Mar. 2020). ISSN: 18734979. DOI: 10.1016/j.matlet.2019.127242.

[55] Blake J. Mason, Shun Wen Chang, Jihan Chen, Stephen B. Cronin, and Adam W. Bushmaker. "Thermoacoustic transduction in individual suspended carbon nanotubes." In: *ACS Nano* 9.5 (May 2015), pp. 5372–5376. ISSN: 1936086X. DOI: 10.1021/acsnano.5b01119.

[56] Stepan Romanov, Ali E. Aliev, Boris Fine, Anton S. Anisimov, and Albert G Nasibulin. "Highly efficient thermophones based on freestanding single-walled carbon nanotube films." In: *Nanoscale Horizons* (2019). ISSN: 2055-6756. DOI: 10.1039/c9nh00164f.

[57] V. Vesterinen, A. O. Niskanen, J. Hassel, and P. Helistö. "Fundamental efficiency of nanothermophones: Modeling and experiments." In: *Nano Letters* (2010). ISSN: 15306984. DOI: 10.1021/nl1031869.

[58] Michael Thompson Pettes, Hengxing Ji, Rodney S. Ruoff, and Li Shi. "Thermal transport in three-dimensional foam architectures of few-layer graphene and ultrathin graphite." In: *Nano Letters* (2012). ISSN: 15306984. DOI: 10.1021/nl300662q.

[59] Manuela Loeblein, Roland Yingjie Tay, Siu Hon Tsang, Wei Beng Ng, and Edwin Hang Tong Teo. "Configurable three-dimensional boron nitride-carbon architecture and its tunable electronic behavior with stable thermal performances." In: *Small* (2014). ISSN: 16136829. DOI: 10.1002/smll.201400292.

[60] Manuela Loeblein, Siu Hon Tsang, Matthieu Pawlik, Eric Jian Rong Phua, Han Yong, Xiao Wu Zhang, Chee Lip Gan, and Edwin Hang Tong Teo. "High-Density 3D-Boron Nitride and 3D-Graphene for High-Performance Nano-Thermal Interface Material." In: *ACS Nano* (2017). ISSN: 1936086X. DOI: 10.1021/acsnano.6b08218.

[61] Long Zhang et al. "Porous 3D graphene-based bulk materials with exceptional high surface area and excellent conductivity for supercapacitors." In: *Scientific Reports* 3 (2013). ISSN: 20452322. DOI: 10.1038/srep01408.

[62] Yingpeng Wu et al. "Three-dimensionally bonded spongy graphene material with super compressive elasticity and near-zero Poisson's ratio." In: *Nature Communications* (2015). ISSN: 20411723. DOI: 10.1038/ncomms7141.

[63] Wenwen Fei, Jianxin Zhou, and Wanlin Guo. "Low-voltage driven graphene foam thermoacoustic speaker." In: *Small* (2015). ISSN: 16136829. DOI: 10.1002/smll.201402982.

[64] Tao Tu et al. "A novel thermal acoustic device based on vertical graphene film." In: *AIP Advances* 9 (2019). DOI: 10.1063/1.5096220.

[65] Lu-Qi Tao, Ying Liu, He Tian, Zhen-Yi Ju, Qian-Yi Xie, Yi Yang, and Tian-Ling Ren. "A novel thermal acoustic device based on porous graphene." In: *AIP Advances* (2016). DOI: 10.1063/1.4939935.

[66] Lu Qi Tao, Hao Sun, Ying Liu, Zhen Yi Ju, Yi Yang, and Tian Ling Ren. "Flexible graphene sound device based on laser reduced graphene." In: *Applied Physics Letters* (2017). ISSN: 00036951. DOI: 10.1063/1.5002113.

[67] Akbar Ghasemi Yeklangi, S. E. Khadem, and Sara Darbari. "Fabrication and investigation of a thermoacoustic loudspeaker based on carbon nanotube coated laser-scribed graphene." In: *Journal of Applied Physics* (2018). ISSN: 0021-8979. DOI: 10.1063/1.5038729.

[68] Hanping Hu, Yandong Wang, and Zedong Wang. "Wideband flat frequency response of thermo-acoustic emission." In: *Journal of Physics D: Applied Physics* (2012). ISSN: 00223727. DOI: 10.1088/0022-3727/45/34/345401.

[69] Dongdong Wang, Hanping Hu, and Jianhua Wang. "On the thermo-acoustic emission from the surface of a suspended carbon nanotube film." In: *Advances in Engineering Research (ICSEEE)* 179 (2018).

[70] Lin Xiao, Peng Liu, Liang Liu, Qunqing Li, Zhenghe Feng, Shoushan Fan, and Kaili Jiang. "High frequency response of carbon nanotube thin film speaker in gases." In: *Journal of Applied Physics* (2011). ISSN: 00218979. DOI: 10.1063/1.3651374.

[71] Choong Sun Kim, Seul Ki Hong, Jung Min Lee, Dong Soo Kang, Byung Jin Cho, and Jung Woo Choi. "Free-Standing Graphene Thermophone on a Polymer-Mesh Substrate." In: *Small* (2016). ISSN: 16136829. DOI: 10.1002/smll.201501673.

[72] L. H. Tong, C. W. Lim, S. K. Lai, and Y. C. Li. "Gap separation effect on thermoacoustic wave generation by heated suspended CNT nano-thinfilm." In: *Applied Thermal Engineering* (2015). ISSN: 13594311. DOI: 10.1016/j.applthermaleng.2015.04.031.

[73] Paolo La Torraca, Marco Bobinger, Paolo Pavan, Markus Becherer, Shanyu Zhao, Matthias Koebel, Luca Cattani, Paolo Lugli, and Luca Larcher. "High Efficiency Thermoacoustic Loudspeaker Made with a Silica Aerogel Substrate." In: *Advanced Materials Technologies* 1800139 (2018). DOI: 10.1002/admt.201800139. URL: https://doi.org/10.1002/admt.201800139..

[74] J J Brown, N C Moore, O D Supekar, J C Gertsch, and V M Bright. "Ultrathin thermoacoustic nanobridge loudspeakers from ALD on polyimide." In: *IOP Nanotechnology* (2016).

[75] Qianhe Xing, Shuang Li, Xueliang Fan, Anhua Bian, Shi Jie Cao, and Cheng Li. "Influential factors on thermoacoustic efficiency of multilayered graphene film loudspeakers for optimal design." In: *Journal of Applied Physics* (2017). ISSN: 10897550. DOI: 10.1063/1.5004124.

[76] P. La Torraca, L. Larcher, M. Bobinger, P. Pavan, B. Seeber, and P. Lugli. "Physical modeling and characterization of thermo-acoustic loudspeakers made of silver nano-wire films." In: *Journal of Applied Physics* (2017). ISSN: 10897550. DOI: 10.1063/1.4984755.

[77] Ricardo R. Boullosa and Arturo O. Santillán. "Sound radiation from thermal non-resonant sources: Planar and nonplanar geometries." In: *Japanese Journal of Applied Physics, Part 1: Regular Papers and Short Notes and Review Papers* (2006). DOI: 10.1143/JJAP.45.2794.

[78] C. W. Lim, L. H. Tong, and Y. C. Li. "Theory of suspended carbon nanotube thinfilm as a thermal-acoustic source." In: *Journal of Sound and Vibration* (2013). ISSN: 0022460X. DOI: 10.1016/j.jsv.2013.05.020.

[79] M. Daschewski, M. Kreutzbruck, and J. Prager. "Influence of thermodynamic properties of a thermo-acoustic emitter on the efficiency of thermal airborne ultrasound generation." In: *Ultrasonics* (2015). ISSN: 0041624X. DOI: 10.1016/j.ultras.2015.06.008.

[80] Jonghoon Bin, William S. Oates, and Kunihiko Taira. "Thermoacoustic modeling and uncertainty analysis of two-dimensional conductive membranes." In: *Journal of Applied Physics* (2015). ISSN: 10897550. DOI: 10.1063/1.4908067.

[81] Jun Xu. Hanping Hu Tao Zhu. "Model for thermoacoustic emission from solids." In: *Applied Physics Letters* 96.214101 (2010). DOI: 10.1063/1.3435429.

[82] He Tian et al. "Graphene-on-paper sound source devices Supplementary paper." In: *ACS Nano* (2011). DOI: 10.1021/nn2009535.

[83] Hanping Hu, Zedong Wang, Hao Wu, and Yandong Wang. "Analysis of spherical thermo-acoustic radiation in gas." In: *AIP Advances Applied Physics Letters* 2.101 (2012), pp. 32106–107114. DOI: 10.1063/1.4738497. URL: https://doi.org/10.1063/1.4738497.

[84] Hanping Hu, Dongdong Wang, and Zedong Wang. "Solution for acoustic field of thermo-acoustic emission from arbitrary source." In: *AIP Advances* (2014). ISSN: 21583226. DOI: 10.1063/1.4898149.

[85] Yaping Yin and Hanping Hu. "Analysis of cylindrical thermo-acoustic radiation in gas." In: *Applied Physics Letters* 1101.10 (2017), pp. 20033–141105. URL: https://doi.org/10.1063/1.4979765.

[86] Yida Mao, C. W. Lim, and Tianyun Li. "Thermo-acoustic radiation of free-standing nano-thin film in viscous fluids." In: *International Journal of Engineering Science* 139 (June 2019), pp. 11–23. ISSN: 00207225. DOI: 10.1016/j.ijengsci.2019.03.002.

[87] Lihong Tong, C. W. Lim, Xiushao Zhao, and Daxing Geng. "Theory and modeling of cylindrical thermo-acoustic transduction." In: *Physics Letters, Section A: General, Atomic and Solid State Physics* (2016). ISSN: 03759601. DOI: 10.1016/j.physleta.2016.05.002.

[88] Y. S. Liu, L. H. Tong, and S. K. Lai. "Thermo-acoustics generated by periodically heated thin line array." In: *Journal of Sound and Vibration* (2018). ISSN: 10958568. DOI: 10.1016/j.jsv.2018.04.034.

[89] S S Asadzadeh, A Moosavi, C Huynh, and O Saleki. "Thermo acoustic study of carbon nanotubes in near and far field: Theory, simulation, and experiment." In: *Journal of Applied Physics* (2015). DOI: 10.1063/1.4914049.

[90] G. W. Swift. "Streaming in thermoacoustic engines and refrigerators." In: *AIP Conference Proceedings* 524.105 (2000), pp. 105–114. DOI: 10.1063/1.1309184.

[91] Tao Jin, Jiale Huang, Ye Feng, Rui Yang, Ke Tang, and Ray Radebaugh. *Thermoacoustic prime movers and refrigerators: Thermally powered engines without moving components*. Dec. 2015. DOI: 10.1016/j.energy.2015.09.005.

[92] Muluken Z. Getie, François Lanzetta, Sylvie Bégot, Bimrew T. Admassu, and Abdulkadir A. Hassen. *Reversed regenerative Stirling cycle machine for refrigeration application: A review*. Oct. 2020. DOI: 10.1016/j.ijrefrig.2020.06.007.

[93] Jiaxiang Song, Yanhong Li, Yuanyuan Li, and Guoqiang Liu. "Three-dimensional model of thermoacoustic tomography with electric excitation." In: *Citation: Journal of Applied Physics* 124 (2018), p. 164504. DOI: 10.1063/1.5045510. URL: http://aip.scitation.org/toc/jap/124/16.

[94] Nima Akhlaghi, T. Joshua Pfefer, Keith A. Wear, Brian S. Garra, and William C. Vogt. "Multidomain computational modeling of photoacoustic imaging: verification, validation, and image quality prediction." In: *Journal of Biomedical Optics* 24.12 (Nov. 2019), p. 1. ISSN: 1083-3668. DOI: 10.1117/1.JBO.24.12.121910. URL: https://www.spiedigitallibrary.org/journals/journal-of-biomedical-optics/volume-24/issue-12/121910/Multidomain-computational-modeling-of-photoacoustic-imaging--verification-validation-and/10.1117/1.JBO.24.12.121910.full.

[95] Manojit Pramanik, Geng Ku, Changhui Li, and Lihong V. Wang. "Design and evaluation of a novel breast cancer detection system combining both thermoacoustic (TA) and photoacoustic (PA) tomography." In: *Medical Physics* 35.6 (2008), pp. 2218–2223. ISSN: 00942405. DOI: 10.1118/1.2911157.

[96] He Tian, Yi Yang, Dan Xie, Ya Long Cui, Wen Tian Mi, Yuegang Zhang, and Tian Ling Ren. "Wafer-scale integration of graphene-based electronic, optoelectronic and electroacoustic devices." In: *Scientific Reports* (2014). ISSN: 20452322. DOI: 10.1038/srep03598.

[97] Zhong Yan, Denis L. Nika, and Alexander A. Balandin. "Thermal properties of graphene and few-layer graphene: applications in electronics." In: *IET Circuits, Devices & Systems* (2015). DOI: 10.1049/iet-cds.2014.0093.

[98] Luqi Tao, Danyang Wang, Song Jiang, Ying Liu, Qianyi Xie, He Tian, Ningqin Deng, Xuefeng Wang, Yi Yang, and Tian Ling Ren. *Fabrication techniques and applications of flexible graphene-based electronic devices*. Apr. 2016. DOI: 10.1088/1674-4926/37/4/041001.

[99] Timothy A. Brungart, James J. Chatterley, Benjamin S. Beck, Brian L. Kline, and Zachary W. Yoas. "Thermal saturation and its suppression in high-power, compact carbon nanotube thin-film thermophones." In: *Meetings on Acoustics*. ASA, 2016, p. 030002. DOI: 10.1121/2.0000479.

[100] Ali E. Aliev, Nathanael K. Mayo, Ray H. Baughman, Brent T. Mills, and Ed Habtour. "Subwoofer and nanotube butterfly acoustic flame extinction." In: *Journal of Physics D: Applied Physics* 50.29 (June 2017). ISSN: 13616463. DOI: 10.1088/1361-6463/aa78e5.

[101] Andrew R Barnard, Mahsa Asgarisabet, and Troy Bouman. "The Carbon Nanotube Thermophone: A Near-Weightless Audio Driver With No Moving Parts." In: ed. by Michigan Technological University. Alma International: Symposium & Expo, 2016.

[102] Paolo La Torraca, Yuri Ricci, Andreas Albrecht, Marco Bobinger, Paolo Pavan, Luca Cattani, Markus Becherer, Paolo Lugli, and Luca Larcher. "Printed Technology Solutions for Audio Transducers." In: *Proceedings of the IEEE Conference on Nanotechnology*. Vol. 2018-July. IEEE Computer Society, Jan. 2018. ISBN: 9781538653364. DOI: 10.1109/NANO.2018.8626422.

[103] Qin Zhou and Alexander K. Zettl. *US Patent - Electrostatic Graphene Speaker*. 2019.

[104] Joseph F. Pinkerton, David A. Badger, William Neil Everett, and William Martin Lackowski. *US Patent - Compact Electroacoustic Transducer and loudspeaker system and method of use thereof*. 2020.

[105] Kyoung-Ryul Lee, Sung Hwan Jang, and Inhwa Jung. "Acoustic performance of dual-electrode electrostatic sound generators based on CVD graphene on polyimide film." In: *IOP Nanotechnology* (2018).

[106] Luqi Tao, Song Jiang, Cheng Li, He Tian, Ningqin Deng, Danyang Wang, Yi Yang, and Tian-Ling Ren. "The Use of Graphene-Based Earphones in Wireless Communication." In: *Tsinghua Science and Technology* 20.3 (2015), pp. 270 –276. DOI: 10.1109/TST.2015.7128939.

[107] He Tian, Yi Yang, Cheng Li, Wen Tian Mi, Mohammad Ali Mohammad, and Tian Ling Ren. "A flexible, transparent and ultrathin single-layer graphene earphone." In: *RSC Advances* 5.22 (2015), pp. 17366–17371. ISSN: 20462069. DOI: 10.1039/c4ra16047a.

[108] Yang Wei, Xiaoyang Lin, Kaili Jiang, Peng Liu, Qunqing Li, and Shoushan Fan. "Thermoacoustic chips with carbon nanotube thin yarn arrays." In: *Nano Letters* (2013). ISSN: 15306984. DOI: 10.1021/nl402408j.

[109] Guang-Yang Gou et al. "Flexible Two-Dimensional Ti ₃ C ₂ MXene Films as Thermoacoustic Devices." In: *ACS Nano* (Sept. 2019), acsnano.9b03889. ISSN: 1936-0851. DOI: 10.1021/acsnano.9b03889. URL: https://pubs.acs.org/doi/10.1021/acsnano.9b03889.

[110] Andrea Harrer, Maxim Daschewski, Jens Prager, Marc Kreutzbruck, Matthias Guderian, and Asmus Meyer-Plath. "Thermoacoustic generation of airborne ultrasound using carbon materials at the micro-and nanoscale." In: *International Journal of Applied Electromagnetics and Mechanics*. 2012. DOI: 10.3233/JAE-2012-1440.

[111] Takuya Nishioka, Yu Teshima, Takashi Mano, Ken Sakai, Takaaki Asada, Mami Matsukawa, Tetsuo Ohta, and Shizuko Hiryu. "Ultrasound radiation from a three-layer thermoacoustic transformation device." In: *Ultrasonics* (2015). ISSN: 0041624X. DOI: 10.1016/j.ultras.2014.10.019.

[112] K.L. Jiang, Y.C. Yang, Z. Chen, L. Xiao, and S.S. Fan. *US patent - Ultrasonic Thermoacoustic Device*. 2008.

[113] He Tian, Cheng Li, Mohammad Ali Mohammad, Ya Long Cui, Wen Tian Mi, Yi Yang, Dan Xie, and Tian Ling Ren. "Graphene earphones: Entertainment for both humans and animals." In: *ACS Nano* 8.6 (June 2014), pp. 5883–5890. ISSN: 1936086X. DOI: 10.1021/nn5009353.

[114] M. Daschewski, A. Harrer, J. Prager, M. Kreutzbruck, and A. Meyer-Plath. "Carbon nanomaterials as broadband airborne ultrasound transducer." In: *AIP conference Proceedings* (2012). DOI: 10.1063/1.3703262.

[115] Simon Julius, Ronald Gold, Alex Kleiman, Boris Leizeronok, and Beni Cukurel. "Modeling and experimental demonstration of heat flux driven noise cancellation on source boundary." In: *Journal of Sound and Vibration* 434 (Nov. 2018), pp. 442–455. ISSN: 10958568. DOI: 10.1016/j.jsv.2018.02.007.

[116] Walter Santi. *US Patent - Thermoacoustic Soundproofing Panel*. 2018.

[117] Steven A Senczyszyn. *Commercialization of the Carbon Nanotube Thermophone for Active Noise Control Applications*. Tech. rep. Open Access Master's Report: Michigan Technological University, 2018. URL: http://digitalcommons.mtu.edu/etdr/621.

[118] Lu Qi Tao et al. "An intelligent artificial throat with sound-sensing ability based on laser induced graphene." In: *Nature Communications* (2017). ISSN: 20411723. DOI: 10.1038/ncomms14579. arXiv: 9809069v1 [gr-qc].

[119] Yuhong Wei et al. "A Wearable Skinlike Ultra-Sensitive Artificial Graphene Throat." In: *ACS Nano* 13.8 (Aug. 2019), pp. 8639–8647. ISSN: 1936086X. DOI: 10.1021/acsnano.9b03218.

[120] Saewon Kang, Seungse Cho, Ravi Shanker, Hochan Lee, Jonghwa Park, Doo-Seung Um, Youngoh Lee, and Hyunhyub Ko. "Transparent and conductive nanomembranes with orthogonal silver nanowire arrays for skin-attachable loudspeakers and microphones." In: *Applied Sciences and Engineering* (2018). URL: http://advances.sciencemag.org/.

[121] Huijun Ding, Xiaolan Shu, Han Zhang, Yukun Jin, and Taojian Fan. "Recent advances in nanomaterial-enabled acoustic devices for audible sound generation and detection." In: *Nanoscale* (Feb. 2019). ISSN: 2040-3364. DOI: 10.1039/c8nr09736d.

[122] Ali E. Aliev, Marcio D. Lima, Shaoli Fang, and Ray H. Baughman. "Underwater sound generation using carbon nanotube projectors." In: *Nano Letters* (2010). ISSN: 15306984. DOI: 10.1021/nl100235n.

[123] L. H. Tong, S. K. Lai, and C. W. Lim. "Broadband signal response of thermo-acoustic devices and its applications." In: *The Journal of the Acoustical Society of America* 141.4 (Apr. 2017), pp. 2430–2439. ISSN: 0001-4966. DOI: 10.1121/1.4979667.

[124] Ali E. Aliev, Nathanael K. Mayo, Ray H. Baughman, Dragan Avirovik, Shashank Priya, Michael R. Zarnetske, and John B. Blottman. "Thermoacoustic excitation of sonar projector plates by free-standing carbon nanotube sheets." In: *Journal of Physics : Applied Physics* (2014). DOI: 10.1088/0022-3727/47/35/355302.

[125] Erin Gauch. *Présentation QINETIQ - Low-Frequency Thermal-Acousic Source (Thermophone) Housed SeaScout UUV*. Tech. rep. Newport, Rhode Island: NAVSEA Warfare Centers, 2018.

[126] Geoff Fein. *US Navy demonstration converts heat into sound*. Tech. rep. Washington, DC: Jane's International Defence Review, 2018.

[127] Zhenhuan Zhou, Wang Xu, Zhenzhen Tong, C.W. Lim, and Xinsheng Xu. "Theory and modeling of multi-layer carbon nanotube thin film thermoacoustic transducer." In: *Applied Thermal Engineering* (2019). ISSN: 13594311. DOI: 10.1016/j.applthermaleng.2019.01.001.

[128] Andrew R. Barnard, Timothy A. Brungart, Timothy E. McDevitt, Ali E. Aliev, David M. Jenkins, Brian L. Kline, and Ray H. Baughman. "Advancements toward a high-power, carbon nanotube, thin-film loudspeaker." In: *Noise Control Engineering Journal* (2014). ISSN: 07362501. DOI: 10.3397/1/376235.

[129] Kyoung Ryul Lee, Sung Hwan Jang, and Inhwa Jung. "Analysis of acoustical performance of Bi-layer graphene and graphene-foam-based thermoacoustic sound generating devices." In: *Carbon* 127 (Feb. 2018), pp. 13–20. ISSN: 00086223. DOI: 10.1016/j.carbon.2017.10.078.

[130] Nick M. Sbrockey, Tom Salagaj, Gary S. Tompa, and T. S. Kalkur. "Synthesis and characterization of graphene based thermoacoustic devices." In: *Journal of Crystal Growth* 493 (July 2018), pp. 41–44. ISSN: 00220248. DOI: 10.1016/j.jcrysgro.2018.04.019.

[131] Junwei Sha et al. "Three-Dimensional Printed Graphene Foams." In: *ACS Nano* (2017). ISSN: 1936086X. DOI: 10.1021/acsnano.7b01987.

[132] L H Tong, C W Lim, and Y C Li. "Gas-Filled Encapsulated Thermal-Acoustic Transducer." In: *Journal of Vibration and Acoustics* 135.051033 (2013). DOI: 10.1115/1.4024765.

[133] Ali E. Aliev, Yuri N. Gartstein, and Ray H. Baughman. "Increasing the efficiency of thermoacoustic carbon nanotube sound projectors." In: *Nanotechnology* (2013). ISSN: 09574484. DOI: 10.1088/0957-4484/24/23/235501.

[134] Andrew R. Barnard, David M. Jenkins, Timothy A. Brungart, Timothy M. McDevitt, and Brian L. Kline. "Feasibility of a high-powered carbon nanotube thin-film loudspeaker." In: *The Journal of the Acoustical Society of America* (2013). ISSN: 0001-4966. DOI: 10.1121/1.4817261.

[135] Benjamin R Dzikowicz, James F Tressler, and Jeffrey W Baldwin. "Cylindrical heat conduction and structural acoustic models for enclosed fiber array thermophones." In: *Citation: The Journal of the Acoustical Society of America* 142 (2017), p. 3035. DOI: 10.1121/1.5011160. URL: http://asa.scitation.org/toc/jas/142/5.

[136] Eui Joong Shin, Soo Yeon Park, Choong Sun Kim, Byung Jin Cho, and Jung Woo Choi. "Construction of a Multiway Carbon Nanotube Loudspeaker with Finely Tunable Resonance Frequencies." In: *Advanced Materials Technologies* 3.2 (Feb. 2018). ISSN: 2365709X. DOI: 10.1002/admt.201700197.

[137] Troy M. Bouman, Andrew R. Barnard, and Mahsa Asgarisabet. "Experimental quantification of the true efficiency of carbon nanotube thin-film thermophones." In: *The Journal of the Acoustical Society of America* (2016). ISSN: 0001-4966. DOI: 10.1121/1.4944688.

[138] M. S. Heath and D. W. Horsell. "Multi-frequency sound production and mixing in graphene." In: *Scientific Reports* (2017). ISSN: 20452322. DOI: 10.1038/s41598-017-01467-z.

[139] R. R. Boullosa and Arturo O. Santillán. "Acoustic signal recovery by thermal demodulation." In: *Applied Physics Letters* 89.17 (2006). ISSN: 00036951. DOI: 10.1063/1.2372444.

[140] Ali E Aliev et al. "Thermoacoustic sound projector: exceeding the fundamental efficiency of carbon nanotubes." In: *Nanotechnology* 29 (2018), pp. 325704–17. URL: https://doi.org/10.1088/1361-6528/aac509.

[141] Troy Bouman, Andrew Barnard, and Joshua Alexander. "Continued Drive Signal Development for the Carbon Nanotube Thermoacoustic Loudspeaker Using Techniques Derived from the Hearing Aid Industry." In: *SAE Technical Papers*. Vol. 2017-June. June. SAE International, June 2017. DOI: 10.4271/2017-01-1895.

[142] Takehiro Sugimoto and Yoshiki Nakajima. "Second harmonic distortion suppression of thermoacoustic transducer using square root circuit." In: *Acoustical Science and Technology* 37.3 (2016), pp. 99–105. ISSN: 13475177. DOI: 10.1250/ast.37.99.

[143] P. La Torraca, Y. Ricci, M. Bobinger, P. Pavan, and L. Larcher. "Linearization of thermoacoustic loudspeakers by adaptive predistortion." In: *Sensors and Actuators A: Physical* (Aug. 2019), p. 111551. ISSN: 09244247. DOI: 10.1016/j.sna.2019.111551. URL: https://linkinghub.elsevier.com/retrieve/pii/S0924424719307903.

[144] L.D. Landau and E.M. Lifshitz. *Fluid Mechanics, Course of Theoretical Physics Vol. 6*. 3rd ed. Oxford: Butterworth Heinemann, 1986.

[145] Frank W.J. Olver, Daniel W. Lozier, Ronald F. Boisvert, and Charles W. Clark. *NIST Handbook of Mathematical Functions*. Cambridge University Press, 2010, p. 968. ISBN: 9780521140638. URL: https://www.cambridge.org/gb/academic/subjects/mathematics/abstract-analysis/nist-handbook-mathematical-functions?format=WW&isbn=9780521140638.

[146] J. L. Auriault and P. Royer. "Double conductivity media: a comparison between phenomenological and homogenization approaches." In: *International Journal of Heat and Mass Transfer* (1993). ISSN: 00179310. DOI: 10.1016/S0017-9310(05)80198-X.

[147] M. Quintard, M. Kaviany, and S. Whitaker. "Two-medium treatment of heat transfer in porous media: numerical results for effective properties." In: *Advances in Water Resources* (1997). ISSN: 03091708. DOI: 10.1016/S0309-1708(96)00024-3.

[148] Ali Nouri-Borujerdi, Amin R. Noghrehabadi, and D. Andrew S Rees. "The effect of local thermal non-equilibrium on impulsive conduction in porous media." In: *International Journal of Heat and Mass Transfer* (2007). ISSN: 00179310. DOI: 10.1016/j.ijheatmasstransfer.2006.12.016.

[149] A. D'Hueppe, M. Chandesris, D. Jamet, and B. Goyeau. "Coupling a two-temperature model and a one-temperature model at a fluid-porous interface." In: *International Journal of Heat and Mass Transfer* (2012). ISSN: 00179310. DOI: 10.1016/j.ijheatmasstransfer.2012.01.009.

[150] Stefano Giordano and Fabio Manca. "Analysis of heterogeneous structures described by the two-temperature model." In: *International Journal of Heat and Mass Transfer* (2014). ISSN: 00179310. DOI: 10.1016/j.ijheatmasstransfer.2014.06.074.

[151] * A Peigney, Ch Laurent, E Flahaut, R R Bacsa, A Rousset´´, and Rousset´ Rousset´´. *Specific surface area of carbon nanotubes and bundles of carbon nanotubes*. Tech. rep. 2001, pp. 507–514.

[152] Simon Drieschner, Michael Weber, Jörg Wohlketzetter, Josua Vieten, Evangelos Makrygiannis, Benno M. Blaschke, Vittorio Morandi, Luigi Colombo, Francesco Bonaccorso, and Jose A. Garrido. "High surface area graphene foams by chemical vapor deposition." In: *2D Materials* 3.4 (Oct. 2016). ISSN: 20531583. DOI: 10.1088/2053-1583/3/4/045013.

[153] Cinzia Silvestri, Michele Riccio, René H. Poelma, Bruno Morana, Sten Vollebregt, Fabio Santagata, Andrea Irace, Guo Qi Zhang, and Pasqualina M. Sarro. "Thermal characterization of carbon nanotube foam using MEMS microhotplates and thermographic analysis." In: *Nanoscale* 8.15 (Apr. 2016), pp. 8266–8275. ISSN: 20403372. DOI: 10.1039/c6nr00745g.

[154] Fabio Pavanello, Fabio Manca, Pier Luca Palla, and Stefano Giordano. "Generalized interface models for transport phenomena: Unusual scale effects in composite nanomaterials." In: *Journal of Applied Physics* 112.084306 (2012). DOI: 10.1063/1.4759017. URL: https://aip.scitation.org/doi/abs/10.1063/1.4759017.

[155] Fabio Pavanello and Stefano Giordano. "How imperfect interfaces affect the nonlinear transport properties in composite nanomaterials." In: *Journal of Applied Physics* 113.154310 (2013). DOI: 10.1063/1.4801889. URL: https://aip.scitation.org/doi/10.1063/1.4801889.

[156] Philip M. Morse and K. Uno Ingard. *Theoretical Acoustics*. McGraw Hill Book Company, 1968. ISBN: 9780070433304.

[157] Michel Bruneau and Thomas Scelo. *Fundamentals of Acoustics*. Wiley, 2006. ISBN: 9781905209255.

[158] Finn Jacobsen and Peter Møller Juhl. *Fundamentals of General Linear Acoustics*. Wiley, 2013. ISBN: 9781118346419.

[159] Zhi Lin Ngoh, Fei Ni Leong, Roland Yingjie Tay, Matthew David Whiteside, Soon Siang Chng, Jong Jen Yu, Siu Hon Tsang, Dunlin Tan, Geok Ing Ng, and Edwin Hang Tong Teo. "Boron Nitride Coated Three-Dimensional Graphene as an Electrically Insulating Electromagnetic Interference Shield." In: *IEEE MTT-S Inter-*

national Microwave Workshop Series on Advanced Materials and Processes for RF and THz Applications (IMWS-AMP) (2019), pp. 127–129.

[160] Zongping Chen, Wencai Ren, Libo Gao, Bilu Liu, Songfeng Pei, and Hui Ming Cheng. "Three-dimensional flexible and conductive interconnected graphene networks grown by chemical vapour deposition." In: *Nature Materials* (2011). ISSN: 14764660. DOI: 10.1038/nmat3001.

[161] Ranjana Shivakumar et al. "POSS enhanced 3D graphene - Polyimide film for atomic oxygen endurance in Low Earth Orbit space environment." In: *Polymer* 191 (Mar. 2020). DOI: 10.1016/j.polymer.2020.122270.

[162] Andrea C. Ferrari and Denis M. Basko. "Raman spectroscopy as a versatile tool for studying the properties of graphene." In: *Nature Nanotechnology* 8.4 (2013), pp. 235–246. DOI: 10.1038/nnano.2013.46.

[163] Sumio Iijima. "Helical Microtubules of graphitic carbon." In: *Nature* 354 (1991), pp. 56–58.

[164] K S Novoselov, A K Geim, S V Morozov, D Jiang, Y Zhang, S V Dubonos, I V Grigorieva, and A A Firsov. "Electric Field Effect in Atomically Thin Carbon Films." In: *Science* 306.5696 (2004), pp. 666–669. URL: http://science.sciencemag.org/.

[165] C. Zhu, C. Cheng, Y. H. He, L. Wang, T. L. Wong, K. K. Fung, and N. Wang. "A self-entanglement mechanism for continuous pulling of carbon nanotube yarns." In: *Carbon* 49.15 (2011), pp. 4996–5001. DOI: 10.1016/j.carbon.2011.07.014.

[166] Manuela Loeblein. "Boron nitride carbon foams for various thermal applications." PhD thesis. Nanyang Technological University, 2018.

[167] Daschewski Maxim. "Thermophony in real gases : theory and applications." PhD thesis. Potsdam, 2016.

[168] Q. Leclère and B. Laulagnet. "Particle velocity field measurement using an ultra-light membrane." In: *Applied Acoustics* (2008). ISSN: 0003682X. DOI: 10.1016/j.apacoust.2006.11.009.

[169] Quentin Leclère and Bernard Laulagnet. "Nearfield acoustic holography using a laser vibrometer and a light membrane." In: *The Journal of the Acoustical Society of America* 126.124 (2009), pp. 1245–1395. DOI: 10.1121/1.3180132ÍŤ. URL: https://doi.org/10.1121/1.3180132.

[170] Andrew R. Harland. "The application of laser Doppler velocimetry to the measurement of underwater acoustic pressure fields." PhD thesis. Loughborough, 2002. URL: https://dspace.lboro.ac.uk/2134/14061.

[171] Daniele Passeri, Ugo Sassi, Andrea Bettuci, Emanuela Tamburri, Francesco Toschi, Silvia Orlanducci, Maria Letizia Terranova, and Marco Rossi. "Thermoacoustic Emission from Carbon Nanotubes Imaged by Atomic Force Microscopy." In: *Advanced Functional Materials* 22 (2012), pp. 2956–2963. DOI: 10.1002/adfm.201200435.

Modelling and Evaluation of Carbon Based Foam Thermoacoustic Effect for Effective Sound Generation in Liquids

Electroacoustic transducers along with piezoelectric devices are the most widely used methods for acoustic sound generation in gas and liquids. A mechanical movement of a membrane induces fluid vibration thus creating an acoustic wave. The thermoacoustic process on the other hand uses fast paces temperature variations in a sample to excite the fluid (generally air). The rapidly changing temperature generate a compression expansion of the air and thus creates an acoustical wave. Such materials are called thermophones. They were discovered in the same time period as traditional electroacoustic transducers but their limited efficiency coupled with the technological limits of fabrication prevented scientific craze at the time. In 1999 a new thermophone was presented with a significant improvement compared to the samples used a century prior. This article coupled with the newly found ease of access to complex fabrication process of nanomaterials rekindle the interest in thermoacoustic for audio purposes. In this thesis a thorough literature review is presented and a novel multilayer model for thermoacoustic sound generation is derived. This model was solved for plane wave, cylindrical wave and spherical wave generation. Another model based on a two temperatures hypothesis for plane wave generation is also solved to represent more accurately the generation of thick porous thermophones. An extensive analysis of those models allowed for a detailed understanding of the thermoacoustic sound generation: its strengths, weaknesses and differences with traditional speakers. Lastly, experimental investigations of porous carbon foams in partnership with CINTRA Singapore are presented. Validation of the models and insights about the handling of such flexible and lightweighted but fragile samples are presented as well at their potential applications for scientific or commercial purposes.

Keyword Thermoacoustic, Thermophone, Sound Generation, Nanomaterials, Carbon, Porous Media, Theoretical Modelling

Analyse Théorique et Expérimentale de l'Efficacité de Mousse de Carbone pour Génération Acoustique dans des Milieux Visqueux

Les transducteurs électroacoustiques ainsi que les dispositifs piézoélectriques font partie des principales méthodes de génération acoustique dans un gaz ou un liquide. Un mouvement mécanique d'une membrane crée une vibration du fluide générant une onde acoustique. La thermoacoustique en revanche utilise des variations rapides de température d'un matériel pour exciter le fluide (généralement de l'air). Ces changements thermiques rapides créent une compression dilatation de l'air qui va générer une onde acoustique. De tels matériaux sont appelés thermophones. Ces derniers ont été découverts à la même période que les transducteurs électroacoustiques mais leur faible efficacité ainsi que les limitations scientifiques de l'époque ont empêché le domaine de se développer. En 1999 un nouveau thermophone avec des capacités acoustiques bien supérieures à ses prédécesseurs a été présenté. La publication de cet article associé à une plus grande facilité d'accès à des machines permettant la fabrication de matériaux nanostructurés a permis un nouvel engouement pour la thermoacoustique audio. Dans cette thèse une vaste revue de littérature est présentée et un modèle innovant multicouche de génération thermoacoustique en est déduit. Ce modèle est résolu pour la génération d'ondes planes, cylindriques et sphériques. Un second modèle basé sur une hypothèse dite de deux températures est aussi créé pour représenter de façon plus fidèle la génération thermoacoustique dans un milieu poreux épais. Une analyse étendue des résultats découlant de ces modèles est ensuite faite permettant la compréhension des forces, faiblesses et particularités des thermophones par rapport aux transducteurs traditionnels. Enfin une analyse expérimentale de mousses carbonées en partenariat avec CINTRA Singapour est présentée. Cela permet la validation des modèles théoriques et procure une compréhension expérimentale sur la manipulation de ce type de matériaux flexibles et légers mais fragiles, ainsi que leurs potentielles applications scientifiques et commerciales.

Mots-clés Thermoacoustique, Thermophone, Génération Sonore, Nanomateriaux, Carbone, Matériaux Poreux, Modèle Théorique